



ALMA MATER STUDIORUM  
UNIVERSITÀ DI BOLOGNA

## DOTTORATO DI RICERCA IN

Scienze e Tecnologie Aerospaziali

Ciclo 36°

**Settore Concorsuale: 09/A3**

**Settore Scientifico Disciplinare: ING-IND/14**

Geometry Projection for Additively Manufacture Variable Stiffness Continuous  
Fiber-Reinforced Polymer Structures—A Unified Topology Optimization Approach  
for Multi-layered Composite Laminates.

**Presentata da:** *Yogesh Gandhi*

**Coordinatore Dottorato**  
**Prof. Alessandro Talamelli**

**Supervisore**  
**Prof. Giangiacomo Minak**

**Co-Supervisore**  
**Prof. Ana Pavlovic**

Esame finale anno 2024

*Design and optimization  
framework for variable stiffness  
composite laminates considering  
both additive or conventional  
manufacturing processes!*

Yogesh Gandhi  
Department of Aerospace and Science Tech-  
nology  
Doctor of Philosophy



ALMA MATER STUDIORUM  
UNIVERSITÀ DI BOLOGNA

**UConn**  
UNIVERSITY OF CONNECTICUT



UNIVERSITÀ  
DEGLI STUDI  
DI PADOVA



**TU Delft**

## *Abstract*

Continuous fiber fused filament fabrication (CF4) is a layer-by-layer technique used to print carbon fiber-reinforced polymers (CFRPs) with a spatial in-plane variation of the fiber orientation, thus offering great flexibility in fabricating variable-stiffness CFRP laminates (VS-CFRP-Ls). However, not only is the design of VS-CFRP-Ls unintuitive, but the material directionality also introduces a nonconvex design space further amplified by the various VS-CFRP-Ls' design parameters. Designing multi-layered VS-CFRP-Ls, therefore, requires advanced computational design tools—such as topology optimization based on the geometry projection method—to take full advantage of the design freedom compatible with CF4.

This thesis addresses these challenges by developing computational tools for optimizing multilayered VS-CFRP-Ls. Unlike constant stiffness composites, VS-CFRP-Ls lack analytical formulations, necessitating discretization techniques like finite element analysis. The research develops and investigates several topology optimization formulations to streamline the design process, considering CF4's manufacturing constraints and material distribution strategies. The method reduces design variables by employing geometry projection within TO while ensuring manufacturability. Extensions of this approach cater to additive manufacturing requirements, yielding multilayered VS-CFRP-L designs with enhanced mechanical properties. Numerical examples demonstrate the efficacy of the proposed methodology in achieving stiffness-driven VS-CFRP-Ls designs, which can be manufactured using conventional and additive manufacturing processes.

Keywords: topology optimization, continuous fiber, fused-filament-fabrication, variable-stiffness, composite laminates

## Acknowledgments

Although this section may not have any scientific relevance, it holds the most significant value. I am thankful for my family's unwavering support and encouragement and the relationships and friendships I have fostered and strengthened over the last three years. Many of these individuals had been by my side before I embarked on my PhD journey. I am grateful to them for allowing me the freedom and time to explore, allowing me to make mistakes, and always guiding me toward the right path. The meaningful conversations with them helped me challenge my assumptions, whereas some helped me to reboot my mind—allowing me to advance further. I thank them for their reassurance and for always being ready to help me focus on what was important. Lastly, I am thankful for their attentive listening and pretentious-face to understanding my discussions till the end.

At the same time, I am deeply grateful to several experts from various scientific fields who have contributed to the scientific outcome of this thesis. With their valuable guidance and intensive discussions, I can complete this research journey. I express my deepest gratitude to my thesis advisor, Prof. Giangiacomo Minak, for his invaluable guidance, support, and encouragement throughout this research journey. Despite encountering several failures, Prof. Giangiacomo Minak's patience, insightful feedback, and expertise in advanced materials and their utility to manufacture lightweight structures have been instrumental in shaping this thesis.

I am indebted to Prof. Julián Norato from the Department of Mechanical Engineering, University of Connecticut, for his assistance and collaboration during various stages of this research. His expertise in computational topology and shape optimization techniques for the design exploration of novel and highly efficient structures laid the foundation of this research work. I want to thank Prof. Alejandro M. Aragón from the Faculty of Mechanical Engineering, Delft University of Technology, for organizing a sec-

ondment to conduct research at Delft University of Technology in the fall of 2021. With his constant supervision, we investigated advanced techniques for structure optimization, showcasing their versatility in employing various methodologies to achieve structures that could be additively manufactured.

I have been fortunate to cross paths with Prof. Alfonso Pagani from the Department of Mechanical and Aerospace Engineering, Politecnico di Torino. His Ph.D. student Alberto Racionero Sánchez-Majano helped me to understand the crux of MUL<sup>2</sup> software and made it feasible to integrate with my ongoing research fully. A special shout-out to Pierto Cuccarollo, a Ph.D. student at Università degli Studi di Padova, for teaching me the practical aspects of additive manufacturing. I am also thankful to him for sharing his rock climbing expertise and allowing me to experience it firsthand.

# Table of Contents

List of Figures	viii	
List of Tables	xvi	
Nomenclature	xviii	
1	Introduction	1
1.1	3D printing with continuous fiber—An overview	1
1.2	Motivation	3
1.3	Thesis Objectives	5
2	Literature review—Topology optimization approaches for additively manufacturable continuous fiber-reinforced polymers.	9
2.1	Introduction	9
2.2	Topology Optimization for Continuum Structures	13
2.3	Parameterization Schemes for Fiber Orientation	22
2.4	Discussion	35
2.5	Conclusions	41
3	Topology optimization using geometric components made of isotropic materials.	44
3.1	Key ingredients of feature-mapping methods	45
3.2	Geometry projection formulation	48
3.3	Setting and implementation of the optimization problem	52
3.4	Computer Implementation	54
3.5	Examples	55
3.6	Conclusions	62
4	Geometry Projection method for Variable Stiffness Continuous Fiber-Reinforced Polymer Laminates.	68
4.1	Combining Components	71
4.2	Geometry projection formulation for VS-CFRP-Ls based on overlapping criterion.	75

4.3	Elasticity tensor for laminated components	78
4.4	Setting and implementation of the optimization problem	80
4.5	Examples	84
4.6	Summary and conclusions	107
5	Geometry Projection method for Variable Stiffness Continuous Fiber-Reinforced Polymer Laminates—Simple Overlap formulation with length constraint.	110
5.1	Formulation for Simple Overlapping FRBs	112
5.2	Definition of length constraint formulation	115
5.3	Examples	121
5.4	Conclusion	141
6	A Unified Topology Optimization Framework for Multilayered Variable Stiffness Composite Laminates.	143
6.1	Continuous Fiber Used Fabrication—Markforged Printers	143
6.2	Multilayered Composite Laminates—A brief background	147
6.3	Introduction to the Carrera Unified Formulation	149
6.4	Unified Formulation for Multilayered Structure	149
6.5	A Four-Index Fundamental Nucleus	151
6.6	Integrating CUF-based analysis in the geometry projection method	154
6.7	Examples	158
6.8	Conclusion	164
7	Conclusion and Recommendations	166
7.1	Conclusion	166
7.2	Recommendation	168
	References	171
	Appendices	188
A	Examples for Multi-layered Variable-Stiffness Composite Laminate—Simple Overlap formulation	189
A.1	Examples	189
B	Examples for Single layer Variable-Stiffness Composite Laminate—Overlap Criterion	195

## List of Figures

- 1.1 A simple guide to geometry projection method—The method comprises three modules—geometric design space, finite element analysis, and optimization. The high-level parameterized primitives span the geometric design space module, which then projects onto the computational design space discretized using finite elements. The finite element analysis module computes the field variables for the projected arrangements of the primitives on the computational grid. Finally, the optimization modules update the geometric primitives by computing the sensitivities of objective functions and constraints defined in the optimization problem. 8
- 2.1 The flowchart outlines the essential components required to develop a general topology optimization framework, irrespective of the approach. Regularization is a technique widely used in density-based methods, and its implementation is detailed here.[51] 12
- 2.2 Extended design domain and boundary conditions for the state equation (adapted from [54]). 14
- 2.3 Binary Density-based Topology Optimization 18
- 2.4 Continuous Density-based Topology Optimization 18
- 2.5 Illustration of DTO considering anisotropic material via fiber orientation parameterization. 23
- 2.6 Finite elements are considered design variables in DTO: (a) Continuous material orientation; (b) Discrete material orientation. 25
- 2.7 (Left)—Schematic the diagram represents the design variables of an element and parameterizes continuous orientation variables in the discrete-continuous setting. **Right**—Implementation of the multiple print plane to design MBB [96] 29

- 2.8 The illustration describes an algorithm for designing a continuous fiber-reinforced polymer laminate specifically tailored for the geometry projection method. The algorithm proposes a laminate with variable stiffness, optimized using GP and then stacked together to create a multi-layered, optimized laminate. Various CF4 constraints are incorporated during the design process to ensure the final product is ready to print and meets all required specifications. 30
- 2.9 A similar algorithm as described in Fig. 2.8 can be utilized to design single-layered variable-stiffness composite laminate using composite laminate equivalent single-layer theory. The subsequent chapters provide a detailed explanation of these concepts. 31
- 2.10 The example demonstrates the design of MBB using the geometry projection method. The top of the left column shows the MBB beam design region, support, and unit load, whereas the bottom depicts colored penalized element densities for the optimal MBB beam designs. Note that the color denotes the orientation of the rest of the changes. In the right column, iteration histories of an objective function indicate the attained compliance value  $f^{(i)}$  at an iteration  $i$ . [126] 34
- 2.11 **MBB**—post-processed design result of FRC structure with fixed (**top-row**) and varying fiber volume fraction (**bottom-row**) using a micro-structure unit cell with rectangular-shape (**left-column**) and cross-shaped (**right-column**) fiber layout. The black color represents matrix material, and the yellow colored part is fiber material [135]. 36
- 2.12 Typical cross-sectional view of a CF/PA6 filament by optical microscopy [9]. 40
- 3.1 Geometric design variables for a bar 48
- 3.2 Projection of bar on  $x \in \mathcal{D}$  49
- 3.3 **MBB**—The features' initial arrangement in rectangular plates of the aspect ratio of  $1 \times 6$ , which are subjected to supports and unit load, i.e., 3-point bending 56
- 3.4 **MBB**—The density plot for two volume fraction  $\bar{v} \in [0.25, 0.35]$ . Color assignment to bars is based on the bar's orientation to the global coordinate system; thus, it only serves the purpose of visualization for bars made of isotropic material. 57

- 3.5 **MBB**—The design plot for two volume fraction  $\bar{v} \in [0.25, 0.35]$ . Different bar intersections can be observed: merged bars with in-plane width offset, concatenated merged bars, collinear merged bars, and in-plane width stacking of merged bars. 58
- 3.6 **MBB**— The compliance history plot also depicts a large difference in the convergence behavior for two volume fractions  $\bar{v} \in [0.25, 0.35]$  59
- 3.7 **Bridge**—The features' initial arrangement in the rectangular domain of the aspect ratio of  $1 \times 2$ , subjected to supports and uniform distributed load over a non-designable bar. 60
- 4.1 The figure presents a comprehensive outlook on employing the geometry projection technique to design and optimize multi-layered or single-layered variable-stiffness continuous fiber-reinforced polymer laminates. Designing for single-layered VS-CFRP-Ls is based on equivalent single-layer theories, referred to as GP-AM formulations, and is discussed in the chapter and the subsequent chapter. On the other hand, designing for multi-layered VS-CFRP-Ls requires higher-order composite plate theories, and the corresponding formulation is GP-MUL2. 69
- 4.3 **Overlapping Criterion**—Darker grey regions represent overlapping regions  $\omega_e$ , while the lighter grey region depicts fiber mixture. Thus, the overlapping criterion selects the regions whose stack bar's densities,  $\rho_b$ , are equal to 1 for all intersecting FRBs. 71
- 4.2 The dual nature of the geometry projection method is exploited to define the overlapping regions for intersecting FRBs at the density level, which enables the computation of VS-CFRP-L's stiffness matrices—membrane  $D_{me}$ , bending  $D_{be}$ , and shear  $D_{se}$ . The illustration demonstrates the evaluation of membrane stiffness for overlapping bars using the first-shear deformation theory, wherein the out-of-plane thickness is a fixed constant for the ease-in-manufacturable solution. 72
- 4.4 A fiber-reinforced bar with geometric design variables and material orientation. 73
- 4.5 Projecting FRB to the centroid of a finite element using density approach. 73
- 4.6 Color wheel used for density plots to indicate the orientation of the primitive. 85

- 4.7 The features initial arrangement in rectangular plates of varying aspect ratios, which are subjected to different loading conditions, including 3–point bending  $1 \times 6$ , pure torsional  $1 \times 4$ , bending  $1 \times 1$ ; and multi  $1 \times 2$ . 86
- 4.8 **MBB**—The design plot for GP method and converge after 191 iterations. 87
- 4.9 **MBB**—The density plot for GP method and attained compliance is 1.199431. 87
- 4.10 **MBB**—The design plot for GP-AM method and converge after 163 iterations. 87
- 4.11 **MBB**—The density plot for GP-AM method and attained compliance is 1.138311. 88
- 4.12 **MBB**—The design plot for standard-GP method. 90
- 4.13 **MBB**—The density plot for standard-GP method 90
- 4.14 **MBB**—Comparison of the objective and constraint history of the GP method with the GP-AM method on a logarithmic and linear scale plotted on the left and right axes, respectively. 91
- 4.15 **Bending**—The design and their densities for the GP method, considering  $\beta = 100$ . The compliance for a given volume fraction limit 0.5 is 1.396162, and the design converges after 97 iterations. 92
- 4.16 **Bending**—The design and their densities for the GP-AM method, considering  $\beta = 10$ . The compliance for a given volume fraction limit 0.5 is 1.485798, and the design converges after 104 iterations. 93
- 4.17 **Bending**—Comparison of the objective and constraint history of the GP method with the GP-AM method on a logarithmic and linear scale plotted on the left and right axes, respectively. The objective history inset plot from iteration 20 – 70 shows oscillation in the GP method due to rapid changes in membership variables. 96
- 4.18 **Torsion**—The design plot for GP method. The transparency of FRBs depicts the membership variable attained intermediate value, i.e.,  $\alpha < 1$  98
- 4.19 **Torsion**—The density plot for GP method. The compliance for a given volume fraction limit 0.5 is 184.893393. 98
- 4.20 **Torsion**—The design plot for the GP-AM method shows that FRBs’ membership variable always approaches 1. 99
- 4.21 **Torsion**—The density plot for GP-AM method. The compliance for a given volume fraction limit 0.5 is 141.048719. 99

- 4.22 **Torsion**—The design plot for GP method. The transparency of FRBs depicts the membership variable attained intermediate value, i.e.,  $\alpha < 1$ . 100
- 4.23 **Torsion**—The density plot for GP method. The compliance for a given volume fraction limit 0.6 is 135.665506. 100
- 4.24 **Torsion**—The design plot for the GP-AM method shows that FRBs' membership variable always approaches 1. 100
- 4.25 **Torsion**—The density plot for GP-AM method. The compliance for a given volume fraction limit 0.6 is 112.607709. 101
- 4.26 **Torsion**— $\bar{v} = 0.5$ . The objective history plot of the GP method from iteration 10 – 60 showed no oscillation due to the dissolution of FRBs. 102
- 4.27 **Torsion**— $\bar{v} = 0.6$ . The objective history inset plot from iterations 10 – 60 shows oscillation due to large overlapping, which cannot be avoided due to the increase in the volume fraction limit. 103
- 4.28 **Multiload**—The design plot for GP method. The transparency of FRBs depicts the membership variable attained intermediate value, i.e.,  $\alpha < 1$ . 104
- 4.29 **Multiload**—The density plot for GP method. The compliance for a given volume fraction limit 0.5 is 226.575885. 105
- 4.30 **Multiload**—The design plot for the GP-AM method shows that FRBs' membership variable always approaches 1. 105
- 4.31 **Multiload**—The density plot for GP-AM method. The compliance for a given volume fraction limit 0.5 is 195.571698. 106
- 4.32 **Multiload**—The multi-load example using GP and GP-AM methods converges in 186 and 114 iterations respectively. 107
- 5.1 **Simple Overlap**—Darker grey region effective densities,  $\bar{\rho}_{eff}$ , are greater than lighter grey regions, given that the membership variable,  $\alpha$ , is equal to 1 for intersecting bars. The complete region, including intermediate densities, defines an overlapping region,  $\omega_e$ , in simple overlap. 112
- 5.2 Properties of a sigmoid function: Most functional forms share these characteristics—an initial lag with slow growth, rapid exponential growth, and reduced growth rate leading to saturation (adapted from [166]). 118

- 5.3 For  $\ell = 10$ —The plot shows how the steepness of the sigmoid function is increased using a continuation approach to achieve a discrete weight value. 120
- 5.4 The features initial arrangement in rectangular plates of varying aspect ratios, which are subjected to different loading conditions, including 3–point bending  $1 \times 6$ , pure torsional  $1 \times 4$ , bending  $1 \times 1$ ; and multi  $1 \times 2$ . 122
- 5.5 **MBB**—The design and density of all formulations used to optimize single-layer VS-CFRP-L are listed row-wise. Starting with GP, GP-AM with overlapping criterion, and LGP-AM without and with length constraint. 123
- 5.6 **MBB**—The objective history plot demonstrates that the optimization traces a typical smooth convergence behavior for compliance with a sharp drop in the first few iterations, followed by small design variable adjustments in the later optimization stage for with and without length constraint formulation. 124
- 5.7 **Bending**—The optimized design using GP formulation for bending example 127
- 5.8 **Bending**—The optimized design using GP-lAM formulation for bending example 127
- 5.9 **Bending**—The objective history plot depicts that LGP-AM ( $\ell = 0$ ) takes more iterations compared to LGP-AM( $\ell > 0$ ) formulation. This is because small features get stuck in the overlapping bars listed in Table 5.4. Moreover, LGP-AM( $\ell > 0$ ) takes a similar number of iterations to converge, irrespective of the imposed threshold length,  $\ell$ , on FRBs. This indicates that small features cause manufacturing issues and lead to optimizer oscillation. The plot is arranged in increasing order of  $\ell$ . 128
- 5.10 **Bending**—The components are imposed with various minimum length constraints, ranging from 0 to 15 with 5 unit increments—design plotted column-wise. 130
- 5.11 **Bending**—The components are imposed with various minimum length constraints, ranging from 0 to 15 with 5 unit increments—density plotted column-wise. 131
- 5.12 **Torison**—The objective history plots for volume fraction constraint of 0.5 with corresponding length thresholds of  $\ell = \{0, 5, 10\}$  are shown. 134
- 5.13 **Torison**—The objective history plots for volume fraction constraint of 0.5 with corresponding length thresholds of  $\ell = \{0, 5, 10\}$  are shown. 135

- 5.14 **Torison**—Adjacent design and density plots for volume fraction constraint of 0.5 with corresponding length thresholds of  $\ell = \{0, 5, 10\}$  are shown. 136
- 5.15 **Torison**—Adjacent design and density plots for volume fraction constraint of 0.5 with corresponding length thresholds of  $\ell = \{0, 5, 10\}$  are shown. 137
- 5.16 **Torison**—The LGP-AM design ( $\ell = 10$ ) is plotted for two different initial conditions. The bound on the design variables is given in (5.18), and the volume fraction is set to  $\bar{v} = 0.5$ . 139
- 5.17 **Multiload**—The design, density, and objective history plot of gP-IAM and LgP-IAM ( $\ell = 10$ ) are illustrated in column-wise fashion, respectively. 142
- 6.1 **Bending**—The design plots for volume fraction constraint of 0.4 for each layer are arranged in two columns—the 1<sup>st</sup> column contain the 1<sup>st</sup> and 2<sup>nd</sup> layers and 2<sup>nd</sup> column contain the 3<sup>rd</sup> and 4<sup>th</sup> layers. 156
- 6.2 **Bending**—The design plots for volume fraction constraint of 0.4 for each layer are arranged in two columns—the 1<sup>st</sup> column contain the 1<sup>st</sup> and 2<sup>nd</sup> layers and 2<sup>nd</sup> column contain the 3<sup>rd</sup> and 4<sup>th</sup> layers. 157
- 6.3 **Bending**—The optimized design using GP method. 159
- 6.4 **Bending**—The optimized design using GP-AM method. 159
- 6.5 **Bending**—The graph shows the history of objectives and constraints for all the layers on a logarithmic and linear scale, plotted on the left and right axes, respectively. Each iteration generates four data points for every layer. Therefore, the x-axis represents the total number of iterations to converge all the layers. The first layer converged on the 89<sup>th</sup> iteration, the 353<sup>rd</sup> iteration overall. The second layer converged on the 79<sup>th</sup> iteration and the 314<sup>th</sup> iteration overall. The third and fourth layers converged on the 90<sup>th</sup> iteration, which is the 359<sup>th</sup> and 360<sup>th</sup> overall. 160
- 6.6 **Torison**—The design plots for volume fraction constraint of 0.4 for each layer. 161
- 6.7 **Torison**—The density plots for volume fraction constraint of 0.4 for each layer. 162

- 6.8 **Torsion**—The graph shows the history of objectives and constraints for all the layers on a logarithmic and linear scale, plotted on the left and right axes, respectively. Each iteration generates four data points for every layer. Therefore, the x-axis represents the total number of iterations to converge all the layers. The second layer converged on the 81<sup>th</sup> iteration, the 322<sup>nd</sup> iteration overall. The first, third, and fourth layers converged on the 93<sup>rd</sup> iteration, which is the 370, 371<sup>st</sup> and 372<sup>nd</sup> overall. 163
- 6.9 **Torsion**—The optimized design using GP method. 164
- 6.10 **Torsion**—The optimized design using GP-AM method. 164
- 7.1 **Method of Cells**—Illustration of a laminate whose plies are now represented with micromechanics, thereby incorporating the detail of the fiber and matrix constituent materials at a lower length scale. Adapted from [182] 170
- A.1 Comparing GP and gP-IAM design for a plate under unit bi-axial load. 190
- A.2 Comparing GP and gP-IAM design for a plate under shear load. 192
- A.3 Design and density plots for multi-layered VS-CFRP-L structures with variable volume fractions—analysis considers bi-axial and shear loading conditions and their respective boundary conditions. 194
- B.1 **Bending**—The plot for volume fraction limit of  $\bar{v} = 0.50$  195
- B.2 **Torsion**—The plot for volume fraction limit of  $\bar{v} = 0.50$ . The final compliance achieved is 173.642046, and the design converged in 253 iterations. 196
- B.3 **Torsion**—The plot for volume fraction limit of  $\bar{v} = 0.60$ . The final compliance achieved is 157.389650, and the design converged in 323 iterations. 196
- B.4 **Multiload**—The plot for volume fraction limit of  $\bar{v} = 0.50$ . The final compliance achieved is 192.429452, and the design converged in 220 iterations. 197

## List of Tables

- 2.1 Various attributes and comparison of enumerated parameterization techniques. 33
- 3.1 Material properties used for all the examples 55
- 4.1 Material properties used for all the examples 84
- 4.2 For a given laminate<sup>1</sup> configuration, stiffness matrices' components are used for GP and GP-AM method. 97
- 5.1 **MBB**—The compliance value for all the geometry projection formulations developed to optimize VS-CFRP-L. 124
- 5.2 **MBB**—FRBs' length and membership values are tabulated—for LGP-AM methods—only for the bars that define the final topology as shown in Fig. 5.5. The minimum lengths of FRBs achieved by LGP-AM are bolded when the length's threshold value is set to  $\ell = 10$ . 126
- 5.3 **Bending**—The compliance value for different length constraint 127
- 5.4 **Bending**—The lengths, membership variable, and their corresponding weight for FRBs achieved by LgP-lAM when the length's threshold value is set to  $\ell = \{0, 5, 10, 15\}$  are shown. For gP-lAM, a special case of LGP-AM ( $\ell = 0$ ) results in non-manufacturable design features. Implementing threshold value,  $\ell > 0$  still results in the membership variable acquiring intermediate values; however, the corresponding weights attain a discrete value based on the bar's length in the design. Tabulated data indicates that the design does not retain intermediate membership value by augmenting the geometry projection method with a weighting mechanism because their corresponding weights always attained discrete values. 132

- 5.5 **Torsion**—The compliance values for two different volume fraction limits are indicated for comparison among formulations. 133
- 6.1 Elastic material properties of Onyx[171] 144
- 6.2 Anisotropic material properties of carbon fiber [171] 144
- 6.3 The first five Legendre polynomials 151

## Nomenclature

$\tau, s$	Expansion function indexes
$\sigma$	Stress vector
$B$	Differential operator of the strain-displacements relations
$F$	Load vector
$\mathbf{U}, \mathbf{u}$	Displacement vector
$\delta$	Virtual variation
$\kappa$	Shear correction factor
$\mathbf{e}_1, \mathbf{e}_2, \mathbf{e}_3$	Material Cartesian reference system
$\mathbf{k}^{\tau sij}$	Fundamental nucleus of the stiffness matrix
$\mathbf{u}_\tau$	Generalized displacement vector
$\mathbf{u}_{\tau i}$	Nodal displacement vector
$\nu$	Poisson's ratio
$\psi$	Rotation
$\rho$	Material density variable
$\sigma_{xx}, \sigma_{yy}, \sigma_{zz}$	Axial stress components
$\sigma_{xy}, \sigma_{yz}, \sigma_{xz}, \tau_{xy}, \tau_{yz}, \tau_{xz}$	Shear stress components
$\theta$	Material orientation
$\varepsilon$	Strain vector
$\varepsilon_{xx}, \varepsilon_{yy}, \varepsilon_{zz}$	Axial strain components
$\varepsilon_{xy}, \varepsilon_{yz}, \varepsilon_{xz}, \gamma_{xy}, \gamma_{yz}, \gamma_{xz}$	Shear strain components
$b$	Bar index
$C$	Hooke's law stiffness matrix
$C_{11}, C_{12}, C_{21}, C_{13}, C_{23}, C_{66}$	Hooke's law stiffness coefficients
$E$	Young's modulus
$F_\tau, F_s$	Expansion functions
$G$	Shear modulus
$i, j$	Shape function indexes

$K$  Stiffness matrix  
 $k$  Layer index  
 $k_{xx}^{\tau sij}, k_{xy}^{\tau sij}, \dots, k_{zz}^{\tau sij}$  Components of the stiffness matrix fundamental nucleus  
 $N_i, N_j$  Shape functions  
 $u, v, w$  Displacement components  
 $V$  Volume  
 $x, y, z$  Global Cartesian reference system

## Introduction

### 1.1 3D printing with continuous fiber—An overview

Designing continuous fiber-reinforced polymer (CFRP) structures for 3D printing is a complex process involving several levels of consideration. These levels can be classified into three categories, each of which has multiple variables that can impact the final properties of the CFRP structures—manufacturing processes, materials, and structures. This multi-level design approach allows for a wide range of applications for 3D-printed CFRP structures, which has been the subject of increasing interest in recent studies. By carefully considering each level of design, designers can create high-quality CFRP structures that meet the specific needs of their intended applications.

**Manufacturing processes** At this level, optimizing 3D printing and slicing parameters can improve the microstructural characteristics and mechanical properties of the final product while also minimizing manufacturing defects. This level of consideration is crucial for ensuring that the CFRP structures are built with precision and accuracy, resulting in a high-quality final product.

**Material level** By selecting suitable fibers and matrix materials, designers can achieve synergistic reinforcement of the composite material, enhancing structural performance. This level of consideration involves a careful balance of multiple variables, such as fiber length, orientation, and volume fraction, as well as the choice of matrix material. Further literature on designing and optimizing CFRP structures using conventional manufacturing processes can be utilized and applied at this level.

**Structures level** The mechanical performance of CFRP structures can be significantly influenced by the cell geometrics, patterns, and filling density at the structure level. This consideration requires a thorough understanding of the final product's intended application and the specific mechanical properties needed to meet

the requirements. By carefully selecting the appropriate cell geometries, patterns, and filling densities, designers can ensure that the final CFRP structure meets all necessary mechanical requirements.

### 1.1.1 Classification of Continuous Fiber-Fused Filament Fabrication Process

Various techniques have been developed to print composites reinforced by continuous fibers. Continuous fiber-fused filament fabrication (CF4) processes are broadly classified as in-situ or in-line impregnation methods using dry fiber bundles and applying pre-impregnated towpregs.

**In-situ impregnation** The process involves feeding continuous dry fibers and thermoplastic matrix filament into the print head simultaneously in designated proportions. The thermoplastic polymer is then heated above its melting point in the nozzle. At the same time, the dry fibers are pre-heated before being impregnated with the molten thermoplastic resin within the nozzle. The impregnated fibers and molten polymer are then extruded and deposited directly for 3D printing. This printing method has been extensively studied and has yielded successful results in manufacturing various CFRS structures, such as corrugated, honeycomb, sandwich, diamond cellular, and 4D lightweight structures. The in-situ impregnation process is a versatile and efficient method for producing high-quality composites reinforced by continuous fibers.

**Inline impregnation** The process uses continuous dry fibers like the in-nozzle impregnation method. However, the dry fibers were impregnated before being transported into the print nozzle. This process was a complex approach in CFRC 3D printing because it required multiple manufacturing steps to co-occur.

**Towpreg Extrusion** "Towpreg extrusion" is often referred to as "fused deposition modeling" in the 3D printing industry. "Fused filament fabrication" (FFF) is also used interchangeably with FDM, which involves printing a thin strand of polymer called a filament, often compared to spaghetti. FFF can be used for printing using different filaments, such as unreinforced, chopped fiber-filled, or continuous fiber-reinforced filaments. "Continuous filament fabrication" (CFF), on the other hand, refers explicitly to 3D printing using continuous fiber reinforcement. In the Towpreg Extrusion process, Towpreg filaments provide convenience as they contain

a polymer matrix and continuous fibers and can be heated and extruded without any additional material. This process was quite convenient since it splits the complexity of the filament preparation from the printing process.

**Co-extrusion with Towpreg** Instead of dry fiber, Prepreg continuous fibers can be co-extruded using the towering process, which feeds prepreg filament and matrix material. Both filaments are heated in a nozzle and co-extruded together, with the matrix in the prepreg filament identical to that in the co-extrusion polymer.

**In-situ consolidation** Towpreg or Prepreg filaments are consolidated at the nozzle through an external energy source during deposition. This is a scaled-down version of thermoplastic automated fiber placement (AFP), where the input thermoplastic towering/prepreg tape is consolidated when deposited.

### 1.1.2 Limitations of CF4 process

The strength of 3D-printed carbon fiber reinforced polymer (CFRP) structures depends on how well the fibers are impregnated with the matrix material. However, it's hard to compare impregnation during 3D printing or towered filament production to traditional molding processes because of the low pressure and short impregnation time. In-situ impregnation is particularly problematic because sometimes the matrix material doesn't fully impregnate the fibers, exposing them. Even 3D-printed towering filaments can have defects due to low processing pressure. Size is also a challenge for 3D printing CFRP structures. Printers with fiber-cutting devices have a minimum unit size based on the distance between the cutting devices and the nozzle. For printers without fiber-cutting devices, the cell size can't be smaller than the diameter difference between the nozzle and the fiber bundles. Moving nozzles can cause continuous fibers to be out of place, and the size of the printing platform determines the maximum size of the structures that can be made. Achieving the desired shape for CFRP structures with high-stiffness fibers, large curvature, and small cells without mold restraint is hard.

## 1.2 Motivation

The aerospace, automotive, maritime, and wind-energy industries constantly face challenges in reducing the weight and cost of structures. Therefore, one approach to reducing the weight of structures is to use lighter materials than metals, such as CFRP materials.

These materials offer higher stiffness-to-mass and strength-to-mass ratios than metallic materials, making them a competitive option for lightweight structural design. Moreover, CFRP materials provide additional degrees of freedom in optimization. It is possible to control the anisotropy of the material and adapt it to attain the desired stiffness and stress distribution within the structure. Furthermore, CF4 enables the printing of CFRP material with a spatial variation of the fiber orientation, thus offering great flexibility in fabricating CFRP structures.

Designing composite structures is a challenging task. Composite structures are intricate to optimize due to various design variables and non-convex design problems with multiple solutions. When it comes to variable stiffness laminates, the complexity of the design increases as the optimization problem is no longer limited to a single laminate design but essentially involves obtaining an optimal layup for every point in the structure. The design problem becomes even more complicated when ensuring fiber continuity and laminate manufacturability is necessary. There are a large number of design variables and constraints associated with the design of composite structures. Therefore, advanced computational design tools—such as topology optimization—are required to take full advantage of the design freedom compatible with CF4.

Topology optimization is a technique that involves finding the optimal layout of material distribution, considering an objective function and constraints such as total mass or compliance. Topology optimization is a well-established research area in the design of metallic isotropic structures. It is a numerical design tool to generate structural concepts with optimal load paths to meet specific functional requirements. This tool has helped design lightweight, high-performance structures with 1D, 2D, and 3D stress states. Topology optimization techniques have been extended to design "3D printed" parts. As confidence in designing and manufacturing 3D-printed parts has increased, so has the complexity of part geometry and dimensionality. However, while topology optimization yields end-use structural parts that meet functional requirements for metallic parts, its usefulness is in designing 3D-printed parts. However, TO tools that tailor the CFRP material properties while optimizing the structural topology are limited. Therefore, there is a need to develop topology optimization of spatially CFRP structures. However, addressing this need poses a significant challenge.

Designing 3D-printed CFRP parts using topology optimization techniques is a complex process. One of the biggest challenges is determining how carbon fibers in parts can improve their stiffness and strength. CFRP materials comprise a reinforcement

phase embedded in a continuous phase. The fiber provides high-performance load-carrying properties, while the matrix acts as a binder, holding the fibers together. However, the matrix has lower load-carrying properties. This means the composite material and the part need accurate models to predict their behavior. Additionally, the inherent anisotropy of fiber-reinforced composite materials must be considered during design. This requires the simultaneous design of both the topology and reinforcement orientation, which is a challenging computational problem. Topology optimization involves thousands of design variables, and incorporating reinforcement orientation adds more variables, making the situation even more complex. The adoption of topology optimization for continuous-fiber additive manufacturing faces a significant challenge in computational tractability. Additionally, the limitations of existing manufacturing hardware pose a hurdle. All these limitations must be incorporated into a single optimization framework to understand the correlations of several design parameters better.

### 1.3 Thesis Objectives

On the other hand, manufacturing techniques that are comparatively restrictive in design, such as automated fiber placement (AFP) and automated tape laying (ATL), are paving the way for the increased use of VS-CFRP-Ls [1, 2] at an industrial level. These techniques allow for the manufacturing of VS-CFRP-Ls with fiber tows that conform to curvilinear paths [3, 4], providing greater confidence in their use on a larger-scale application as these techniques are less prone to manufacturing defects and can be further post-processed using conventional consolidation techniques, for example, autoclave. These novel manufacturing processes gradually outdated the subtractive manufacturing approaches because of their capabilities in tailoring the structures' mechanical performance, being cost-effective and time-efficient, and making it easy to manufacture large and complex structures. Most importantly, they prompt a circular economy. Still, manufacturing quality can be poor compared to conventional techniques, and several ongoing research studies are pushing both from the simulation and experimental front. In the same spirit, this thesis is another step toward addressing the challenges posed by CF4, discussing adopted strategies to achieve better mechanical performance and printability, and finally proposing a novel methodology to attain additively manufactured VS-CFRP-Ls demonstrated through several benchmark problems and concluding with the method limitation and possible strategies to overcome these limitations.

The commercially available CF4 process is still limited to a layer-by-layer technique used to print CFRP structures with a spatial in-plane variation of the fiber orientation, thus offering great flexibility in fabricating variable-stiffness CFRP laminates (VS-CFRP-Ls) that can be either single layer or multilayer.

Our study focuses on VS-CFRP-Ls—an assembly of layers (plies or laminae) with different fiber orientations tailored to attain the required mechanical properties, e.g., to maximize the stiffness-to-weight ratio. In addition to the fiber orientation in each layer, the stacking sequence, i.e., the order in which individual laminae are placed on top of one another, determines the overall VSCL's mechanical response. Although these parameters provide significant design freedom, designing the composite structure to target a given mechanical response is not straightforward due to the large number of design variables (fiber orientation, stacking sequence, and thickness) and several constraints. These constraints include a requirement to ensure the continuity in the structure, such as a maximum ply drop [5, 6] and the 10% rule (namely, that at least 10% of the layers has a fiber reinforcement in one of the quad orientations, i.e., 0, 90, 45, and 135) [7], among others. These constraints help mitigate the effects of membrane-bending, membrane-shearing, and bending-shearing coupling terms. Exploring the vast design space of VS-CFRP-Ls thus mandates computational analysis and design tools, which is the main objective of the thesis.

Moreover, augmenting the design variables space with material distribution strategies and obtaining autoclave-level mechanical properties through CF4 is challenging. Studies have reported that the comparatively high void content (10%-12%) and poor interfaces severely affect the mechanical performance of printed CFRP composites [8, 9]. Thus, adopting computational design tools such as topology optimization has become a design practice that accommodates CF4's more advanced manufacturing capabilities and constraints. The third focus is on developing performance-driven design practice that falls within the realm of design for additive manufacturing (DfAM), thus attaining ready-to-manufacture VS-CFRP-Ls. Different from the laminate of constant stiffness composites [10], optimizing VS-CFRP-Ls is challenging since the analytical formulations are restricted to simple geometry with limited variation in fiber orientation [1, 2]. The arrangement of material in the structure, the orientation, layer count, and thickness of the layers can vary throughout the VS-CFRP-Ls. Consequently, VS-CFRP-Ls are analyzed using discretization techniques, such as the finite element method (FEM), assuming a constant fiber orientation within each finite element. This discretization enables the use of analytical methods, such as composite laminate theories, and

facilitates the representation of variations in material constituents within the laminate. Thus, the material's constituents assigned to these discretized elements constitute the design space. As a result, optimizing VS-CFRP-Ls must stay within the inordinately large number of design variables. Therefore, the second goal is to adopt TO computational design tools, which can dramatically reduce design variables in the optimization process without sacrificing the enriched design space offered by CF4's manufacturing capabilities.

The research is built upon geometry projection—a topology optimization approach—and adopted to design and optimize multilayered variable stiffness composite laminates (MUL-VSCLs) to achieve these objectives. The method uses geometric primitives such as bars, described by geometric parameters that are then mapped onto a density field, which is discretized via a fixed mesh in the thesis, as illustrated in Fig. 1.1. This approach, which considers both the material distribution and fiber orientation, has an advantage over density-based methods, as it reduces the number of design variables and limits the spatial distribution of the fiber orientations to attain a readily manufacturable design. As a result, several extensions of the geometry projection method are formulated for designing additively manufacturable VS-CFRP-Ls, and numerical examples for minimizing compliance demonstrate the applicability of the proposed methodology.

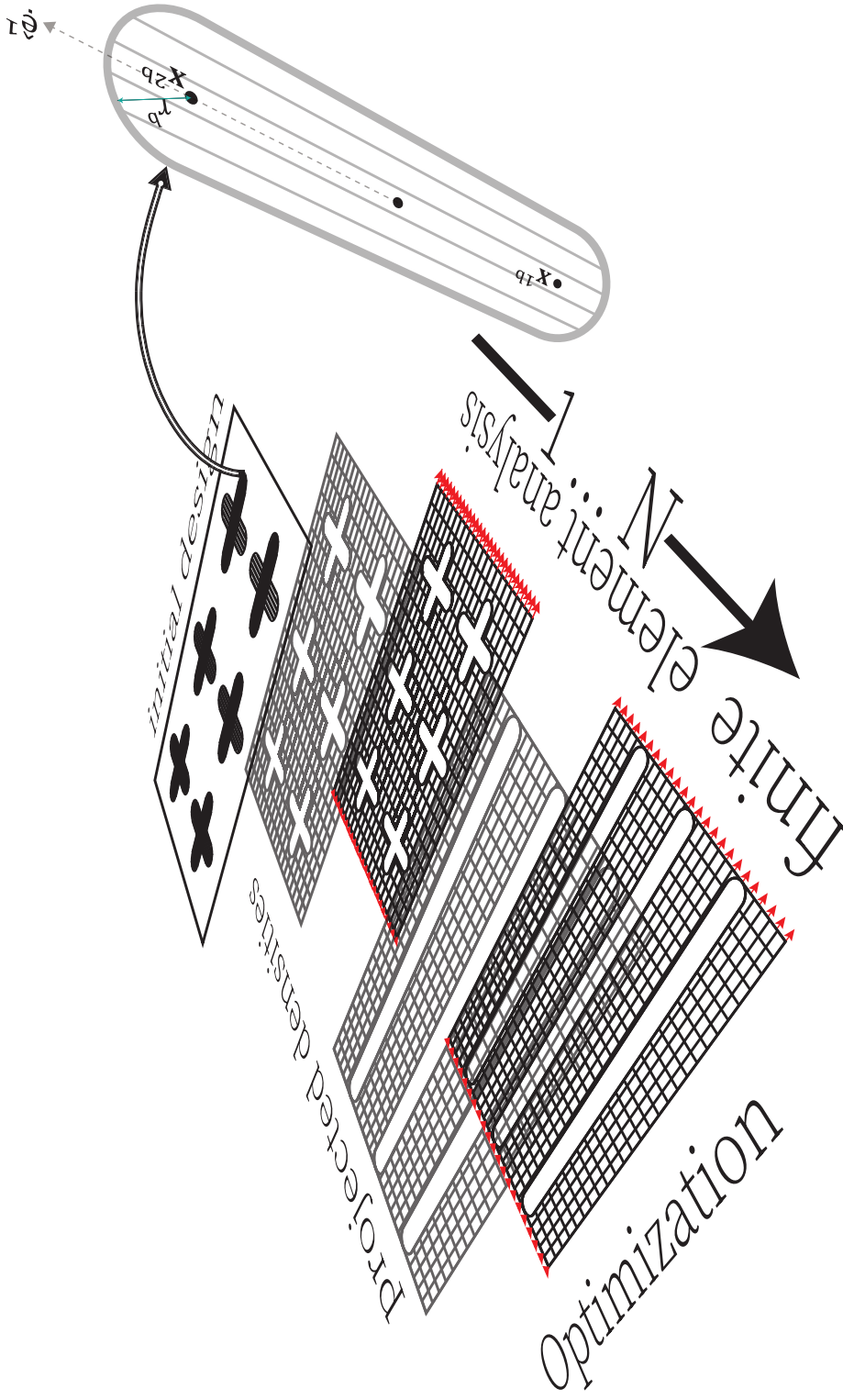


**Figure 1.1:** A simple guide to geometry projection method—The method comprises three modules—geometric design space, finite element analysis, and optimization. The high-level parameterized primitives span the geometric design space module, which then projects onto the computational design space discretized using finite elements. The finite element analysis module computes the field variables for the projected arrangements of the primitives on the computational grid. Finally, the optimization modules update the geometric primitives by computing the sensitivities of objective functions and constraints defined in the optimization problem.

## *Literature review—Topology optimization approaches for additively manufacturable continuous fiber-reinforced polymers.*

### 2.1 Introduction

**Continuous Fiber Fused Filament Fabrication:** The cost-effective and commercially available additive manufacturing (AM) technologies, also known as 3D printing (3DP), eliminate many of the limitations that previously plagued the manufacturing of highly-tailored structural performance for multi-functional [11] and multi-physics [12] applications. Moreover, AM offers unique capabilities to realize the next-generation lightweight structures with great potential for several major industries, such as aerospace [13, 14], automotive [15], and medical [16] sectors. AM techniques can uniquely fabricate highly complex shapes without substantially increasing fabrication costs. In addition, reducing manufacturing preparation time makes these technologies viable for large-scale industries. Moreover, it offers lattice structures, which are lightweight designs compared to solid-filled parts. Thus, AM provides diversification of design to meet the requirements of multifunctional materials, such as weight reduction [17] and the ability to dissipate energy [18], heat [19], and vibrations [20].

Additive manufacturing (AM) encompasses various assembling processes, including material extrusion, vat polymerization, powder bed fusion, material jetting, binder jetting, and sheet lamination. Fused filament fabrication (FFF) is a type of material extrusion that offers low costs and short production cycles, making it advantageous over others. However, FFF-printed polymer parts reinforced with short fibers fall short in mechanical strength compared to those manufactured using conventional tools and continuous fiber-reinforced composite laminate<sup>21,22</sup>. To address this issue, continuous fiber filament fabrication (CF4) was developed to reduce distortion warping and fiber tension to prevent nozzle

<sup>21</sup> Parandoush *et al.*, "A review on additive manufacturing of polymer-fiber composites," 2017.

<sup>22</sup> Sano *et al.*, "3D printing of discontinuous and continuous fibre composites using stereolithography," 2018.

clogging and automatically endowed with greater control of the anisotropic properties of the fabricated structures, maximizing their strength and stiffness.

The categorization of CF4 (continuous fiber-fused filament fabrication) can be based on impregnated fiber filaments, such as out-of-nozzle impregnation, in-nozzle impregnation, and semi-impregnated FRC filaments [23]. This process involves accommodating a coaxial or dual extruder system where fiber filaments are impregnated during printing. The thermoplastic filaments commonly used in this process are amorphous, with acrylonitrile butadiene styrene (ABS), poly-lactic acid (PLA), and PEEK (poly-ether-ether-ketone) being the most common—continuous fibers can be carbon, glass, natural fibers, etc. Several studies [8, 9, 24] compare the mechanical performance of CF4 printed parts to the same structure manufactured by traditional processes. The studies show that the CF4 printed part exhibits a higher mechanical performance than the traditional one. However, the limitation of existing CF4 is the inability to ensure strong interlamellar adhesion between adjacent layers in the build direction, leading to a higher delamination tendency due to poor inter-layer adhesion. Voids are intrinsic structural defects that can form for several reasons, such as the heterogeneous diameters of the filament, uneven matrix distribution, poor filament impregnation, and fiber-rich regions. The layer-by-layer process and the printed bead's shape also cause imperfect overlapping of the beads and void formation between the adjacent beads and layers. These voids are responsible for prospective structural failure. Lastly, a critical review of CF4, including its mechanisms, investigations of CF4 materials, and process parameters, is detailed in the review by Kabir *et al.* .

CF4 technology, despite its limitations, enables the fabrication of continuous fiber-reinforced polymers (CFRP) with continuous spatial variations<sup>26</sup> in fiber angle and volume fraction, thus expanding the design space compared to traditional laminate structures [10]. Additionally, this technology allows for out-of-plane variations in fiber angle due to the self-supporting characteristics of the composite material. Studies have shown that optimizing fiber orientation can significantly improve the structural performance of FRC materials such as stress concentration [27], stiffness [28], buckling load [29], and natural frequency [30]. Therefore, the design of FRC structures requires optimization methods that reflect the design freedom offered by CF4 technology while considering its constraints<sup>31</sup>. Such performance-driven design practice falls within the realm of design for additive manufacturing (DfAM) [32].

<sup>26</sup> Ghiasi *et al.*, "Optimum stacking sequence design of composite materials Part II: Variable stiffness design," 2010.

<sup>31</sup> Xu *et al.*, "A review on the design of laminated composite structures: constant and variable stiffness design and topology optimization," 2018.

**Topology optimization approaches:** Topology optimization (TO), one of the DfAM methods, is an iterative design tool to optimize a quantifiable objective while sustaining loads, constraints, and boundary conditions. In isolation, TO is frequently adopted to design structurally sound parts and has subsequently surpassed design tools, such as shape and size optimization. The seminal work of Bendsøe and Kikuchi[33] introduced the concept of TO for the homogenization method; since then, TO has developed rapidly. TO approaches can be summarized as follows: the homogenization method [33], the Solid Isotropic Material with Penalization (SIMP) method<sup>34,35</sup>, the level set method<sup>36,37</sup>, the Evolutionary Structural Optimization (ESO) method<sup>38</sup>, and the Phase Field<sup>39</sup>. The details of these approaches are discussed in the review papers [40–42], and some emerging TO methods for smooth boundary representation include the ‘Metamorphic Development Method’ (MDM) [43] and the ‘Moving Morphable Method’ (MMM)<sup>44</sup>. The general architecture of TO starts with the definition of maximizing or minimizing a single or multi-target objective function to fulfill a set of constraints such as volume, displacement, or frequency [45]. Then, as part of an iterative process, design variables, finite element analysis, sensitivity analysis, regularization, and optimization steps are repeated until convergence is achieved [46], as depicted in Fig(2.1). Interested readers can find comprehensive studies on topology optimization, including extensive reviews of topology optimization approaches [41, 47–49]. These studies cover the ability to utilize them in various applications and their feasibility for additive manufacturing technologies [32, 50].

Topology optimization of fiber-reinforced composite/polymers (FRC/Ps) structures is a complex process that involves several variables, including material distribution, fiber orientation, and material volume fractions—these attributes for the FRC structures are either optimized simultaneously or sequentially. However, sometimes only one or a few of these attributes are selected for optimization, given the numerous parameters involved in the process and extensive research on optimizing composite structures over the last few decades [52, 53]. Therefore, to construct and understand the TO approach for continuous FRP (CFRP), this chapter briefly introduces the commonly used topology optimization approach, which includes density-based and level-set methods and gradient-based schemes. It focuses on critical works that have been carried out to develop topology optimization methods for additively manufacturable Fiber-Reinforced Polymer (FRP) structures. Additionally, it elaborates on the procedures that enable material anisotropy in the available topology optimization approaches. Moreover, several papers have extended the sug-

34 Bendsøe, “Optimal shape design as a material distribution problem,” 1989.

35 Rozvany *et al.*, “Generalized shape optimization without homogenization,” 1992.

36 Wang *et al.*, “A level set method for structural topology optimization,” 2003.

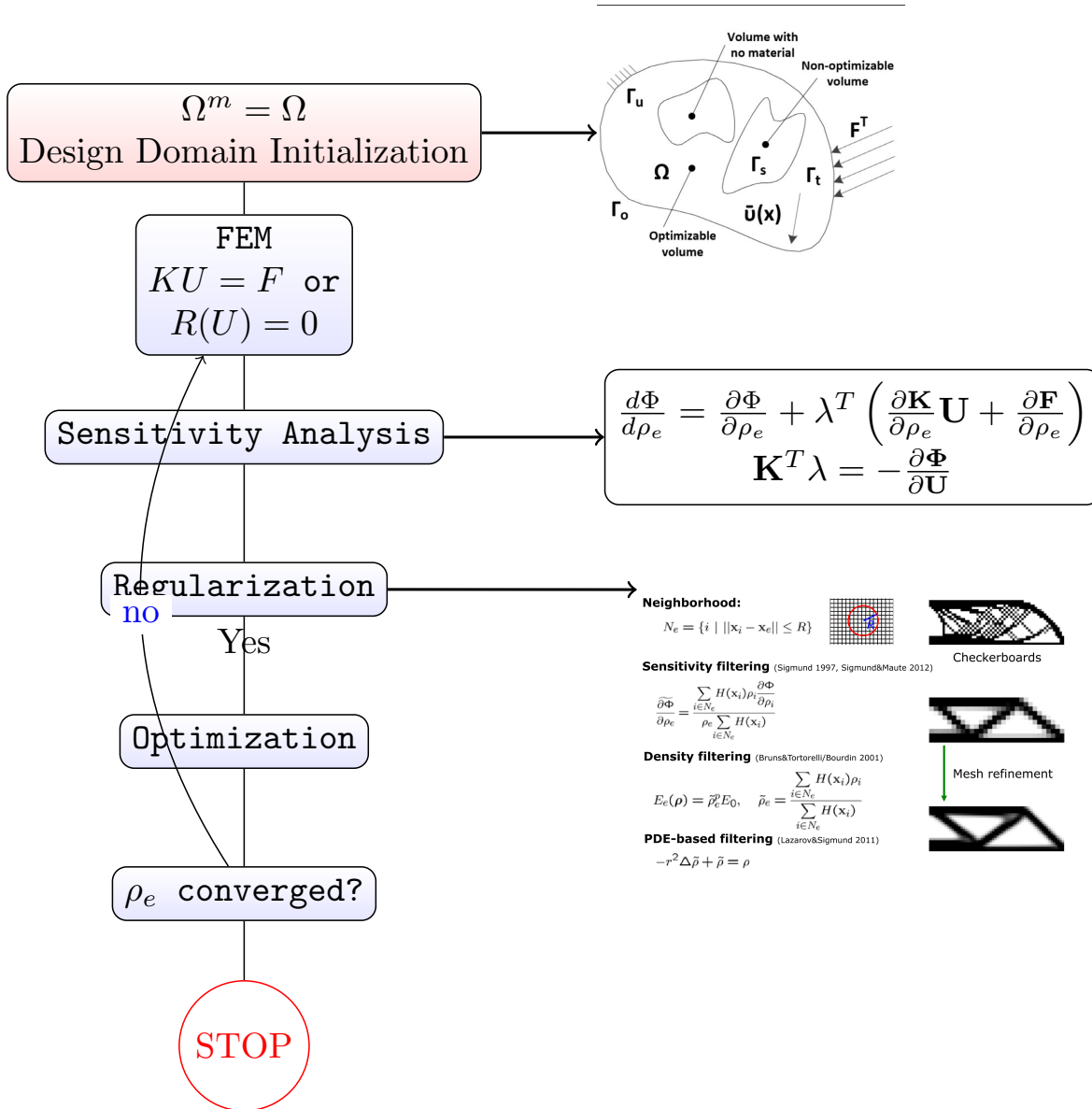
37 Allaire *et al.*, “Structural optimization using sensitivity analysis and a level-set method,” 2004.

38 Xie *et al.*, “A simple evolutionary procedure for structural optimization,” 1993.

39 Bourdin *et al.*, “Design-dependent loads in topology optimization,” 2003.

44 Liu *et al.*, “Additive Manufacturing-Oriented Design of Graded Lattice Structures Through Explicit Topology Optimization,” 2017.

**Figure 2.1:** The flowchart outlines the essential components required to develop a general topology optimization framework, irrespective of the approach. Regularization is a technique widely used in density-based methods, and its implementation is detailed here.[51]



gested methodologies to study multi-physics and multi-objective measures or adapt them for numerical improvement or specific applications. Although many references are available, the chapter includes only essential ones for brevity. The presented information in this chapter aims to provide a comprehensive understanding of the topology optimization approach and its applications in

designing and optimizing CFRP structures.

## 2.2 Topology Optimization for Continuum Structures

Structural optimization can be divided into three main types: size, shape, and topology. Size optimization focuses on finding the best structural design by changing the size parameters of a structure or component, such as the cross-sectional area of a truss bar or the thickness of a plane sheet. Shape optimization works with a fixed topology and a subset of allowable shapes to optimize the structure's performance by changing the shape of its boundary.

Topology optimization is a numerical technique that distributes material over the design space while considering boundary and loading conditions. It is defined by a set of performance criteria, constraints, and bounds on the design variables, which are unknown quantities optimized for the nested optimization problem. The finite element method (FEM) is used to evaluate the design performance, and the design is optimized using either gradient-based mathematical programming techniques or non-gradient-based algorithms. The method relies on repeated analysis and update steps, guided mainly by the gradient computation.

An objective function  $\mathcal{F}$  represents the quantity that must be minimized or maximized to improve the system's performance. The characteristics function  $\chi_\omega$  is associated with the parameter  $\omega$ , which defines the allowable topology  $\mathcal{O}$  in the design domain,  $\Omega \subseteq \mathbb{R}^d$ , for the boundary value and optimization problem. The constraints  $G_i$  are imposed on the allowable topologies, thus ensuring the problem is well-posed, i.e., regularization scheme. The design domain is an extended domain that includes all possible topologies, i.e.,  $\omega \subseteq \Omega \forall \omega \in \mathcal{O}$ . It facilitates the description of the governing boundary value problem. Therefore, the general optimization problem can be expressed as:

$$\begin{aligned}
 \min_{\chi_\omega} : & \mathcal{F}(\chi_\omega, \mathbf{U}) \\
 & := \int_{\Omega} f(\chi_\omega, \mathbf{U}) d\mathbf{x} \\
 \text{s.t.} : & G_0(\chi_\omega) = \int_{\Omega} \chi_\omega(\mathbf{x}) d\mathbf{x} - |\Omega_d| \leq 0, \\
 & : G_i(\chi_\omega, \mathbf{U}) \leq G_i^*, \quad i = 1, \dots, K \\
 & : \chi_\omega(\mathbf{x}) = \begin{cases} 0 \text{ or } 1 \end{cases} \quad \forall \mathbf{x} \in \Omega
 \end{aligned} \tag{2.1}$$

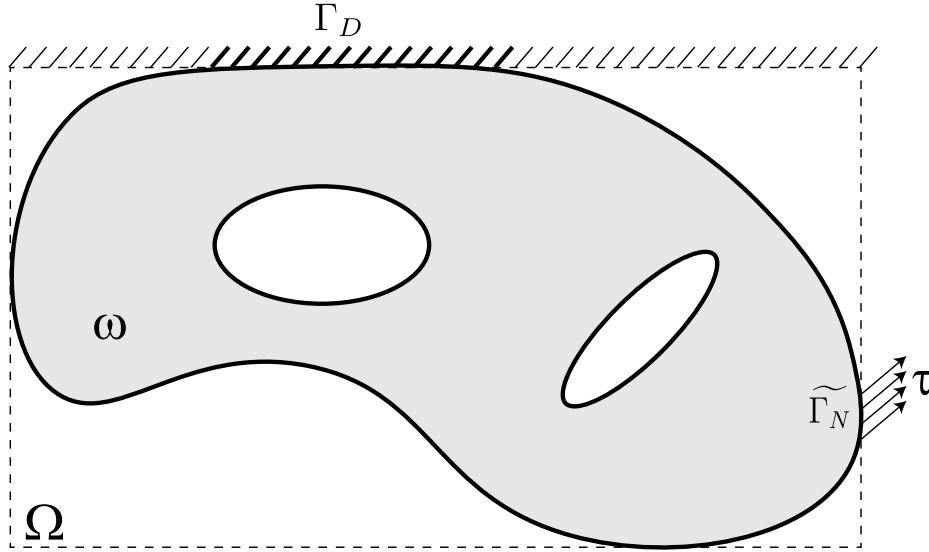


**Figure 2.2:** Extended design domain and boundary conditions for the state equation (adapted from [54]).

The objective function and constraints are dependent on both the material distribution  $\chi_\omega$  and the state variable  $\mathbf{U}(\chi_\omega)$ . The nested approach involves implicitly considering the displacement functions'  $\mathbf{U}(\chi_\omega)$  dependency in the equilibrium equations, which are assumed to be fulfilled at each optimization step. Therefore, to conclude the discussion,  $\mathbf{U}(\chi_\omega) \in \mathcal{V}$  satisfies the variational problem of elasticity.

$$\begin{aligned} \mathbf{U}(\chi_\omega) &= \inf_{\mathbf{U}} \Pi(\mathbf{U}), \text{ such that} \\ \Pi(\mathbf{U}) &= \int_{\Omega} \chi_\omega W_0(\mathbf{U}, \mathbf{x}) d\mathbf{x} - \int_{\tilde{\Gamma}_N} \boldsymbol{\tau} \cdot \mathbf{U} dS, \end{aligned} \quad (2.2)$$

where as shown in Fig 2.1,

- $\mathcal{V} = \{\mathbf{U} \in H^1(\Omega, \mathbb{R}^2) : \mathbf{u}|_{\Gamma_D} = \mathbf{0}\}$  refers to the set of allowable displacements, which is independent of  $\omega$ .
- $\Pi_{\Omega_d}(\mathbf{U})$  represents the total potential energy of the system.
- $W_0(\mathbf{u}, \mathbf{x})$  is the density of strain energy in the solid material located in  $\Omega_d$ .
- $\Gamma_D$  and  $\Gamma_N$  are partitions of  $\partial\Omega$ .
- $\boldsymbol{\tau}$  is an applied traction that is non-zero and acts on  $\tilde{\Gamma}_N \subseteq \Gamma_N$ .

It is widely acknowledged that optimal solutions to equation (2.1) may not be guaranteed due to the infeasibility of the set of feasible designs. Therefore, we assume that design or manufacturing

constraints have been imposed on  $O$ , rendering the problem well-posed. This is known as the restriction settings, which differs from the relaxation strategy, as explained in the review paper [55]

In the discretized design domain  $\Omega_h$ , parameterizing allowable topologies using characteristic functions leads to an integer programming problem. However, this approach becomes intractable for large systems, so the optimization variables in the general problem are mainly due to the continuous parameterization of the topology. For instance, the characteristic function in the state function's description can be replaced by the density function  $\rho$ , which takes continuous values between 0 and 1. Alternatively, it can be replaced by the Heaviside function  $H(\Phi)$ , where an implicit function  $\Phi$  belongs to the bounded interval  $[-\alpha, \alpha]$  for  $\alpha > 0$ , as defined in (2.3).

### 2.2.1 Shape-Based Topology Optimization

The problem (2.1) can be addressed through Lagrangian methods, such as non-parametric shape optimization techniques. In these methods, the nodal positions in the FE model represent geometry and are updated during optimization. Classical shape optimization exhibits a continuous mapping with a continuous inverse function between two topological spaces, implying that homeomorphism exists. Therefore, it must be combined with a criterion to generate new holes, such as the bubble method<sup>56</sup>, topological derivatives<sup>57,58</sup>, etc., for topological changes to solve the general problem. However, this approach is challenging due to the possible adverse effects on boundary changes when perturbing the design variables and the need for re-meshing and adaptive meshing to track moving boundaries and interfaces. Several shape optimization techniques and their current developments are reviewed here<sup>59</sup>. On the other hand, the recent utilization of isogeometric analysis for shape and topology optimizations has several advantages, such as seamless integration between design and analysis, exact geometric representation, and non-parameterized structural boundaries. Interested readers can find several attributes of isogeometric shape and topology optimization in [60, 61].

The Lagrangian formulation is a mathematical framework that employs non-parametric techniques for representing designs using a free-form implicit design representation with level-set methods (LSMs). The LSMs are shape optimization methods with well-defined boundaries but can move to form, remove, and merge void regions that ultimately define the topological design. The LSMs define a level set function (2.3) with a higher dimension to

<sup>56</sup> Eschenauer *et al.*, "Bubble method for topology and shape optimization of structures," 1994.

<sup>57</sup> Sokolowski *et al.*, "On the topological derivative in shape optimization," 1999.

<sup>58</sup> Novotny *et al.*, "Topological sensitivity analysis," 2003.

<sup>59</sup> Upadhyay *et al.*, "Numerical analysis perspective in structural shape optimization: A review post 2000," 2021.

represent the structure. The zero-level set, denoted as  $\Phi$ , describes the material interface  $\partial\Omega$ . In other words,  $\Phi = 0$  represents the boundary between two materials. A level set function (LSF) with negative values defines the voids domain. On the other hand, the LSF with positive values is used to describe the material domain,  $\Omega_d$ , in the design space,  $\Omega$ . This means that positive values of the LSF represent the material while negative values represent the voids. The LSMs-based Lagrangian formulation offers a powerful and flexible approach for representing designs with a crisp interface between several materials (or fluids or mediums) in the design domain.

$$\begin{cases} \Phi(\mathbf{x}, \tau) > 0 \Leftrightarrow \mathbf{x} \in \Omega \text{ (material)} \\ \Phi(\mathbf{x}, \tau) = 0 \Leftrightarrow \mathbf{x} \in \Gamma \text{ (interface)} \\ \Phi(\mathbf{x}, \tau) < 0 \Leftrightarrow \mathbf{x} \in (\Omega_d \setminus \Omega) \text{ (void)} \end{cases} \quad (2.3)$$

where  $\tau$  denotes a pseudo time representing the optimization process's iteration. Hence, the evolution of LSF advances the structure's shape and possibly its topology in the material domain. Evolving the LSF in the optimization process is mainly governed via the solution of the Hamilton–Jacobi equation, which is first-order and models convection only:

$$\frac{\partial\Phi(\mathbf{x}, t)}{\partial t} - v_n \|\nabla\Phi\| = 0, \quad \Phi(\mathbf{x}, 0) = \Phi_0(\mathbf{x}) \quad (2.4)$$

where  $v_n = \mathbf{v} \cdot \mathbf{n}$ , such that the normal to the zero-level contour is related to the gradient of the LSF by  $\mathbf{n} = \frac{-\nabla\Phi}{\|\nabla\Phi\|}$ . For a more mathematical discussion, we refer the reader to the works of Burger and Osher [62–64].

A general form of level-set-based topology optimization (LSTO), together with (2.2), in which the Heaviside function,  $H(\Phi)$ , reflects the characteristic function, can be written as follows:

$$\begin{aligned} \min_{\Phi} : & \mathcal{F}(\mathbf{U}, \Phi) \\ & := \int_{\Omega} f(\mathbf{U}(\Phi))H(\Phi)d\mathbf{x} \\ \text{s.t.} : & G_0(\Phi) = \int_{\Omega} H(\Phi)d\mathbf{x} - |\Omega_d| \leq 0, \\ & : G_i(\Phi, \mathbf{U}(\Phi)) \leq G_i^*, \quad i = 1, \dots, Q \\ & : H(\Phi) = \begin{cases} 0, & \Phi(\mathbf{x}, \tau) < 0 \\ 1, & \Phi(\mathbf{x}, \tau) \geq 0 \end{cases} \end{aligned} \quad (2.5)$$

Level-set topology optimization (LSTO) is a powerful optimization technique that operates on the boundaries of a structure

instead of local density. In this technique, the zero-level set of a scalar function, known as the level-set function (LSF), defines the structure's geometry. Topological changes are based on the evolution of the LSF, and several level-set methods (LSMs) have been developed that are classified based on the LSF's parameterization and the strategy used to solve the optimization problem.

Van Dijk *et al.* review paper provides a comprehensive overview of different LSMs used in LSTO, which includes techniques for mapping the level-set-based geometry onto the mechanical model. The accuracy of the mechanical model's structural response and the convergence of the optimization process is influenced by the structural boundaries in the discretized mechanical model. The structural topology is mapped using different approaches, such as conforming, immersed boundary techniques, or density-based mapping. Conforming and immersed boundary techniques generally provide a crisp representation of the mechanical model's boundaries and are suitable for solving variational problems to perform general topology optimization. However, density-based mapping replaces the Heaviside function with density distribution  $\rho(\Phi)$  to approximate LSTO as  $\int_{\Omega} f H(\Phi) dV \approx \int_{\Omega} f \rho(\Phi) dV$ . The density distribution can map the LSF point-wise or element-wise and is an effective technique for identifying the material interfaces. In summary, LSTO is a well-established methodology for optimizing structural topology, and several LSMs can accurately map the level-set-based geometry onto the mechanical model. The choice of mapping technique depends on the accuracy required for the structural response and the optimization process's convergence.

Finally, we'd end our synopsis of the LSTO on the following grounds. First, most of the works reviewed in the articles follow density-based TO (DTO 2.2.2) to optimize anisotropic materials' orientation and distribution; DTO has also been applied to several other applications in academia and industrial sectors. Secondly, LSTO often adopts Eulerian mesh with ersatz material (point-wise density distribution) and a DTO formulation because of the DTO's simplicity and ease of implementation. Still, the crisp boundary description is maintained throughout the optimization process, allowing shape sensitivity analysis and design updates by solving the HJ equation, i.e., different from DTO. The above deduction is not biased toward following a particular TO approach. No comparative studies are performed on their methodologies, numerical efficiency, numerical verification of the attained optimized design, or their realizability and applicability. Hence, the readers are referred to earlier citations for different TO approaches to adopt the TO formulation that fits their application.

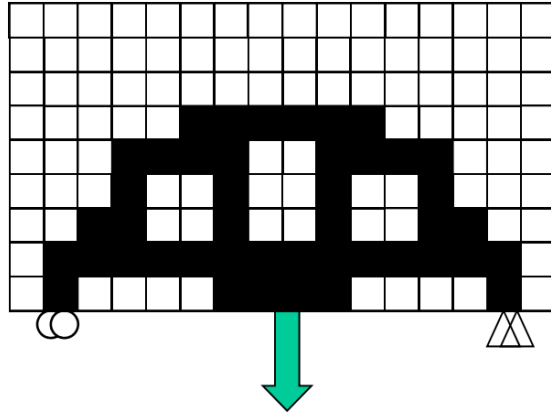


Figure 2.3: Binary Density-based Topology Optimization

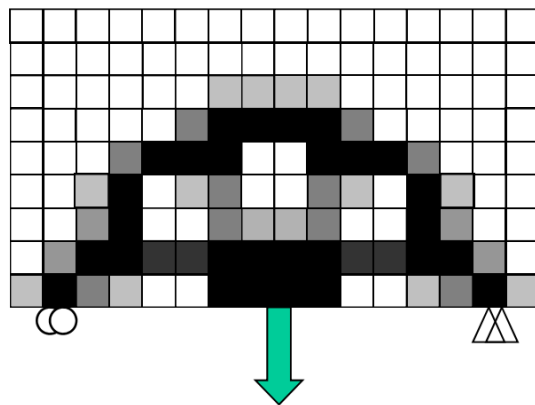


Figure 2.4: Continuous Density-based Topology Optimization

### 2.2.2 Density-Based Topology Optimization

Earlier in this section, we discussed two different topology optimization models—the boundary-following or Lagrangian model and the Eulerian model, also known as the fixed mesh model. The Eulerian model maps the topology through a density function,  $\rho$ , on the discretized design domain. Once the density distribution,  $\rho$ , is obtained, it is fed to the optimization process as design variables. This reformulation is referred to as density-based topology optimization.

Compared to the shape-based TO, the nodes of the structures' boundaries are the optimization variables in topology optimization, i.e., the LSTO method considers the parameterized Level Set Functions (LSFs) to be the design variables for the optimization process. Thus, the structure's boundaries are at least retained in the optimization process, even though it has blurred out the discretized setting of the continuum design space when utilizing density-based mapping.

It is worth noting that when elements or nodes of the mesh are optimized, such as sizing variables, the sense of the exact illustration of the structure's boundaries is physically lost. Mathematically,

the optimization process takes the following form:

$$\begin{aligned}
 \min_{\rho} : & \mathcal{F}(\mathbf{U}, \rho) \\
 & := \sum_i \int_{\Omega_i} f(\rho_i, \mathbf{U}(\rho_i)) dx \\
 \text{s.t.} : & G_0(\rho) = \sum_i v_i \rho_i - |\Omega_d| \leq 0, \\
 & : G_j(\rho, \mathbf{U}(\rho)) \leq G_j^*, \quad j = 1, \dots, Q \\
 & : \rho = \begin{cases} \epsilon, & (\text{void}) \\ 1, & (\text{solid}) \end{cases}, i = 1, \dots, N
 \end{aligned} \tag{2.6}$$

The density distribution,  $\rho$ , denotes the design variable vector of length  $N$ . It is defined such that  $\rho = 1$  if  $\mathbf{x} \in \omega$  and  $\rho = 0$  otherwise. For regions where  $\rho = 0$ , solutions to the boundary value problem are not guaranteed, as the energy's bilinear form is not coercive. Thus, the density function is defined as  $\epsilon + (1 - \epsilon)\rho$ , in which  $\epsilon \ll 1$  is the ersatz parameter:

$$\begin{aligned}
 \mathbf{U} &= \inf_{\mathbf{U}} \Pi(\rho, \mathbf{U}), \text{ s.t.} \\
 \Pi(\rho, \mathbf{U}) &= \int_{\Omega} [\epsilon + (1 - \epsilon)\rho] W_0(\mathbf{U}, \mathbf{x}) dx - \int_{\tilde{\Gamma}_N} \boldsymbol{\tau} \cdot \mathbf{U} dS
 \end{aligned} \tag{2.7}$$

The above formulation represents a binary problem that depicts a structure's void and solid regions, commonly called discrete density-based topology optimization (DDTO), shown in Fig(??). One of the most well-known binary formulations is the Bi-directional Evolutionary Structural Optimization (BESO), which uses various techniques (regularization schemes) commonly used in continuous DTO approaches. Sivapuram et al.<sup>65</sup> combined the features of BESO and the sequential integer linear programming for discrete topology optimization, which shows promising results. Interested readers can find comprehensive reviews of BESO methods in [48, 66].

Another approach to handle the discretizing problem is using a genetic algorithm [67], which can find a "global minimum" and allow handling a discrete variable. However, Sigmund<sup>68</sup> questions the usefulness of non-gradient approaches in TO as this method typically comes with a higher computational cost. In practice, it is recommended to assume the continuous density field together with (2.7) when formulating the TO problem, as this approach has shown to be effective, as portrayed below:

<sup>65</sup> Sivapuram et al., "Topology optimization of binary microstructures involving various non-volume constraints," 2018.

<sup>68</sup> Sigmund, "On the usefulness of non-gradient approaches in topology optimization," 2011.

$$\begin{aligned}
 \min_{\rho} : & \mathcal{F}(\mathbf{U}, \rho) \\
 & := \sum_i \int_{\Omega_i} f(\rho_i, \mathbf{U}(\rho_i)) dx \\
 \text{s.t.} : & G_0(\rho) = \sum_i v_i \rho_i - |\Omega_d| \leq 0, \\
 & : G_j(\rho, \mathbf{U}(\rho)) \leq G_j^*, \quad j = 1, \dots, Q \\
 & : 0 \leq \rho_{min} \leq \rho \leq 1, \quad i = 1, \dots, N
 \end{aligned} \tag{2.8}$$

The continuous density-based formulation (2.8) is a broadly received idea in the TO of continuum structures that utilizes continuous density design variables instead of binary density variables, thus enabling the use of gradient-based information. The density function,  $\rho$ , takes values in  $[0, 1]$  and replaces the characteristic function in the description of the state Equation (2.9) and the objective and constraint functions. In addition, to attain binary design, the density function interpolates the material properties through the material interpolation function as given in the state equation, where  $p = 3$  is a penalization exponent [34, 35]—called as Solid Isotropic Material with Penalization (SIMP), as depicted in Fig(??):

$$\begin{aligned}
 \mathbf{U} &= \inf_{\mathbf{U}} \Pi(\rho, \mathbf{U}), \text{ s.t.} \\
 \Pi(\rho, \mathbf{U}) &= \int_{\Omega} [\epsilon + (1 - \epsilon)\rho^p] W_0(\mathbf{U}, \mathbf{x}) dx - \int_{\tilde{\Gamma}_N} \boldsymbol{\tau} \cdot \mathbf{U} dS.
 \end{aligned} \tag{2.9}$$

Finding an optimal solution for a given problem is not guaranteed due to the need for more closedness in the set of feasible design spaces. This means generating even more holes may decrease the objective function, leading to a less effective solution. Additionally, numerical instabilities can arise in the discretized space, including checkerboarding and mesh dependency. Checkerboarding refers to forming patches of alternating solid-void elements, whereas mesh dependency causes different topologies from similar design domains of different discretization sizes. To prevent the rapid oscillation of the density distribution, restrictions are imposed on the admissible density function in practice, as suggested in the papers <sup>55,69</sup>. This contrasts relaxation settings, which accommodate generalized shapes due to severe oscillation of the density distribution. The concept is called the homogenization approach to topology optimization [33]. To ensure well-posedness, regularization strategies are imposed similarly on the variation in the LSF.

<sup>55</sup> Sigmund *et al.*, “Numerical instabilities in topology optimization: a survey on procedures dealing with checkerboards, mesh-dependencies and local minima,” 1998.

<sup>69</sup> Borrvall, “Topology optimization of elastic continua using restriction,” 2001.

### 2.2.3 A note on Gradient-Based Update Schemes for Topology Optimization

Fiber orientation plays a significant role in handling anisotropic materials and designing lightweight composite structures, making it a critical factor in optimizing the performance of next-generation materials. However, optimizing fiber orientation can be challenging due to local optima and discontinuous functions. To address these challenges, gradient-free algorithms with a global search ability have proven to be more effective [10, 26]. These algorithms, such as those proposed by Hasançebi *et al.*, Reuschel *et al.*, and Voelkl *et al.*, allow for differentiable functions, mixed design variables, and discrete spaces. The relaxed formulation these algorithms offer also has the advantage of obtaining fewer local optima. However, the downside of using gradient-free algorithms is their inefficiency, which requires numerous function evaluations [68]. This can be impractical for expensive finite element simulations. Therefore, adopting gradient-based algorithms like the Optimality Criteria Method (OCM<sup>73</sup>), Method of Moving Asymptotes (MMA) (Svanberg, 1987<sup>74</sup>), and Sequential Linear Programming (SLP) (Dunning, 2015<sup>75</sup>) can be a reasonable choice for tackling the fiber orientation optimization problem.

The OCM (Optimality Criteria Method) is a technique used in topology optimization to find the optimal design by solving a Lagrange function consisting of objective and constraint functions. This function must satisfy the Karush-Kuhn-Tucker (KKT) condition for an optimal solution. The OCM procedure involves two loops: the inner loop that updates the design variable and the outer loop that updates the Lagrange multiplier based on the KKT condition. However, this method cannot handle multiple constraints since coupling the Lagrange multiplier and the design variables requires solving a nonlinear equation. To address this issue, Shen *et al.* suggested a step-length scheme for orientation optimization. This scheme involves normalizing the gradient vector and introducing a parameter to control the magnitude of material orientation in each iteration, which leads to global descent. However, the effect of adding constraints to the orientation optimization problem on the update scheme needs to be verified, which is a critical factor for the OCM. Therefore, a more generalized OCM is required for the topology optimization of an anisotropic material that can handle scalability and multiloading situations. Recently, Kim *et al.* proposed a generalized optimality criteria method for topology optimization problems, which eliminates the need to satisfy the constraints during every optimization iteration but should be met upon convergence. This method is based on the

<sup>73</sup> Andreassen *et al.*, “Efficient topology optimization in MATLAB using 88 lines of code,” 2011.

<sup>74</sup> Svanberg, “The method of moving asymptotes—a new method for structural optimization,” 1987.

<sup>75</sup> Dunning *et al.*, “Introducing the sequential linear programming level-set method for topology optimization,” 2015.

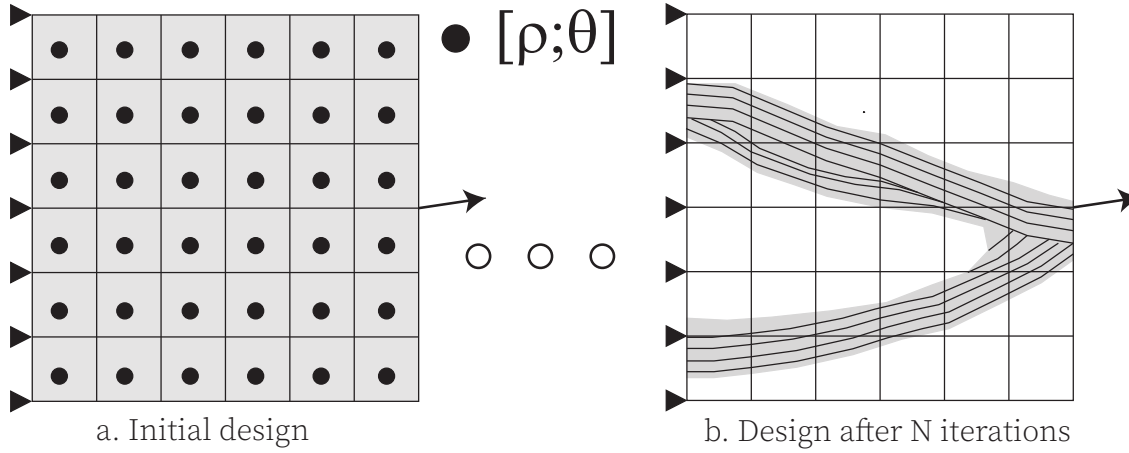
work of Patnaik *et al.* on parametric optimization.

Sequential Linear Programming and Methods of Moving Asymptotes are optimization strategies for solving engineering problems involving multiple objectives and constraints. These methods are based on first-order approximations of the objective and constraint functions using gradient information at a given design point. MMA uses a hybrid linear and reciprocal approximation method [79], known as convex linearization (CONLIN) [80], that is convex and approximates the optimization problem. Svanberg [74] introduced a variation of this method that uses moving asymptotes to stabilize and speed up the convergence of the optimization process. In addition, a dual approach or a primal-dual interior-point method can efficiently solve the non-linear programming problem because the subproblem is separable and convex. However, the reciprocal approximation used in MMA may eliminate the linearity of the approximation [81].

### 2.3 Parameterization Schemes for Fiber Orientation

The parameterization scheme implements a numerical description of fiber orientation patterns and defines variables for optimization. It should ensure the spatial continuity of fiber angles so that the CF4 technology can produce the structure. It should also provide enough design freedom so that the optimization algorithm can consider more candidate designs. For mathematical completeness, the general density-based template for the optimization problem is presented to find the optimal distribution of structural topology, fiber layout, and fiber orientation in functionally graded anisotropic composite structures. In Fig. 2.5, the density distribution accommodates fiber material only; however, the addition of materials is considered through separate density functions in the optimization framework, for example, when optimizing variable fiber fractions or functionally graded anisotropic composites, as depicted in the Equation (2.10). Thus, as detailed in this section, the template accommodates several parameterization schemes used in the literature to optimize fiber-reinforced composite structures. The vector  $\mathbf{z}$  comprises all the design variables, such as isotropic material (matrix) density, fiber material density, and orientation variables. Each design variable has a range of values between  $\underline{z}_i$  and  $\bar{z}_i$ . The total volume of the matrix material,  $G_{m0}$ , is calculated from the density distribution  $\rho_m$ , which is determined by the design variable or density function  $\rho_m$ . Similarly, the fiber material volume is determined using the fiber density function  $\rho(\theta)_f$ . The system of linear equations consists of the stiffness matrix  $\mathbf{K}$  and the force vector  $\mathbf{F}$ , which is derived from the state equation using

**Figure 2.5:** Illustration of DTO considering anisotropic material via fiber orientation parameterization.



finite element formulation.

$$\begin{aligned}
 & \min_{\mathbf{z}} : \mathcal{F}(\mathbf{U}, \mathbf{z}) \\
 & := \sum_i \int_{\Omega_i} f(z_i, \mathbf{U}(z_i)) d\mathbf{x} \\
 & \text{s.t.} : \mathbf{z} := [\rho_m, \rho_f(\theta)] \\
 & : \underline{z}_i \leq z_i \leq \bar{z}_i, \forall z_i \in \mathbf{z}, \quad i = 1, \dots, N \\
 & : G_{m0}(\rho_m) = \sum_i v_i \rho_m^i - V_m \leq 0, \\
 & : G_{f0}(\rho_f) = \sum_i v_i \rho_f^i - V_f \leq 0, \\
 & : G_j(\mathbf{z}, \mathbf{U}(\mathbf{z})) \leq G_j^*, \quad j = 1, \dots, Q \\
 & : \mathbf{K}(\mathbf{z})\mathbf{U} = \mathbf{F}
 \end{aligned} \tag{2.10}$$

### 2.3.1 Continuous Parameterization

The design approach known as continuous parameterization of fiber orientation (CFO) employs the angle as the design variable. This design variable is a continuous and independent parameter that allows for flexibility in changing the orientation across the design points, expanding the orientation design space. This concept is illustrated in Fig. 2.6. The rotation stiffness tensor, denoted by  $\bar{\mathbf{C}}(\theta)$ , is derived from the base anisotropic stiffness tensor  $\mathbf{C}$  using a rotation tensor,  $\mathbf{T}(\theta)$ , where  $\theta$  corresponds to the direction of the fiber. In this context,  $c$  and  $s$  represent  $\cos \theta$  and

$\sin \theta$ , respectively.

$$\bar{\mathbf{C}}(\theta) = \mathbf{T}^{-1}(\theta) \cdot \mathbf{C} \cdot \mathbf{T}'(\theta) = \begin{bmatrix} \bar{C}_{11} & \bar{C}_{12} & \bar{C}_{16} \\ \bar{C}_{12} & \bar{C}_{22} & \bar{C}_{26} \\ \bar{C}_{16} & \bar{C}_{26} & \bar{C}_{66} \end{bmatrix} \quad (2.11)$$

$$\mathbf{T}(\theta) = \begin{bmatrix} c^2 & s^2 & 2cs \\ s^2 & c^2 & -2cs \\ -cs & cs & c^2 - s^2 \end{bmatrix}, \quad \mathbf{T}'(\theta) = \begin{bmatrix} c^2 & s^2 & cs \\ s^2 & c^2 & -cs \\ -2cs & 2cs & c^2 - s^2 \end{bmatrix} \quad (2.12)$$

The optimization process for parameterized fiber orientation, denoted by  $\theta$ , involves continuously varying the angle within the range of  $[-\frac{\pi}{2}, \frac{\pi}{2}]$ . However, designing a continuous fiber orientation presents a challenge due to the complex fourth-order transform tensor that rotates to a given angle, which involves multivalued sine and cosine functions, resulting in a non-convex optimization problem. Additionally, the optimization process for fiber orientation is sensitive to the initial fiber configuration, making it difficult to obtain the optimized solution. Previous studies have shown that suboptimal solutions are common in continuous fiber orientation design problems. One way to tackle this issue is by expanding the design space. For instance, free material optimization (FMO) [82, 83] parameterizes each stiffness tensor element independently as a design variable. This approach avoids the complexity of orientation design variables. Still, point-wise nonlinear constraints are required to ensure the positive semi-definiteness of the stiffness tensor and link it to the feasible physical design, making this method challenging. Nomura et.al.<sup>84</sup> have simplified the first tensor invariant constraint and removed the nonlinear constraints by formulating an orientation design variable as a tensor field. However, these constraints can still be violated at the joint point of the structural members where the orientation shows a discontinuous distribution. Studies on optimizing fiber orientation using the analytically derived optimality criterion [85] date back to the pioneering work of Pedersen on the strain-based method<sup>86–88</sup>. In Pedersen's work, it was concluded that material orientation axes that lie along principal strain axes always give stationary energy density. However, Cheng [89] argued that this conclusion is limited to a unit cell case where the orientation variable is separated from the design domain to obtain extreme strain energy. A similar deduction using iterative optimality criteria [90, 91] formulated the stress-based method [92] by exercising an invariant stress field for material orientation. Diaz and Bendsoe [93] then extended the stress-based method to determine the optimal orientation optimization problem corresponding to multiple loads. While both

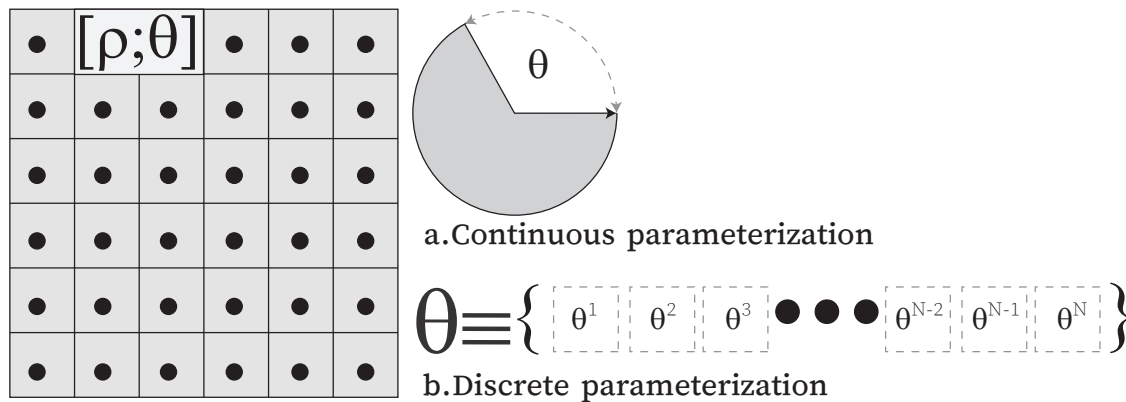
<sup>84</sup> Nomura *et al.*, "Inverse design of structure and fiber orientation by means of topology optimization with tensor field variables," 2019.

<sup>86</sup> Pedersen, "On optimal orientation of orthotropic materials," 1989.

<sup>87</sup> Pedersen, "Bounds on elastic energy in solids of orthotropic materials," 1990.

<sup>88</sup> Pedersen, "On thickness and orientational design with orthotropic materials," 1991.

**Figure 2.6:** Finite elements are considered design variables in DTO: (a) Continuous material orientation; (b) Discrete material orientation.



methods are similar, the stress-based method produces a slightly stiffer structure than the strain method because strong couplings exist among the orientational variables when the strain field is used [89]. In conclusion, Gea and Luo [94] demonstrated that the fiber orientation coincides with the principal stress/strain fields for relatively weak shear and some strong shear types of anisotropic materials. Recently<sup>95</sup>, a strain-based method framework has been utilized to optimize laminate topology and fiber orientation for various in-plane and out-of-plane loading conditions.

In the field of CFO (Continuum Fiber Orientation), the methods used for analysis heavily rely on the fibers' initial configuration. However, as explained in an article by Qiu<sup>96</sup>, there may be better methods for shear 'strong' type materials due to multiple global minimum solutions. While these shortcomings have led to the development of new methods, one such method is the energy-based approach proposed by Luo and Gea [97, 98]. This approach utilizes an inclusion cell to estimate the dependence of the strain and stress fields on the fiber orientation using an approximate energy factor. However, the factors that affect the energy, such as traction stress, material properties, and the direction of the inclusion cell and its surroundings, make applying this method for 3D and complex loading problems challenging. Building on the energy-based method, Yan *et al.* proposed a hybrid stress-strain approach by considering the optimality condition of the mean compliance in both the stress and strain forms. They demonstrated their method using numerical examples of weak and strong shear materials and extended them to 3D problems. However, the assumption regarding the elemental strain and stress field invariant to the neighboring elemental orientation may limit the solution of 3D problems and lead to suboptimal results.

<sup>95</sup> Lu *et al.*, "Concurrent optimization of topologies and fiber orientations for laminated composite structures," 2022.

<sup>96</sup> Qiu *et al.*, "Concurrent topology and fiber orientation optimization method for fiber-reinforced composites based on composite additive manufacturing," 2022.

An alternative is employing curvilinear parameterization schemes that define fiber paths as the graphs of analytical function, guarantee the continuity of the fiber angle, and have a few numbers of design variables<sup>100–102</sup>. Nevertheless, the restrictive design search space will limit the tailoring of the fiber path, thus deteriorating the stability of the optimization problem [26] and the quality of the optimized solution. In addition, the parameterization schemes can follow equidistant iso-contours of a level set function to represent curvilinear fiber paths<sup>103,104</sup>, naturally ensuring fiber continuity and often being parallel to the neighboring fiber paths. Furthermore, the optimization result depends on the initial configuration, and local solutions often appear [105].

### 2.3.2 Discrete Parameterization

The counter scheme is a method that limits the design options for orientation by using a specific optimization process. This is done to prevent problems with multiple solutions. The original method used a genetic algorithm, which was computationally demanding [106–108]. However, Stegmann *et al.* simplified the process by transforming the base anisotropic stiffness tensor for the given fiber orientation and selecting the material candidates beforehand. This transformed the combinatorial problem into a continuous optimization problem. Finally, the effective anisotropy elasticity tensor is calculated as a combination of material candidates that meets certain conditions and is convex.

$$\mathbf{C}_{eff} = \sum_{i=1}^{n_c} w_i \bar{\mathbf{C}}_i, \quad \begin{matrix} 0 \leq w_i \leq 1 \\ \sum_{i=1}^{n_c} w_i = 1 \end{matrix} \quad (2.13)$$

The discussed scheme shares similarities with the multi-material optimization problem mentioned in [110, 111]. In this scheme, weighting functions are assigned to different candidates. It employs gradient-based optimization with a penalization coefficient, which forces the weighting functions to seek a binary design and fiber convergence, meaning there is only one discrete material at each design point. This method is known as Discrete Material Optimization (DMO).

DMO was a significant development and laid the foundation for Shape Function with Penalization (SFP)<sup>112</sup> and Bi-value Coding Parameterization (BCP) [113]. These methods were used to perform discrete fiber orientation optimization. Later, DMO was extended for laminated composite structures to determine the material distribution and thickness variation. This process is known as Discrete Material and Thickness Optimization (DMTO) [114].

100 Bruyneel *et al.*, “A modified Fast Marching Method for defining fiber placement trajectories over meshes,” 2013.

101 Lemaire *et al.*, “Optimization of composite structures with curved fiber trajectories,” 2015.

102 Hao *et al.*, “Isogeometric analysis and design of variable-stiffness aircraft panels with multiple cutouts by level set method,” 2018.

103 Brampton *et al.*, “New optimization method for steered fiber composites using the level set method,” 2015.

104 Papapetrou *et al.*, “Stiffness-based optimization framework for the topology and fiber paths of continuous fiber composites,” 2020.

112 Bruyneel, “SFP—a new parameterization based on shape functions for optimal material selection: application to conventional composite plies,” 2011.

Some recent works [6, 115, 116] have further improved the applicability of DMTO. A comparison of these methods using various numerical examples can be found in <sup>116,117</sup>.

Another work proposed a self-penalization interpolation model for fiber orientation (SPIMFO). This model is based on the convergent Taylor series for sine and cosine functions to optimize composite hyperelastic material <sup>118</sup> and the dynamic design of laminated piezo-composite actuators [119].

DMO does not incorporate design problems for continuously varying orientation distributions. First, it is an imperative design consideration to circumvent stress constraints and degradation in the strength by order of magnitude compared to that for continuous fiber paths due to fiber discontinuity. Secondly, these methods must address the fiber convergence, even against the significant penalization factor; hence, their benefit relies on an optimization algorithm to circumvent impractical mixtures of fiber orientations. Third, the discrete parameterization schemes should minimize the number of design candidates for efficient optimization.

### 2.3.3 Discrete-Continuous Parameterization

One way to optimize fiber orientation is by combining continuous and discrete methodology. By utilizing the benefits of both approaches, it is possible to improve computational efficiency, avoid local optima, and address issues related to fiber continuity and manufacturability. To achieve this, a combination of discrete and continuous parameterization is suggested. A recent study by Luo *et al.* proposed a coarse-to-fine strategy that divides the orientation design space into discrete sub-intervals. The CFO then searches for an optimized solution in each sub-interval using the DMO approach. However, the number of sub-intervals needed is still being determined. This approach reduces the risk of falling into local optima while maintaining fiber continuity.

Nevertheless, Nomura *et al.* proposed a flexible strategy that integrates alternatives suggested for DMO and CFO approaches. Their study explored the Cartesian system for orientation design variables to improve the initial design dependency and local optima issues encountered in the continuous parameterization approach. They extended the parameterization scheme to yield an optimized design for a given discrete orientation set. Additionally, the vectorial form of the orientation design variables considered the  $2\pi$  ambiguity, which occurs due to the periodic nature of the orientation design variable. By introducing vectorial design variable as a point-wise quadratic inequality constraint, they obtained more interpolated elasticity tensors than the single variable polar

<sup>116</sup> Hozic *et al.*, "A new method for simultaneous material and topology optimization of composite laminate structures using Hyperbolic Function Parametrization," 2021.

<sup>117</sup> Kiyono *et al.*, "A novel fiber optimization method based on normal distribution function with continuously varying fiber path," 2017.

<sup>118</sup> Silva *et al.*, "Topology optimization of composite hyperelastic material using SPIMFO-method," 2021.

representation. However, the optimization algorithm treats continuous and discrete problems as two different problems. Therefore, investigating the coupled optimization framework might be an outlook for consideration. Another proposed parameterizing scheme by Kiyono *et al.* continued the computational approach suggested by Yin and Ananthasuresh [111]. They introduced a normal distribution function as a weighting function in their parameterizing strategy, which guaranteed fiber convergence, low sensitivity to the initial fiber configuration, and continuity of the fiber orientation.

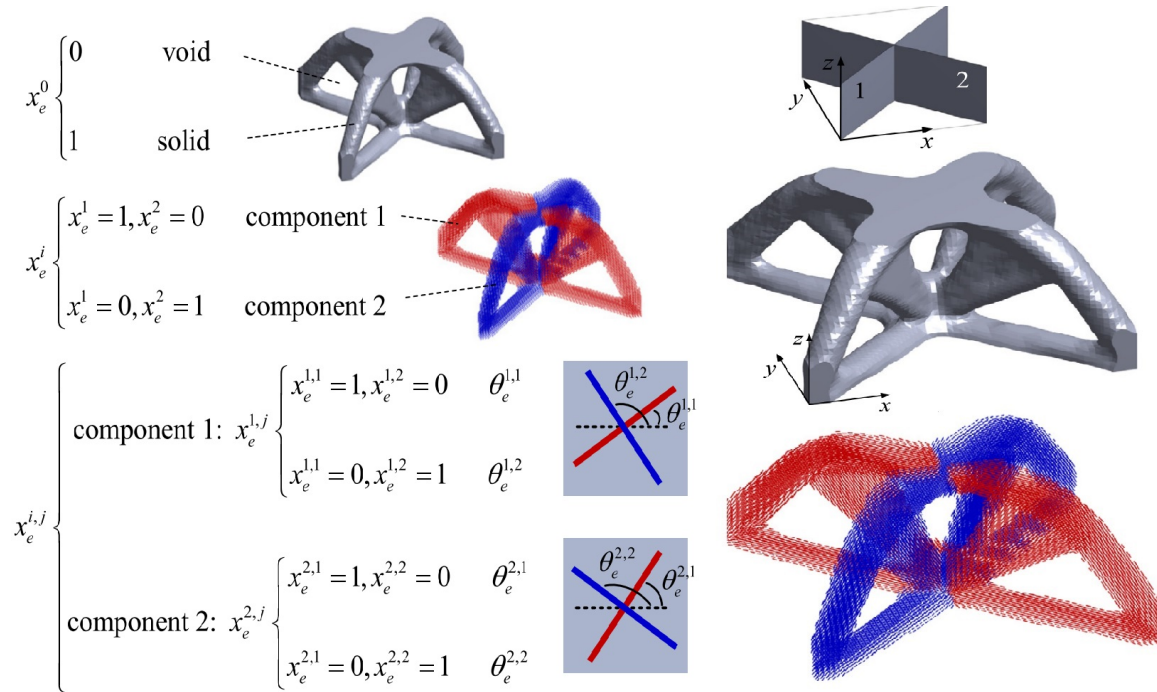
Xia and Shi [122] have proposed a method to represent the fiber orientation throughout the design domain using a continuous global function. This is achieved by applying the shepherd interpolation method at scattered design points. The interpolation function ensures fiber continuity while considering a reduced orientation design space compared to CFO. However, this method needs an initial configuration and may end up with a sub-optimal solution. In another work Xia *et al.*, multilevel optimization was applied for fiber orientation optimization. It was more efficient than single-level optimization; however, the optimization results in different fiber arrangements for different initial fiber orientations. Therefore, the efficiency of the multilevel approach depends on the attained fiber orientation field at a coarse level since the optimization at the successive refined level starts from an initial design computed at its neighboring coarser level.

A recent study by Ding *et al.* proposed a framework that combines discrete and continuous optimization techniques, drawing inspiration from previous works by Kiyono [117] and Luo [120]. However, the framework has yet to be compared to other optimization methods and may lead to local minima when the discrete-continuous interval is greater than two. Another study by Qiu *et al.* focused on optimizing material orientations using multiple print planes, as shown in Figure 2.7. The authors implemented their optimization framework using nylon filaments with chopped carbon fibers, and their results demonstrated a significantly lower compliance value compared to previous methods. Finally, the authors provided an example to illustrate the choice of a discrete-continuous interval.

#### 2.3.4 Feature-Based Parameterization

Parameterization schemes are widely used for representing designs using low-level fiber material representations, such as pixel or voxel-based representations. These representations allow for complex and free-form designs, which can be further refined

**Figure 2.7:** (Left)—Schematic the diagram represents the design variables of an element and parameterizes continuous orientation variables in the discrete-continuous setting. **Right**—Implementation of the multiple print plane to design MBB [96]



using variables based on the number of pixels or voxels in the design space. To make these designs more manufacturable, high-level parameters are introduced to represent fiber material as geometric features. These high-level parameters refer to the spatial dimensions of a feature's size, position, or orientation. This approach allows for creating more efficient and effective designs with fewer variables. Finally, to analyze these designs, feature-mapping techniques are employed to map the geometric features onto a fixed mesh. This process allows for a more detailed design analysis and helps identify potential issues and improvement areas. A comprehensive review of feature-mapping methods conducted by Wein *et al.* details the various components of feature-mapping techniques and their implementation in structural optimization. By using these advanced techniques, designers can create more efficient and practical designs that are easier to produce and analyze.

The feature-mapping methodology is a design technique that helps to connect two crucial elements of the product design process: topology optimization and easy-to-manufacture designs. Mapping the optimized topology onto a predefined feature space enables

**Figure 2.8:** The illustration describes an algorithm for designing a continuous fiber-reinforced polymer laminate specifically tailored for the geometry projection method. The algorithm proposes a laminate with variable stiffness, optimized using GP and then stacked together to create a multi-layered, optimized laminate. Various CF4 constraints are incorporated during the design process to ensure the final product is ready to print and meets all required specifications.

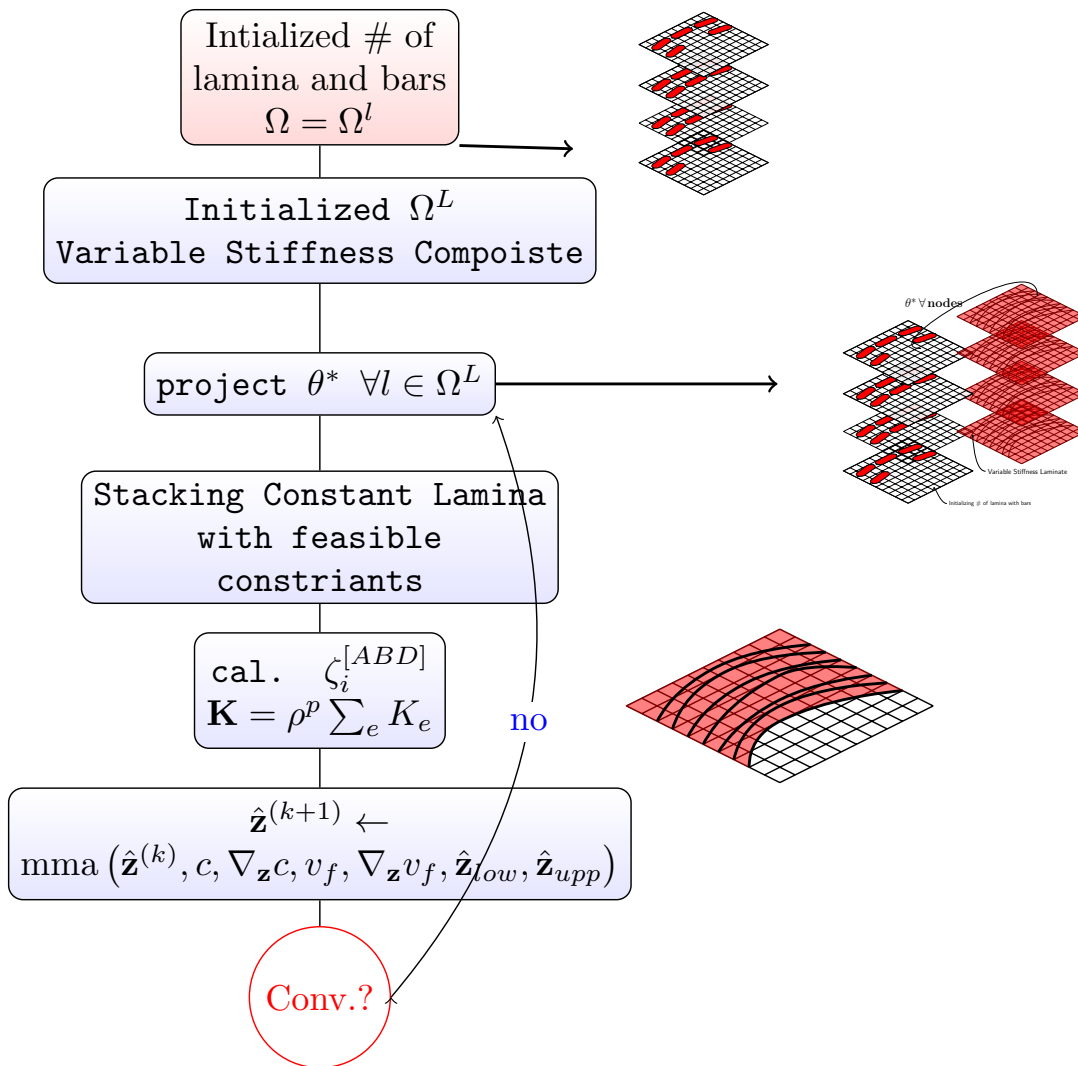
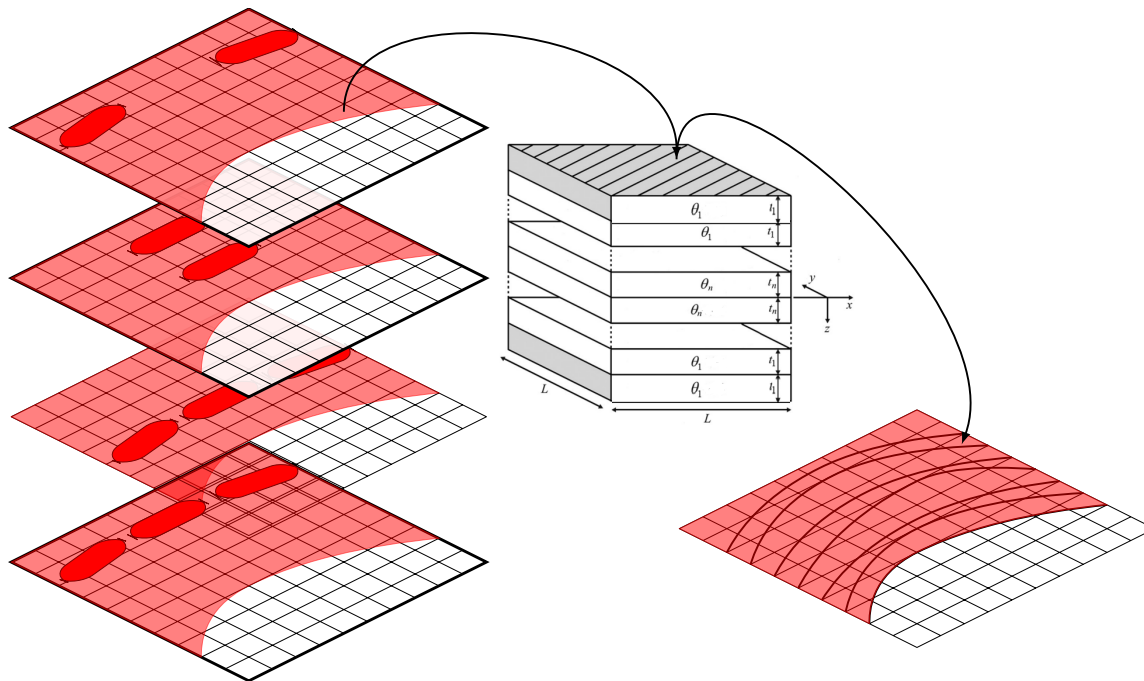


**Figure 2.9:** A similar algorithm as described in Fig. 2.8 can be utilized to design single-layered variable-stiffness composite laminate using composite laminate equivalent single-layer theory. The subsequent chapters provide a detailed explanation of these concepts.



generating geometric features that can be readily manufactured using conventional processes. This approach provides a seamless transition from the initial design stage to the final manufacturing stage, optimizing the product design for performance and manufacturability. When exploring the possibilities of additive manufacturing processes, it is essential to consider feature-based mapping as a suitable framework for designing and optimizing additively manufactured structures. By incorporating specific features and AM's requirements into the design process, designers can create functional and optimized structures for the additive manufacturing process, reducing production costs and improving efficiency.

The emergence of CF4 technology has opened up new possibilities for developing advanced lightweight structures made from continuous fiber-reinforced polymers, thus providing an opportunity to exploit feature-mapping methods for these young manufacturing techniques yet to be formulated for monolithic structures. The thesis builds upon the promising work carried out by various researchers in the past who have pioneered the use of the geometry projection method for topology optimization of structures made of components that are ready to assemble.

However, the authors have taken a different approach by applying this method to optimize the topology of monolithic structures made entirely of CFRP material.

Geometry projection (GP) [125] is an explicit feature-mapping technique that represents the design using cylindrical bars reinforced with continuous fibers [126]. It performs the analysis using a fixed finite element mesh. The method penalizes the interpolation of material properties at the junction of multiple bars made of an anisotropic material as a convex combination of the penalized effective densities for each component. CF4 offers shape constraints on the structural form that can be easily integrated into the method, as shown in Fig. 2.10. This work lays the groundwork for using the geometry projection method for fiber-orientation optimization design problems. However, the fiber can only be unidirectional along the bars, which restricts the design freedom offered by CF4. The method can control the structure's size by explicitly representing features. For example, Sun *et al.* proposed a trapezoidal component made of primary material and wound by fiber layers.

When integrating GP with CF4, it's important to remember the CF4 design principle and the manufacturing constraints that go with it. One of these constraints involves adopting a layer-wise approach to print CFRP (Carbon Fiber Reinforced Polymer) structures using commercial printers available in the market, such as Markforged®, Anisoprint®, Prusa®, and others. This layer-wise approach ensures that the carbon fibers are laid down in a specific pattern and orientation, which is critical to achieving the desired strength and stiffness of the final product. It's worth noting that this approach requires careful optimization of the printing parameters, such as the layer thickness, printing speed, and temperature, to ensure that the carbon fibers are fully embedded in the matrix. With the right approach and parameters, however, GP-CF4 composite structures can be manufactured with excellent mechanical performance and dimensional accuracy, making them ideal for various applications, including aerospace, automotive, etc.

### 2.3.5 Material Parameterization

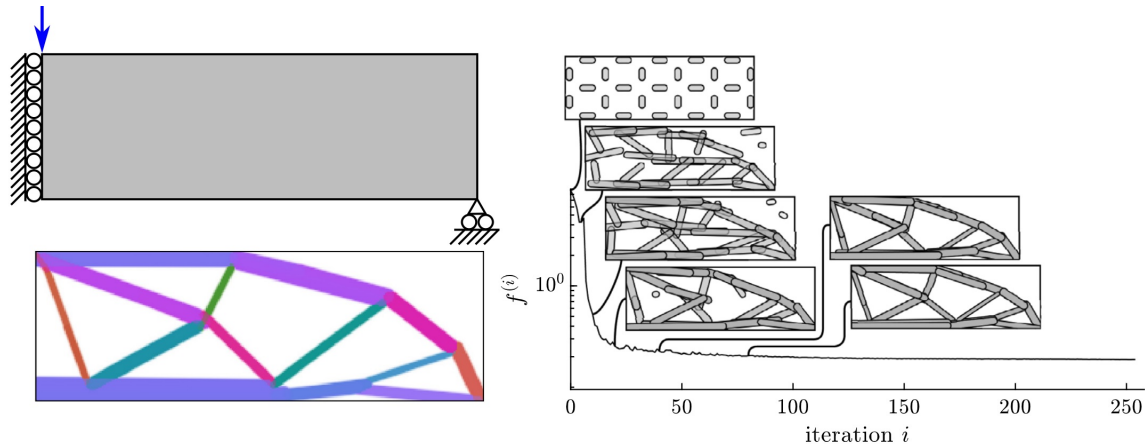
It is possible to introduce further relaxation in the feasible design space through material heterogeneity. Heterogeneous composite materials, for example, consist of two or more materials and are engineered to vary the spatial composition and structure continuously [128]. This variation allows for a broader range of material properties beyond natural limits. Recent studies have shown that CF4 is ready to manufacture FRC structures with continuous yet

**Table 2.1:** Various attributes and comparison of enumerated parameterization techniques.

Parameterization	Design Freedom	Advantages	Applicability	Drawbacks
<b>Continuous</b>	Fully relaxed material orientation space.	Spatially varying fiber path both in 2D and 3D.	Adopted scheme for CF4 part design and verification.	Initial design dependency, significant variation in fiber angles, and $\pi$ ambiguity result in poor local minima.
<b>Discrete</b>	Most restrictive material orientation space.	Most effective gradient-based method for discrete settings <sup>1</sup> , e.g., multi-phase TO.	Numerous studies on designing multi-layered composite laminates.	Several design variables, fiber convergence, and material discontinuity lead to ambiguous design.
<b>Discrete-continuous</b>	Continuous orientations are penalized for attaining assigned discrete directions.	General framework for both continuous and discrete settings.	Promising framework to withstand various FRC manufacturing units.	Only a few works are available, and an efficient optimization formulation is needed to tackle the general setting. <sup>1</sup>
<b>Feature-based</b>	Most restrictive material distribution space <sup>2</sup> .	Least number of optimization variables, easy-to-control feature size, and ready-to-manufacture design.	Favorable for large-scale application and industrial manufacturing units due to its simple topology.	Topology is restricted <sup>3</sup> to feature shape, thus limiting CF4 capabilities
<b>Material</b>	Completely relaxed in material distribution and orientation space	Allows spatially varying fiber path and volume fraction, complex loading, integration of failure criteria, damage model, etc.	Fully exploit the capabilities of CF4 with a design that can follow the response of the actual part.	Validation of numerical framework is difficult because the attained topology is complex

Genetic algorithms are used in the discrete framework;<sup>2</sup> Mainly for explicit feature-mapping;<sup>3</sup> Implicit features can allow free-form topology at the cost of computing the distance function numerically.

**Figure 2.10:** The example demonstrates the design of MBB using the geometry projection method. The top of the left column shows the MBB beam design region, support, and unit load, whereas the bottom depicts colored penalized element densities for the optimal MBB beam designs. Note that the color denotes the orientation of the rest of the changes. In the right column, iteration histories of an objective function indicate the attained compliance value  $f^{(i)}$  at an iteration  $i$ . [126]



spatially varying fiber paths and fiber volume fractions. Variable FRC material properties may perform better if optimized adequately than a fixed FRC material volume fraction. Therefore, a composite structure comprising heterogeneous FRC material distribution provides considerably larger design freedom to CF4 [129–131]. Lee *et al.* have considered a sequential approach to designing FRC structures by considering fiber and material fractions in a given design space. A sequential process begins with designing an isotropic-material matrix with voids, selecting fiber fractions, and optimally orienting the fibers. However, this approach sacrifices exploring new topologies that might be optimal for variable FRC structures. To address this issue, Desai *et al.* work investigated the simultaneous design of matrix topology, fiber material layout, and orientation using an anisotropic topological derivatives framework. In addition, the dense arrangement of fibers was evenly spaced for the part’s manufacturability while retaining their specific patterns. However, the structural performance resulting from simplifying the dense fiber arrangement needed to be evaluated, thus questioning the reliability of the printed part.

As previously discussed, the work involved optimizing the distribution and orientation of FRC material through mono-scale approaches. However, CF4 can also be used to create mono-scale and multi-scale structures. Multi-scale approaches can be divided into lattice-based and hierarchical-based topology optimization

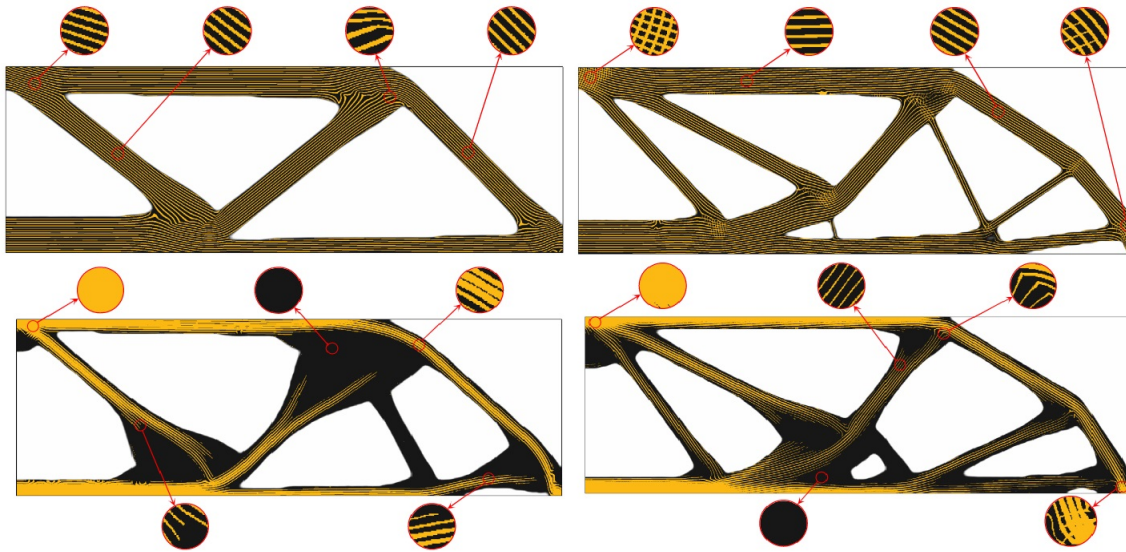
based on their micro-scale optimization methodology. The lattice-based approach calculates effective elastic coefficients through offline homogenization of a fixed or a set of multi-variable microstructures. The computed coefficients are then interpolated to achieve continuous variations for corresponding variations in the microstructure parameters. On the other hand, the hierarchical approach solves a spatially varying micro-structural and macro-scale optimization problem at each material point, which leads to high computational costs and connectivity issues. Despite the challenges, designing next-generation lightweight structures is promising, as FRCs have inherent multi-scale characteristics and geometric patterns that span at least two or more scales. Spatially varying material distributions are critical to this approach. Interested readers can refer to the review paper by Wu *et al.*, which provides the general framework for multi-scale topology optimization and diverse applications the framework has been utilized.

The multi-scale approach for anisotropic materials is challenging due to various factors such as length scale controls, connectivity between adjacent micro-structures, the ability to produce models for damage criteria to capture actual anisotropic behavior, and unique treatments at the domain's boundaries. These factors require investigation through experiments or appropriate numerical tools to estimate the actual performance of printed parts. Only a few works have addressed the multi-scale approach for FRCs. Kim *et al.* adopted the homogenization method for designing spatially varying fiber volume fractions and orientations. Their work used SIMP to design the macro-structure's composite topology. The de-homogenization procedure applied to fiber microstructures obtained in the coarser mesh was visualized by projecting at a finer mesh. Various benchmark and multi-load structure problems were studied, and it was concluded that locally varying FRC materials augment the global stiffness of the structure more than a fixed fiber volume fraction or isotropic multi-material structure. In continuation of the Kim methodology, Jung *et al.* proposed a 3D TO approach for designing FRC structures with spatially varying fiber fractions and orientations. Finally, Boddeti *et al.* introduced a complete design to the manufacturing workflow for laminated continuous fiber-reinforced composites with variable stiffness enabled by spatially varying microstructures.

## 2.4 Discussion

The discussion centers around the effectiveness of a specific topology optimization for materials that exhibit anisotropic properties.

**Figure 2.11: MBB**—post-processed design result of FRC structure with fixed (**top-row**) and varying fiber volume fraction (**bottom-row**) using a micro-structure unit cell with rectangular-shape (**left-column**) and cross-shaped (**right-column**) fiber layout. The black color represents matrix material, and the yellow colored part is fiber material [135].



However, it should be noted that this discussion is a partial analysis of CF4 and its differences when adopting a particular topology optimization method. The main objective is to explore topology optimization strategies that can fully leverage the design freedom offered by CF4 technologies. As previously mentioned in Section 2.3, there are five primary categories of existing techniques for material orientation, including continuous, discrete, discrete-continuous, feature, and material parameterization.

The Discrete Material Orientation (DMO) approach is a popular method used in the aerospace, automotive, and wind turbine industries to optimize a prescribed set of alternative discrete angles for manufacturability reasons. This approach is particularly favorable for multi-layer composite laminate designs [138–140], as it allows a mixed-integer programming problem to be formulated as a continuous problem that can be solved efficiently using gradient-based optimizers. This makes it possible to solve complex problems that may not be amenable to gradient-free methods, and the simplicity of DMO, combined with its ability to attain the discrete setting for material orientation, has led to its adoption in various industrial applications. However, it should be noted that the DMO approach has some limitations, particularly regarding its restrictive measures on the material orientation design space. While it is effective in many cases, there needs to be more literature

on its applicability to CF4, and it may not fully exploit the potential of this material. As such, it is essential to carefully consider the benefits and limitations of the DMO approach when applying it to different materials and designs.

The optimization of multi-layered composite laminates [141] can be approached using an indirect method known as lamination parameterization. Tsai and Pagano [142] introduced this method to parameterize the composite laminate's stiffness using twelve linearly dependent parameters. This approach offers the advantage of reducing the number of optimization variables, making obtaining a globally optimal solution easier. However, the lamination parameters are not independent design variables, which makes it challenging to incorporate composite failure criteria and design and manufacturing constraints. Although lamination parameterization is a popular method, it has limitations. For example, it is limited to considering only one candidate material and does not provide a direct description of the laminate data for the design. To overcome these limitations, additional optimization steps are required to convert the stiffness properties to optimal fiber orientation angles and to introduce design guidelines and manufacturing constraints. Therefore, a multi-level optimization strategy that exploits the benefits of achieving global optima at its first stage is used. However, this approach limits the capability of CF4 processes that enable multi-axial and micro-scale prints. Additionally, it is essential to consider additive manufacturing-related manufacturing constraints, such as minimum turning angles, feature sizes, etc., to achieve a realizable AM design. The LP framework needs to be expanded to achieve scalability for numerical verification of the CF4 prints. The LP framework is briefly discussed for completeness on available parameterization schemes. Still, interested readers can look at the review by Albazzan *et al.* and recent work on the TO of laminates in the following citations [144–147]

Advanced manufacturing techniques are revolutionizing the field of composite materials, and continuous fiber orientation methods are emerging as a promising parameterizing scheme for CF4 processes. These methods offer the highest degree of freedom regarding shape and variable stiffness, making them ideal for directing material deposition path planning. Unlike discrete methods, continuous orientation formulation ensures that the fiber trajectory curvature, fiber continuity, fiber fraction, and offset distance between adjacent fibers are optimized, thereby making fiber convergence and continuity easier to achieve. Papapetrou *et al.* have designed parts' topology and material orientation simultaneously, followed by post-processing using continuous fiber path planning to ensure realizability. A sequential scheme has also

been proposed by Chen and Wang [23, 148], where fiber placement based on load transmission follows isotropic TO, in contrast to Liu *et al.*, who adopted concurrent fiber path planning and structural topology optimization. Multi-axis material deposition technology using a robotic arm requires an extension of the TO algorithm to envelop the 3D fiber orientation, which is unnecessary in in-plane printing. Schmidt *et al.* introduced azimuth and elevation angles to extend the CFO method for 3D fiber orientation. They have also emphasized the issues of the non-convexity of compliance and sensitivity to initial fiber orientations and have investigated the orientation parameter space to mitigate these problems [151]. Finally, the realizability of 3D-printed composites has been studied by Fedulov *et al.*, who have proposed a filtering technique for fast convergence. The method aims to ensure that the printing process meets the requirements for fiber placement, allowing for the production of high-quality composite materials.

Topology optimization techniques in exploring the potential of CF4 technology can be pretty costly, mainly when these methods are applied to produce large-scale structural parts. Therefore, it is essential to balance commercial aspects, such as feasibility, practicality, and structural design, by considering the benefits of various methodologies, such as discrete, continuous, and multi-component approaches. A discrete-continuous parameterization scheme is beneficial in optimizing the structural topology and material orientation, and multi-component optimization (MTO) can be employed to decompose product geometry while ensuring that manufacturing constraints are met. This approach is crucial in minimizing the impact of quality and cost on the end product. Initially, a genetic algorithm was used to solve MTO, as proposed by Lyu *et al.*. Recently, Zhou *et al.* have used a gradient-based optimization algorithm to enhance this approach. They have extended their work to structures consisting of multiple composite components with tailored material orientations without a prescribed set of alternative discrete angles. This has made it possible to produce regions that can be fabricated separately and joined with continuous or discrete material orientation methods, as demonstrated by Qiu *et al.*. Overall, these TO methods offer a promising avenue for exploring the potential of CF4 technology while minimizing the associated costs. The optimization algorithms employed in this approach can provide a more efficient and effective means of designing and producing composite materials.

The principle of feature mapping is rooted in being ready for manufacturability while imposing necessary limitations on the spatial distribution of fiber orientations. This approach considers commercial aspects to ensure that composite parts can be easily

manufactured by introducing CAD-based features that help simplify the layerwise design process. It also significantly reduces the number of design variables, further streamlining the design space. It is worth noting that previous research in this area has only considered stiffness-driven design. However, it is equally important to consider the failure modes of composite parts that may arise during the layerwise additive manufacturing process. Such failure criteria can result in substantially different designs, making this method particularly relevant in fabricating fiber-reinforced composite structures.

In this particular study, optical microscopy images of the cross-sectional area of a fiber-reinforced plastic material are shown in Figure 2.12. The material comprises carbon fibers impregnated with nylon plastic, known as polyamide 6. The fibers are wound on a filament spool placed in a material chamber, resulting in a somewhat circular cross-section. However, once the filament is deposited on the platen, the cross-section takes on a rectangular shape due to the carbon fiber bundle filament passing through a roller. It is worth noting that the presence of voids in the material can significantly impact its mechanical performance. According to He *et al.*, poor fiber-matrix interfaces can reduce mechanical performance due to voids. The study observed void content as high as 12% for CF/PA6 composites despite having a fiber volume fraction of 35%. Based on these experimental observations, the design space for such materials encompasses both micro and macro-scale behaviors. Therefore, multi-scale models that utilize disposable parameterization schemes can accurately predict the actual response of the print structure. One of the main benefits of using a micro-mechanics approach is that it enables the prediction of all of the elastic properties of the composite, as well as its complex, multi-axial, nonlinear response based on the properties of its constituents. By fully exploiting the capabilities of CF4, multi-scale modeling can help optimize the performance of fiber-reinforced plastic materials.

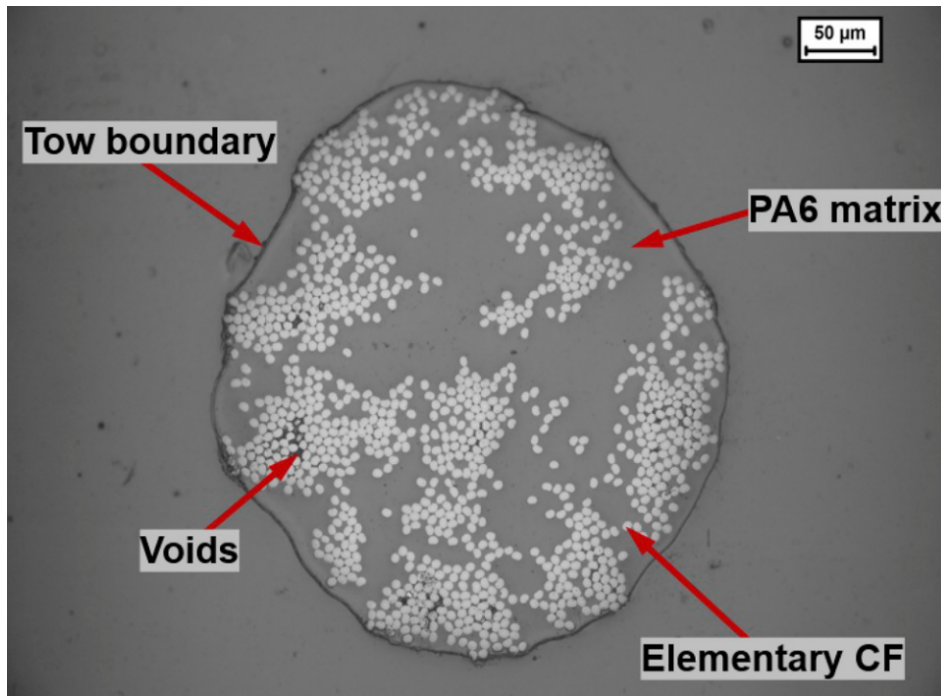


**Figure 2.12:** Typical cross-sectional view of a CF/PA6 filament by optical microscopy [9].

The field of multi-scale modeling is constantly evolving and advancing, with the ultimate goal of eliminating the need for mono-scale topology optimization. Despite this, multi-scale modeling is still considered an extension of the design for additive manufacturing (DfAM) framework. It plays a crucial role in understanding the complex physics that connects the materials and structures in a given system. In addition, future research in DfAM may include exploring new multi-objective performance measures. This could involve extending the framework to include objectives beyond compliance. For instance, researchers could focus on optimizing the performance of a system in terms of its strength, stiffness, or other properties. Furthermore, there is a growing interest in integrating manufacturing constraints into the optimization process. One way to achieve this is through emerging feature-based topology optimization approaches. These approaches allow for the easy integration of manufacturing restrictions, enabling more accurate modeling and simulation of complex systems. This could prove particularly useful for optimizing the performance of complex systems subject to various manufacturing constraints.

Knowing the advantages and limitations of feature-mapping methods—the main focus of the thesis is the integration of GP-CF4 (Fig. 2.8), which aims to propose a comprehensive design for an additive manufacturing framework for CF4. This framework utilizes GP as a topology optimization framework to optimize the

design process. The goal is to create a general framework that is flexible enough to accommodate various design requirements while ensuring efficient and effective manufacturing of CF4 components. The thesis explores multiple aspects of the integration process, including the design methodology, process optimization, and performance analysis. Ultimately, the aim is to provide a robust and reliable framework for various research applications.

## 2.5 Conclusions

The chapter reviews topology optimization (TO) methods for continuous fiber-reinforced polymers (CFRP) structures applied to CF4 design principles. Firstly, the study emphasizes the single-scale TO approaches that simultaneously or sequentially design fiber orientation and structural topologies. To accomplish this, the analysis classifies various parameterizing techniques for anisotropic materials' topology optimization. Continuous parameterization schemes are considered for spatially varying fiber orientations and/or fiber volume fractions, which can be easily applied to CF4 and multi-axis material deposition technologies. However, to meet established manufacturable units, such as automatic fiber placement or automated tape layup, discrete material optimization (DMO) is widely chosen to optimize composite laminates. The study further reports the usefulness of multi-scale TO for realizing FRC and extending it for variable fiber fraction structures. Moreover, it highlights emerging methodologies such as feature mapping, multi-component, and isogeometric optimization that can be applied to CF4, which sets a new bar for designing FRC structures. Therefore, the study aims to address the main challenges in designing TO for anisotropic materials.

*General applicability:* To tackle various structural problems, researchers often employ performance measures that aim to reduce compliance and material distribution on a basic structure. However, it is essential to note that these methods may not be sufficient to address more complex issues such as buckling stability, compliant mechanisms, eigenvalue analysis, and other related challenges. As a result, further validation and testing are required to ensure that these approaches are effective and reliable in dealing with intricate structural problems.

*Solution dependency on an initial guess:* The effectiveness of CFO methods is highly dependent on the initial assumptions made, yet they are commonly preferred for their straightforward approach and capacity to enhance the continuous fiber orientation design. Integrating CFO and DMO techniques is a promising avenue for developing free-form CFRP structures through additive manu-

facturing. It is often difficult to avoid initial design dependency when designing materials that exhibit anisotropic behavior. This is especially true for methods that use pixel or voxel data as design variables. The challenge is that anisotropic materials have different material properties in different directions, making optimizing their performance difficult due to non-convex design space. However, constantly exploring new methods, e.g., feature-mapping and MTO, to overcome these challenges and develop a TO framework that can be optimized for various applications.

*Multiple constraints:* To ensure that the optimization process for CF4 is successful, it is essential to integrate it with manufacturing constraints. Some manufacturing constraints must be considered, including minimum curvature, fiber filament cut-out, and feature size. These constraints are crucial in validating the optimization process and ensuring that the final printed part is viable and can be manufactured without issues. Considering these constraints, it is possible to create high-quality 3D-printed parts that meet the desired specifications and are fully optimized for their intended use.

*Revival of shape-based TO:* In recent years, topology optimization (TO) has gained significant attention in the field of design for additive manufacturing (DfAM) due to its capability to generate optimized designs that can be produced using additive manufacturing (AM) technology. Voxel-based methods are widely used due to their simple implementation. Still, they may not be a suitable choice to attain computer-aided (CAD)-friendly designs and may not necessarily adapt to other freeform fabrication processes. Hence, emerging TO methodologies such as feature mapping, isogeometric shape optimization, and multi-component methods have been considered for the DfAM framework. These methodologies are expected to provide better solutions for complex design problems by using higher-order geometric entities such as curves and surfaces rather than voxels or pixels. They also enable users to generate more designs compatible with CAD systems and quickly adapt to various freeform fabrication units.

*Three-dimensional printing of continuous FRCs:* CF4 has been gaining popularity as a promising technology for designing structures with improved mechanical properties, such as tensile, flexural, compression, and impact resistance. However, CFRPs produced using additive manufacturing techniques are weaker than those produced using traditional methods. This is due to several factors, including low fiber content, poor interface bonding force, void formation, and printing limitations. Therefore, to enhance the performance of CFRCs manufactured using 3D printing, a comprehensive investigation of the material and morphological

properties of continuous fiber-reinforced composites is necessary. This should be conducted in tandem with developing a theoretical optimization (TO) framework. By studying the material and morphological properties of CFRCs, researchers can identify ways to overcome the limitations of 3D printing and improve the strength and durability of printed parts. Ultimately, this could lead to the development of more robust, more reliable, and cost-effective structures.

## Topology optimization using geometric components made of isotropic materials.

The geometry projection (GP)<sup>125</sup> methodology optimizes a high-level parametric description of geometric components  $\Omega_b \in \mathbb{R}^2$  or  $\mathbb{R}^3$ . Given the layer-wise approach of CF4 to print structure, our research focuses on optimizing linearly elastic planar structures composed of bars with fixed width and semicircular ends. The design space for optimization includes the endpoint locations of the bar's medial axes and their constant out-of-plane thicknesses. A differentiable mapping for efficient gradient-based optimization projects the bar design onto the computational design domain  $\mathcal{D}$  by converting the endpoint positions into a continuously varying density field. This density field indicates the fraction of solid material in  $\mathcal{D}$ , similar to density-based topology optimization methods. This enables penalized density to be employed in determining the material properties as in SIMP<sup>73</sup> topology optimization techniques. A zero penalized density means bar  $\Omega_b$  does not affect the material properties at  $\mathbf{x} \in \mathcal{D}$ . Therefore, the bar's membership variables  $\alpha_b$  and the penalization allow the optimizer to remove or reinsert the bars in the design, regardless of the bar's dimensions, position, or orientation. This characteristic is a hallmark of GP techniques and promotes better optimization convergence. The membership variable and the projected density must be penalized to ensure that intermediate-density regions satisfy the Hashin-Shtrikman bounds. Lastly, the method naturally accommodates the imposition of several fixed-length scales, which allows different bar widths. Using bars with semicircular ends instead of rectangles simplifies geometry projection and sensitivity analysis, improving robustness and design. For completeness, the method demonstrated its capabilities for primitives made of fiber-reinforced plates<sup>155,156</sup>.

This chapter details the critical ingredients of the feature-mapping methods. Then, it describes the formulation of the geom-

<sup>125</sup> Norato *et al.*, "A geometry projection method for continuum-based topology optimization with discrete elements," 2015.

<sup>73</sup> Andreassen *et al.*, "Efficient topology optimization in MATLAB using 88 lines of code," 2011.

<sup>155</sup> Smith *et al.*, "Topology optimization of structures made of fiber-reinforced plates," 2022.

<sup>156</sup> Smith *et al.*, "Simultaneous material and topology optimization of composite laminates," 2023.

etry projection for isotropic material, discusses implementation aspects, and demonstrates some of its capabilities by presenting several 2D compliance minimization examples. The chapter discusses the main components of the GP method to construct the building block for extrapolating the implementation for continuous fiber-reinforced polymer (CFRP) materials. The subsequent chapter explains how to apply the GP method to variable stiffness CFRP laminates for both single-layer and multilayered approaches.

### 3.1 Key ingredients of feature-mapping methods

Over the past twenty years, a new set of methods for implementing and solving structural optimization problems has emerged: feature-mapping methods. These methods rely on a high-level geometric description to parameterize the design and map features onto a non-body-fitted mesh for analysis. The primary purpose of using these methods is to have greater control over the geometry, which can help impose direct constraints on geometric features while avoiding re-meshing problems. We examine the key definitions and elements that these methods employ to map geometric features onto a fixed mesh and other feature-mapping techniques, including methods for combining features.

**High-level geometric features** —A collection of defined points that are either solid components or holes in a solid component are called high-level geometric features. These features are distinguished by their size, location, or orientation. Examples of such parameters include the position of a primitive shape like a bar or a circle. These parameters frequently represent solid objects in CAD systems, thus managing their dimensions more straightforwardly. Their parameterization describes high-level geometric features, representing solid components or openings and the direct spatial dimensions linked with their size, location, or orientation.

**Mapping features onto a fixed grid** —Mapping high-level geometric features onto a fixed grid is crucial for feature-mapping techniques applied in structural optimization. This step involves representing these features in a way that enables them to be analyzed on a fixed grid, which serves as a spatial partition of the design region that remains unchanged throughout the optimization process. This, in turn, facilitates the analysis of high-level geometric features within a structured spatial discretization, providing a means to perform structural optimization without re-meshing during the optimization process. Two main types of geometry

mapping approaches are used for analyzing high-level geometric features in structural optimization: pseudo-density-based mapping and immersed boundary/XFEM approaches.

Representation of high-level geometric features is achieved through pseudo-density-based mapping, which involves using element-constant pseudo-densities. These densities estimate the volume fraction of the elements that intersect the features. The advantage of this method is that it allows for analysis to be performed on a fixed grid without re-meshing. On the other hand, immersed boundary/XFEM approaches rely on techniques such as the eXtended Finite Element Method (XFEM)<sup>157</sup> to analyze structures with complex geometries. These approaches enhance the finite element approximation with additional degrees of freedom, allowing for accurate capture of the behavior of the structure, particularly at the boundaries and interfaces.

<sup>157</sup> Bergen *et al.*, "An interface-enriched generalized finite element method for the analysis and topology optimization of 2-D electromagnetic problems," 2024.

**Material interpolation functions** —Interpreting material properties for intermediate pseudo-density values in structural optimization heavily relies on material interpolation functions. These functions determine the stiffness corresponding to the intermediate values of the pseudo-density field for a given material properties. The material interpolation function scales the material properties based on the pseudo-density values, thereby impacting the interpretation of material properties for intermediate values. It determines the changes in the stiffness properties of the material as the pseudo-density varies between the solid and void states. Accurately interpreting the material properties for intermediate pseudo-density values is challenging because these values represent the transition between solid and void. Hence, the form of the material interpolation function is crucial in ensuring that the resulting material properties align with the physical behavior of the material.

**Combining features** —Two primary methods exist to combine individual mapped features before or after mapping to the fixed grid in the context of structural optimization. The first method is "combine-then-map," aggregating individual geometric features to form a unified representation. Afterward, this unified representation is mapped onto the fixed grid for analysis. An example of this method is using Boolean operations to combine individual features before mapping them to the fixed grid. The second method is called "map-then-combine." Here, each geometric feature is initially mapped onto the fixed grid. Once the mapping is complete, the resulting mapped variables, such as pseudo-densities or

material property values, are combined. This combination can be element-wise or at integration points, depending on the specific method used.

**Implicit vs explicit feature representations** —Structural optimization can be represented in two ways: implicit and explicit feature representations. Implicit feature representations use rules to determine if a point belongs to a feature, while explicit feature representations generate points that form the feature geometry. Implicit representations are ideal for complex and irregular feature geometries, while explicit representations are better suited for well-defined and regular geometries. Density-based and level-set methods typically use implicit representations, while high-level parameters define explicit representations, such as the geometry projection method.

**Sensitivity analysis** —Feature-mapping methods follow density-based topology optimization methods for computing sensitivities. Both methods allow for design sensitivities to be calculated more quickly than approaches that require the computation of boundary sensitivities, like some level-set methods. Density-based topology optimization has an established process for calculating design sensitivities, which can be easily performed for a wide range of functions, including multiphysics problems that comply with the chain rule. Density-based topology optimization involves the calculation of sensitivities with respect to the element pseudo-densities, which is closely related to the calculation of sensitivities in feature-mapping methods. By leveraging the established methods used in density-based topology optimization, feature-mapping methods provide a simple and efficient approach to sensitivity analysis.

**Feature-based topology optimization** —Topology optimization problems are addressed using feature-mapping methods that rely on high-level parametric descriptions of voids in a solid design region or solids in a void design region to define the structure. This approach involves parameterizing the design with a high-level geometric description and mapping features onto a fixed grid for analysis. Feature-mapping methods provide a way to change the shape and connectivity of the structure simultaneously and allow for mapping the geometry of individual features onto a fixed analysis grid, which is essential for topology optimization. This approach also offers better control over the structure's geometry, making imposing direct constraints on geometric features easier

while avoiding re-meshing. The Geometry Projection method discussed in the thesis includes the map-then-combine method, which explicitly uses high-level geometric parametric descriptions to optimize topology. In summary, feature-mapping methods are a unique solution to topology optimization problems, relying on high-level geometric parameterization and mapping features onto a fixed grid for analysis.

### 3.2 Geometry projection formulation

Geometry Projection (GP) is a topology optimization methodology that represents the design using geometric components such as 2D flat or 3D cylindrical bars or 3D rectangular plates mapped onto a component density field. This field is then discretized using a fixed analysis mesh ( $\mathcal{D} \subset \mathbb{R}^2$ ), avoiding the need to re-mesh upon design updates. The GP mapping is differentiable, readily allowing for sensitivity calculations with respect to the geometric parameters so that efficient gradient-based nonlinear programming methods can be employed for the optimization. The chain rule used to compute sensitivities requires derivatives of the optimization functions concerning the densities. However, the technique can benefit from sensitivity formulations already developed for density-based topology optimization approaches.

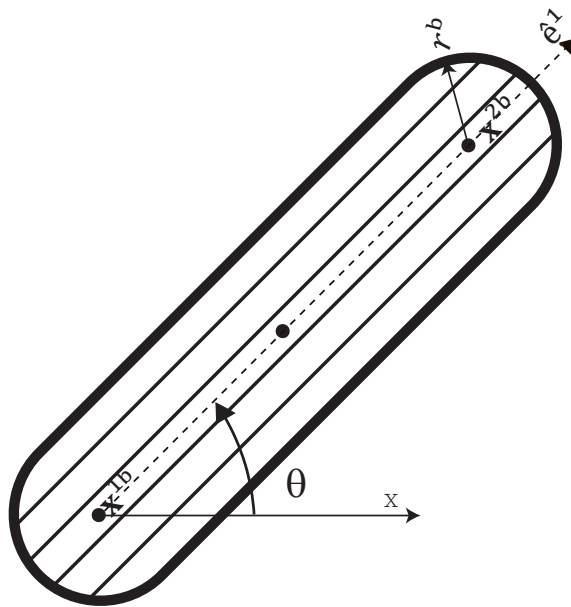


**Figure 3.1:** Geometric design variables for a bar

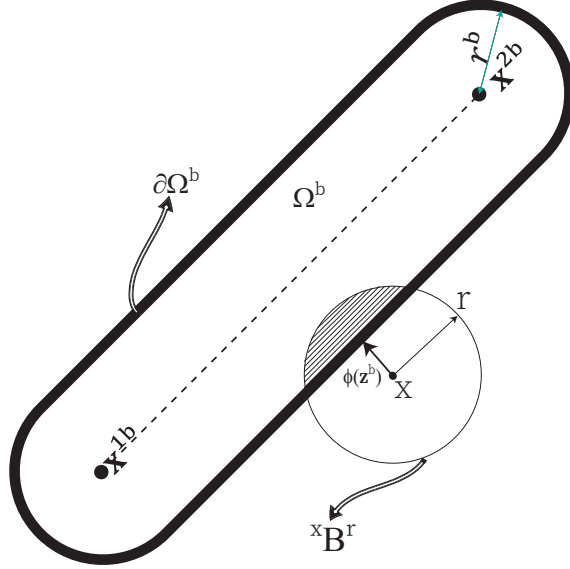


Figure 3.2: Projection of bar on  $\mathbf{x} \in \mathcal{D}$

### 3.2.1 Definition of components and their projected densities

To begin the GP procedure, we first map the design variables of the component to a component-wise density field  $\rho_b(\mathbf{x}; \mathbf{z}_b)$  for any point  $\mathbf{x}$  in the design region. The dual geometric parameters/density representation can treat individual components as high-level geometric objects or field variables in component densities. Each bar  $b \in \mathcal{B}$ , where  $\mathcal{B}$  represents the set of all bar indices, is characterized by an offset solid whose medial axis is a line segment, which corresponds to a rectangle with semicircular ends (see Fig. 7.1) and occupies a region  $\Omega_b \in \mathbb{R}^2$ . The medial axis is defined by its two endpoints  $(\mathbf{x}_{1b}, \mathbf{x}_{2b})$ , and the offset distance is given by the bar's radius  $r_b$ . A membership variable  $\alpha_b \in [0, 1]$  is assigned to each bar and penalized as in density-based methods, which allows the optimizer to remove it from or reinsert it in the design. The vector of the design variable  $\mathbf{z}_b$  for bar  $b$  is thus given by

$$\mathbf{z}_b := (\mathbf{x}_{1b}, \mathbf{x}_{2b}, r_b, \alpha_b). \quad (3.1)$$

As illustrated in Fig. 3.2, the projected density at a point  $\mathbf{x}$  is defined as the intersection of a ball with a radius  $r$  and centered at  $\mathbf{x}$  with  $\Omega_b$ , i.e.

$$\rho_b(\mathbf{x}; \mathbf{z}_b) := \frac{|B_{\mathbf{x}}^r \cap \Omega_b(\mathbf{z}_b)|}{|B_{\mathbf{x}}^r|}. \quad (3.2)$$

In 2D, assuming  $r$  is much smaller than the bar's dimensions,  $B_{\mathbf{x}}^r \cap \partial\Omega_b$  can be approximated as a line segment. Therefore, the area fraction of (5.7) can be computed as the area fraction of the

circular segment of height  $h = r - \phi_b$ , where  $\phi_b$  denotes the signed distance from  $\mathbf{x}$  to  $\partial\Omega_b$ . That is, the projected density for bar  $b$  is a single-valued function of  $\phi_b$ , which effectively constitutes a regularized Heaviside function:

$$\rho_b(\mathbf{x}; \mathbf{z}_b) := \tilde{H} \left( \frac{\phi_b(\mathbf{x}; \mathbf{z}_b)}{r} \right). \quad (3.3)$$

The expression for  $\tilde{H}$  is given as,

$$\tilde{H}(x) = \begin{cases} 0, & \text{if } x \leq -1 \\ 1 + \frac{1}{\pi} \left( x\sqrt{1-x^2} - \arccos x \right), & \text{if } |x| < 1 \\ 1, & \text{if } x \geq 1 \end{cases} \quad (3.4)$$

$$\frac{d\tilde{H}}{dx} = \begin{cases} 2\sqrt{1-x^2}/\pi, & \text{if } |x| < 1 \\ 0, & \text{otherwise} \end{cases}$$

We follow the convention that the signed distance from points that are inside the bar (i.e.,  $\mathbf{x} \in \Omega_b$ ) is positive, while the signed distance to points outside the bar (i.e.,  $\mathbf{x} \in \mathbb{R}^2 \setminus \Omega_b$ ) is negative. The signed distance function for a bar is thus the offset less the distance to the medial line segment, as detailed in the next Section.

A penalized density is computed for each bar that is subsequently used to calculate its elastic stiffness tensor using a method similar to the solid-isotropic material penalization (SIMP) approach used in density-based topology optimization [110]. The penalized density is given by

$$\check{\rho}_b^{\text{eff}}(\mathbf{x}; \mathbf{z}_b) := (\alpha_b \rho_b(\mathbf{x}; \mathbf{z}_b))^q, \quad (3.5)$$

where we recall  $\alpha_b$  represents the bar's membership variable. The geometry projection method involves assigning a membership variable, denoted as  $\alpha_b \in [0, 1]$ , to each component in addition to the parameters that describe its shape. This variable penalizes the size of each component, similar to the penalization schemes used in density-based topology optimization. A value of  $\alpha_b = 1$  means the geometric component must be included in the structure, while  $\alpha_b = 0$  means the component must be removed from the design. This feature makes it easier for the optimizer to modify the topology by removing geometric components.

### 3.2.2 Combining Components

When multiple bars overlap, the penalized densities for all bars into a combined density given by

$$\rho(x, \mathbf{Z}, p) := \begin{cases} \rho_{\min}, & \text{if } \check{\rho}_b^{\text{eff}} = 0, \text{ for } b = 1, \dots, n_b \\ \max_b \check{\rho}_b^{\text{eff}}, & \text{otherwise,} \end{cases} \quad (3.6)$$

where  $n_b$  is the number of geometric components,  $\widetilde{\max}$  denotes a smooth approximation of the maximum function, and  $0 < \rho_{\min} \ll 1$  is a positive lower bound to prevent an ill-posed analysis.

$$\rho(x, Z, p) := \left[ \rho_{\min}^p + \left(1 - \rho_{\min}^p\right) \sum_{b=1}^{n_b} \check{\rho}_b^{\text{eff} p} \right]^{\frac{1}{p}} \quad (3.7)$$

This modified  $p$  norm renders  $\rho = \rho_{\min}$ , if  $\widehat{\rho}_b = 0 \forall b$  and  $\rho = 1$  if  $\widehat{\rho}_b = 1 \forall b$ , regardless of the number of geometric components. Finally, the combined density is reflected in the analysis by using an artificial material, with the elasticity tensor modified as

$$\mathbb{C}(x, Z) := \rho \mathbb{C}_0 \quad (3.8)$$

where  $\mathbb{C}_0$  is the elasticity tensor for the isotropic material.

For the finite element analysis, we assume an element-uniform projected density. As such, the element projected density  $\rho_{be}$  is computed at its centroid  $\mathbf{x}_e$ . The sample window radius  $r$  is fixed and taken to be at least the smallest semi-diagonal of the element.

### 3.2.3 Distance function

The section describes the computation of the signed distance  $\phi_b$  in (5.7) of bars represented as offset surfaces<sup>125</sup>. The set of all points gives the boundary of the bar at a distance  $r_b$  of the line segment with endpoints  $\mathbf{x}_{1b}$  and  $\mathbf{x}_{2b}$  (Fig. 7.1). This definition portrays bars in 2D as rectangles with semicircular ends and 3D as cylinders with semispherical ends.

The vector of design parameters for bar  $b$ , which is given by  $\mathbf{z}_b := (\mathbf{x}_{1b}, \mathbf{x}_{2b}, r_b, \alpha_b)$ . The offset surface representation has an added advantage: the ability to compute the signed distance to the bar's boundary. This can be achieved by subtracting the bar radius by taking the distance to the medial axis, denoted as  $d_b$ .

$$\phi_b(\mathbf{x}; \mathbf{z}_b) = d_b(\mathbf{x}; \mathbf{z}_b) - r_b$$

To determine the distance to the boundary of a bar, it is only required to calculate the distance to the bar's medial axis. Thus,

<sup>125</sup> Norato *et al.*, "A geometry projection method for continuum-based topology optimization with discrete elements," 2015.

computing the distance to the medial axis can effectively determine the minimum distance to any point on the bar's boundary. The distance to the medial segment from  $\mathbf{x}$  is given by

$$d_b = \sqrt{\left(d_b^\perp\right)^2 + \left(d_b^\parallel\right)^2},$$

where,

$$\begin{aligned} d_b^\perp &= \|\mathbf{P}_b^\perp \mathbf{x}_b\| & d_b^\parallel &= \max\left\{0, \|\mathbf{P}_b^\parallel \mathbf{x}_b\| - \frac{\|\mathbf{v}_b\|}{2}\right\} \\ \mathbf{P}_b^\perp &= \mathbf{I} - \mathbf{P}_b^\parallel & \mathbf{P}_b^\parallel &:= \frac{\mathbf{v}_b \otimes \mathbf{v}_b}{\|\mathbf{v}_b\|^2} \\ \mathbf{x}_b &:= \mathbf{x} - \mathbf{x}_{1b} & \mathbf{v}_b &:= \mathbf{x}_{2b} - \mathbf{x}_{1b} \end{aligned}$$

In these expressions,  $\mathbf{P}_b^\perp$  and  $\mathbf{P}_b^\parallel$  denote the perpendicular and parallel projectors to the medial axis vector  $\mathbf{v}_b$  of bar  $b$ , respectively, and  $\otimes$  denotes the tensor product.

### 3.3 Setting and implementation of the optimization problem

A domain  $\mathcal{D}$  is discretized using linear quadrilateral plane-stress 4-noded finite elements of size  $1 \times 1$ , in which the displacements are interpolated within each element as

$$\mathbf{u} = \begin{Bmatrix} u_0 \\ v_0 \end{Bmatrix} = \sum_{i=1}^4 \mathbf{N}_i \mathbf{a}_i^{(e)} = [\mathbf{N}_1, \mathbf{N}_2, \mathbf{N}_3, \mathbf{N}_4] \begin{Bmatrix} \mathbf{a}_1^{(e)} \\ \mathbf{a}_2^{(e)} \\ \mathbf{a}_3^{(e)} \\ \mathbf{a}_4^{(e)} \end{Bmatrix} = \mathbf{N} \mathbf{a}^{(e)} \quad (3.9)$$

where  $N_i(\xi, \eta)$  is the  $C^0$  continuous shape function of node  $i$ .

$$\mathbf{N}_i = \begin{bmatrix} N_i & 0 \\ 0 & N_i \end{bmatrix}; \quad \mathbf{a}_i^{(e)} = [u_{0i}, v_{0i}]^T \quad (3.10)$$

The stiffness matrix  $\mathbf{K}_{ij}^{(e)}$  for an element is obtained by taking the contribution from the stiffness matrices due to membrane, bending, and transverse shear effects. This results in an element stiffness matrix, which is used to compute its design sensitivity:

$$\begin{aligned} \mathbf{K}_{a_{ij}}^{(e)} &= \iint_{\Omega^{(e)}} \mathbf{B}_{a_i}^T \mathbf{D}_a \mathbf{B}_{a_j} d\Omega^{(e)} \quad , \quad a = m \\ \nabla_z \mathbf{K}_{a_{ij}}^{(e)} &= \iint_{\Omega^{(e)}} \mathbf{B}_i^T \nabla_z \mathbf{D}_a \mathbf{B}_j d\Omega^{(e)} \end{aligned} \quad (3.11)$$

$\mathbf{B}_i$  is the symmetric gradient for the  $i^{\text{th}}$  node, which can be defined as

$$\mathbf{B}_i = \{ \mathbf{B}_{m_i} \} \quad \text{with} \quad \mathbf{B}_{m_i} = \begin{bmatrix} \frac{\partial N_i}{\partial x} & 0 \\ 0 & \frac{\partial N_i}{\partial y} \\ \frac{\partial N_i}{\partial y} & \frac{\partial N_i}{\partial x} \end{bmatrix} \quad (3.12)$$

The density at the centroids of each element is used to calculate the structural volume, which estimates the solid volume fraction  $v^{(e)}$  in the domain  $\Omega^{(e)}$  that the element  $e \in \mathcal{D}$  occupies.

$$v^{(e)} := \frac{1}{|\Omega^{(e)}|} \sum_b \rho_{be}^{\text{eff}} \quad (3.13)$$

We consider the compliance minimization problem subject to a given volume fraction. The optimization problem may be formally stated as

$$\begin{aligned} & \min_{\{z_b\}} f := \log(c + 1) \\ \text{subject to:} & \\ & v \leq \bar{v} \\ & \mathbf{KU} = \mathbf{f} \\ & \underline{z}_i \leq z_i \leq \bar{z}_i, i = 1, 2, \dots, n_z, \end{aligned} \quad (3.14)$$

where  $c = \mathbf{U}^\top \mathbf{f}$  is the compliance,  $\mathbf{U}$  and  $\mathbf{f}$  are the global displacement and force vectors, respectively,  $\bar{v}$  is a prescribed upper limit on the volume fraction,  $\mathbf{K}$  is the global stiffness matrix,  $[\underline{z}_i, \bar{z}_i]$  is a lower and upper bound on the  $i^{\text{th}}$  design variable,  $\bar{v}$  is a prescribed upper-limit on the volume fraction and  $v$  is the volume fraction defined as

$$v := \frac{\sum_e v^{(e)} \Omega^{(e)}}{\sum_e \Omega^{(e)}} \quad (3.15)$$

As addressed in previous works [125, 126], to prevent convergence issues during the optimization steps, precautionary steps are taken as follows: first, log-scaled compliance  $f(\mathbf{z}) = \log(1 + c(\mathbf{z}))$  damps the large oscillation in compliance when the structure becomes disconnected from the load/support. Second, scaling the design variables allows us to impose a uniform move limit  $m$  at each iteration  $I$  as

$$\begin{aligned} \hat{z}_i & := \frac{z_i - \underline{z}_i}{\bar{z}_i - \underline{z}_i} \\ \max \left( 0, z_i^{I-1} - m \right) & \leq z_i^I \leq \min \left( 1, z_i^{I-1} + m \right) \end{aligned} \quad (3.16)$$

Finally, for the design-independent loading, the problem (4.22) is self-adjoint, and so the sensitivity of the compliance and volume

fraction is as follows:

$$\begin{aligned}\nabla_z c &= - \sum_e \mathbf{u}^\top \left( \nabla_z \mathbf{K}^{(e)} \right) \mathbf{u} \\ \nabla_z v &= \frac{\sum_e \left( \nabla_z v^{(e)} \right) \Omega^{(e)}}{\sum_e \Omega^{(e)}}\end{aligned}\quad (3.17)$$

For isotropic materials, the stiffness matrix derivative  $\nabla_z \mathbf{K}^{(e)}$  is equal to zero because material properties are independent of geometric parameters, where we denote the design sensitivity operator as  $\nabla_z := \frac{\partial}{\partial z_i}$ . Unlike anisotropic materials where material properties depend on geometric parameters, implies  $\nabla_z \mathbf{K}^{(e)} \neq 0$  as seen in Chapter 4.

### 3.4 Computer Implementation

The finite element (FE) code used in this work is implemented in MATLAB using linear quadrilateral/hexahedral elements. The `sparse()` function is employed to assemble the stiffness matrix, which is subsequently partitioned by Neumann (free) and Dirichlet (essential) degrees of freedom on the CPU. The stiffness matrix, compliance, volume fraction function, and their sensitivities are computed using multidimensional arrays, avoiding loops and calling built-in MATLAB functions whenever possible.

Calculating the objective and constraint function is divided into three steps. Firstly, the geometry projection is performed, which involves computing the element volume fractions  $v_e$  and element elasticity tensors  $\mathbf{C}_e$  for each element in the mesh based on their definitions in Section 3.2. Additionally, we also calculate and store their analytical design sensitivities. Secondly, we assemble the finite element system corresponding to the current design and solve for the unknown displacements. Finally, we calculate compliance and its sensitivity using geometry projection and finite element analysis. In addition, we determine the structural volume fraction and its sensitivity using the result of the geometry projection.

For all the examples, the following settings are considered until mentioned otherwise. The method-of-moving-asymptotes (MMA) [74] is employed for the optimization routine, using the default parameters described in [158], i.e.,  $a_0 = 1$  for the objective function, and  $a_i = 0$ ,  $c_i = 1000$  and  $d_i = 1$  for every constraint  $i$  in the optimization. The void material is isotropic with Young's modulus  $E^{\text{void}} = 10^{-3}E_1$  and Poisson's ratio  $\nu^{\text{void}} = 0.3$ . During initialization, the radius of the bars is set to the average of their

upper and lower bounds. The sizing variable is set to  $\alpha = 0.5$ , and the move limit is fixed to  $m = 0.05$  throughout the optimization process.

The optimization procedure involves three stopping criteria. The first criterion is met when the 2-norm of the change in the design variable vector is less than 0.003. The second criterion is reached when the norm of the Karush-Kuhn-Tucker optimality conditions falls below 0.005. The third criterion is satisfied when the change in the objective function is less than  $10^{-6}$ . The optimization process is stopped if any of these criteria are met.

**Table 3.1:** Material properties used for all the examples

Material	$E_1$ [GPa]	$E_2$ [GPa]	$\nu_{12}$	$G_{12}$ [GPa]	$G_{13}$ [GPa]	$G_{23}$ [GPa]
Aluminum 6061-T-6	68.9	-	0.33	6.0	-	-

### 3.5 Examples

For all four numerical examples—We consider bars made of isotropic and components are joined together as described in Section 3.2.2. Table (3.1) lists Aluminum 6061-T-6 material properties used for the bars. The geometry projection method employs a compact design representation more prone to getting stuck in unfavorable local minima based on the initial design than the verbose representation used by density-based and level-set methods. The initial design plays a crucial role in all topology optimization techniques, but its significance is more evident in feature-mapping techniques. The dependence on the initial design is not specific to any feature-mapping technique but is due to the restrictive geometric representation.

The orientation of the bar to the global coordinate system determines the color assignment in the density plot. The colormap to the bars has no physical significance for isotropic bars and only serves as a visualization tool. However, when bars are assigned with FRP material properties, the colormap illustration of bars helps to differentiate between bars with varying material properties based on their orientation to the global coordinate system.

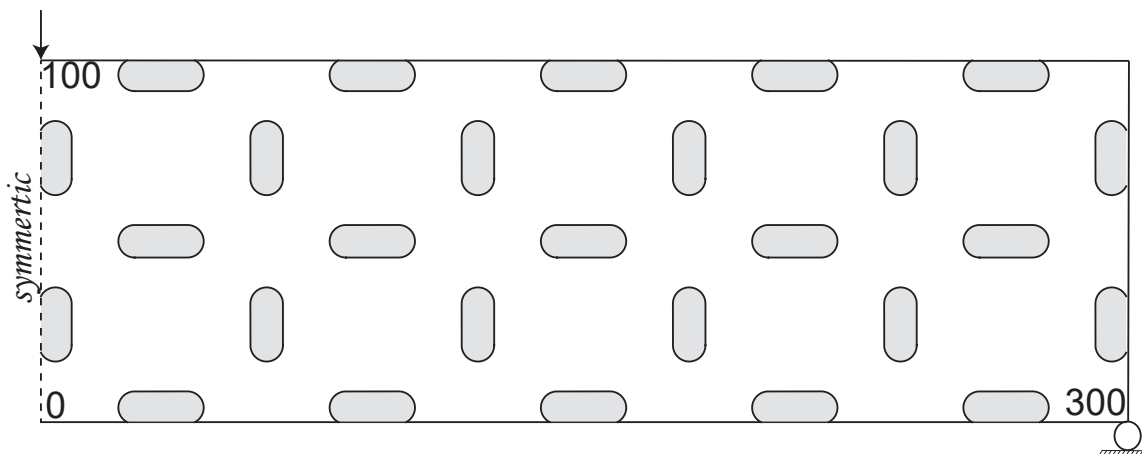
#### 3.5.1 A rectangular plate under 3–point bending—MMB

In this example, a Messerschmitt-Bölkow-Blohm (MBB) beam is designed with an aspect ratio of 1:6 over a sweep of volume fraction limits in the range of  $\bar{v} \in [0.25, 0.35]$ . Since the problem is

symmetric, only the right half of the geometry is modeled. The dimensions, supports, and loading are depicted alongside the initial design in Fig. 3.3. The initial design is made of 27 bars.

$$\begin{Bmatrix} (0, 0) \\ 3 \\ 0 \end{Bmatrix} \leq \begin{Bmatrix} (\mathbf{x}_{b1}, \mathbf{x}_{b2}) \\ r_b \\ \alpha_b \end{Bmatrix} \leq \begin{Bmatrix} (300, 100) \\ 6 \\ 1 \end{Bmatrix} \quad (3.18)$$

**Figure 3.3: MBB**—The features' initial arrangement in rectangular plates of the aspect ratio of  $1 \times 6$ , which are subjected to supports and unit load, i.e., 3-point bending



There are a few noteworthy things about this run. Firstly, despite the complexity of the design space, the optimizer can identify the optimal topology in less than 20 iterations. This is demonstrated in Fig. 3.6. Secondly, the optimizer can effectively remove bars by reducing their  $\alpha_b$  value to approximately zero and setting their length to almost zero, collapsing them into a circle. This suggests that the sensitivities provide the optimizer with quick and efficient guidance towards a good solution.

It is important to note that the members in our structure are mostly connected, without gaps between intersecting bars. The disconnected structure can cause a jump in compliance, as demonstrated in Fig. 3.6. This is due to structural requirements, as we do not impose any geometric constraint that enforces this, for example, connected features as carried out in the ground structure-based topology optimization<sup>159</sup>. Achieving this quality requires the void region material to be sufficiently soft, meaning that  $E^{\text{void}}$  must not be too large—the void material will be stiff enough to transfer the load if it is. On the other hand,  $E^{\text{void}}$  can be relatively small, as the analysis will become ill-posed. This is particularly

<sup>159</sup> Zegard *et al.*, “GRAND—Ground structure based topology optimization for arbitrary 2D domains using MATLAB,” 2014.

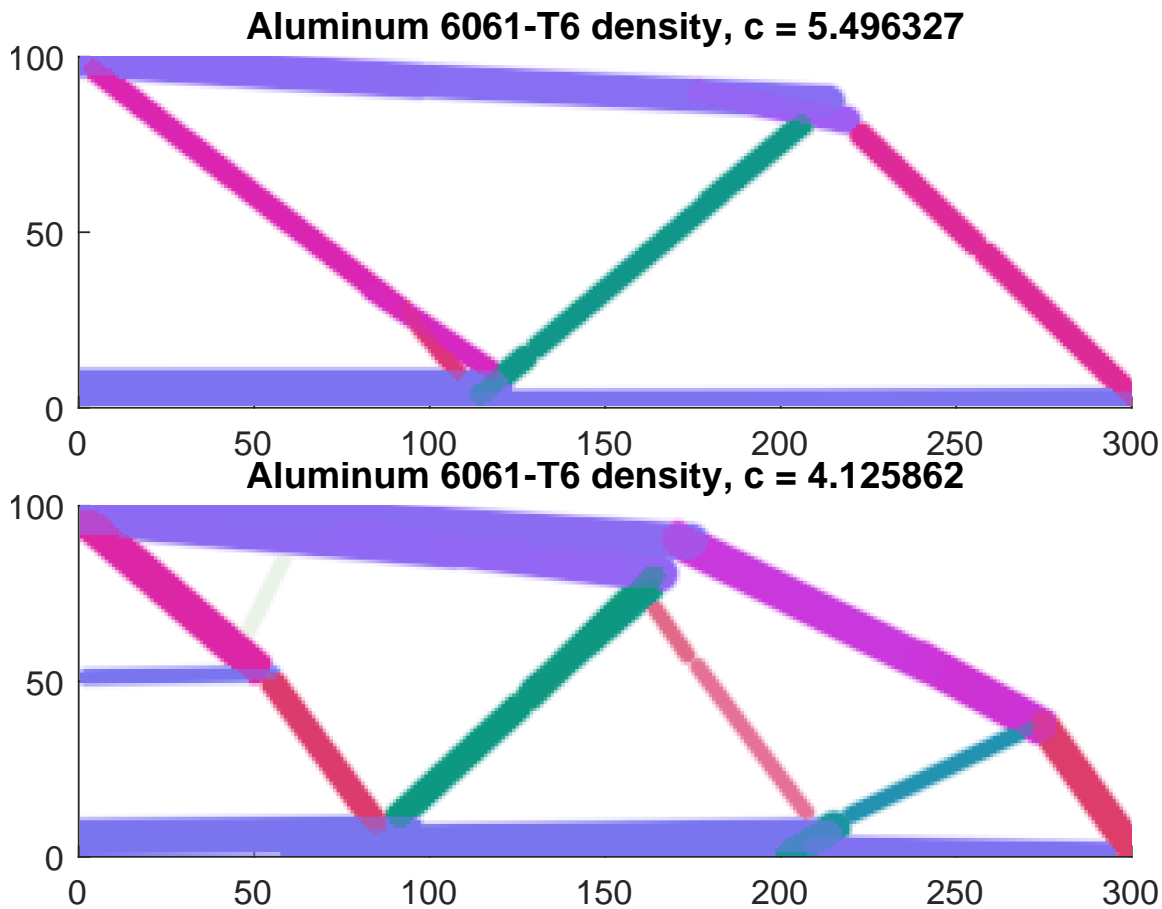


**Figure 3.4: MBB**—The density plot for two volume fraction  $\bar{v} \in [0.25, 0.35]$ . Color assignment to bars is based on the bar’s orientation to the global coordinate system; thus, it only serves the purpose of visualization for bars made of isotropic material.

important in early iterations when there may need to be a connected path of bars between the loads and the supports—our experience shows that the value  $E^{\text{void}} = 10^{-3}E_1$  is appropriate and produce comparable results to those of SIMP<sup>73</sup>. Another observation that must be made is that the optimizer can offset two (or more) bars to increase the effective width and the bending stiffness (see Fig. 3.5). This can be seen, for example, in the bottom and top members on the left edge of the last iteration in Fig. 3.4. Similarly, the optimizer concatenates bars to produce a more extended member or a curved load path. If one bar engulfs another, the adequate thickness is the maximum thickness between the two bars (Section 3.2.2), and the sensitivity of the composite density with respect to a change in the position of the engulfed bar’s endpoint along its medial axis is zero. Finally, it is worth noting that the convergence behavior of this and all other examples is good. There is a significant difference in the convergence behavior

<sup>73</sup> Andreassen *et al.*, “Efficient topology optimization in MATLAB using 88 lines of code,” 2011.

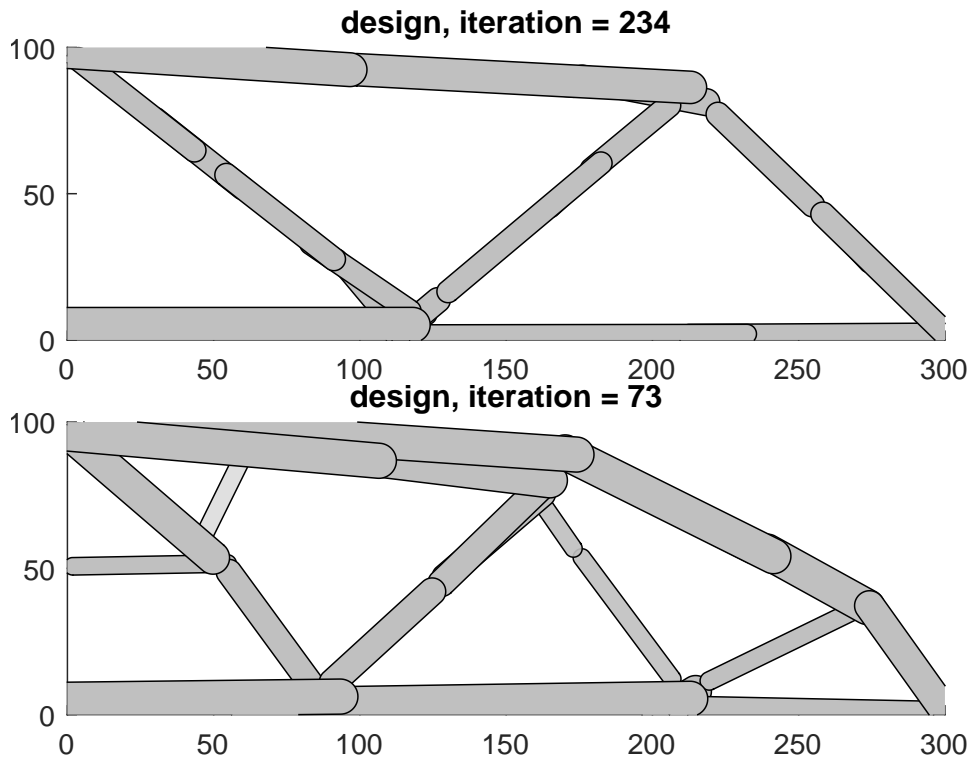


**Figure 3.5: MBB**—The design plot for two volume fraction  $\bar{v} \in [0.25, 0.35]$ . Different bar intersections can be observed: merged bars with in-plane width offset, concatenated merged bars, collinear merged bars, and in-plane width stacking of merged bars.

for two volume fraction limits. When the volume fraction is lower, the design variable of the component can change substantially at every iteration for a move limit of ( $m = 0.05$ ), unlike at higher volume fractions. This is not because of the volume fraction limit but because of the hyperparameters used for the MMA optimizer. These hyperparameters can cause oscillation in some instances before the optimizer reaches the desired convergence criteria. The following will be discussed in the subsequent chapters, yet a primary analysis can be made between isotropic and CFRP material. We can consider a hypothetical isotropic material with the same Young's modulus as the CFRP fiber-direction modulus of  $E_1 = 113.6[\text{GPa}]$  but the same Poisson's ratio as aluminum of  $\nu_{12} = 0.33$ . Although the bars' width is relatively small, we might think the two materials will comply similarly. However, there will be a significant difference in strain-energy density at the intersections of components. At these intersections, the internal forces of the adjacent members converge in different directions. This poses no issue for the isotropic material since it is equally stiff in all directions. However, the transversely compliant CFRP will have a much higher strain-energy density at the intersections of

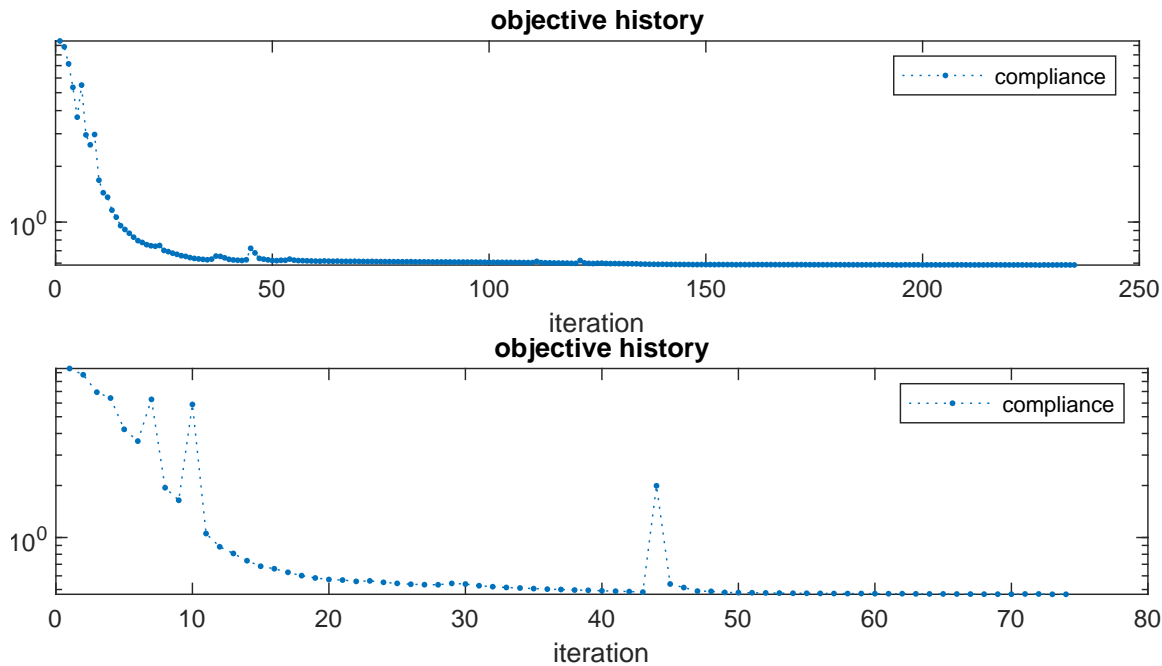


**Figure 3.6: MBB**— The compliance history plot also depicts a large difference in the convergence behavior for two volume fractions  $\bar{v} \in [0.25, 0.35]$

members because the stiff fiber direction cannot simultaneously align with all the intersecting load paths. Therefore, considerable research has been done to enable overlapping fiber-reinforced bars in the GP method and still attain additively manufacturable designs.

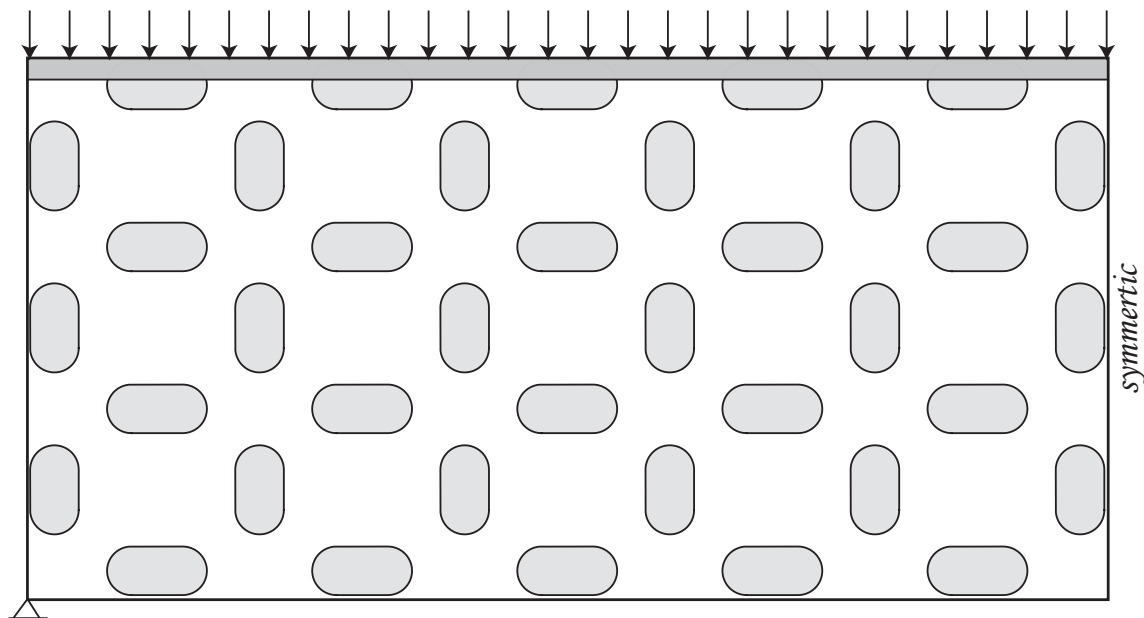
### 3.5.2 A rectangular domain under uniform load—Bridge

A bridge with an aspect ratio of 1 : 4 is designed to support a distributed load with a net magnitude of 1.0. The design considers volume fraction limits in the  $\bar{v} \in [0.25, 0.35]$ . Since the problem is symmetric, only the left half of the geometry is modeled. Fig. 3.7 shows the dimensions, supports, and loading alongside the initial design, which consists of 38 bars. In addition to the designable bars, a non-designable bar  $\underline{b}$  with a fixed offset radius of  $r_{\underline{b}} = 4.0$  and a fixed size variable of  $\alpha_{\underline{b}} = 0.99$  is placed with its medial axis aligned with the top edge, along the distributed load.

$$\begin{Bmatrix} (0, 0) \\ 3 \\ 0 \end{Bmatrix} \leq \begin{Bmatrix} (\mathbf{x}_{b1}, \mathbf{x}_{b2}) \\ r_b \\ \alpha_b \end{Bmatrix} \leq \begin{Bmatrix} (200, 100) \\ 6 \\ 1 \end{Bmatrix} \quad (3.19)$$

The optimizer can identify the optimal topology in less than 20 iterations. This is demonstrated in Fig. 3.8a, 3.8b. Secondly,

**Figure 3.7: Bridge**—The features' initial arrangement in the rectangular domain of the aspect ratio of  $1 \times 2$ , subjected to supports and uniform distributed load over a non-designable bar.

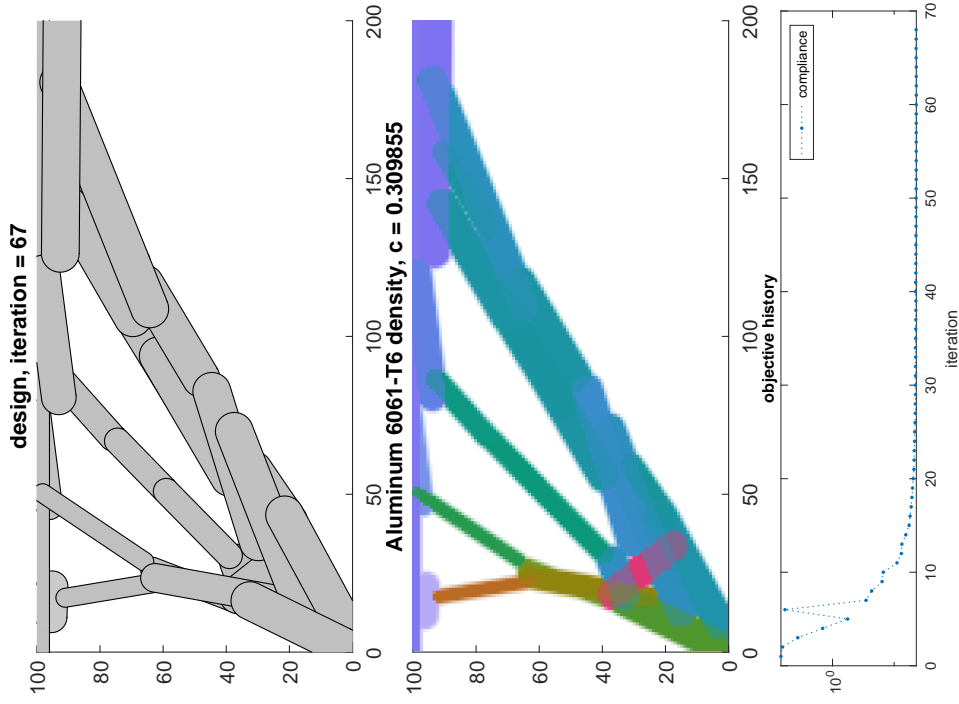


the convergence behavior of both cases is good, and the solution converges approximately at 100 iteration in contrast to the previous example, where a significant difference is observed in convergence behavior. Similarly to the MMB beam example, the optimizer can offset bars to increase the effective width and concatenates' bars to produce a more extended member as seen in Fig. 3.8a, 3.8b.

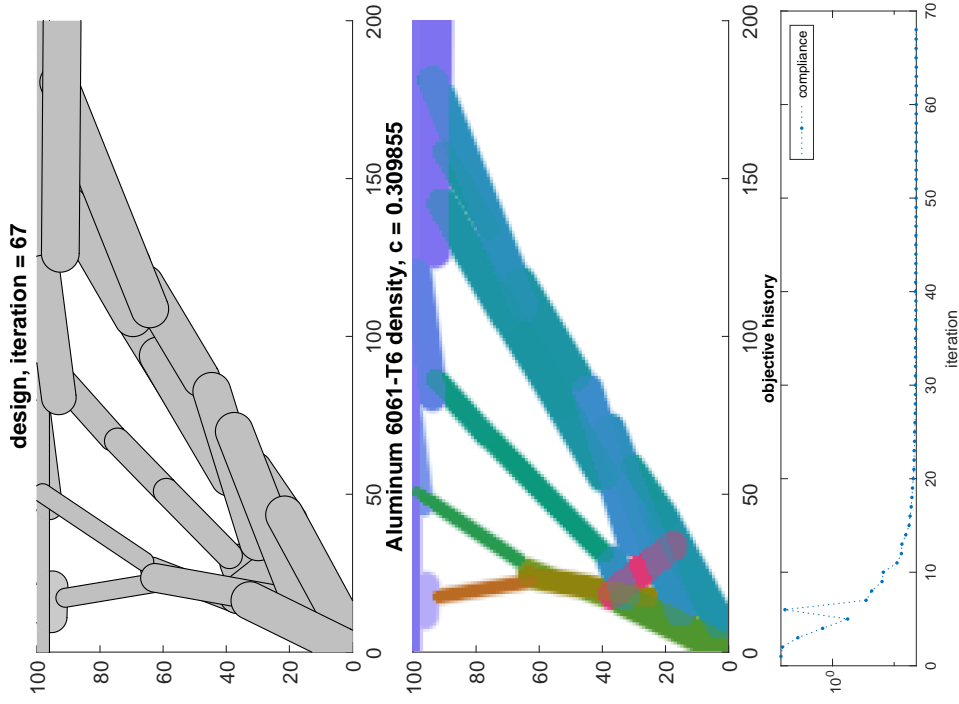
When comparing both bridge designs optimized for different volume fraction limits, the dendrite bar arrangements are almost identical for both cases—regions closer to the distributed load. A drop in compliance for higher volume fractions is not due to a significant change in the topology but the excessive bars merging at the fixed support conditions. It demonstrates the usefulness of general topology optimization, which is that the volume fraction of a material does not necessarily determine the structure's stiffness. In other words, a lower-volume structure can still be stiff enough to rival the designs with a higher volume fraction. This indicates that other factors beyond the volume fraction, such as topology, length scales, etc., can influence a structure's stiffness.

### 3.5.3 A square plate under bi-axial and shear load

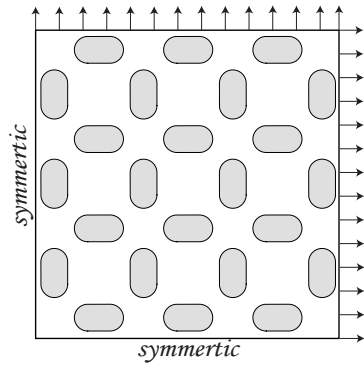
last example considered the bi-axial (Fig. 3.9a) and shear (Fig. 3.9b) loading problem (independently) with an aspect ratio of  $1 : 1$ ; the volume fraction limits in the  $\bar{v} \in [0.25, 0.5]$ . The whole plate has



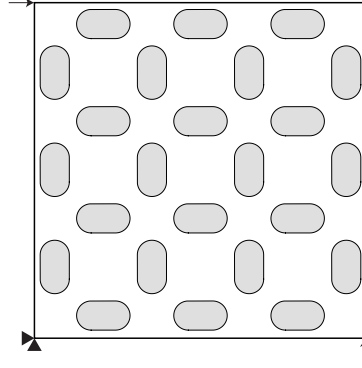
**(a) Bridge**—The design, density, and objective history plot for volume fraction limit of  $\bar{v} = 0.25$ .



**(b) Bridge**—The design, density, and objective history plot for volume fraction limit of  $\bar{v} = 0.35$ .



**(a) Biaxial**—The features' initial arrangement in the rectangular domain of the aspect ratio of  $1 \times 1$ , subjected to supports and biaxial loading.



**(b) Shear**—The features' initial arrangement in the rectangular domain of the aspect ratio of  $1 \times 1$ , subjected to supports and shear loading.

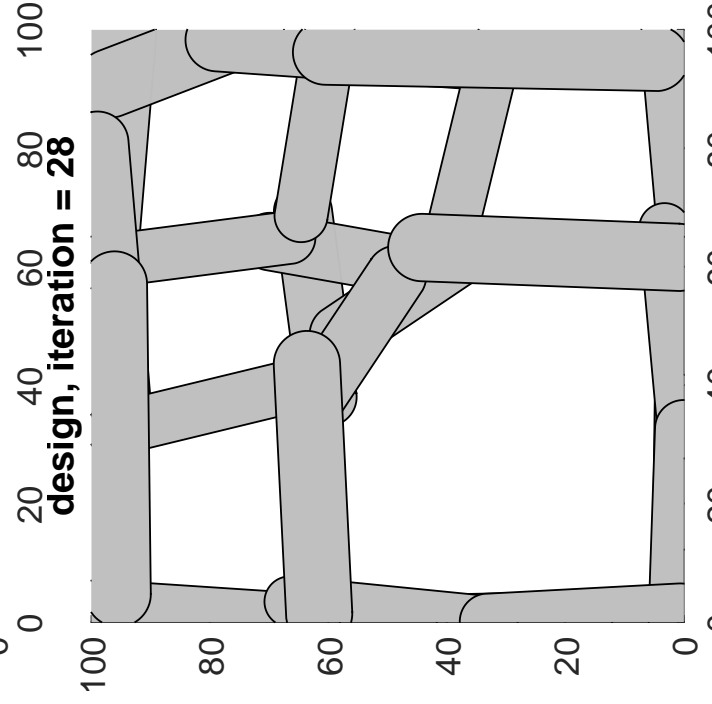
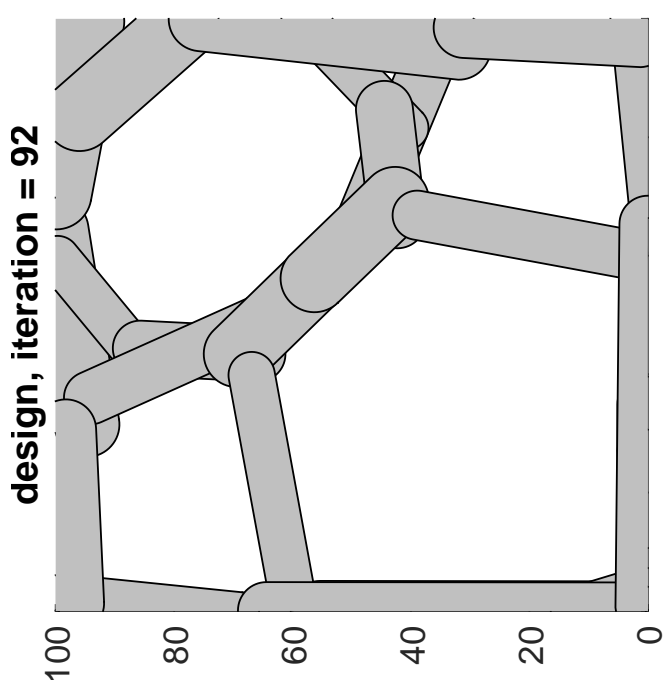
been initialized with 24 bars, and the design variables have been restricted within the following bounds.

$$\begin{Bmatrix} (0, 0) \\ 3 \\ 0 \end{Bmatrix} \leq \begin{Bmatrix} (\mathbf{x}_{b1}, \mathbf{x}_{b2}) \\ r_b \\ \alpha_b \end{Bmatrix} \leq \begin{Bmatrix} (100, 100) \\ 6 \\ 1 \end{Bmatrix} \quad (3.20)$$

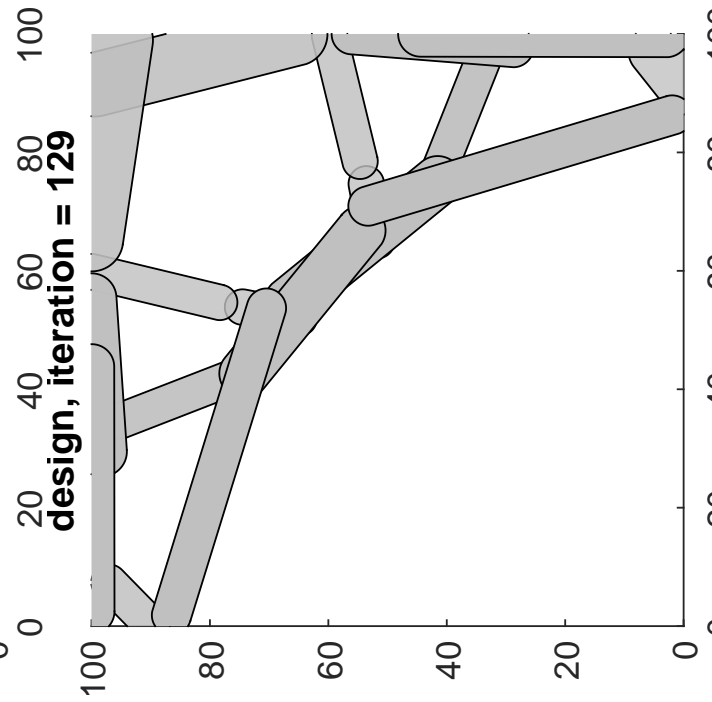
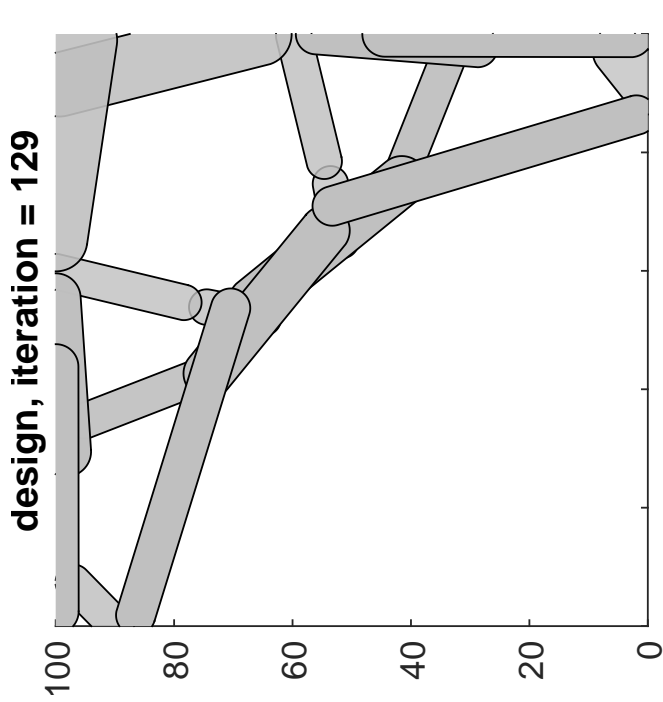
### 3.6 Conclusions

We have presented an approach for topology optimization of discrete element structures, which relies on a differentiable projection of the structure's geometry onto a fixed analysis grid. This projection allows for simplified analysis and continuous sensitivities, similar to density-based topology optimization. The sensitivities can be easily obtained using the chain rule, providing a means to use standard nonlinear programming algorithms with multiple constraints. The approach can also modify material properties and penalize intermediate-size members, similar to SIMP methods, and can be readily combined with existing density-based topology optimization methodologies. Unlike ground structure methods, the discrete elements in the GP need not be connected during optimization, providing greater freedom to optimize member placement and size. Examples exhibit designs consistent with well-known topologies in the literature without numerical parameter tuning, except for a possible move limit adjustment, which is also typical in density-based methods.

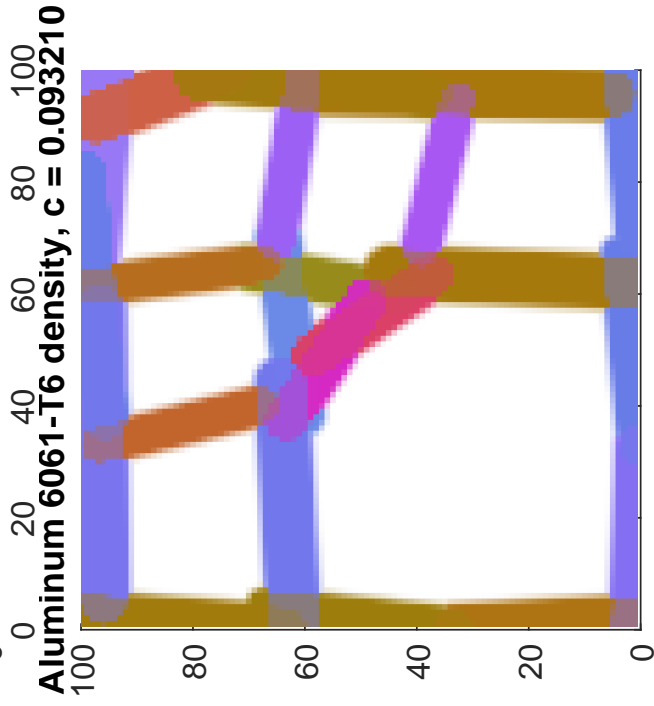
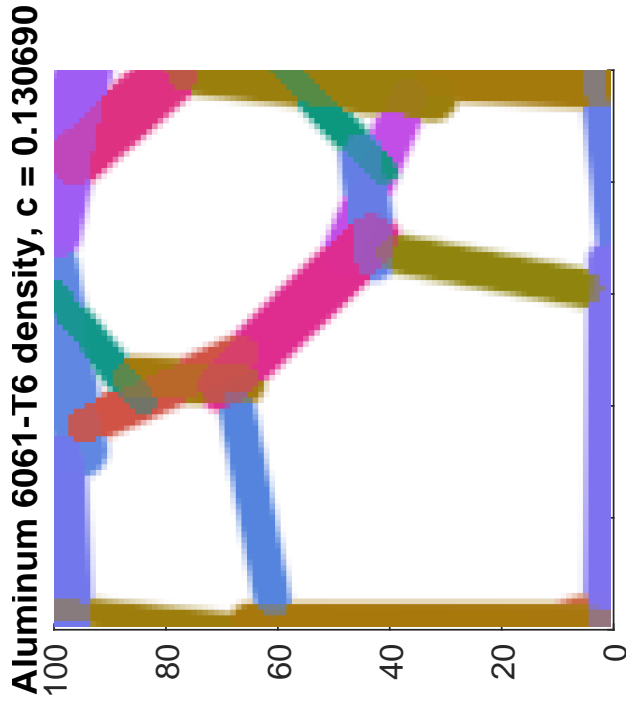
In the following chapters, we explore using the GP method for designing and optimizing variable stiffness continuous fiber-reinforced polymer laminates (VS-CFRP-Ls). Specifically, we



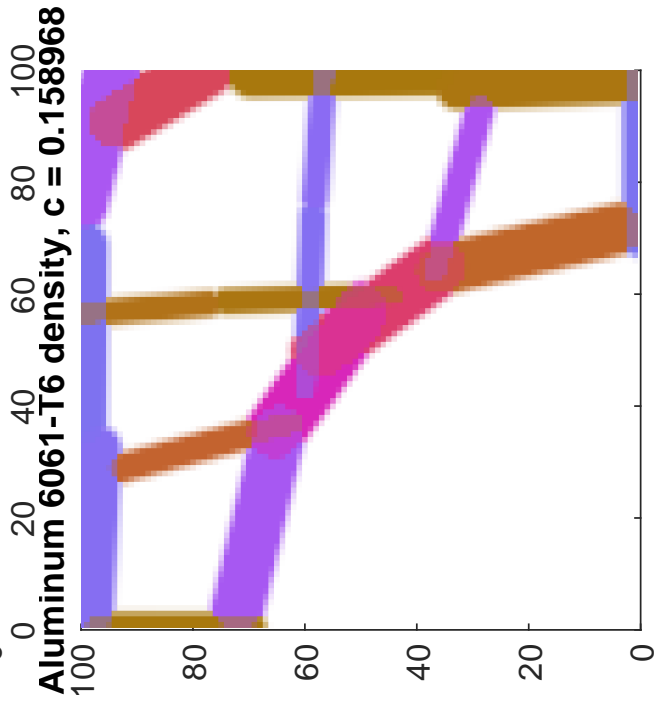
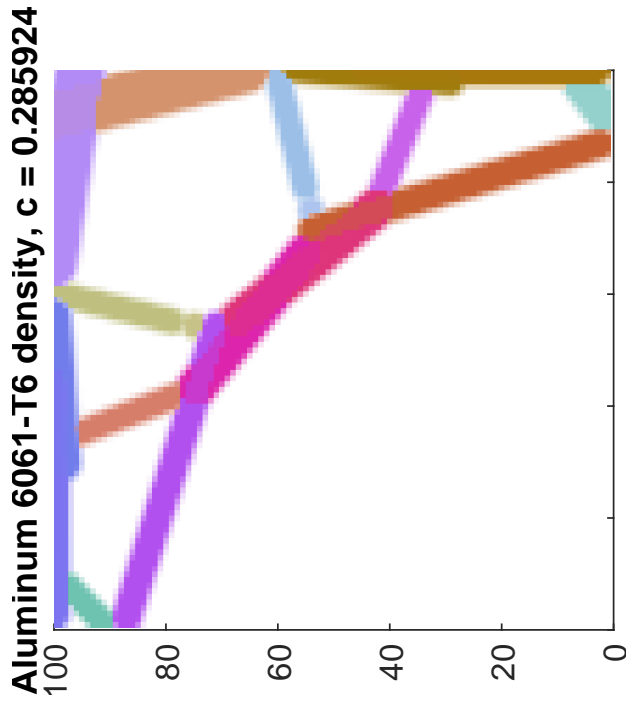
(b) Biaxial—The design plot for volume fraction limit of  $\bar{v} = 0.40$  and  $\bar{v} = 0.50$ .



(a) Biaxial—The design plot for volume fraction limit of  $\bar{v} = 0.25$  and  $\bar{v} = 0.35$ .

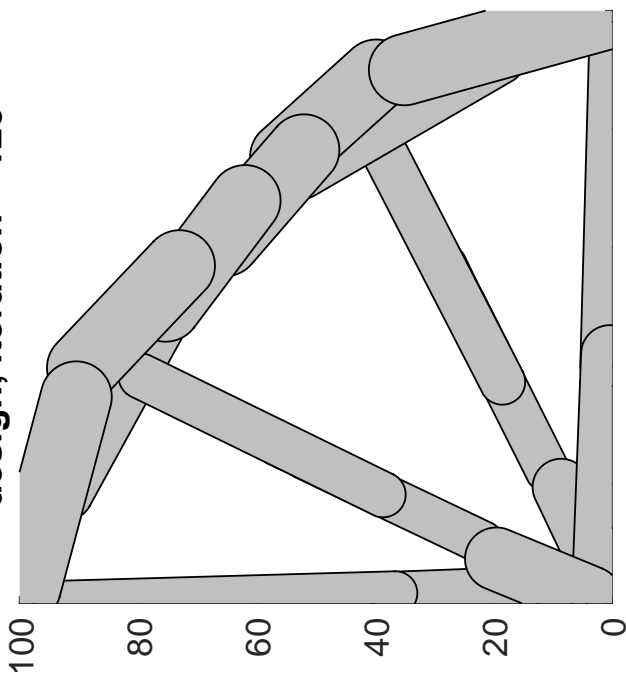


**(b) Biaxial**—The design plot for volume fraction limit of  $\bar{v} = 0.40$  and  $\bar{v} = 0.50$ .

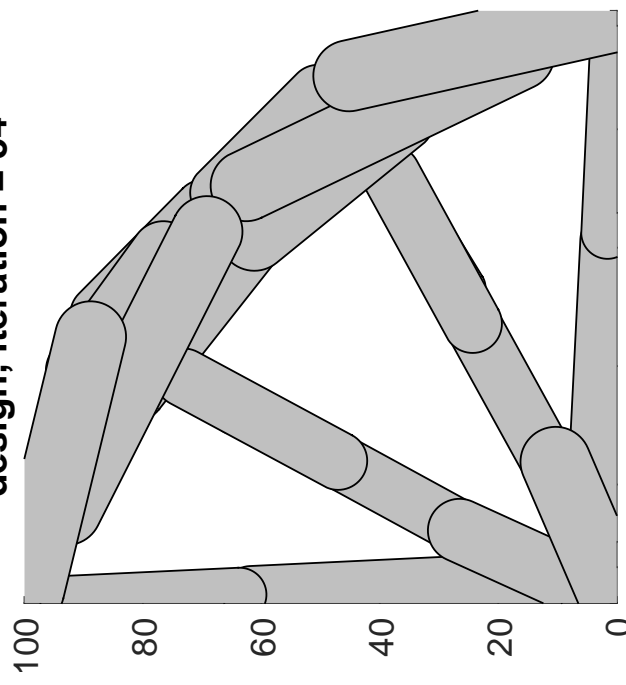


**(a) Biaxial**—The density plot for volume fraction limit of  $\bar{v} = 0.25$  and  $\bar{v} = 0.35$ .

**design, iteration = 129**

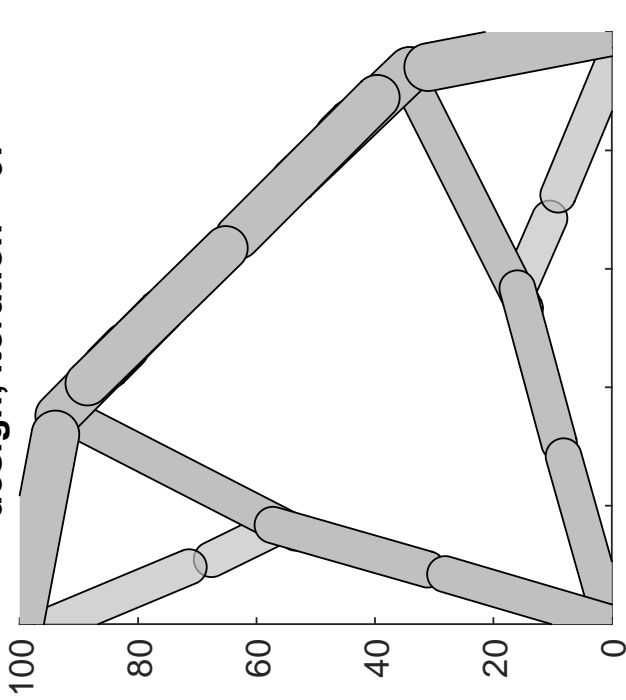


**design, iteration = 54**

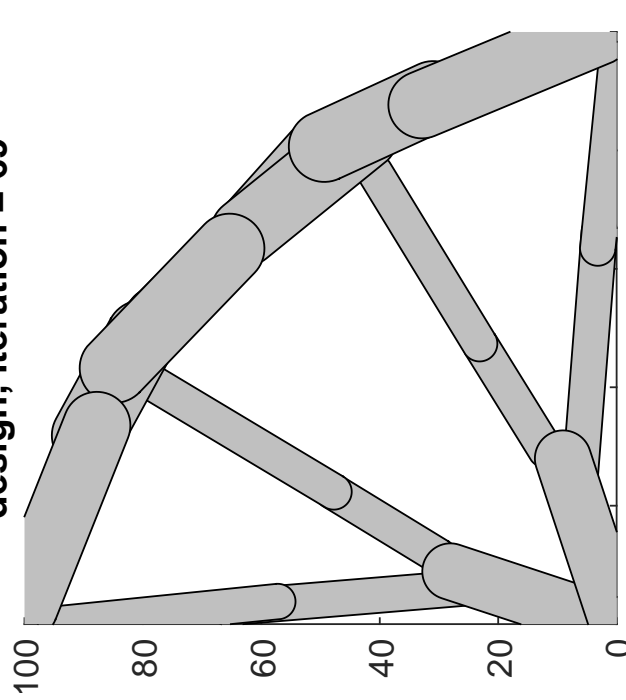


**(b) Biaxial**—The design plot for volume fraction limit of  $\bar{v} = 0.40$  and  $\bar{v} = 0.50$ .

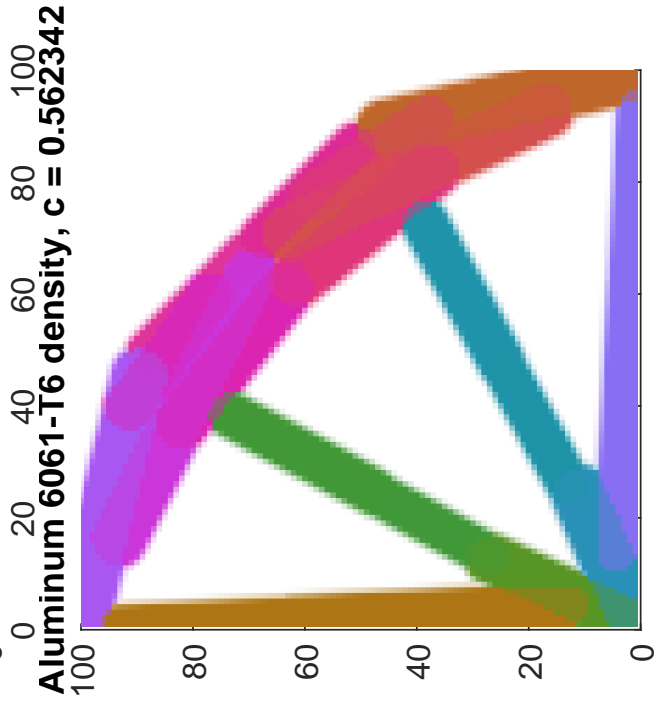
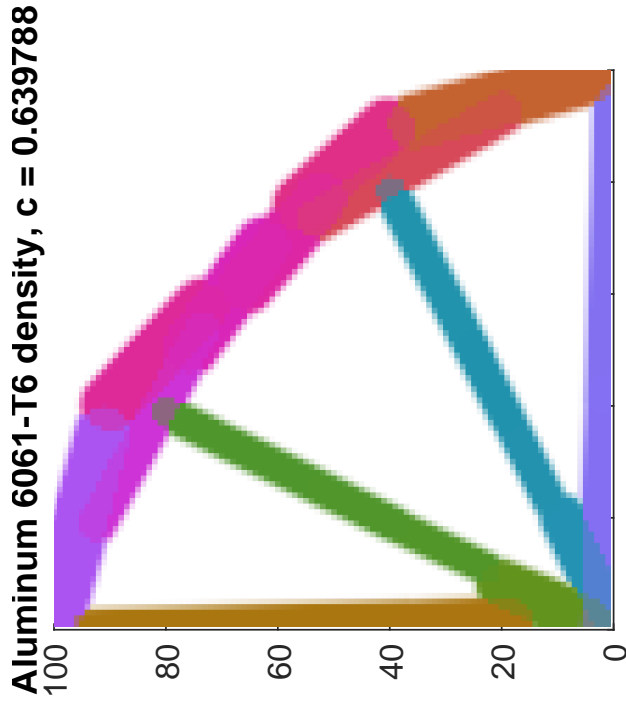
**design, iteration = 67**



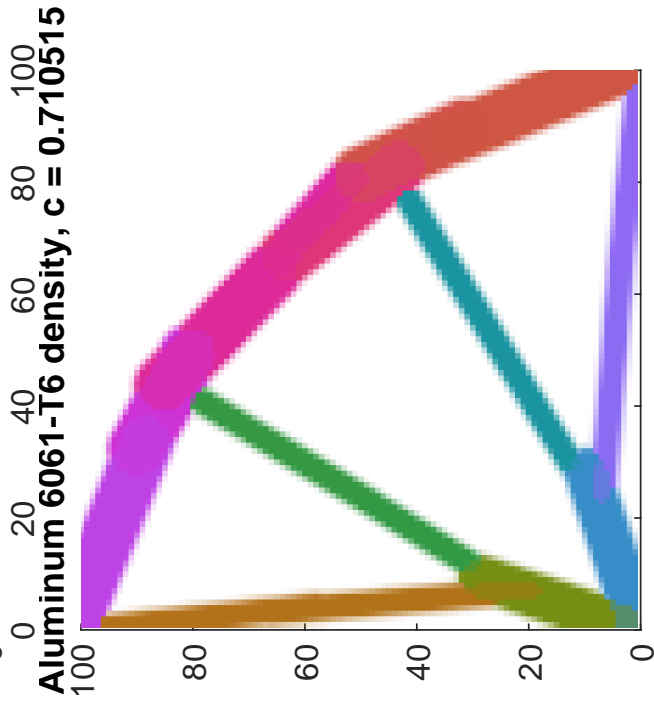
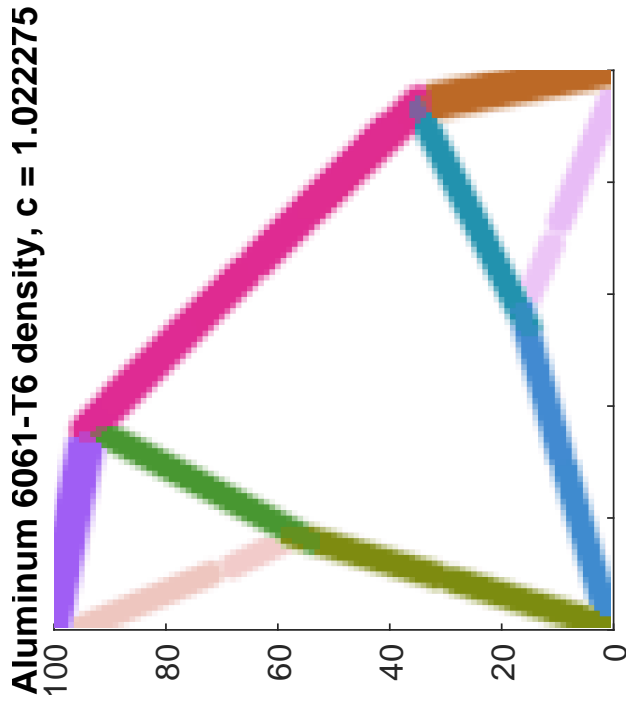
**design, iteration = 69**



**(a) Biaxial**—The design plot for volume fraction limit of  $\bar{v} = 0.25$  and  $\bar{v} = 0.35$ .



**(b) Biaxial**—The design plot for volume fraction limit of  $\bar{v} = 0.40$  and  $\bar{v} = 0.50$ .



**(a) Biaxial**—The density plot for volume fraction limit of  $\bar{v} = 0.25$  and  $\bar{v} = 0.35$ .

extend the GP method to include fiber-reinforced polymer materials, which can be used to design laminates with varying stiffness properties. We also investigate several formulations allowing overlapping GP components rather than merging them as introduced in Section 3.2.2. This is particularly important when dealing with anisotropic materials, where overlapping components can help to find better solutions by modeling the material's behavior more accurately.

In addition, we introduce a length constraint formulation within the GP framework that is not a constraint in the optimization process but rather an intrinsic attribute of GP methodology. Finally, we proposed a multilayered formulation for designing and optimizing VS-CFRP laminates that integrate Multilayered Structures and Multifield Analyses (MUL<sup>2</sup>) software with GP. This provides a general framework for optimizing and analyzing multiobjective and multiphysics designs, which can be used to design more efficient and effective VS-CFRP-L laminates. Overall, these chapters provide a detailed exploration of the GP method for designing and optimizing VS-CFRP-L laminates and introduce several new formulations and techniques that can be used to improve their performance.

# 4

## *Geometry Projection method for Variable Stiffness Continuous Fiber-Reinforced Polymer Laminates.*

Chapter 3 focuses on optimizing planar structures made of isotropic material bars with fixed width and semicircular ends. The design space for the optimization process involves determining the endpoint positions of the bar's medial axes and their radius and membership variables. A differentiable mapping projects the bar design onto the analysis grid to facilitate efficient gradient-based optimization. This mapping converts the endpoint positions into a continuously varying density field, representing the fraction of solid material in the design space, similar to density-based topology optimization methods.

The GP framework has recently been utilized to optimize the layout of fiber-reinforced bars (FRBs) in both 2D and 3D for maximum structural stiffness [126]. Further research has demonstrated the framework's capabilities for primitives made of fiber-reinforced plates [155, 156]. However, the GP methods are mainly designed for structures made of individual fiber-reinforced components that are later assembled. Designing structures where the fiber-reinforced components can overlap to form a joint is yet to be demonstrated using the GP procedure.

When designing for CFRP components, overlaps at angles that are not parallel can be crucial to exhibit an almost isotropic response. This poses an issue when seeking designs for discrete components because they cannot simultaneously align with all the intersecting load paths. Therefore, designing VS-CFRP-Ls requires customization of the GP procedure to leverage the design opportunities presented by CF4. However, the constraint of preventing overlapping components can be daunting. On the other hand, freely allowing components to overlap can result in suboptimal solutions, particularly for higher-volume fractions. This is because the optimizer may try to compensate for the transversely compliant response of CFRPs by increasing component overlaps in the design

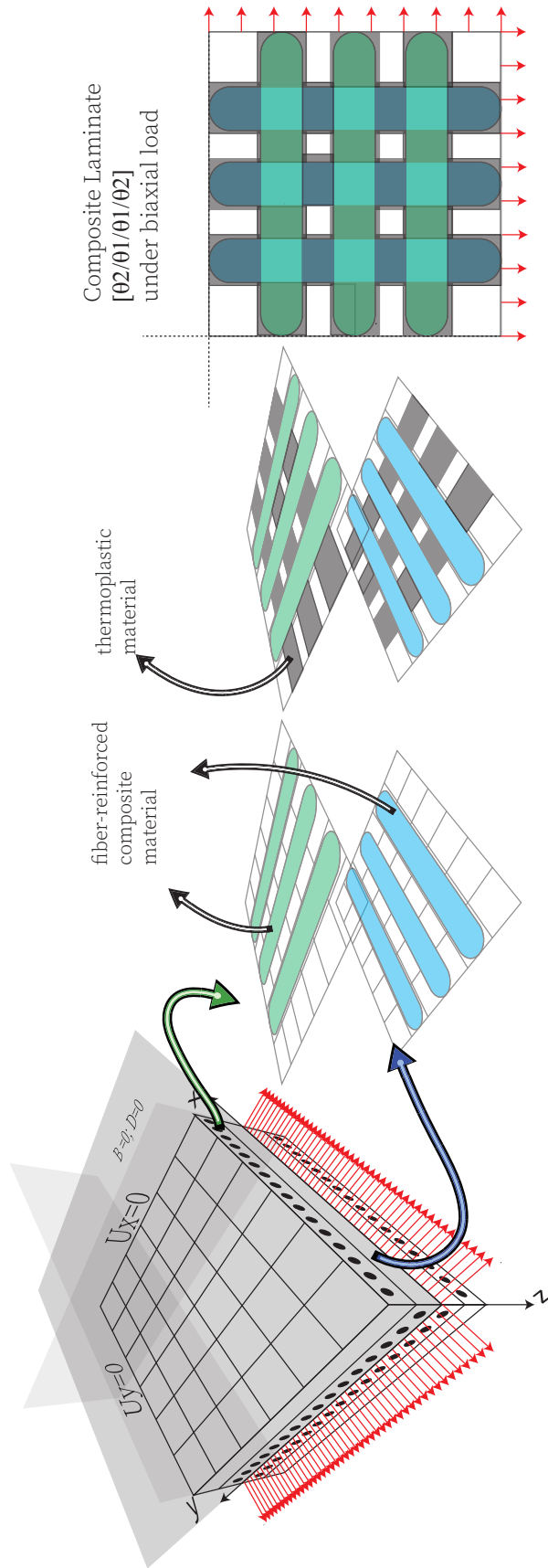


**Figure 4.1:** The figure presents a comprehensive outlook on employing the geometry projection technique to design and optimize multi-layered or single-layered variable-stiffness continuous fiber-reinforced polymer laminates. Designing for single-layered VS-CFRP-Ls is based on equivalent single-layer theories, referred to as GP-AM formulations, and is discussed in the chapter and the subsequent chapter. On the other hand, designing for multi-layered VS-CFRP-Ls requires higher-order composite plate theories, and the corresponding formulation is GP-MUL2.

domain, which leads to a non-manufacturable design. Moreover, the utility of overlapping constraints in the GP procedure can cause the optimization process to oscillate in the pursuit of determining the dominant component, resulting in the dissolution of features during the early optimization stages.

In this chapter, we build upon the work of Smith and Norato<sup>126</sup>. A GP-based procedure is formulated to enable the design of VS-CFRP-Ls. While using fiber-reinforced bars (FRBs) as features, we relax the GP methodology on multiple fronts.

<sup>126</sup> Smith *et al.*, "Topology optimization with discrete geometric components made of composite materials," 2021.

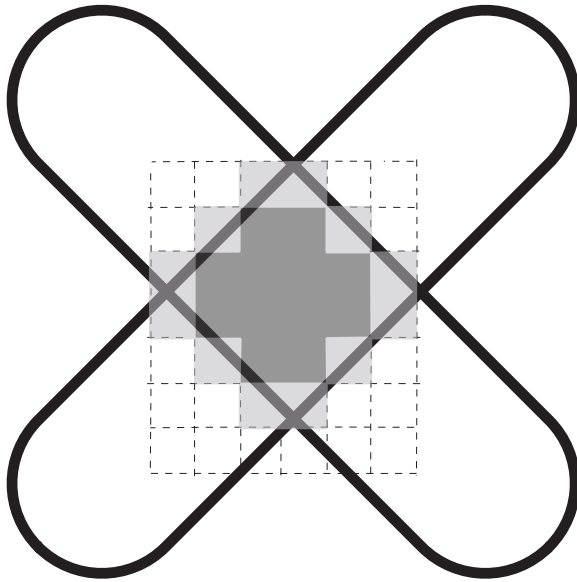
1. The overlapping FRBs in the design domain are retained and modeled using composite laminate theory to compute homogenized stiffness matrices (Fig. 4.2), enabling a local orthotropic material response.
2. Describing the overlap of FRBs can be difficult because the components are mapped onto density fields that obscure the accurate representation of the FRBs. Therefore, the dual nature of the geometry projection is utilized to postulate a criterion that defines the overlapping regions at the density level.
3. The GP method uses weights to determine the level of dominance for intersecting FRBs. This helps to identify a discrete component by augmenting FRBs' densities with weights and using a softargmax function. On the other hand, overlapping FRBs can assist in lessening the high-strain energy density at intersecting load paths and introduce variable fiber paths. Thus, the softmax function is not considered.
4. By reformulating the sensitivity of FRBs, the dependency introduced through the weights is removed, enabling the formation of intersecting FRBs and removing small features in the design domain.

Extending GP above strategies and thanks to the component-wise formulation allows us for the seamless printing of VS-CFRP-Ls with the clear manifestation of overlapping components. Nonetheless, our approach can be used to optimize the material distribution and fiber orientation in variable stiffness laminates—limited here to a single layer—which we call GP-AM. Finally, we compare the procedure with the GP method on four numerical examples as illustrated in Fig. 5.4 that minimize compliance, demonstrating the applicability of the proposed methodology.

**Remarks** The notation standard-GP refers to the work wherein the bars are made of isotropic material [125, 160]—the previous chapter loosely annotated it with GP. From here on, the work of Smith and Norato <sup>126</sup>, GP notation will refer to the formulation discussed in Section 4.1. Meanwhile, the GP-AM notation referred to several formulations adopted for designing and optimizing variable-stiffness continuous fiber-reinforced polymer laminates.

<sup>126</sup> Smith *et al.*, “Topology optimization with discrete geometric components made of composite materials,” 2021.

**Figure 4.3: Overlapping Criterion**—Darker grey regions represent overlapping regions  $\omega_e$ , while the lighter grey region depicts fiber mixture. Thus, the overlapping criterion selects the regions whose stack bar’s densities,  $\rho_b$ , are equal to 1 for all intersecting FRBs.



## 4.1 Combining Components

The definition of the geometric components and their geometric design variable 4.4, the component’s projection on the computation design domain 4.5, and the penalization of projected densities and membership variable, referred to as penalized densities,

$$\check{\rho}_b^{eff}(\mathbf{x}; \mathbf{z}_b) := (\alpha_b \rho_b(\mathbf{x}; \mathbf{z}_b))^q, \quad (4.1)$$

these attributes of the geometry projection method are thoroughly discussed in Chapter 3 and the same for the GP formulation, thus omitted here. The section describes the formulation for combining anisotropic components, which differs from combining isotropic components.

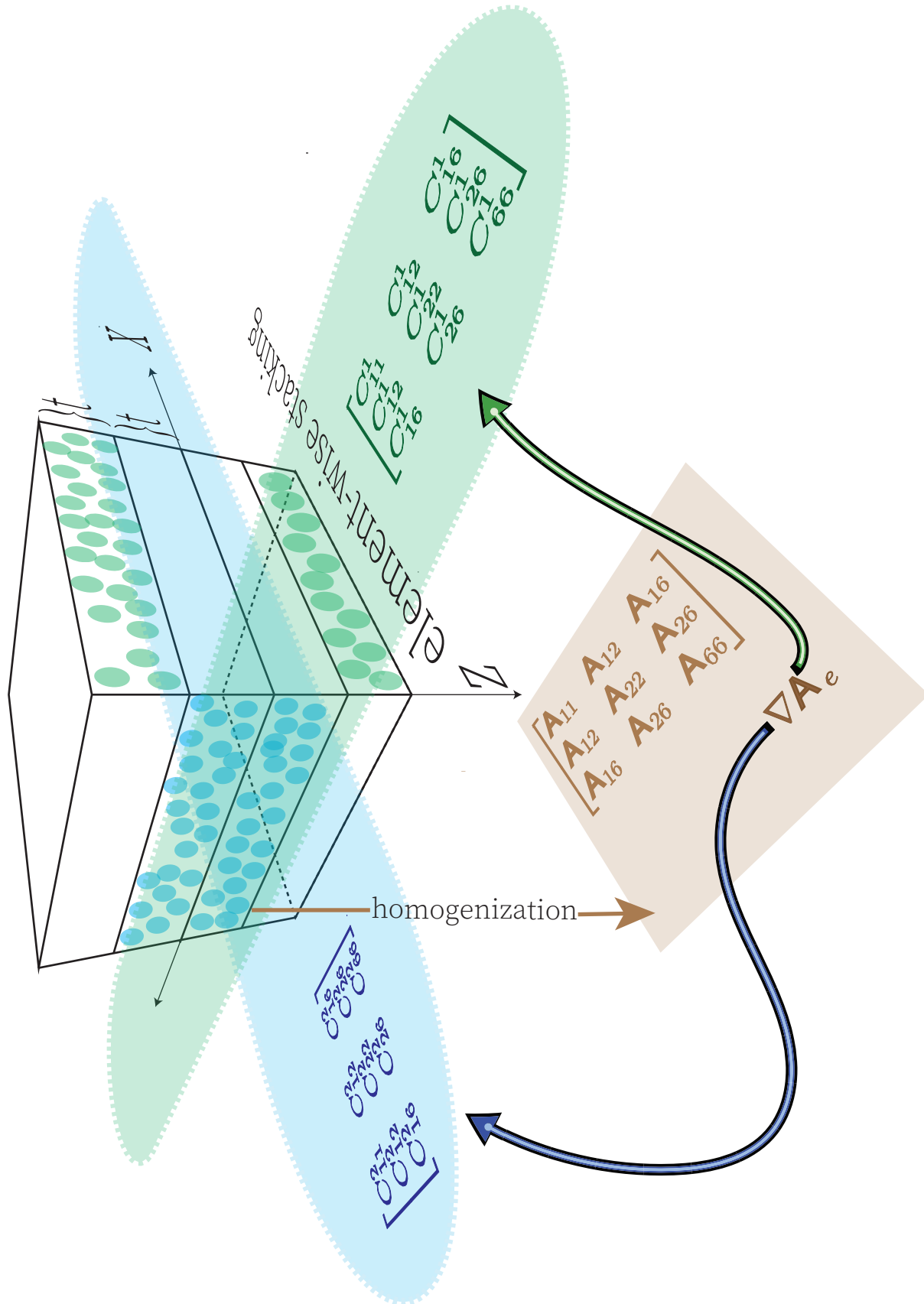


**Figure 4.2:** The dual nature of the geometry projection method is exploited to define the overlapping regions for intersecting FRBs at the density level, which enables the computation of VS-CFRP-L's stiffness matrices—membrane  $D_{me}$ , bending  $D_{be}$ , and shear  $D_{se}$ . The illustration demonstrates the evaluation of membrane stiffness for overlapping bars using the first-shear deformation theory, wherein the out-of-plane thickness is a fixed constant for the ease-in-manufacturable solution.

When multiple bars are present, they must be combined in a manner that is consistent with the intended manufacturing process. For previous GP techniques for design with fiber-reinforced primitives (cf., [126, 155, 156]), the intent is to have structures made of individually manufactured fiber-reinforced primitives that are subsequently assembled. In that case, the combination of components is done such that at overlapping regions, only one of the reinforcements of the intersecting bars is selected; in other words, no overlaps of fiber reinforcements are considered. The goal of this work, on the other hand, focuses on continuous fiber reinforcement and, therefore, on overlaps where multiple reinforcements are present. It should be noted that an overlap of bars made of isotropic materials was considered in [125], in which it was assumed that the thicknesses of 2D bars were stacked together by simply defining the combined density as the sum of effective densities.

In the previous GP method [126], when considering multiple FRBs, the combined penalized effective element density is defined as a convex combination of each component,

$$\check{\rho}_e^{\text{eff}} = \sum_b w_{be} \check{\rho}_{be}^{\text{eff}} \quad (4.2)$$

Such that the weights  $w_{be} \in [0, 1]$ ,  $\sum_b w_{be} = 1$  denote the fractional contribution of each bar to the penalized element density, which is analogous to the DMO method [109]. The GP method employs an aggregation scheme called softmax (4.3) to calculate the weights. When the value of the softargmax parameter  $\beta$  increases towards infinity, the approximation reaches its maximum, and the weights are determined as  $w_i(\{x_j\}_{j=1}^n, \beta \rightarrow \infty) = \delta_{ij}$ . This means that the highest penalized effective densities for the intersecting components can be identified, thus allowing us to single out the dominant feature in the overlapping region and streamline the assembly process.

$$w_i(\mathbf{x}) = \widetilde{\text{argmax}}_j(x_j; \beta) = \frac{e^{\beta x_i}}{\sum_j e^{\beta x_j}} \quad (4.3)$$

$$\frac{\partial w_i}{\partial x_j} = \beta w_i (\delta_{ij} - w_j)$$

As the value of  $\beta$  increases, the weights can approach a discrete one-hot vector, which can identify the highest density. This means that different fiber orientations can coexist in areas where bars intersect, leading to an unavoidable fiber mixture when  $\beta$  is finite. However, substantial values of  $\beta$  can result in highly non-linear aggregation schemes and optimization functions, which can cause issues when

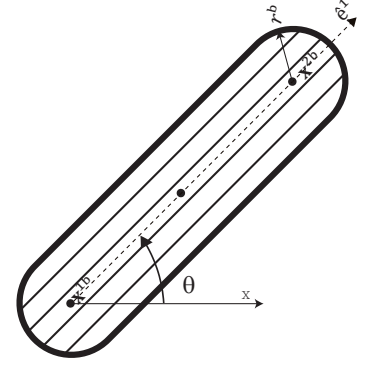


Figure 4.4: A fiber-reinforced bar with geometric design variables and material orientation.

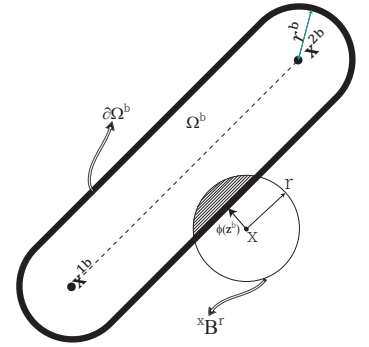


Figure 4.5: Projecting FRB to the centroid of a finite element using density approach.

using gradient-based optimizers. While it is challenging to avoid overlapping bars, in GP, the elasticity tensors are calculated by combining the contributions of all elasticity tensors for elements in the overlapping regions.

$$\mathbf{C}_e = \mathbf{C}^v + \sum_b w_{be} \check{\rho}_{be}^{\text{eff}} (\mathbf{C}_b - \mathbf{C}^v) \quad (4.4)$$

The elasticity tensor interpolation equation (4.4) can be used to interpolate between the solid material (bar material  $\mathbf{C}_b$ ) and void material  $\mathbf{C}^v$  for isotropic material. However, for anisotropic materials, i.e., FRBs, this can overestimate stiffness in the overlapping regions with a significant gap in FRBs' orientation. The membrane stiffness matrices  $\mathbf{D}_{me}$  can be evaluated as a convex combination of layers in the composite laminate. This evaluation can be achieved by establishing a relationship between weights and the thickness of the layers in the fiber mixture region. However, the same cannot be done for the bending stiffness  $\mathbf{D}_{be}$  of the laminate due to the nonlinear material distribution along the stacking direction. Therefore, equation (4.4) must be modified to represent regions for intersecting FRBs in VS-CFRP-Ls.

Lastly, the criterion to evaluate the weights of the components is biased on their densities  $\check{\rho}_b^{\text{eff}}$  than their orientation  $\theta$  in the design space  $\mathcal{D}$ . It can be demonstrated from the softargmax expression that the bar's densities are the decisive argument to compute the weights. At the same time, the component's orientation is considered as a feedback effect transmitted through the membership variable  $\alpha$  (i.e.,  $\check{\rho}_b^{\text{eff}} := (\alpha_b \rho_b)^q$ ). Augmenting the densities of components with weights can be an effective way to optimize material distribution. However, penalizing fiber orientations through the same weights without considering their impact on the design and optimization process may result in a less-than-optimal solution.

Therefore, the work focuses on enhancing GP procedures' capabilities to achieve a design with overlapping bars while ensuring that the resulting VS-CFRP-Ls can be printed with minimal post-processing. To achieve this, the following propositions are introduced in the GP procedure. First, composite laminate theory models the overlapping FRBs in the design domain, enabling a local orthotropic material response. Second, a criterion is postulated to define the overlapping regions at the density level to ensure printability. Third, to take full advantage of the design freedom offered by CF4, the softmax function is disregarded from GP procedures, which results in intersecting fiber paths in the optimized design. The intersecting fiber path can be printed in

subsequent layers, but fiber path planning is postponed for future work. These propositions for the GP-AM procedure are discussed in Section 4.2, and Section 4.4 details the GP-AM implementation and modifications made to the sensitivity analysis.

## 4.2 Geometry projection formulation for VS-CFRP-Ls based on overlapping criterion.

The starting approach to design and optimize VS-CFRP-Ls was based on simple overlap, in the same spirit as formulated previously for components made of isotropic material Chapter 3. However, as discussed and concluded in the Chapter 5, the optimized design falls into poor local minima, resulting in a non-manufacturable design. Therefore, in the pursuit of designing and optimizing additively manufactured VS-CFRP-Ls, several restrictions were initially imposed on defining the overlapping regions. These limitations were then refined and tested numerically, resulting in an overlapping criterion that ensures the design can be produced using conventional and additive manufacturing techniques. The section goes through the overlapping criterion in detail and the modeling of components using first-shear deformation theory for composite laminate.

### 4.2.1 Definition of overlapping components

The high-level geometric-based design in the GP formulation is represented by density mapping on a fixed grid  $\mathcal{D}$ . However, accurately representing the boundary of the FRB can be difficult as the projected densities may not match the analytical portions of the components  $\Omega_b$ . As indicated previously [160], FRBs' projected densities  $\rho_{b\omega_e} \in [0, 0.5)$  lie outside the analytical geometry  $\Omega_b$ . Different from isotropic material [125], simply defining overlaps using projected densities when designing for materials with directional stiffness can cause the optimization process to lock at early stages, leading to arbitrary and excessive overlapping FRBs that may not be optimal for manufacturing. Therefore, a criterion is developed to describe overlapping FRBs to address this issue. The dual nature of the geometry projection method is exploited to postulate a criterion that defines the overlapping areas at the density level to optimize the bar's material properties and create a stiffer manufacturable design.

Consider a bar  $\Omega_b$  that overlaps with other bars  $\{\Omega_i\}_{i \in \mathcal{B} \setminus \{b\}}$ . The stack of bars forming the overlapping region  $\omega_e$  (as shown in Fig 4.3) can be modeled as an equivalent single layer using the first-shear deformation theory (FSDT) as formulated in Section 4.2.2.

When calculating the stiffness matrices (4.14) for a stack, the thickness of the FRBs can be determined based on their projected densities, i.e.,

$$h_b := \frac{\rho_b}{\sum_{i=b}^{\mathcal{B}} \rho_b} \quad (4.5)$$

A normalized FRB thickness distribution can be used to compare the two methods, i.e., GP and GP-AM. This is necessary because the computational design domain has a fixed thickness in the GP method, which doesn't allow out-of-plane overlapping components. In practice, from a manufacturing point of view, a fixed thickness assigned to FRBs resembles fiber-fused filament extruded from the printer's nozzle. So, the thickness of the FRBs is fixed, i.e.,  $h_b = 1$  for all the numerical examples 5.4. However, it is also possible to assign the thickness given by Eq (4.5) to FRBs without any changes in the GP-AM formulation.

- **Overlapping criterion:** An overlapping region  $\omega_e$  is defined when overlapping component densities are equal to one, represented as  $\rho_{b\omega_e} = 1$  and illustrated in Fig. 4.3. As a result, the derivatives of these components' densities with respect to design variables must be zero.

$$\nabla_{z_i} \rho_{b\omega_e}^{\text{eff}}(\mathbf{x}; \mathbf{z}_b) := \nabla_{z_i} (\alpha_b \rho_{b\omega_e}(\mathbf{x}; \mathbf{z}_b))^q = 0, \quad \mathbf{z}_i := (\mathbf{x}_{1b}, \mathbf{x}_{2b}, r_b) \quad (4.6)$$

Equation (5.3) is a result of Equation (3.3), which is equal to zero when  $\rho_{b\omega_e} = 1$ . The definition of overlaps simplifies the calculation of the stiffness matrices (4.14) and their sensitivities, as shown in Section 4.4. Additionally, the criterion requires that all  $\rho_i$  values for  $i \in \mathcal{B}$  are equal to 1.0, which allows for unconstrained movement of FRBs during the optimization process. This facilitates the formation of intersecting FRBs and prevents design lock-in during the early stages.

## 4.2.2 Definition of laminated components

Mathematically, we considered a symmetric composite laminate,  $\mathcal{O}$ , comprised of the superposition of  $2n_b$  layers, each layer of thickness  $h_b > 0$ , and constant material orientation in a layer of shape  $\omega_e$  as follows:

$$\mathcal{O} = \{\omega_e^i\}_{i \in \mathcal{B} \setminus \{0\}, i = -n_b \dots n_b} \quad (4.7)$$

The index  $i$  grows from the inside to the outside of the laminated composite structure. Assuming  $\mathcal{O}$  symmetric, i.e.,  $\omega_e^{-i} = \omega_e^i$ , is desirable in zeroing membrane-bending coupling matrix  $\mathbf{D}_{mb}$  and

to minimize the wrapping of the printed laminate; thus, only  $n_b$  layers are modeled, which implies  $\mathcal{O} = \{\omega_e^i\}_{i=1\dots n_b}$ , where  $n_b$  is a total number of intersecting bars. Each layer in the given context corresponds to each bar of shape  $\omega_e$ . As a result, the terms layer and bar are used interchangeably in the following sections. We assume that

- Each layer  $k$  is defined by the planes  $z = h_k$  and  $z = h_{k+1}$  with  $h_k \leq z \leq h_{k+1}$ ,
- The orthotropy directions  $\hat{\mathbf{e}}_1$  and  $\hat{\mathbf{e}}_2$  can vary for each layer and are represented by the angle  $\theta_i$  between the global axis  $x$  and the directions  $\hat{\mathbf{e}}_1^k$  of the  $k^{\text{th}}$  layer,
- Each layer satisfies the plane stress assumption ( $\sigma_z = 0$ ),
- The continuous displacement field between the layers satisfies Eq. (4.8).

From an analysis viewpoint, we lean on the FSDT assumption to study the mechanical behavior of VS-CFRP-Ls. However, several hypotheses have been considered to model composite laminates, discussed in the book [161]. In the FSDT, *Kirchhoff's theory* is relaxed by considering transverse normal does not remain perpendicular to the mid-plane ( $z = 0$ ) after the deformation, which implies that the elastic displacement field of *Reissner-Mindlin plate theory* is extended by introducing the horizontal (in-plane) displacements  $u_0(x, y)$  and  $v_0(x, y)$  inside the laminate as:

$$\begin{aligned} u(x, y, z) &= u_0(x, y) + z\psi_x(x, y) \\ v(x, y, z) &= v_0(x, y) + z\psi_y(x, y) \\ w(x, y, z) &= w_0(x, y) \end{aligned} \quad (4.8)$$

where  $w_0(x, y)$  is out-plane displacement, and  $(\cdot)_0$  denotes the displacements of the mid-plane.

Considering the kinematics equation (4.8), the optimization approach of GP-AM focuses on optimizing equivalent single-layer VS-CFRP-L. When updating the design variables, it takes into account the in-plane displacements  $(u_0, v_0, w_0)$  and rotation  $(\psi_x, \psi_y)$  of the entire laminate, rather than computing the displacement fields of individual layers, which can be formulated using layer-wise theories [162] therefore limits the GP-AM formulation to consider the stacking sequence optimization.

It is worth noting that when there are overlapping regions with a  $\rho_{\omega_e}$  value less than 1, these regions are considered fiber mixture regions. However, for the sake of simplicity, these regions are

modeled as non-overlapping regions  $\omega_e \cap \mathcal{D}$ . In this case, GP method material interpolation Eq. (4.9) is utilized to compute the laminate stiffness matrices (4.15). Recall that the GP method material interpolation is weighted using the softargmax function to find discrete components in the overlapping region. Thus, dominant components that overlap with intermediates' densities (i.e., non-overlapping region) will push out the other components to compute stiffness matrices of a single FRB, unlike the formulation for the overlapping region.

Therefore, the material interpolation for the overlapping region is defined as follows.

$$\mathbf{C}_e = \sum_b \check{\rho}_{be}^{\text{eff}} \mathbf{C}_b \quad (4.9)$$

To avoid an ill-posed analysis in the void region, the discretized domain,  $\mathcal{D}$ , is initialized with a weak isotropic material  $\mathbf{C}^v$ ; therefore, the bar's elasticity tensor is defined as  $\mathbf{C}_b \equiv \mathbf{C}_b - \mathbf{C}^v$ .

Although it is impossible to eliminate the fiber mixture regions in non-overlapping regions, considering fiber mixture regions as overlapping FRBs can lead to poor design, which is a simple-overlap formulation that will be discussed in Chapter 5. This limits the GP-AM formulation to compute VS-CFRP-L's stiffness based on FSDT formulation in fiber mixture regions. Nevertheless, as the optimization process converges to the final design, the GP-AM procedure lays out the clean regions of overlapping FRBs, and the contribution of these fiber mixtures to the structure's stiffness becomes less relevant.

### 4.3 Elasticity tensor for laminated components

The material coordinate system (MCS) of a bar, denoted by  $\{\hat{\mathbf{e}}_{1b}, \hat{\mathbf{e}}_{2b}, \hat{\mathbf{e}}_{3b}\}$ , is often different from the global coordinate system (GCS),  $\{\mathbf{e}_1, \mathbf{e}_2, \mathbf{e}_3\}$ , as shown in Fig. 4.4. Additionally, the global out-of-plane axis, represented by  $\mathbf{e}_3$ , is the orthotropic axis for all layers, thus satisfying the plane anisotropy condition.

The components of the coordinate transformation matrix for each bar can be obtained from the direction cosines  $R_{ij}^b = \mathbf{e}_I \cdot \hat{\mathbf{e}}_{jb}$ . This allows for the transformation of the coefficients of the elasticity tensor  $\mathbf{C}_b$  for each bar into the global coordinate system:

$$(\mathbf{C}_b)_{ijkl} = \sum_{p,q,r,s} R_{ip}^b R_{jq}^b R_{kr}^b R_{ls}^b (\hat{\mathbf{C}}_b)_{pqrs} \quad (4.10)$$

where  $(\mathbf{C}_b)_{ijkl}$  and  $(\hat{\mathbf{C}}_b)_{pqrs}$  are the components of the fourth-order tensor  $\mathbf{C}_b$  in the global and material coordinate system, respectively.

The stress and strain relationships within a multi-layered laminate subjected to plane stress conditions are defined by constitutive matrices for each layer. These matrices, denoted by  $\hat{\mathbf{C}}_b^p$  and  $\hat{\mathbf{C}}_b^s$ , relate the in-plane stress components  $\sigma_1$ ,  $\sigma_2$ , and  $\tau_{12}$  to the transverse shear strains  $\tau_{13}$  and  $\tau_{23}$  in the material coordinate system  $\hat{\mathbf{e}}_1$ ,  $\hat{\mathbf{e}}_2$ , and  $\hat{\mathbf{e}}_3$ . The five independent coefficients  $E_{11}, E_{12}, E_{22}, G_{13} = G_{12}, G_{23}$ , are depicted in Tab. 4.1.

$$\begin{aligned} \hat{\mathbf{C}}_b^p &= \begin{bmatrix} E_{11} & E_{12} & 0 \\ \text{Sym.} & E_{22} & 0 \\ & & G_{12} \end{bmatrix}, \\ \hat{\mathbf{C}}_b^s &= \begin{bmatrix} G_{13} & 0 \\ 0 & G_{23} \end{bmatrix}, \\ \hat{\mathbf{C}}_b &= \begin{bmatrix} E_{11} & E_{12} & & & \\ & E_{22} & & & 0 \\ & & G_{13} & & \\ \text{Sym.} & & & G_{23} & \\ & & & & G_{12} \end{bmatrix} \end{aligned} \quad (4.11)$$

The coordinate transformation equation (4.10) involves five matrix multiplication with four-subscripts material coefficient, which can be simplified as,

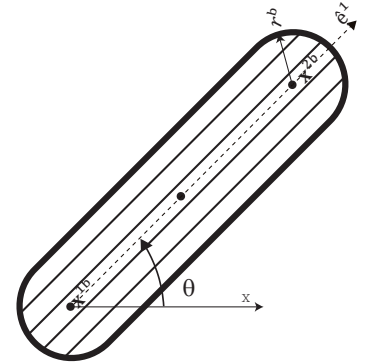
$$\begin{aligned} \mathbf{C}_k^p &= \mathbf{T}_1^T \hat{\mathbf{C}}_b^p \mathbf{T}_1, \quad \mathbf{C}_k^s = \mathbf{T}_2^T \hat{\mathbf{C}}_b^s \mathbf{T}_2 \\ \mathbf{C}_k &\equiv \mathbf{C}_b = \begin{bmatrix} \mathbf{C}_p & \mathbf{0}_{3 \times 2} \\ \mathbf{0}_{2 \times 3} & \mathbf{C}_s \end{bmatrix} \end{aligned} \quad (4.12)$$

with,

$$\begin{aligned} \mathbf{T}_1 &= \begin{bmatrix} c^2 & s^2 & -cs \\ s^2 & c^2 & cs \\ 2cs & -2cs & c^2 - s^2 \end{bmatrix} \\ \mathbf{T}_2 &= \begin{bmatrix} c & -s \\ s & c \end{bmatrix} \end{aligned} \quad (4.13)$$

where  $c = \cos \theta$ ,  $s = \sin \theta$ , and  $\theta$  is the angle between the axes  $\hat{\mathbf{e}}_1$  and  $x$  illustrated in Fig. 4.4

For a symmetric laminate  $O$  with  $n_b$  layers whose properties are symmetrical to the middle plane ( $z = 0$ ), membrane-bending



coupling matrix  $\mathbf{D}_{mb}$  is zero, and we can write

$$\begin{aligned}\mathbf{D}_m &= \sum_{k=1}^{n_b} h_k \left( \check{\rho}_k^{eff} \mathbf{C}_k^p \right) \\ \mathbf{D}_s &= \sum_{k=1}^{n_b} h_k \kappa \left( \check{\rho}_k^{eff} \mathbf{C}_k^s \right) \\ \mathbf{D}_b &= \sum_{k=1}^{n_b} \frac{1}{3} [h_{k+1}^3 - h_k^3] \left( \check{\rho}_k^{eff} \mathbf{C}_k^p \right)\end{aligned}\quad (4.14)$$

where  $t_k = h_{k+1} - h_k$ ,  $\kappa = 5/6$ , and  $\mathbf{C}_k^p$  and  $\mathbf{C}_k^s$  are constitutive matrices for the  $k^{th}$  layer. For the case where  $n_b$  equals one, Eq. (4.14) can be adjusted to calculate the stiffness matrices of a laminate for non-overlapping regions as follows. In this case,  $\mathbf{C}_e^p$  is obtained from Eq. (4.9).

$$\begin{aligned}\mathbf{D}_m &= \sum_{k=1}^{n_b} h_k \mathbf{C}_e^p \\ \mathbf{D}_s &= \sum_{k=1}^{n_b} h_k \kappa (\mathbf{C}_e^s) \\ \mathbf{D}_b &= \sum_{k=1}^{n_b} \frac{1}{3} [h_{k+1}^3 - h_k^3] \mathbf{C}_e^p\end{aligned}\quad (4.15)$$

To compute the stiffness matrices for the GP method,  $\mathbf{C}_e^p$  is obtained from Eq. (4.4). In the GP-AM method, the softargmax function doesn't affect the stiffness matrices of laminates. As a result, the sensitivity of bars is only dependent on their respective design variables  $\mathbf{z}_b$  and not influenced by other FRBs. This differs from the GP method, where the weights  $w_{be}$  create interdependencies between overlapping FRBs, restricting the components' cross-over movements to preserve discrete fiber orientation in the design. In the following Sec. 4.4, the sensitivities of coinciding FRBs are reformulated to enable merging and cross-over of the components.

#### 4.4 Setting and implementation of the optimization problem

A domain  $\mathcal{D}$  is discretized using linear quadrilateral plane-stress 4-noded finite elements of size  $1 \times 1$ , in which the displacements

and rotations are interpolated within each element as

$$\mathbf{u} = \begin{Bmatrix} u_0 \\ v_0 \\ w_0 \\ \psi_x \\ \psi_y \end{Bmatrix} = \sum_{i=1}^4 \mathbf{N}_i \mathbf{a}_i^{(e)} = [\mathbf{N}_1, \mathbf{N}_2, \mathbf{N}_3, \mathbf{N}_4] \begin{Bmatrix} \mathbf{a}_1^{(e)} \\ \mathbf{a}_2^{(e)} \\ \mathbf{a}_3^{(e)} \\ \mathbf{a}_4^{(e)} \end{Bmatrix} = \mathbf{N} \mathbf{a}^{(e)} \quad (4.16)$$

where  $N_i(\xi, \eta)$  is the  $C^\circ$  continuous shape function of node  $i$ .

$$\mathbf{N}_i = \begin{bmatrix} N_i & 0 & 0 & 0 & 0 \\ 0 & N_i & 0 & 0 & 0 \\ 0 & 0 & N_i & 0 & 0 \\ 0 & 0 & 0 & N_i & 0 \\ 0 & 0 & 0 & 0 & N_i \end{bmatrix}; \quad \mathbf{a}_i^{(e)} = [u_{0_i}, v_{0_i}, w_{0_i}, \psi_{x_i}, \psi_{y_i}]^T \quad (4.17)$$

The stiffness matrix  $\mathbf{K}_{ij}^{(e)}$  for an element is obtained by taking the contribution from the stiffness matrices due to membrane, bending, and transverse shear effects. This results in an element stiffness matrix, which is used to compute its design sensitivity:

$$\begin{aligned} \mathbf{K}_{a_{ij}}^{(e)} &= \iint_{\Omega^{(e)}} \mathbf{B}_{a_i}^T \mathbf{D}_a \mathbf{B}_{a_j} d\Omega^{(e)} \quad , \quad a = m, b, s \\ \nabla_z \mathbf{K}_{a_{ij}}^{(e)} &= \iint_{\Omega^{(e)}} \mathbf{B}_i^T \nabla_z \mathbf{D}_a \mathbf{B}_j d\Omega^{(e)} \end{aligned} \quad (4.18)$$

$\mathbf{B}_i$  is the symmetric gradient for the  $i^{th}$  node, which can be defined as

$$\mathbf{B}_i = \begin{Bmatrix} \mathbf{B}_{m_i} \\ \mathbf{B}_{b_i} \\ \mathbf{B}_{s_i} \end{Bmatrix} \quad \text{with} \quad (4.19)$$

$$\mathbf{B}_{m_i} = \begin{bmatrix} \frac{\partial N_i}{\partial x} & 0 & 0 & 0 & 0 \\ 0 & \frac{\partial N_i}{\partial y} & 0 & 0 & 0 \\ \frac{\partial N_i}{\partial y} & \frac{\partial N_i}{\partial x} & 0 & 0 & 0 \end{bmatrix}$$

$$\mathbf{B}_{b_i} = \begin{bmatrix} 0 & 0 & 0 & -\frac{\partial N_i}{\partial x} & 0 \\ 0 & 0 & 0 & 0 & -\frac{\partial N_i}{\partial y} \\ 0 & 0 & 0 & -\frac{\partial N_i}{\partial y} & -\frac{\partial N_i}{\partial x} \end{bmatrix}$$

$$\mathbf{B}_{s_i} = \begin{bmatrix} 0 & 0 & \frac{\partial N_i}{\partial x} & -N_i & 0 \\ 0 & 0 & \frac{\partial N_i}{\partial y} & 0 & -N_i \end{bmatrix}$$

The density at the centroids of each element is used to calculate the structural volume. In GP, this is done by applying the softargmax

function to estimate the solid volume fraction  $v^{(e)}$  in the domain  $\Omega^{(e)}$  that the element  $e \in \mathcal{D}$  occupies.

$$v^{(e)} := \frac{1}{|\Omega^{(e)}|} \sum_b w_{be} \rho_{be}^{\text{eff}} \quad (4.20)$$

For the GP-AM, the contribution of the weighting scheme is disregarded, and the structural volume is calculated as follows:

$$v^{(e)} := \frac{1}{|\Omega^{(e)}|} \sum_b \rho_{be}^{\text{eff}} \quad (4.21)$$

We consider the compliance minimization problem subject to a given volume fraction. The optimization problem may be formally stated as

$$\begin{aligned} & \min_{\{\mathbf{z}_b\}} f := \log(c + 1) \\ \text{subject to:} & \\ & v \leq \bar{v} \\ & \mathbf{K}\mathbf{U} = \mathbf{f} \\ & \underline{z}_i \leq z_i \leq \bar{z}_i, i = 1, 2, \dots, n_z, \end{aligned} \quad (4.22)$$

where  $c = \mathbf{U}^\top \mathbf{f}$  is the compliance,  $\mathbf{U}$  and  $\mathbf{f}$  are the global displacement and force vectors, respectively,  $\bar{v}$  is a prescribed upper limit on the volume fraction,  $\mathbf{K}$  is the global stiffness matrix,  $[\underline{z}_i, \bar{z}_i]$  is a lower and upper bound on the  $i^{\text{th}}$  design variable,  $\bar{v}$  is a prescribed upper-limit on the volume fraction and  $v$  is the volume fraction defined as

$$v := \frac{\sum_e v^{(e)} \Omega^{(e)}}{\sum_e \Omega^{(e)}} \quad (4.23)$$

As addressed in previous works [125, 126], to prevent convergence issues during the optimization steps, precautionary steps are taken as follows: first, log-scaled compliance  $f(\mathbf{z}) = \log(1 + c(\mathbf{z}))$  damps the large oscillation in compliance when the structure becomes disconnected from the load/support. Second, scaling the design variables allows us to impose a uniform move limit  $m$  at each iteration  $I$  as

$$\begin{aligned} \hat{z}_i & := \frac{z_i - \underline{z}_i}{\bar{z}_i - \underline{z}_i} \\ \max \left( 0, z_i^{I-1} - m \right) & \leq z_i^I \leq \min \left( 1, z_i^{I-1} + m \right) \end{aligned} \quad (4.24)$$

Finally, for the design-independent loading, the problem (4.22) is self-adjoint, and so the sensitivity of the compliance and volume

fraction is as follows:

$$\begin{aligned}\nabla_z c &= - \sum_e \mathbf{u}^\top \left( \nabla_z \mathbf{K}^{(e)} \right) \mathbf{u} \\ \nabla_z v &= \frac{\sum_e \left( \nabla_z v^{(e)} \right) \Omega^{(e)}}{\sum_e \Omega^{(e)}}\end{aligned}\quad (4.25)$$

In the GP, to calculate the derivative of the stiffness matrix  $\mathbf{K}^{(e)}$  concerning a specific design variable  $z_i$ , we use the elasticity tensor (4.4) design sensitivity  $\nabla_z \mathbf{C}^{(e)}$ , which is computed as follows:

$$\nabla_z \mathbf{C}^{(e)} = \sum_b \left[ \nabla_z \left( w_{be} \check{\rho}_{be}^{\text{eff}} \right) \right] (\mathbf{C}_b - \mathbf{C}^v) + w_{be} \check{\rho}_{be}^{\text{eff}} (\nabla_z \mathbf{C}_b) \quad (4.26)$$

where, we denote the design sensitivity operator as  $\nabla_z := \frac{\partial}{\partial z_i}$ .

When concerning the GP-AM procedure, modifications are made to compute the design sensitivities for stiffness matrices  $\mathbf{D}_a$ , where  $\{a = m, b, s\}$  from Eq.(4.14), as follows.

$$\nabla_z \mathbf{C}_k^{(e)} = \nabla_z \rho_{ke}^{\text{eff}} (\mathbf{C}_k - \mathbf{C}^v) + \rho_{ke}^{\text{eff}} (\nabla_z \mathbf{C}_k) \quad (4.27)$$

Eq.(4.27) can be simplified by the postulate for overlapping bars. For completeness, the design sensitivities for the GP-AM are written as

$$\begin{aligned}\nabla_z \mathbf{D}^{(e)} &= \begin{bmatrix} \nabla_z \mathbf{D}_m^{(e)} & \mathbf{0}_3 & \mathbf{0}_3 \\ \mathbf{0}_3 & \nabla_z \mathbf{D}_b^{(e)} & \mathbf{0}_3 \\ \mathbf{0}_2 & \mathbf{0}_2 & \nabla_z \mathbf{D}_s^{(e)} \end{bmatrix} \quad \text{where,} \\ \nabla_z \mathbf{D}_m^{(e)} &= \sum_{k=1}^{n_b} t_k \nabla_z \mathbf{C}_k^{(e)p}, \\ \nabla_z \mathbf{D}_b^{(e)} &= \sum_{k=1}^{n_b} \frac{1}{3} [h_{k+1}^3 - h_k^3] \nabla_z \mathbf{C}_k^{(e)p} \\ \nabla_z \mathbf{D}_s^{(e)} &= \sum_{k=1}^{n_b} t_k \nabla_z \mathbf{C}_k^{(e)s}\end{aligned}\quad (4.28)$$

where  $\mathbf{0}_n$  and  $\mathbf{0}_{m \times n}$  is a  $n \times n$  and  $m \times n$  zero matrix, respectively. As mentioned previously, the design sensitivity for stiffness matrices in Eq. (4.28) can be modified for the case where  $n_b$  is equal to one. Lastly, Eq. (4.29) outlines the derivation of the term that represents the dependence of the design on the orientation of the bar elasticity tensor, denoted as  $\nabla_z \mathbf{C}_b$  or  $\nabla_z \mathbf{C}_k$ . The sensitivities of the basis

vectors to the endpoints of each FRB's medial segment are given as follows:

$$\begin{aligned} \frac{\partial (\hat{\mathbf{e}}_{1b})_i}{\partial (\mathbf{x}_{sb})_j} &= \frac{(\delta_2^s - \delta_1^s)}{\|\mathbf{v}_b\|} \left( \mathbf{P}_b^\perp \right)_{ij} \\ \frac{\partial (\hat{\mathbf{e}}_{2b})_i}{\partial (\mathbf{x}_{sb})_j} &= \frac{\varepsilon_{\alpha km}}{\|\mathbf{v}_b \times \hat{\mathbf{e}}_\alpha\|} \left( \mathbf{P}_b^\perp \right)_{im} \frac{\partial (\hat{\mathbf{e}}_{1b})_k}{\partial (\mathbf{x}_{sb})_j} \end{aligned} \quad (4.29)$$

where the index  $s \in \{1, 2\}$  indicates the side of the bar,  $\delta_s^s$  is the Kronecker delta,  $\mathbf{P}_b^\perp$  denote the perpendicular projectors to the medial axis vector, and  $\varepsilon_{ijk}$  is the permutation symbol. Knowing the derivatives of the basis vectors, the sensitivities of the elasticity tensor of a bar can be computed using equation (4.10).

**Remark:** A component can be uniquely defined by a set of design variables represented by  $\mathbf{z}_b$ . For a specific design variable  $z_i \in \mathbf{z}_b$ , the design dependence on orientation  $\nabla_i \mathbf{C}_k$  only affects the layer that corresponds to  $z_i$ . In other words,  $\nabla_i \mathbf{C}_k$  is zero everywhere except for its endpoints. The same applies to  $\nabla_z \check{\rho}_{ke}^{\text{eff}}$ . Therefore, here we differ from the equation (4.26) by computing the design sensitivities of components only to their design variables, relaxing the design to enable intersecting components by disowning the contribution of softargmax function from Eq. (4.26), which eliminates the interdependency of the bar's design variable to other bars in the sensitivity analysis. Furthermore, rather than summing the design sensitivities of component stiffness tensors, their contributions with their corresponding thickness are stacked to compute elasticity tensor design sensitivities.

**Table 4.1:** Material properties used for all the examples

Material	$E_1$ [GPa]	$E_2$ [GPa]	$\nu_{12}$	$G_{12}$ [GPa]	$G_{13}$ [GPa]	$G_{23}$ [GPa]
Carbon epoxy AS4/3501-6	113.6	9.650	0.334	6.0	6.0	3.1

## 4.5 Examples

For all four numerical examples—We consider bars made of carbon-fiber-reinforced polymer, and fiber orientation is aligned to the bar's axis and is continuous. Table (4.1) lists unidirectional carbon-epoxy AS4/3501-6 material properties used for the bars. The transverse modulus of CFRP is ten times less than its longitudinal modulus. This implies that designs assembled with FRBs can achieve a higher stiffness when most of the load is carried along the fiber direction. On the other hand, designs using FRBs have

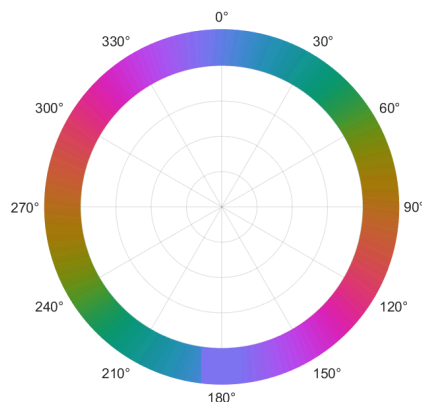
the potential to be substantially more compliant if a significant percentage of the load is held transverse to the reinforcing fibers. In this context, we introduced the methodology of model bars using FSDT to design regions with intersecting load paths without compromising manufacturability for minimum compliance optimization problems.

For all the examples in Fig. 5.4, the following settings are considered until mentioned otherwise. In the following examples, we have included design and density plots to illustrate the overlapping regions and fiber path, respectively. Additionally, the objective history and volume fraction plot demonstrate the convergence of the designs. It's worth noting that the volume fraction plot also displays the deposited mass in the design area during the optimization process, assuming a constant material density, i.e.,  $1.6g/cc$ .

Parameters for method-of-moving-asymptotes (MMA), employed for the optimization routine, using the default parameters described in Section 3.4. The void material is isotropic with Young's modulus  $E^{\text{void}} = 10^{-3}E_1$  and Poisson's ratio  $\nu^{\text{void}} = 0.3$ . During initialization, the radius of the bars is set to the average of their upper and lower bounds. The sizing variable is set to  $\alpha = 0.5$ , and the move limit is fixed to  $m = 0.005$  throughout the optimization process. The penalization factor for the softargmax function is another fixed parameter for the GP, the value of  $\beta = 100$ .

The optimization procedure involves three stopping criteria. The first criterion is met when the 2-norm of the change in the design variable vector is less than 0.005. The second criterion is reached when the norm of the Karush-Kuhn-Tucker optimality conditions falls below 0.002. The third criterion is satisfied when the change in the objective function is less than  $10^{-9}$ . The

**Figure 4.6:** Color wheel used for density plots to indicate the orientation of the primitive.



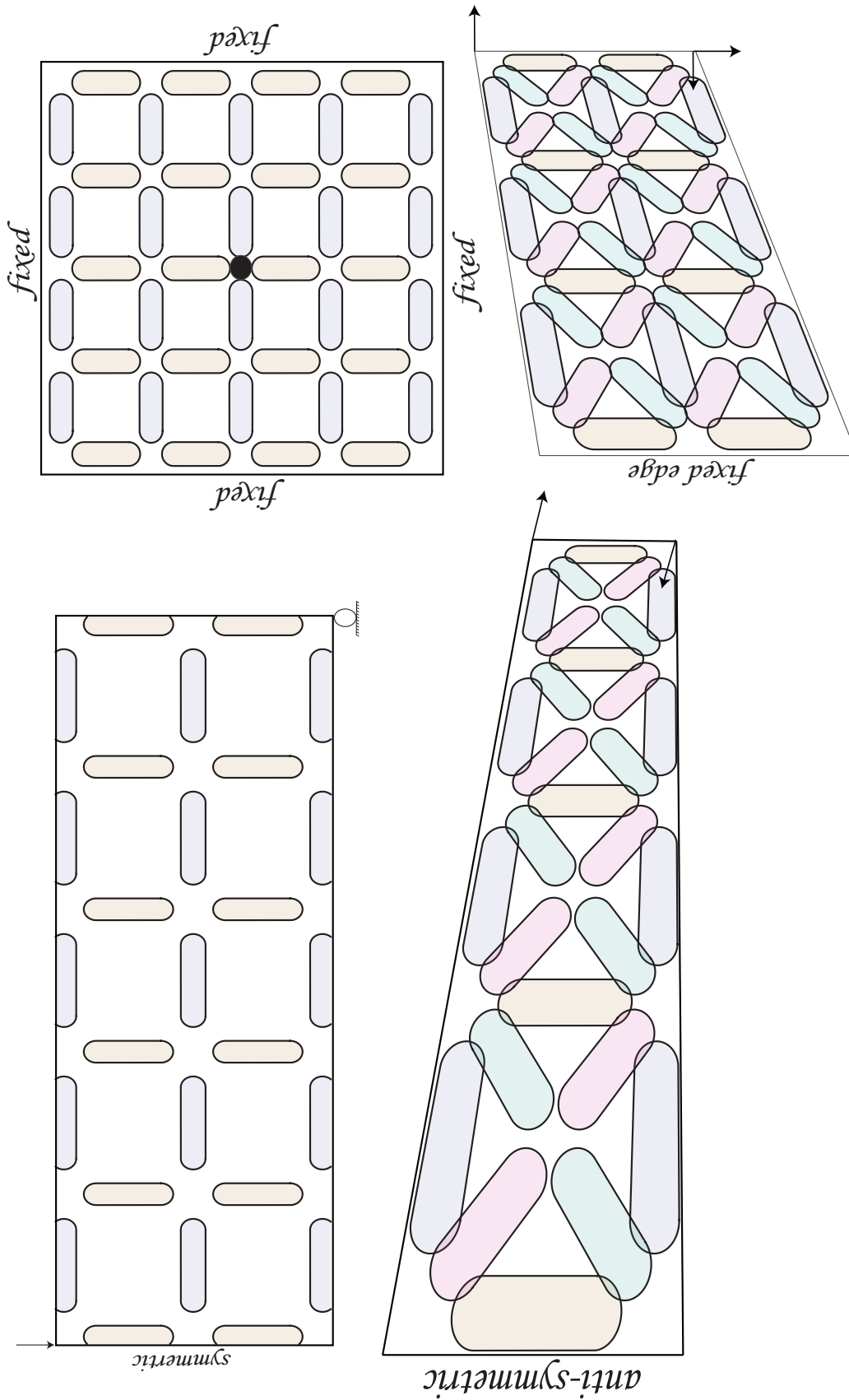


Figure 4.7: The features initial arrangement in rectangular plates of varying aspect ratios, which are subjected to different loading conditions, including 3-point bending  $1 \times 6$ , pure torsional  $1 \times 1$ ; and multi  $1 \times 2$ .

Figure 4.8: MBB—The design plot for GP method and converge after 191 iterations.

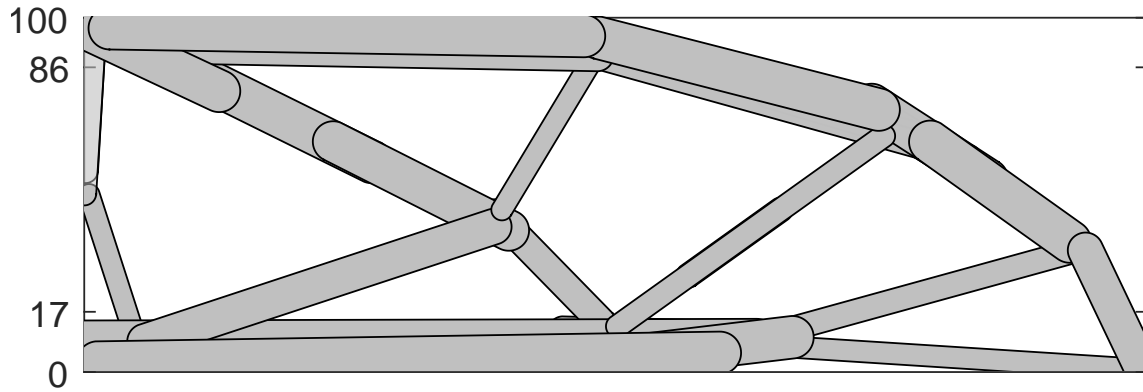


Figure 4.9: MBB—The density plot for GP method and attained compliance is 1.199431.

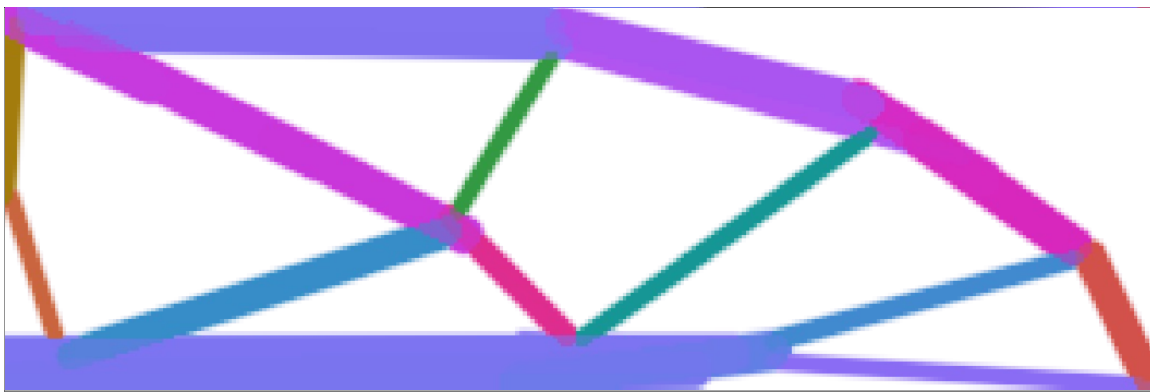
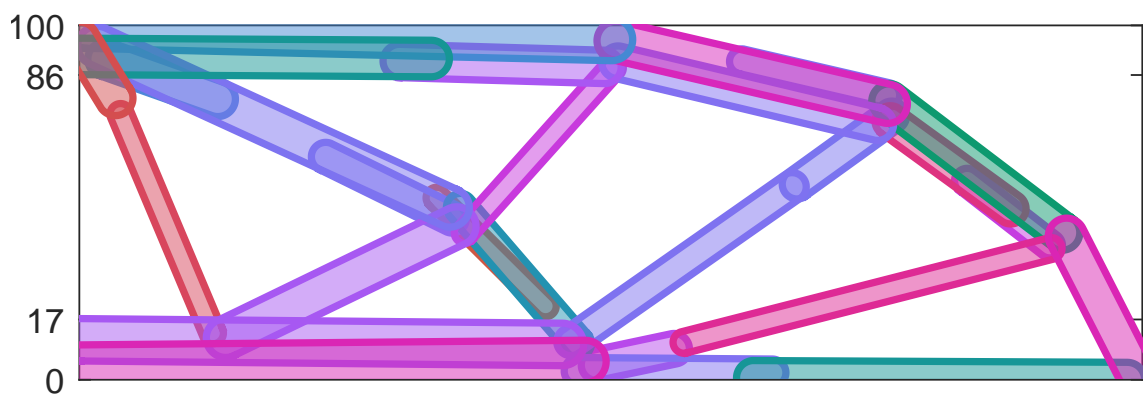
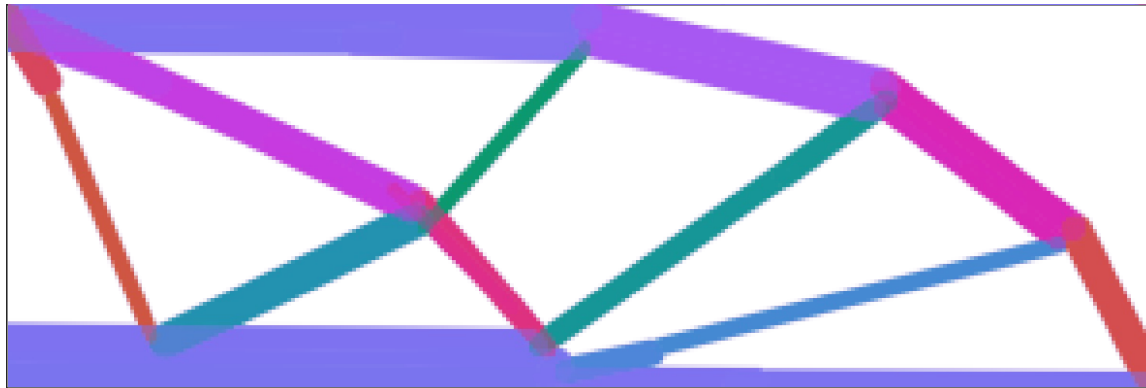


Figure 4.10: MBB—The design plot for GP-AM method and converge after 163 iterations.



**Figure 4.11: MBB**—The density plot for GP-AM method and attained compliance is 1.138311.



optimization process is stopped if any of these criteria are met.

#### 4.5.1 A rectangular plate under 3–point bending—MMB

The first example considered the MMB problem with an aspect ratio of 1 : 6; the volume fraction limit is set to 0.4. Since the problem is symmetrical, only the right side of the geometry has been modeled as depicted in Fig. 5.4. The whole plate has been initialized with 27 bars, and the design variables have been restricted within the following bounds.

$$\left\{ \begin{array}{c} (0, 0) \\ 3 \\ 0 \end{array} \right\} \leq \left\{ \begin{array}{c} (\mathbf{x}_{b1}, \mathbf{x}_{b2}) \\ r_b \\ \alpha_b \end{array} \right\} \leq \left\{ \begin{array}{c} (300, 100) \\ 6 \\ 1 \end{array} \right\} \quad (4.30)$$

The orientation-dependent density is color-coded based on the color wheel in Fig. 4.6. The GP-AM method uses a plot design that displays features with transparency. It is not consistent with the density colormap but is used to help visualize overlapping regions. It's important to note that in this method, all features aim to maximize the membership variable, meaning that transparency does not correspond to the value of the membership variable (represented by  $\alpha$ ) as it does in the GP method.

In the MBB problem, the upper left corner (where the load is applied) experiences the highest bending stress, and the normal stresses are tensile on the bottom edge and compressive on the top edge—an applied load results in bending, normal stress, and significant shear stresses near the neutral axis. Moreover, the optimal design for a single load instance will be the one that aligns the principal material direction with the principal stress at each

point [86]. Therefore, a structure with members that align with the principal stresses would be ideal for minimizing compliance—an optimized design can be attained by assembling the FRBs to align the principal stress directions in the structure.

Both methods show a similar distribution of FRBs and attain optimized design by assembling the FRBs to align the principal stress directions in the structure. It can be observed that the top and bottom have horizontal bars for normal stress distribution, while there are inclined bars for shear stress distribution. However, there is a slight difference in the arrangement of FRBs between the two methods. In Fig. 4.10, the GP-AM method combines FRBs at the top and bottom of the structure to attain thicker features to support stresses. Furthermore, an inclined FRB near the loading region maximizes the shear stiffness. Both observations highlight the importance of the GP-AM strategy that results in lower compliance than the GP approach by 5.4%. Note that in Fig. 4.8, the FRB along the left edge in the design plot is assigned with transparency for visualization purposes only to compare the thickness of the FRBs in the two methods.

Fig. 4.14 demonstrates that the optimization traces a typical convergence behavior for compliance with a sharp drop in the first few iterations, followed by small design variable adjustments in the following optimization iterations. Further, both methods exhibit a typical smooth convergence curve. As demonstrated, the design with GP-AM achieves slightly lower final compliance, but the number of optimization iterations required to achieve convergence is significantly lesser than GP. Fig. 4.14 also represents the history of a volume constraint on the right-side y-axis. The plot shows a pattern with a rapid increase in the material volume to increase the stiffness until it reaches the volume fraction limit set as a constraint in the optimization process.

Finally, a comparison between designs obtained using the standard-GP and the GP-AM method provides insights into the effectiveness of these methods. However, it is essential to note that a direct comparison cannot be made because the standard-GP merges the components by considering the maximum effective densities in the overlapping region as discussed in Section 3.2.2. At the same time, the GP-AM method involves overlapping FRBs to increase the bending stiffness of the structure. Although the slender bars are stiff when subjected to a force applied along their length, they are more flexible when subjected to a force applied perpendicular to their length. As a result, it is most efficient to align the members of a structure with the principal stresses<sup>88</sup>. This is consistent with the established principles for designing structures with heterogeneous orthotropic materials. In such materials, the

<sup>88</sup> Pedersen, "On thickness and orientational design with orthotropic materials," 1991.

optimal design for a single load case involves aligning the principal material direction with the principal stress at each point.

Figure 4.12 and 4.13 depict the design and density plot for the standard-GP method, respectively. As expected, the resulting structure is compliant compared to FRBs, mainly because the standard-GP approach combines components by merging rather than overlapping them. Figure 4.12 illustrates that multiple features are merged on the top and bottom regions adjacent to the line of action—this accommodates the applied load, similar to the FRBs arrangement obtained for GP and GP-AM methods. Overall, a common similarity in the topology, such as bar arrangement in the interior region to attain shear stresses and inclined features to manifest dome structure, is attained in the GP and GP-AM methods.

Figure 4.12: MBB—The design plot for standard-GP method.

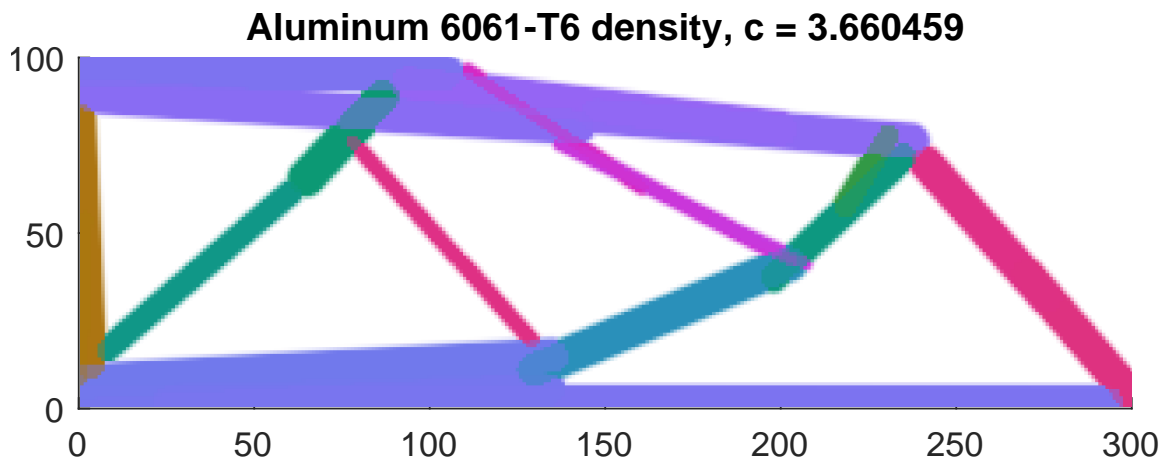
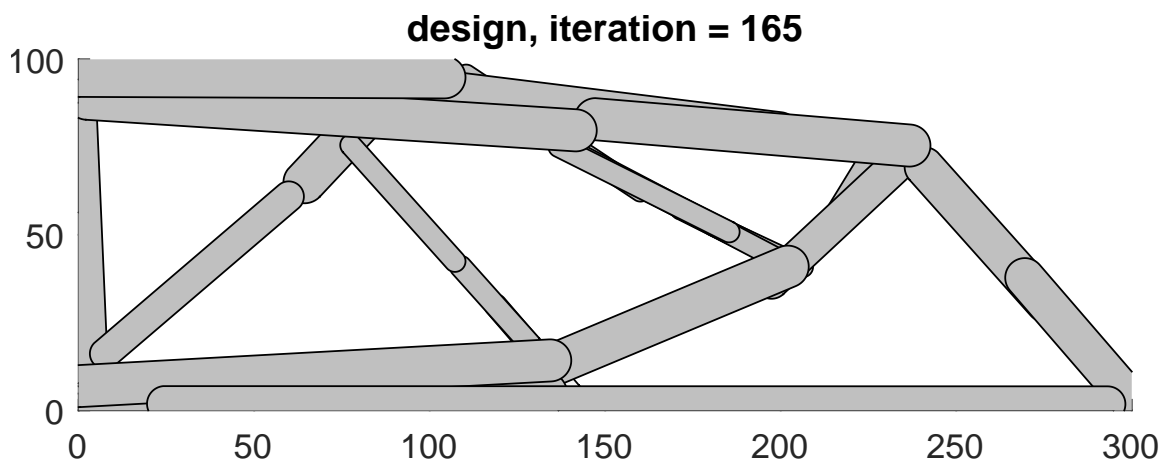
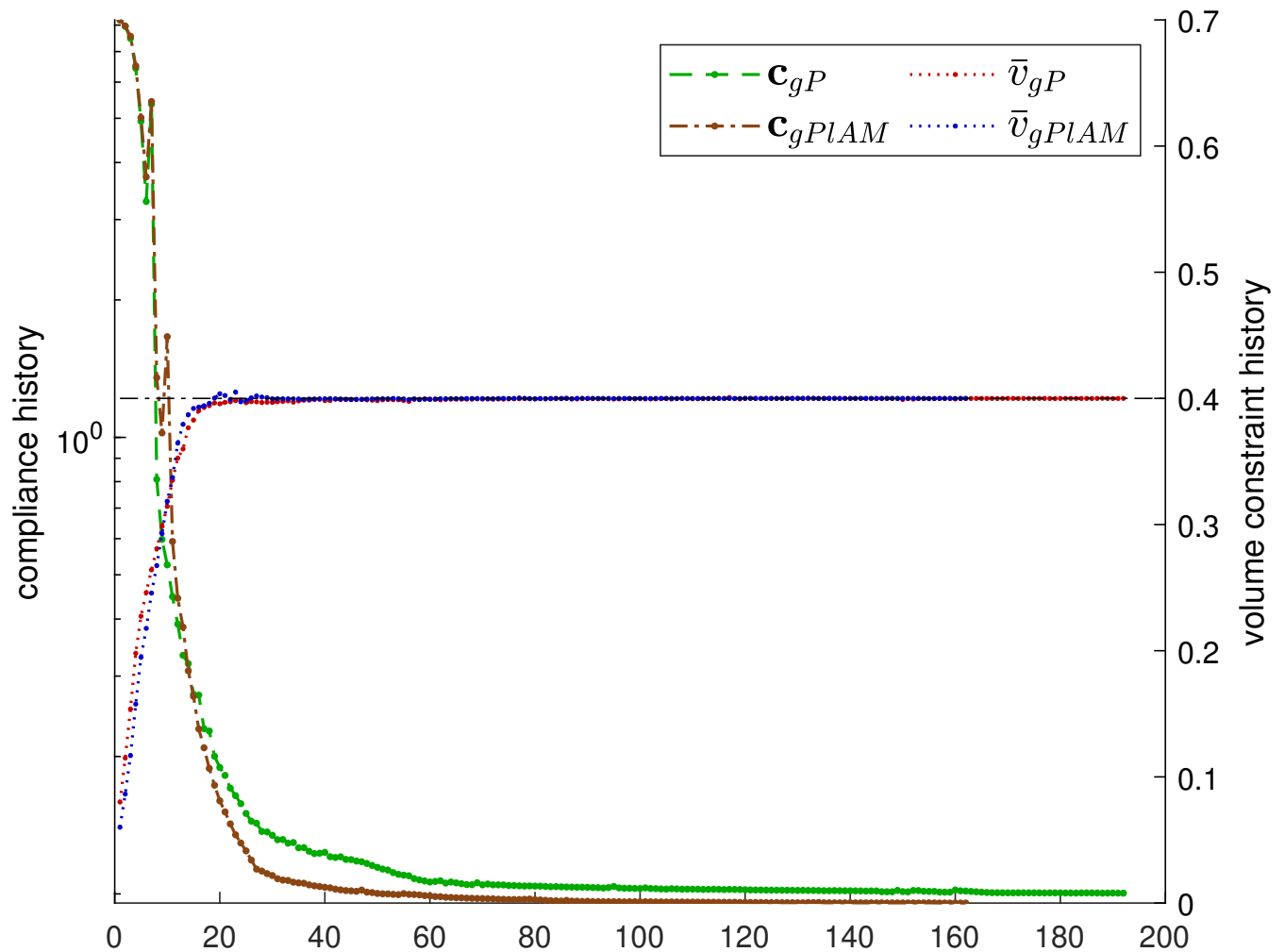


Figure 4.13: MBB—The density plot for standard-GP method



**Figure 4.14: MBB**—Comparison of the objective and constraint history of the GP method with the GP-AM method on a logarithmic and linear scale plotted on the left and right axes, respectively.



#### 4.5.2 A square plate under point bending load

We share our findings on analyzing a clamped square plate under point loading. The load, denoted as  $q \equiv 1$ , is uniformly distributed over a circular region with a radius of  $r = 5$ . The region's center is located at the point of application, as shown in Fig. 5.4. The design region measures dimensions  $150 \times 150 \times 2$ . Although the problem definition has two planes of symmetry, we did not consider the symmetry conditions because they limit the overlapping regions of the design space. Therefore, we analyzed the whole plate for comparison. The plate was initially divided into 24 bars, and we

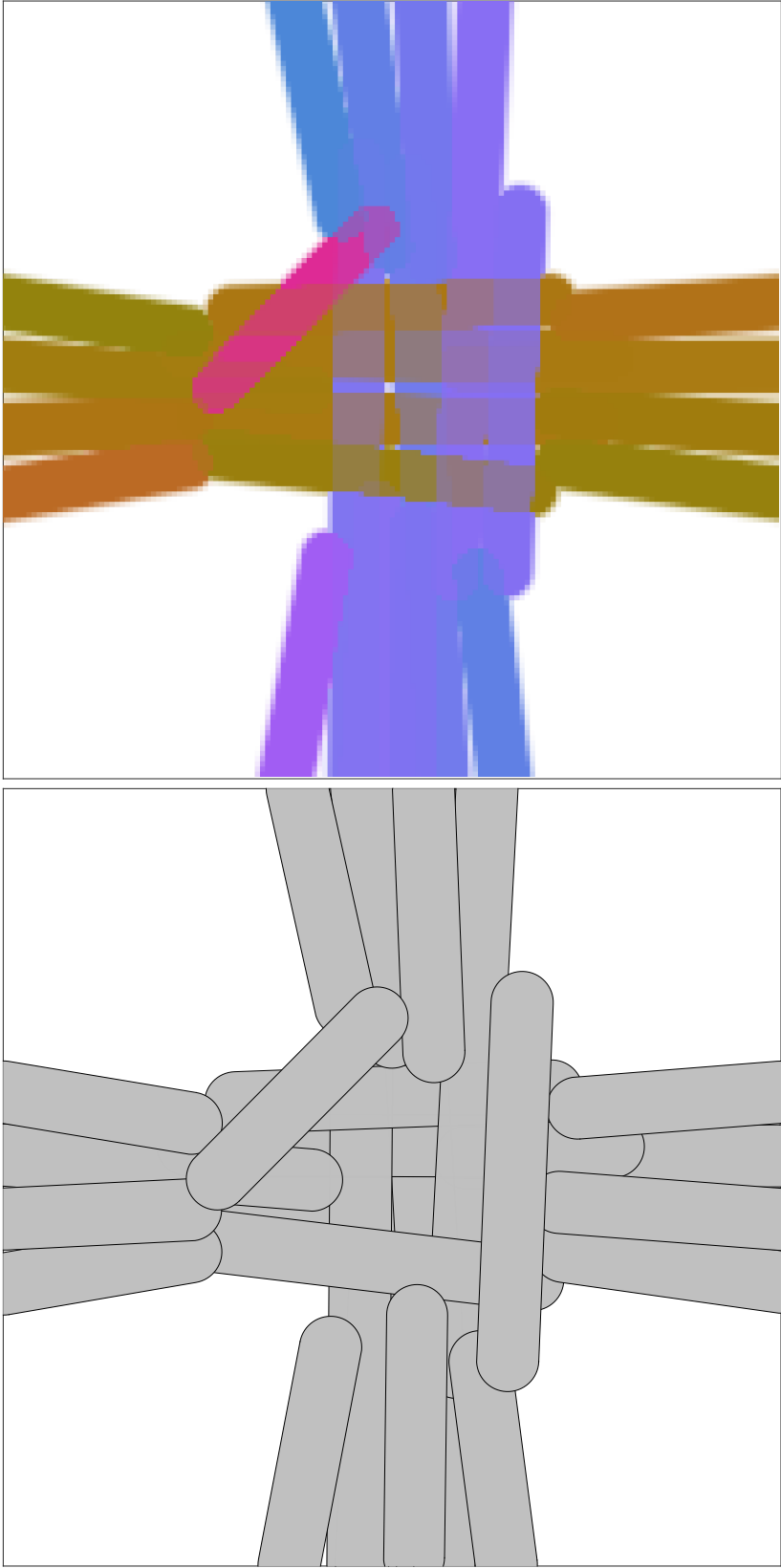


**Figure 4.15: Bending**—The design and their densities for the GP method, considering  $\beta = 100$ . The compliance for a given volume fraction limit 0.5 is 1.396162, and the design converges after 97 iterations.

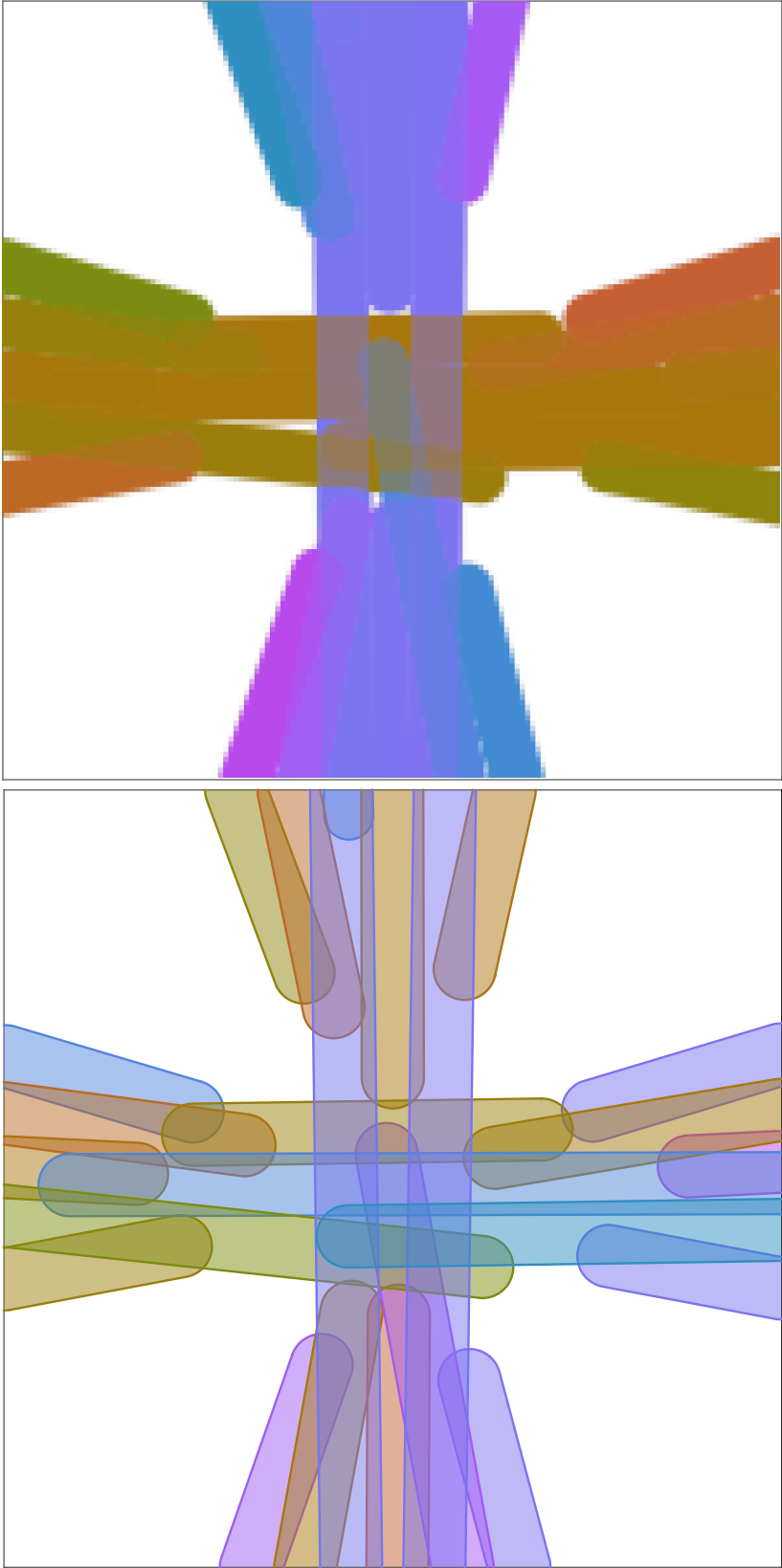


**Figure 4.16: Bending**—The design and their densities for the GP-AM method, considering  $\beta = 10$ . The compliance for a given volume fraction limit 0.5 is 1.485798, and the design converges after 104 iterations.

imposed the following bounds on the design variables:

$$\begin{Bmatrix} (0, 0) \\ 3 \\ 0 \end{Bmatrix} \leq \begin{Bmatrix} (\mathbf{x}_{b1}, \mathbf{x}_{b2}) \\ r_b \\ \alpha_b \end{Bmatrix} \leq \begin{Bmatrix} (150, 150) \\ 6 \\ 1 \end{Bmatrix} \quad (4.31)$$

From the consideration of statics that, owing to the action of the load  $q$ , it will induce bending and twisting moments, and also the shearing forces, the magnitudes of which per unit of length can be defined by the following formula.

$$\begin{aligned} \hat{\sigma}_s &= \begin{Bmatrix} Q_x \\ Q_y \end{Bmatrix} = \int_{-H}^H \begin{Bmatrix} \tau_{xz} \\ \tau_{yz} \end{Bmatrix} dz \\ \hat{\sigma}_b &= \begin{Bmatrix} M_x \\ M_y \\ M_{xy} \end{Bmatrix} = - \int_{-H}^H z \begin{Bmatrix} \sigma_x \\ \sigma_y \\ \tau_{xy} \end{Bmatrix} dz \end{aligned} \quad (4.32)$$

According to Eq. (4.32)), the maximum bending stiffness matrix  $\mathbf{D}_b$  can be achieved by optimizing the in-plane material and fiber distribution. In a study by Boddeti et al.<sup>137</sup>, a multiscale density-based topology optimization framework was used to show that the optimized topology consists of four arms connected to a central region where the fibers are arranged in a circular pattern. Density-based methods are generally more flexible in achieving fiber arrangements with a strong curvature than feature-based methods. The GP-AM approach showed a better trade-off between optimization and manufacturability than GP by not imposing heavy penalties on the fiber mixture regions and allowing for FRBs (fiber-reinforced beams) cross-over, as shown in Fig. 4.16.

<sup>137</sup> Boddeti et al., "Optimal design and manufacture of variable stiffness laminated continuous fiber reinforced composites," 2020.

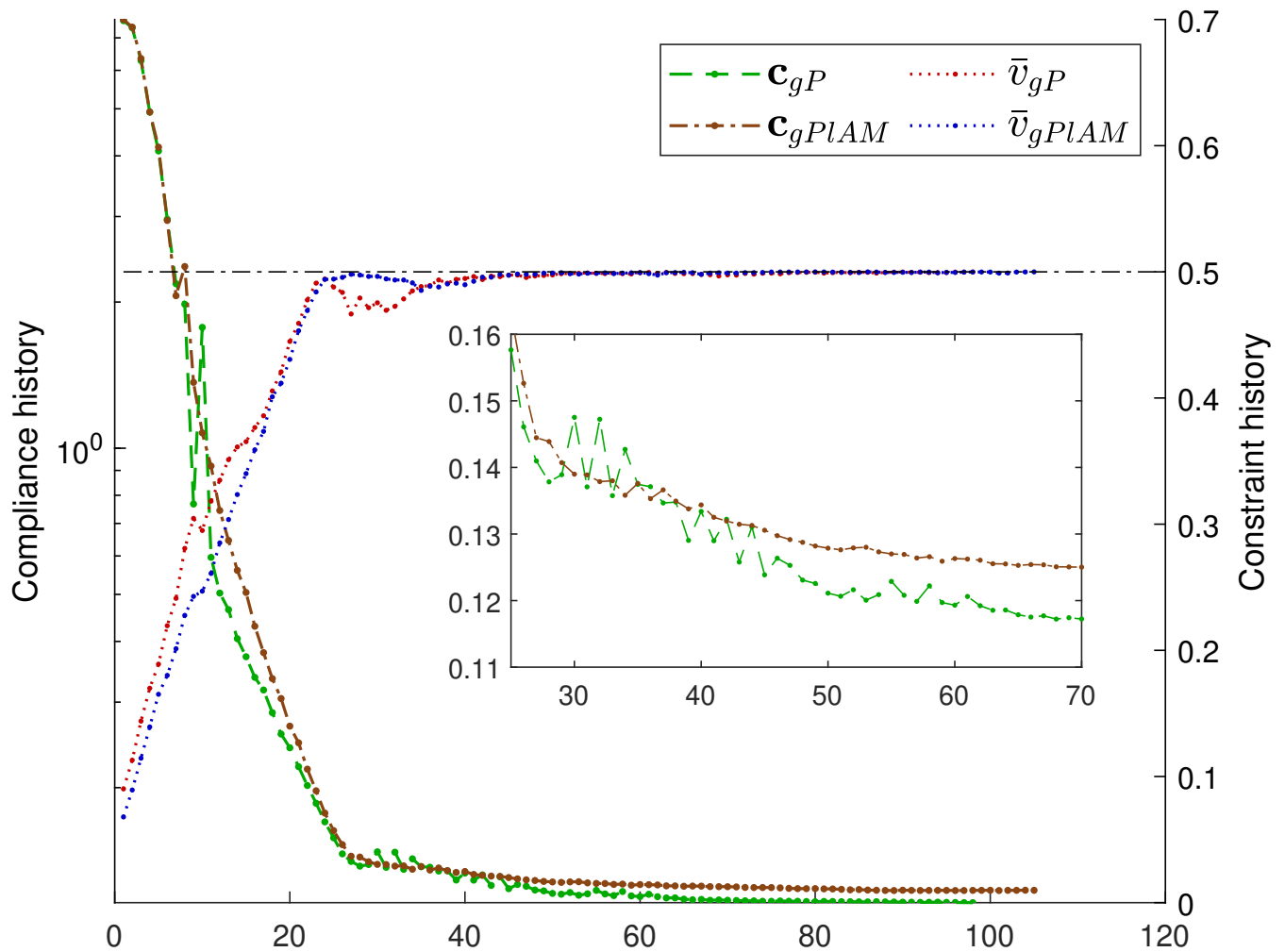
The optimized design achieved through the GP method is depicted in Fig. 4.15, outperforming the GP-AM method. The compliance value increment for GP-AM is 6.42%. In both designs, four branches connect to the central region. However, the GP-AM method comprises mostly overlapping bars arranged in a stacking sequence  $[0^\circ/90^\circ]_s$  to maximize bending stiffness components. This design is suboptimal because it requires fiber orientations such as  $45^\circ$  and  $135^\circ$  to maximize the laminate's stiffness component  $D_{b33}$ . On the other hand, the GP method produces similar FRBs to the GP-AM method, resulting in a  $[0^\circ/90^\circ]_s$  stacking sequence arrangement. By implementing a considerable penalty in the GP method, the aggregation of bars is prevented during the initial stages of the optimization process. This is particularly effective when the membership variable is relatively low, but it leads to a less optimal arrangement of bars in the central region. The example also highlights the difficulty of attaining a discrete material orientation at each design point when designing for intersecting load paths.

Both methods have a geometric constraint that limits the design space for material distribution. Additionally, the GP method increases the stiffness contribution through fiber mixture regions, resulting in a lower compliance value. Acquiring a discrete fiber orientation is challenging, even with a high value of  $\beta$ . Eq. (4.4) calculates a weighted sum of elasticity tensors  $C_b$  of overlapping FRBs, which increases the transversal elasticity component. This overestimates the stiffness matrices  $D_a$  when FRBs overlap. However, the component weights penalize the densities of FRBs and do not address their directional properties. As a result, a single feature is oriented at  $135^\circ$ . The GP-AM method uses a low value of  $\beta$ , which can cause bars to group around the loading area to compensate for their smaller size during the early optimization stages. This can result in a limited range of orientation for the bars in the design space. As a result, the GP-AM method is more sensitive to the initial design than the GP. However, these limitations can be resolved by simultaneously optimizing the topology of multiple layers.

Note that even if the design requirements call for a symmetric design, the final design results in an asymmetric layout. For density-based and level-set topology optimization methods can easily create designs that meet those requirements due to enriched topological space. However, when using discrete geometric components to represent the design, the optimizer may produce asymmetrical designs that meet the weight requirements exactly but have lower compliance than the optimal symmetric designs created using the available components. In other words, it is possible to find an asymmetric design that perfectly meets the weight fraction constraint despite having less compliance than the best symmetric design that can be made with the available components, as discussed in more detail in [125].

The figure labeled Fig. 4.17 shows the objective and constraint history for the GP and GP-AM at various  $\beta$  values. The GP formulation aims to identify discrete components by removing mixed fiber regions, which requires updating membership design variables. This update significantly affects material properties at intersections in GP. Even a slight change in membership variable  $\alpha$  can cause the intersection to be dominated by a different component, making GP highly sensitive to these changes. This sensitivity can result in more oscillations as the gradients become very steep, as shown in Fig. 4.17.

**Figure 4.17: Bending**—Comparison of the objective and constraint history of the GP method with the GP-AM method on a logarithmic and linear scale plotted on the left and right axes, respectively. The objective history inset plot from iteration 20 – 70 shows oscillation in the GP method due to rapid changes in membership variables.



### 4.5.3 A rectangular plate under pure torsion

In the third example, we consider a rectangular plate with dimensions of  $400 \times 100 \times 2$  subjected to pure torsion, as shown in Figure 5.4. Due to anti-symmetry conditions, the finite element analysis was performed on half of the plate. The plate is discretized using  $200 \times 50$  plate elements. Initially, the design has 36 bars, and the design variables have the following bounds:

$$\begin{Bmatrix} (0, 0) \\ 3 \\ 0 \end{Bmatrix} \leq \begin{Bmatrix} (\mathbf{x}_{b1}, \mathbf{x}_{b2}) \\ r_b \\ \alpha_b \end{Bmatrix} \leq \begin{Bmatrix} (200, 50) \\ 6 \\ 1 \end{Bmatrix} \quad (4.33)$$

Under pure torsion conditions, each point in a plate is subject to pure shear, defined by the components  $\tau_{xy}$  and  $\tau_{xz}$ . When seeking an optimized design for a symmetric laminate, the most significant contributors are the  $D_{m33}$ ,  $D_{b33}$ , and  $D_s$  components of the laminate stiffness matrices. Additionally, it's possible to assume that the displacements and rotations are proportional to the angle of twist, i.e.,  $u$ ,  $w$ ,  $\psi_x$ , and  $\psi_y$  are proportional to  $\zeta$ . The relationship between the applied torque,  $T$ , and the twist angle,  $\zeta$ , can be expressed as follows.

$$T \propto D_{33b} \zeta \quad (4.34)$$

Maximizing the  $D_{33b}$  component of its stiffness matrix is essential to minimize the displacements and rotations of a laminate. This is why the ideal design arranges the FRBs at angles of either  $45^\circ$  or  $135^\circ$ . For example, we can compare the membrane-shear coupling, bending-shear coupling, and torsional rigidity components of two symmetric laminates,  $A$  and  $B$ , representing GP and GP-AM formulations, respectively. Both laminates have the same ply thickness and a stacking sequence of either  $[45/45]_s$  (or  $[135/135]_s$ ) and  $[45/135]_s$ . Table (4.2) displays the stiffness components for both configurations. It is important to note that when computing overlapping FRB stiffness, the GP method adds penalized material properties while the GP-AM method computes homogenized material properties.

**Table 4.2:** For a given laminate<sup>1</sup> configuration, stiffness matrices' components are used for GP and GP-AM method.

Laminate	$D_{m13}$ [Nmm]	$D_{m23}$ [Nmm]	$D_{b13}$ [Nmm]	$D_{b23}$ [Nmm]	$D_{b33}$ [Nmm]
A (GP)	52375	52375	17459	17459	19728
B (GP-AM)	0	0	13094	13094	19728

<sup>1</sup> The material properties mentioned in Tab. 4.1 have been converted into MPa

It should be noted that the torsional rigidity, denoted as  $D_{b33}$ , is equal for both laminates. This suggests that the overlapping components in the GP-AM method do not provide any additional benefits to the design. However, the GP-AM can alleviate the effect of membrane-shear coupling. To better understand the effects of these stiffness components on the overall layout, a comparison between the GP-AM and GP methods is conducted in two different design cases by altering the volume constraint limit, i.e., for 50% and 60%. The design and density plots of the GP-AM method in

**Figure 4.18: Torsion**—The design plot for GP method. The transparency of FRBs depicts the membership variable attained intermediate value, i.e.,  $\alpha < 1$

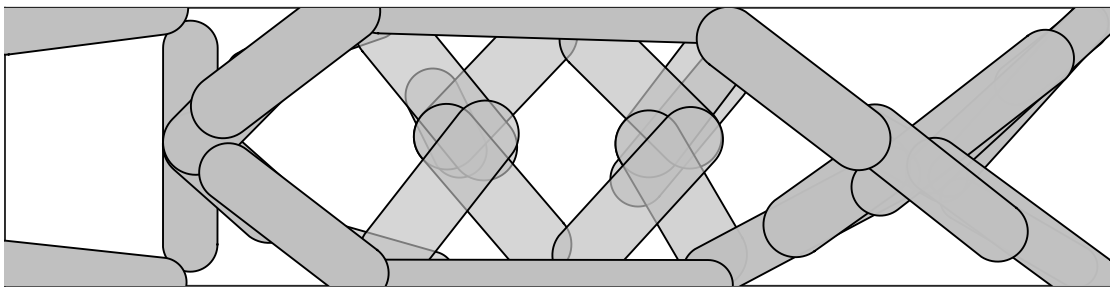


**Figure 4.19: Torsion**—The density plot for GP method. The compliance for a given volume fraction limit 0.5 is 184.893393.

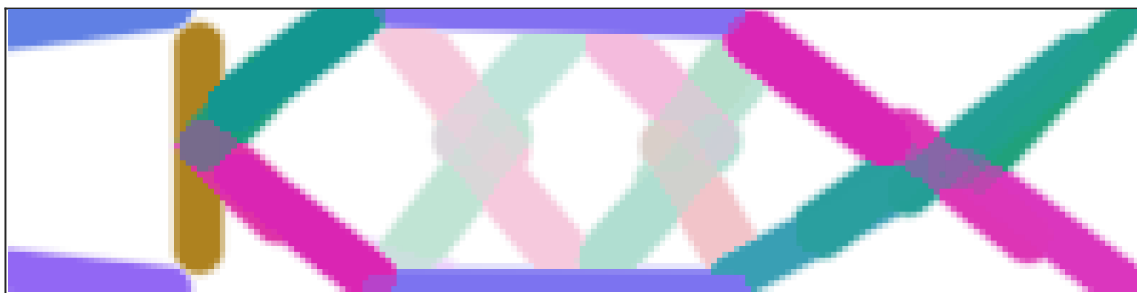
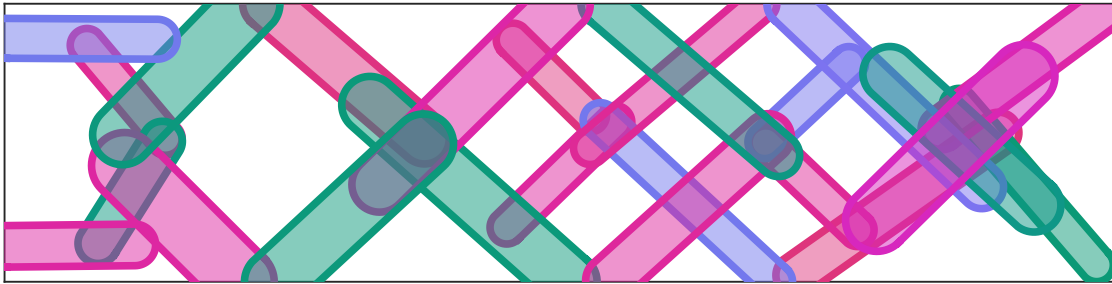
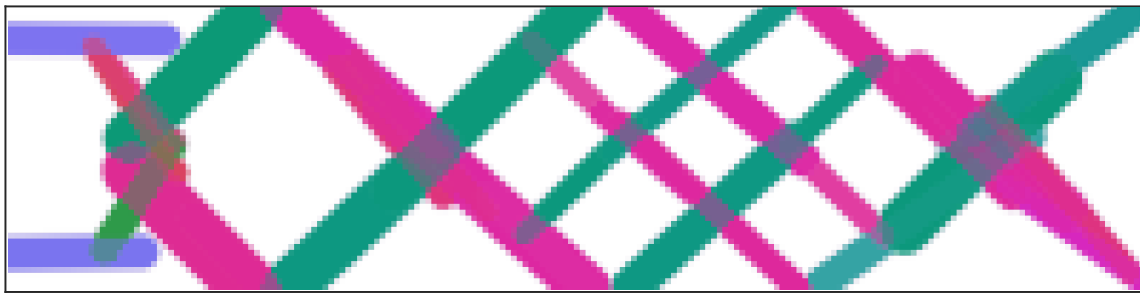


Fig. 4.20, 4.21 show the arrangements of FRBs and their overlapping regions for volume fraction limits of  $\bar{v} = 0.5$ . The FRBs are arranged in a way that forms a cross-over at angle  $45^\circ$  and  $135^\circ$ , and the design fulfills the anti-symmetric boundary condition on the left edge by placing the bars at  $0^\circ$ , which supports the initial analysis. The design plots show that the cross-over features of different sizes are stacked on top of each other instead of introducing variability in the orientation of FRBs, i.e., to achieve a stiffer structure without altering the topology of the design.

**Figure 4.20: Torsion**—The design plot for the GP-AM method shows that FRBs' membership variable always approaches 1.



**Figure 4.21: Torsion**—The density plot for GP-AM method. The compliance for a given volume fraction limit 0.5 is 141.048719.



In Fig. 4.18 and Fig. 4.19, we can see the design and density plots of the GP method. However, it is difficult to predict the expected assembly of FRBs when comparing it with GP-AM for the case of  $\bar{v} = 0.5$ . This is because the softmax function imposes a heavy penalty on overlapping bars. The central region, i.e., the region between the boundary and loading condition, of the computational domain bars tends to dissolve first, then the components near both ends of the computational domain. To design connected VS-CFRP-L and counteract the membrane-shear coupling effect, the bars orient themselves at  $0^\circ$  by penalizing the formation of overlapping FRBs in the central region. This means the GP method settled in a sub-optimal design by avoiding intersecting FRBs as arranged in the GP-AM method (Fig. 4.21). The FRBs cannot be dissolved near the loading region, resulting in a disconnected structure. This leads to a compliant VS-CFRP-L since the GP method must still comply with the constraint of inhibited overlapping regions in the design. Similarly, near the boundary condition, a feature at  $90^\circ$  is due to similar consequences. To demonstrate the effectiveness of the GP-AM method, we have solved a similar problem with a

**Figure 4.22: Torsion**—The design plot for GP method. The transparency of FRBs depicts the membership variable attained intermediate value, i.e.,  $\alpha < 1$

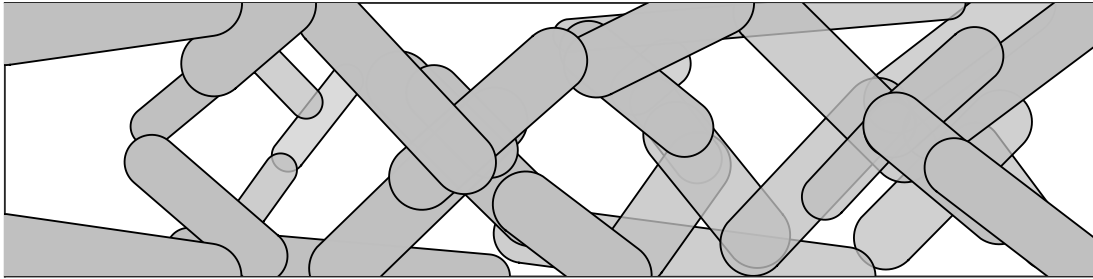


**Figure 4.23: Torsion**—The density plot for GP method. The compliance for a given volume fraction limit 0.6 is 135.665506.



**Figure 4.24: Torsion**—The design plot for the GP-AM method shows that FRBs' membership variable always approaches 1.

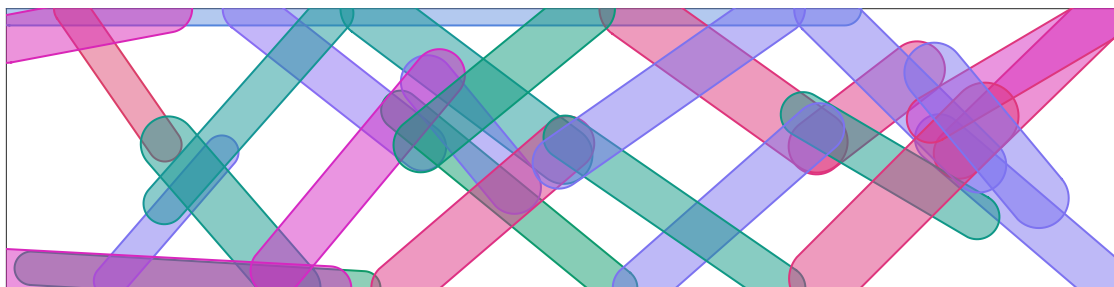
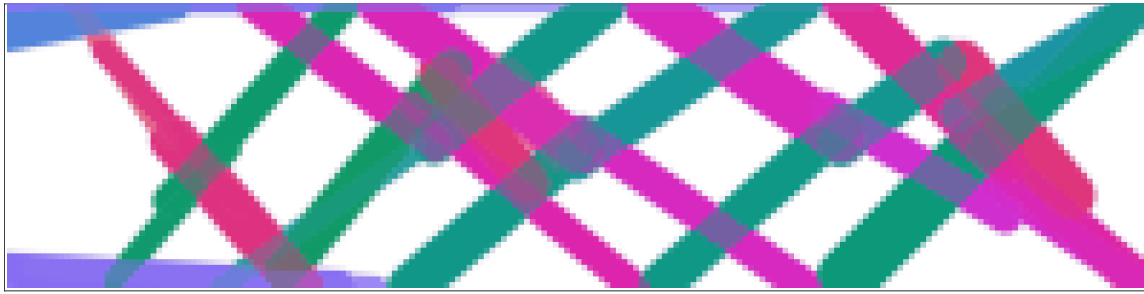


**Figure 4.25: Torsion**—The density plot for GP-AM method. The compliance for a given volume fraction limit 0.6 is 112.607709.

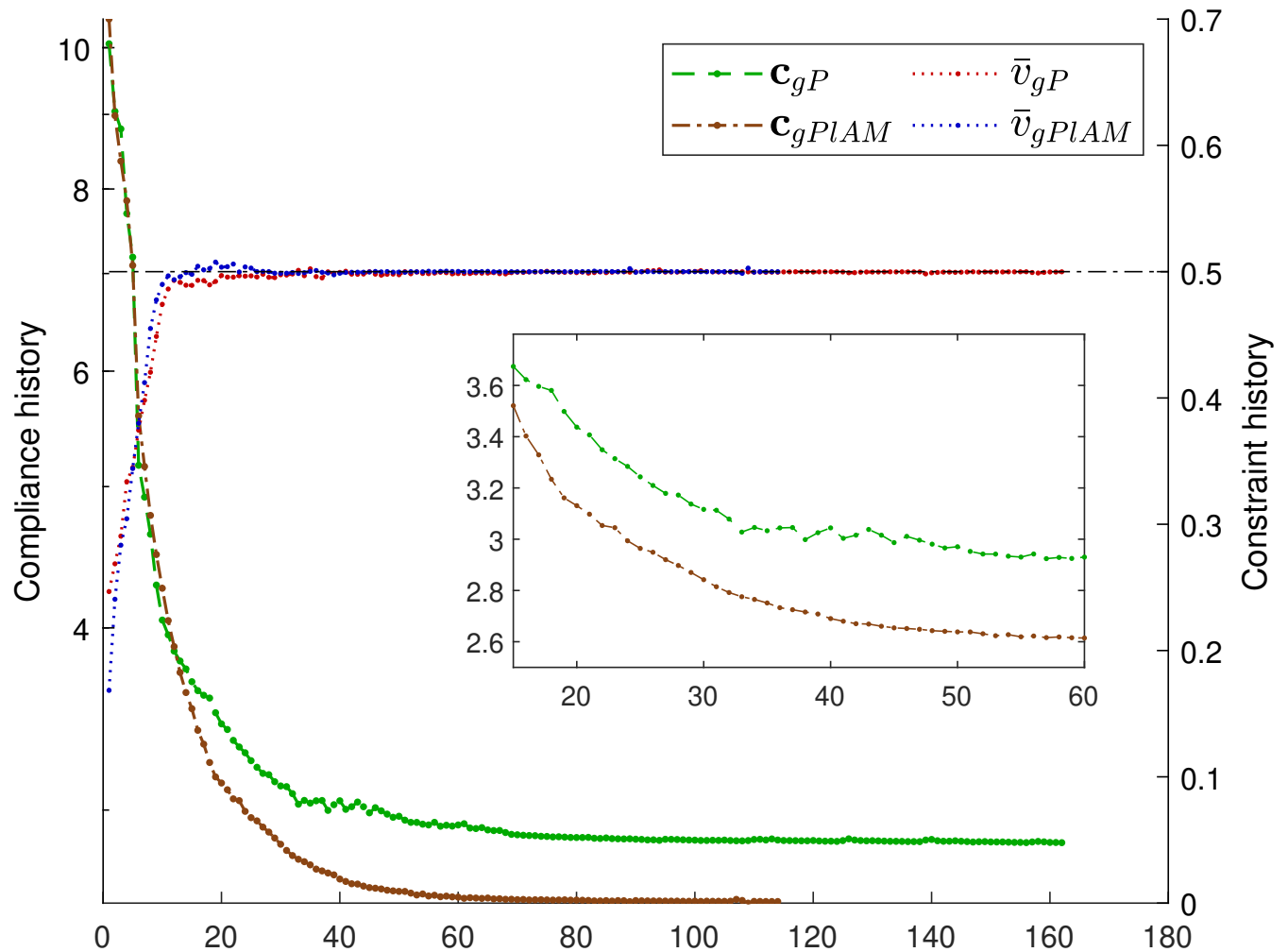


volume fraction limit of  $\bar{v} = 0.6$ . The design and density plots of the GP-AM method are shown in Fig.4.24 and 4.25, respectively, which display the arrangement of FRBs and their overlapping regions for a volume fraction limit of  $\bar{v} = 0.6$ . On the other hand, Fig.4.22 and 4.23 illustrate the design and density plots of the GP method, respectively.

When using the GP method, overlapping bars near the loading region are expected to dissolve. This occurs because significant material accumulates during the initial optimization stages to minimize compliance. These results demonstrate that the GP formulation is susceptible to considering higher volume fractions and designs with intersecting load paths simultaneously, which can directly impact the manufacturability of the final design, as shown in Fig. 4.22 and Fig. 4.23. While the GP-AM produces better designs than the GP approach (are shown in Fig. 4.24 and Fig. 4.25), it is essential to note that the overlaps in the design are more free-form than for the case of  $\bar{v} = 0.5$ . This is because higher volume fractions allow for significant overlap regions, which in turn offer the opportunity to achieve a substantial variability in fiber orientation during the stages of the design process. Additionally, it is crucial to carefully consider the initial bar arrangement (as shown in Fig. 5.4) to ensure the manufacturability of a design. For example, if the problem is initialized with bars arranged only at  $0^\circ$  and  $90^\circ$  angles, as carried out in the previous examples, it may accumulate more bars near the loading region. Despite the limitations of GP-AM, the method demonstrates that the design can be optimized for intersecting load paths and large volume fractions simultaneously.

The results presented in Fig. 4.26 and Fig. 4.27 demonstrate that optimizing the intersecting load region improves the design. Our assertion that this approach provides benefits is supported by the GP-AM method, which led to compliance reductions of

**Figure 4.26: Torsion**— $\bar{v} = 0.5$ . The objective history plot of the GP method from iteration 10 – 60 showed no oscillation due to the dissolution of FRBs.

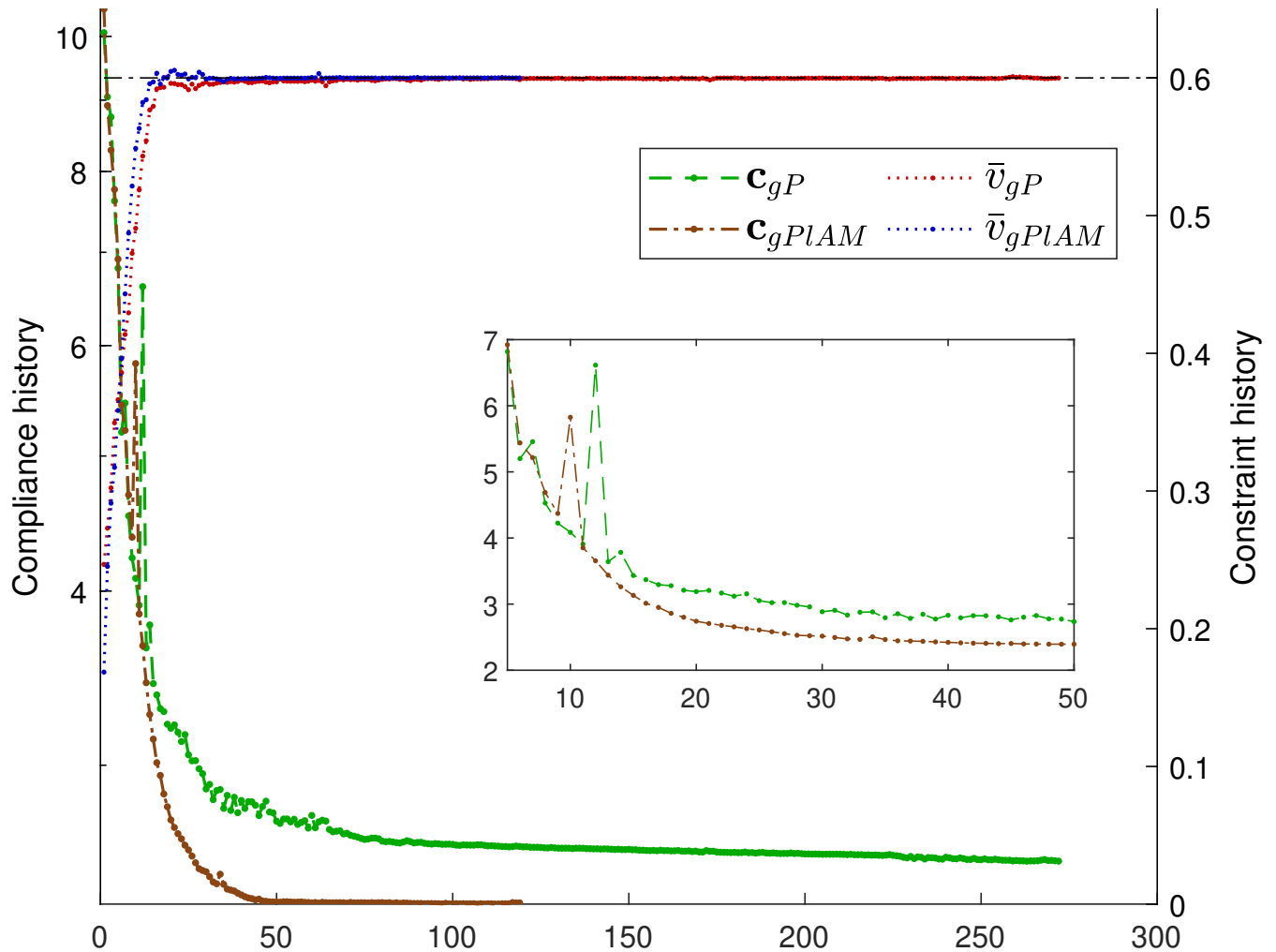


23.7135% and 17% for volume fraction constraints of 0.5 and 0.6, respectively. Furthermore, the approach reached convergence after only 113 and 118 iterations, which is quicker than GP's 161 and 271 iterations for the same two cases. The inset of Fig. 4.26 and Fig. 4.27 shows the effects of high sensitivity to design variables in GP formulation. In the early optimization stage, the overlapping bars disappear, enabling distinct features that result in moderate and limited oscillations to occur in a narrow region. This contrasts the previous example (Fig. 4.17), where the features are not eliminated, leading to significant oscillations. Defining overlapping regions and their modeling to optimize the design for intersecting load paths achieves better design and a smoother optimization process, resulting in a design that can be manufactured. Failure to consider the postulate defined for overlapping regions and only relaxing

the penalization parameter of the GP formulation's aggregation function will result in an unrealizable solution.

It is important to note that the transparency of the FRBs in Fig. 4.18 and Fig. 4.22 represents the membership variable ( $\alpha$ ) for each bar. The membership variable indicates the presence or absence of specific features in the design space. However, this explanation does not apply to Fig. 4.20 and Fig. 4.25. In these figures, each bar's membership variable approaches unity. Therefore, a constant transparency factor is used to visualize overlapping FRBs in the GP-AM method.

**Figure 4.27: Torsion**— $\bar{v} = 0.6$ . The objective history inset plot from iterations 10 – 60 shows oscillation due to large overlapping, which cannot be avoided due to the increase in the volume fraction limit.



#### 4.5.4 Multiple load cases

The following example considers a rectangular plate with dimensions of  $160 \times 80 \times 2$  subjected to two load cases. The plate is fixed at the left edge, and a unit out-of-plane load is applied at the center while a couple is applied at the right edge corner, as shown in Figure 5.4. The initial design comprises 22 bars, and the design variables are bounded as follows:

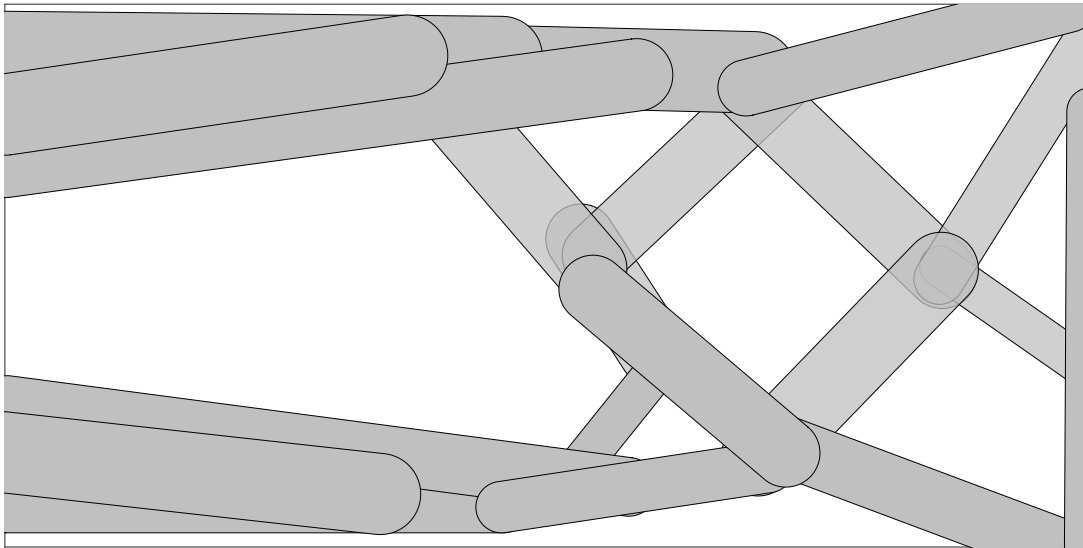
$$\begin{Bmatrix} (0, 0) \\ 3 \\ 0 \end{Bmatrix} \leq \begin{Bmatrix} (\mathbf{x}_{b1}, \mathbf{x}_{b2}) \\ r_b \\ \alpha_b \end{Bmatrix} \leq \begin{Bmatrix} (160, 80) \\ 6 \\ 1 \end{Bmatrix} \quad (4.35)$$

Furthermore, we define the objective compliance function for the two load cases in this example according to equation(5.20) the net compliance, i.e., the sum of the compliance of each load case

$$c := \sum c_i. \quad (4.36)$$

In Fig 4.32, we see a combined plot displaying objective and

**Figure 4.28: Multiload**—The design plot for GP method. The transparency of FRBs depicts the membership variable attained intermediate value, i.e.,  $\alpha < 1$



constraint history for a fixed  $\bar{v} = 0.5$ . Additionally, design and density plots for GP and GP-AM are depicted in Figures 4.28, 4.29 and Figures 4.30, 4.31, respectively.

We can observe common similarities between the approaches, such as inclined tapered long bars contributing to the torsional

**Figure 4.29: Multiload**—The density plot for GP method. The compliance for a given volume fraction limit 0.5 is 226.575885.

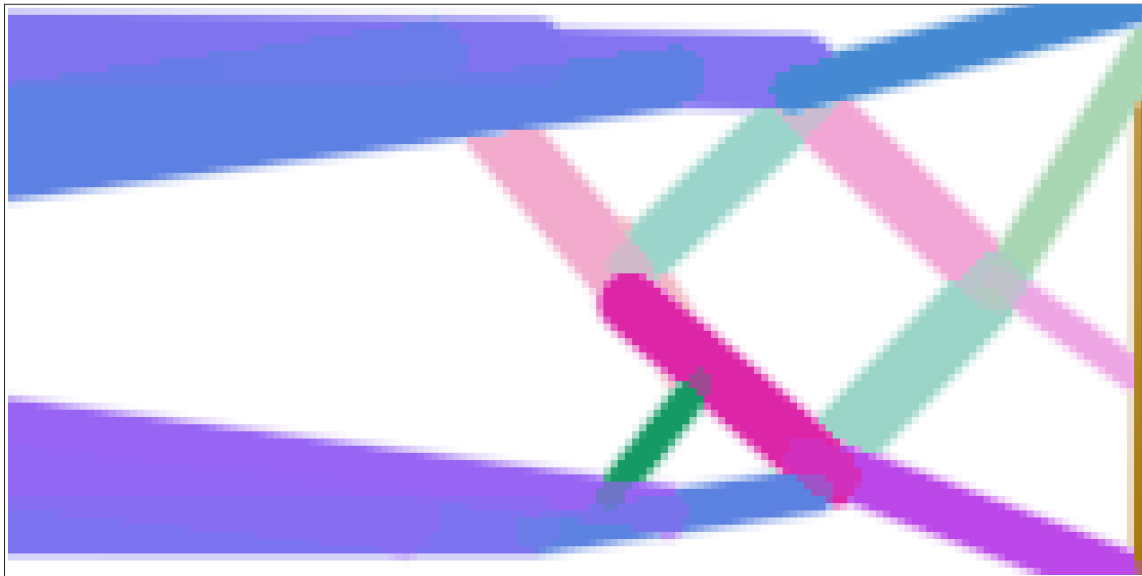


**Figure 4.30: Multiload**—The design plot for the GP-AM method shows that FRBs' membership variable always approaches 1.

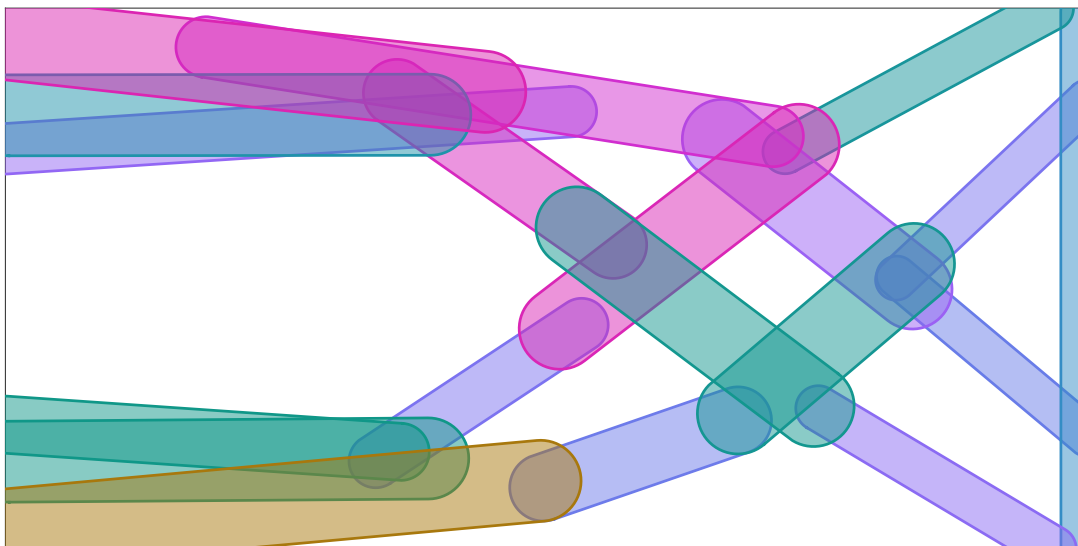
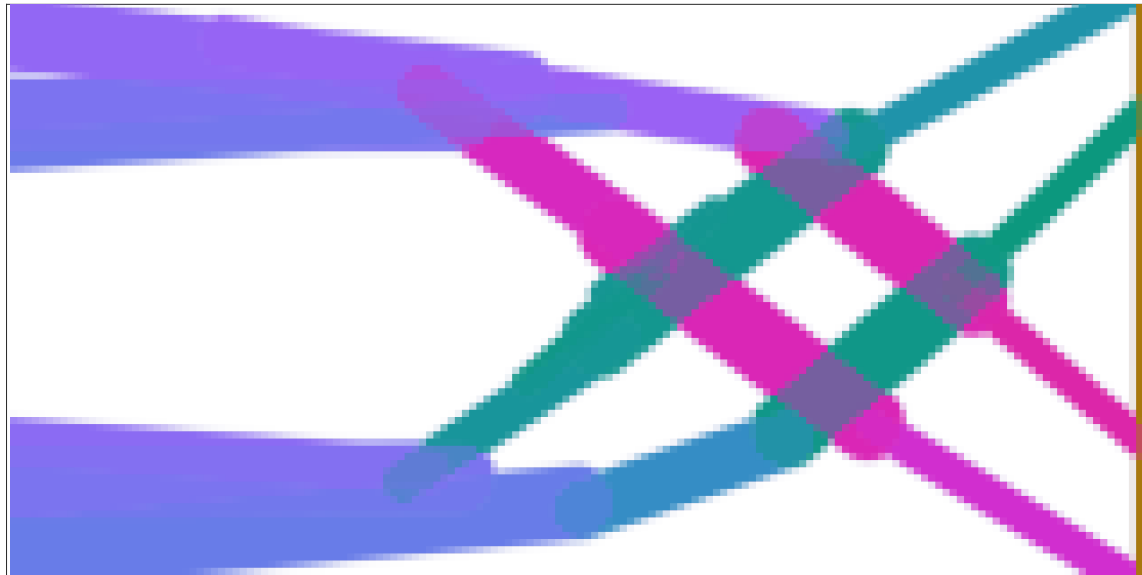


**Figure 4.31: Multiload**—The density plot for GP-AM method. The compliance for a given volume fraction limit 0.5 is 195.571698.

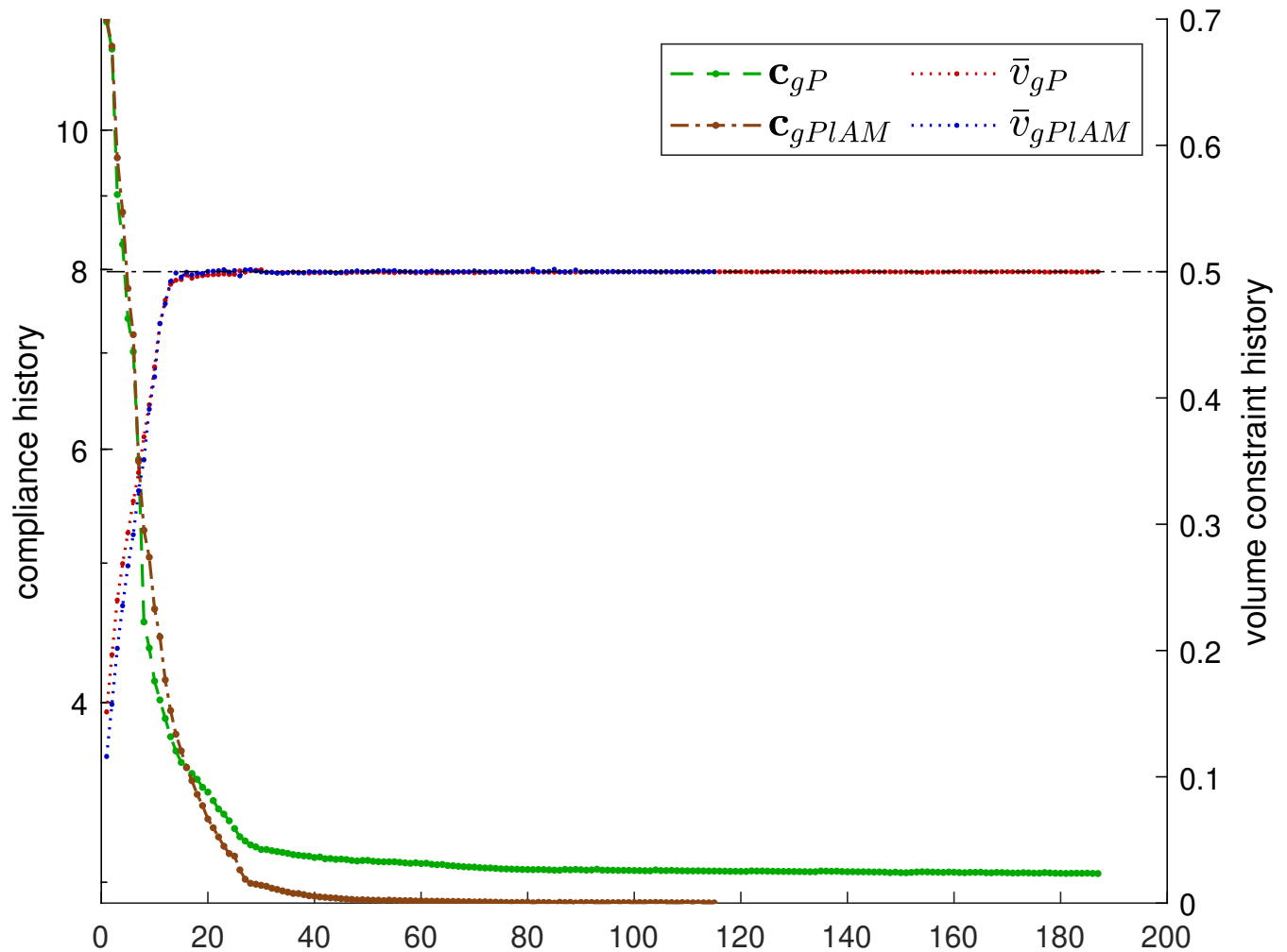


rigidity and bending stiffness simultaneously through coupling terms and inclined and traverse features at structure boundaries near the loading region. This shows that both approaches are well-suited to optimize non-intersecting load path regions and achieve similar FRB orientation in the design space.

For the torsion load, the GP method pushes the bars towards structure extremities to avoid overlapping bars. In contrast, GP-AM combines the tapered feature with other features to provide a smooth transition to achieve crossed bars near the loading region. This demonstrates the optimized layout for the twisting moment. Moreover, the GP-AM method can merge features to introduce thicker features at the boundary condition, which can be advantageous when the upper limit of the design variables is fixed.

As a result, the GP-AM produces a design that is 13.684% stiffer than the GP. Unfortunately, the GP does not allow for the inclusion of these crossed features due to imposed restrictions, as discussed before—resulting in a suboptimal arrangement of the FRBs. The multi-load case highlights the difference between the GP-AM and GP method—the former produces better designs and achieves faster convergence, even for complex examples.

**Figure 4.32: Multiload**—The multi-load example using GP and GP-AM methods converges in 186 and 114 iterations respectively.



## 4.6 Summary and conclusions

This chapter introduces the GP-AM methodology for designing variable stiffness composite laminates. The process leverages the geometry projection method’s dual representation—i.e., to utilize both high-level parameterized primitives and low-level density-based design spaces—to design for intersecting load path regions. Therefore, it accommodates multiple fiber orientations by enabling multiple component intersections and merging features within the design. While in GP, the softargmax function is used to attain discrete components, in GP-AM, this is not utilized so that features can overlap. However, because removing the aggregation scheme may render the design unrealizable, we postulate a criterion to define overlapping regions to ensure the design matches the manufac-

turability standards proposed in the geometry projection method. Thus, these regions are modeled using composite laminate theory, where multiple fiber orientations are represented as layers in the laminate; sensitivities are reformulated to enable the cross-over and merging of features, yielding an optimized design for intersecting load path regions. We demonstrated the effectiveness of GP-AM with several computational design domains of different aspect ratios under various boundary conditions. By comparing GP-AM and GP designs, we showed that the upper bounds on the bar's radius could limit the GP design from achieving a better solution; GP-AM can overcome this limitation by merging components to increase their thickness and introducing tapered features. Additionally, GP-AM attains a stiff and manufacturable design by modeling fiber mixture regions and demonstrates that the formulation to achieve a discrete fiber orientation must be considered cautiously for optimizing VS-CFRP-Ls.

The GP-AM formulation also showed a fast and smooth convergence by subduing the FRB's compliant transversal response. Mitigating the steep gradients stemming from slight changes in sizing variables enables GP-AM to reach significant variations in material properties within intersecting regions. This is important because seeking a dominant feature could make optimizing the design challenging for areas under intersecting load paths, leading to a suboptimal design that may not be manufacturable.

In the geometry projection method, defining overlapping regions can be complex due to the limitations of the density-based approach in accurately representing the boundaries of FRBs. As a result, the analytical portions of the components are approximated by their projected densities  $\rho_{b\omega_e}$ . It is worth noting that selecting a value of  $\rho_{b\omega_e}$  within the range of  $(0.5, 1]$  can significantly affect the final design, as discussed in the Appendix B. For instance, using a less restrictive definition of overlaps (e.g.,  $\rho_{b\omega_e} \geq 0.5$ ) allows the formation of several overlapping FRBs to attain varying fiber orientations in the design space but can make the manufacturing process complicated. On the other hand, a value  $\rho_{b\omega_e} = 1$  can limit the variability of the fiber orientation by forming overlaps for regions where  $\nabla_{z_i} \check{\rho}_{b\omega_e}^{eff}(\mathbf{x}; \mathbf{z}_b)$  is zero, thereby allowing free movements of the FRBs by not influencing the individual bar's sensitivity through the formation of overlaps. For single-layer VS-CFRP-L,  $\rho_{b\omega_e} \geq 1$  is chosen to approximate intersecting areas successfully, yielding manufacturable designs.

The criteria for overlapping fibers introduce variability of fiber path by concatenating FRBs and moderate overlapping FRBs that may hinder the smooth printability of the design by inducing fiber

cut-outs. The simplicity of the feature prompts the question of whether the design can be further simplified to attain more manufacturable VS-CFRP-Ls through GP-AM methodology. The next chapter investigates simple overlap, i.e., no overlapping criteria, and discusses the consequence of using simple overlap formulation in terms of the optimization process and printability to design. To resolve these issues, we introduce length constraint formulation that minimizes the overlapping FRBs but retains features that enable a stiffer and more manufacturable structure.

# 5

## *Geometry Projection method for Variable Stiffness Continuous Fiber-Reinforced Polymer Laminates—Simple Overlap formulation with length constraint.*

Chapter 4 formulates the GP-AM procedure to design monolithic structures where fiber-reinforced components overlap to form a joint, using a GP procedure where primitives structure is intended to assemble with fiber-reinforced components. The intention is to align the stiff fiber direction with all the intersecting load paths. This can be crucial for exhibiting an orthotropic (or almost isotropic) response and lowering the strain energy. This challenges the GP method, as seeking designs for discrete components can only align with a single load path. As already demonstrated in the Chapter 4, the softargmax function can cause the optimization process to oscillate in determining the dominant component, leading to the dissolution of features during the early optimization stages. Therefore, customizing the GP procedure for designing VS-CFRP-Ls to leverage the design opportunities presented by CF4 is daunting due to the constraint of preventing overlapping components. Thus, the GP-AM methodology postulates a criterion that defines the overlapping regions at the density level because freely allowing components to overlap can result in suboptimal solutions. On the other hand, allowing components to overlap using overlapping criteria can still lead to suboptimal solutions, especially for higher-volume fractions. This is because the optimizer may try to compensate for the transversely compliant response of CFRPs by increasing component overlaps in the design domain, resulting in a non-manufacturable design.

In the chapter on geometry projection of isotropic bars ( Chapter 3), a standard-GP method was introduced that combined isotropic components (see Section 3.2.2), which was later extended by Smith *et al.* in the context of components made of CFRP material.

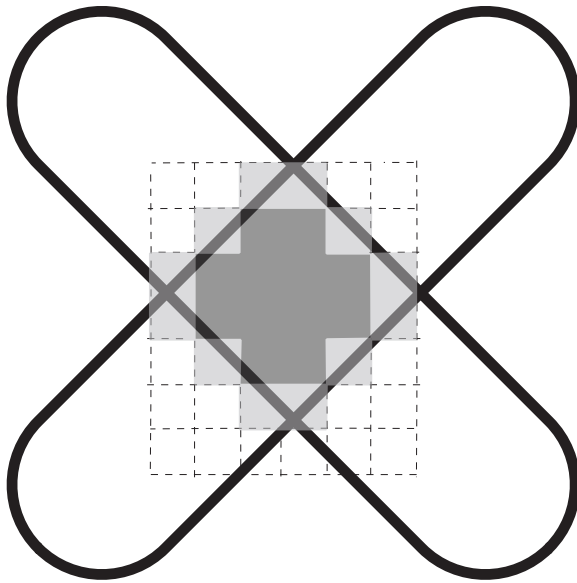
Similarly, this chapter reformulates [125] the definition of overlapping isotropic components and applies it to the VS-CFRP-Ls framework, i.e., it defines simple overlap definition to the components made of CRP material. Instead of using overlapping criteria, the chapter discusses the consequences of simple overlap formulation and demonstrates its limitations through several numerical examples. Finally, to overcome the limitation of the simple overlap formulation related explicitly to poor manufacturability, we integrate minimum length constraint formulation in the geometry projection methodology, which is not considered as a constraint in the optimization process, such as volume constraint, but is regarded as the intrinsic definition of the geometry projection method.

The membership variable can control the structural topology but sometimes eliminates all small members. This was demonstrated in the Appendix A.1. For instance, in the ground structure topology optimization, Ramos et al. [163] studied the effect of not having a discrete structure filtering tool in the optimization process. They found that when using the conventional elastic formulation for compliance minimization with a low cross-sectional area, the entire ground structure is obtained as part of the solution. This results in many bars with small regions of the final topology, even though not all the cross-sectional areas of thin members go to zero. Such examples highlight the need for an effective filtering scheme to filter structures out of ground structures.

Adopting a filtering scheme enforces the global equilibrium and structural resolution (ratio between the minimum and maximum member areas in the topology) while also allowing control of the variation of the objective function between consecutive non-linear iterations. This leads to a well-defined topology in which all structural members have a finite area. In another study, Groen and Sigmund<sup>164</sup> used a smooth Heaviside function to filter out small details in microstructural layouts. Due to the need for the length scale constraint in the GP-AM method, a weighting mechanism is formulated using a Sigmoid function with a threshold value on the minimum length of the FRB to improve the topological decision. Using the Sigmoid function makes the optimization process more stabilized and less likely to oscillate than formulating an optimization problem with a length constraint. The continuous weighting procedure utilizes smooth, differentiable Sigmoid functions that include a continuation scheme to narrow the transition zone of the Sigmoid function gradually. Nonetheless, the approach is still limited to a single layer—which we call LGP-AM.

<sup>164</sup> Groen *et al.*, “Homogenization-based topology optimization for high-resolution manufacturable microstructures,” 2017.

**Figure 5.1: Simple Overlap**—Darker grey region effective densities,  $\check{\rho}_{eff}$ , are greater than lighter grey regions, given that the membership variable,  $\alpha$ , is equal to 1 for intersecting bars. The complete region, including intermediate densities, defines an overlapping region,  $\omega_e$ , in simple overlap.



## 5.1 Formulation for Simple Overlapping FRBs

Norato et al. [125] formulated the overlapping of bars made of isotropic materials, in which it was assumed that the thicknesses of 2D bars were stacked together by simply defining the combined density as the sum of effective densities. For computing stiffness matrices of laminate, the membrane stiffness matrices can be evaluated by defining the combined density as the sum of effective densities. However, due to the nonlinear material distribution along the stacking direction, the sum of effective densities cannot be used for the laminate's bending stiffness. Therefore, Eq.(5.1) compute laminate stiffness matrices accurately, as follows.

$$\begin{aligned} \mathbf{D}_m &= \mathbf{C}_{iso}^p \sum_{k=1}^{n_b} h_k \left( \check{\rho}_k^{eff} \right) \quad ; \quad \mathbf{D}_s = \mathbf{C}_{iso}^s \sum_{k=1}^{n_b} h_k \kappa \left( \check{\rho}_k^{eff} \right) ; \\ \mathbf{D}_b &= \mathbf{C}_{iso}^p \sum_{k=1}^{n_b} \frac{1}{3} \left[ h_{k+1}^3 - h_k^3 \right] \left( \check{\rho}_k^{eff} \right) \end{aligned} \quad (5.1)$$

At each design update, the stiffness of overlapping regions depends solely on the combined densities—the elasticity tensor  $\mathbf{C}_{iso}$  of the bar is a constant. Similarly, the component's sensitivities can be

computed as below:

$$\nabla_z \mathbf{D}^{(e)} = \begin{bmatrix} \nabla_z \mathbf{D}_m^{(e)} & \mathbf{0}_3 & \mathbf{0}_3 \\ \mathbf{0}_3 & \nabla_z \mathbf{D}_b^{(e)} & \mathbf{0}_3 \\ \mathbf{0}_2 & \mathbf{0}_2 & \nabla_z \mathbf{D}_s^{(e)} \end{bmatrix} \quad \text{where,}$$

$$\nabla_z \mathbf{D}_m^{(e)} = \mathbf{C}_{\text{iso}}^p \sum_{k=1}^{n_b} t_k \nabla_z \check{\rho}_k^{\text{eff}},$$

$$\nabla_z \mathbf{D}_b^{(e)} = \mathbf{C}_{\text{iso}}^p \sum_{k=1}^{n_b} \frac{1}{3} [h_{k+1}^3 - h_k^3] \nabla_z \check{\rho}_k^{\text{eff}}$$

$$\nabla_z \mathbf{D}_s^{(e)} = \mathbf{C}_{\text{iso}}^s \sum_{k=1}^{n_b} t_k \nabla_z \check{\rho}_k^{\text{eff}}$$
(5.2)

where  $\mathbf{0}_n$  and  $\mathbf{0}_{m \times n}$  is a  $n \times n$  and  $m \times n$  zero matrix, respectively, and  $t_k = h_{k+1} - h_k$ ,  $\kappa = 5/6$ , and  $\mathbf{C}_{\text{iso}}^p$  and  $\mathbf{C}_{\text{iso}}^s$  are constitutive matrices for the  $k^{\text{th}}$  layer.

When examining the overlapping region  $\omega_e$  where the overlapping component densities are equal to one, denoted as  $\rho_{b\omega_e} = 1$ , it is essential to note that the derivatives of these component densities with respect to design variables must be zero. This is because the derivative of the Heaviside function of projected densities (5.7) is zero.

$$\nabla_{z_i} \check{\rho}_{b\omega_e}^{\text{eff}}(\mathbf{x}; \mathbf{z}_b) := \nabla_{z_i} (\alpha_b \rho_{b\omega_e}(\mathbf{x}; \mathbf{z}_b))^q = 0, \quad \mathbf{z}_i := (\mathbf{x}_{1b}, \mathbf{x}_{2b}, r_b)$$

$$\nabla_{z_\alpha} \check{\rho}_{b\omega_e}^{\text{eff}}(\mathbf{x}; \mathbf{z}_b) = q.$$
(5.3)

As the membership variable approaches 1,  $\nabla_{z_\alpha} \check{\rho}_{b\omega_e}^{\text{eff}}(\mathbf{x}; \mathbf{z}_b) = q$  reaches a fixed constant value. Later in the optimization stages, it can be deduced that the sensitivity of stiffness (5.2) becomes zero and a fixed constant, for  $\mathbf{z}_i := (\mathbf{x}_{1b}, \mathbf{x}_{2b}, r_b)$  and  $\alpha$ , respectively. For these conditions, the design update becomes less sensitive to changes in the design variables as  $\nabla_z \mathbf{D}^{(e)}$  becomes inactive, and the design gradually locks into an optimized configuration.

Similarly to isotropic formulation, the GP optimizer seeks to achieve the design sensitivities (Eq. (5.5)) to be inactive with respect to design update. Different from isotropic material<sup>125</sup>, simply defining overlaps when designing for materials with directional stiffness, the elasticity tensor has a design dependency on the bar's endpoint ( $\mathbf{z}_i := (\mathbf{x}_{1b}, \mathbf{x}_{2b})$ ), which makes the formulation highly sensitive to design update in the regions of overlapping FRBs

<sup>125</sup> Norato *et al.*, "A geometry projection method for continuum-based topology optimization with discrete elements," 2015.

results in Eq. (5.4).

$$\begin{aligned}\nabla_z \mathbf{D}_m^{(e)} &= \sum_{k=1}^{n_b} t_k \nabla_z (\check{\rho}_k^{eff} \mathbf{C}_{ani k}^P), \\ \nabla_z \mathbf{D}_b^{(e)} &= \sum_{k=1}^{n_b} \frac{1}{3} [h_{k+1}^3 - h_k^3] \nabla_z (\check{\rho}_k^{eff} \mathbf{C}_{ani k}^P) \\ \nabla_z \mathbf{D}_s^{(e)} &= \sum_{k=1}^{n_b} t_k \nabla_z (\check{\rho}_k^{eff} \mathbf{C}_{ani k}^S)\end{aligned}\quad (5.4)$$

where  $\mathbf{C}_{ani}^P$  and  $\mathbf{C}_{ani}^S$  are constitutive matrices for the  $k^{th}$  layer, and equivalent to elasticity tensor of FRB, i.e.,  $\mathbf{C}_b$ .

$$\nabla_z (\check{\rho}_k^{eff} \mathbf{C}_{ani k}) = \nabla_z \check{\rho}_k^{eff} (\mathbf{C}_k - \mathbf{C}^v) + \check{\rho}_k^{eff} (\nabla_z \mathbf{C}_k) \quad (5.5)$$

Additionally, in the compliance problem described by equation (4.22), the design sensitivities outlined in equation (5.6) are significantly influenced by the displacement field.

$$\nabla_z c = - \sum_e \mathbf{u}^\top \left( \nabla_z \mathbf{K}^{(e)} \right) \mathbf{u} \quad (5.6)$$

Unlike the density-based method, where design variables are nodes or elements of the FE mesh, the GP design update is based on each component's design variables. Therefore, updating each component requires the displacement fields obtained from FEA to be evaluated for the corresponding bar's projected densities and directional stiffness and, finally, to update them iteratively. As a result, it is vital to examine how design updates are influenced in overlapping and non-overlapping regions. In the non-overlapping areas, the displacement fields are computed for the elasticity tensor of the FRBs, thus only considering the corresponding effective densities and direction stiffness of the bar being updated. However, the elemental stiffness of overlapping areas,  $\omega_e$ , is homogenized using first-shear deformation theory. Using this, the displacement fields at the reference plane of the laminate are computed. As a result, reference displacement fields—evaluated elemental-wise instead of component-wise—are utilized to update each component, which doesn't map to each FRB in the stack, thereby ignoring the corresponding component's effective density and elasticity tensor. Consequently, for significant variations in the stacking effective densities, the dominant component in the overlaps, whose effective density is more significant than others, primarily influences displacement fields, resulting in the achieved design with

small features, features with intermediate membership variables, or excessive overlaps that may not be optimal for manufacturing.

These speculations are demonstrated by performing optimization of several examples as depicted in Fig.(5.4) and discussed in the Appendix A.1.

## 5.2 Definition of length constraint formulation

The high-level geometric-based design in the GP formulation is represented by density mapping on a fixed grid  $\mathcal{D}$ . The projected bar density is calculated as follows.

$$\rho_b(\mathbf{x}; \mathbf{z}_b) := \frac{|B_{\mathbf{x}}^r \cap \Omega_b(\mathbf{z}_b)|}{|B_{\mathbf{x}}^r|}. \quad (5.7)$$

As discussed in the Section 3.2.1 of Chapter 3, the component's effective penalized density can be defined as,

$$\tilde{\rho}_b^{\text{eff}}(\mathbf{x}; \mathbf{z}_b) := (\alpha_b \rho_b(\mathbf{x}; \mathbf{z}_b))^q, \quad (5.8)$$

where  $\alpha_b$  represents the membership variable of a bar, the process of the geometry projection method involves assigning a membership variable, denoted as  $\alpha_b \in [0, 1]$ , to each component. A value of  $\alpha_b = 1$  means that the geometric component must be included in the structure, whereas  $\alpha_b = 0$  implies that the component must be removed from the design. This feature makes it easier for the optimizer to modify the topology by removing geometric components.

A method to introduce geometric constraints to optimize designs that are more feasible to manufacture is to formulate an exclusive constraint in the geometry projection optimization process, for example, the minimum angle between bars. This particular constraint considers both the angle between the members and their proximity. As a result, it can be utilized to restrict the angle between the nearby members and ensure a minimum distance between the parallel members<sup>165</sup>. Similarly, a direct length constraint on the components can be imposed and integrated into the optimization process, penalizing the objective function if the length of the components,  $\ell_b$ , is less than the threshold, i.e.,  $\ell_b \leq \underline{\ell}_b$ . Generally, adding constraints heavily penalizes the performance measure for even small negative changes in the component's length, which influences the optimization process by, i.e., causing further non-convexity in the design space.

This section introduces a new method of integrating geometric constraints in the geometry projection approach. Instead of explicitly defining the constraint in the compliance problem definition

<sup>165</sup> Smith *et al.*, "Geometric constraints for the topology optimization of structures made of primitives," 2019.

(as shown in Eq. (4.22)), a geometric constraint can be intrinsically defined in the geometry projection formulation. This is similar to the membership variable, combined with the component projected density to enable the removal or reinsertion of the primitives in the computational design domain. Since the membership variable of a component is not determined by its geometric attributes, such as length, radius, and orientation. Therefore, we augment the component's effective projected density ( $\alpha_b \rho_b$ ) by assigning a weights factor, denoted as  $w_b \in [0, 1]$ , to each feature. Similarly to the definition of membership variable, the value of  $w_b = 1$  means that the geometric component must be included in the structure, whereas  $w_b = 0$  implies that the component must be removed from the design.

By assigning weight to the components, the component's effective projected density in the geometry projection method can be redefined as,

$$\rho_b^{eff}(\mathbf{x}; \mathbf{z}_b) := \rho_b(\mathbf{x}; \mathbf{z}_b) \alpha_b w_b(\ell_b(\mathbf{x})) \quad (5.9)$$

Therefore, the effective penalized density of the components, Eq. (5.7) can be written as,

$$\check{\rho}_b^{eff}(\mathbf{x}; \mathbf{z}_b) := (\rho_b(\mathbf{x}; \mathbf{z}_b) \alpha_b w_b(\ell_b(\mathbf{x})))^q \quad (5.10)$$

The technique of weighting augmentation is used to enhance the components in a way that allows the geometry projection to ignore their projected density if the length of FRB is shorter than the predetermined threshold onto the computational domain. This is done regardless of the value of the membership variable. Therefore, it provides a way to avoid considering short features even if their membership value is one. This technique enhances the geometry projection methodology and helps design and optimize stiffer, more straightforward manufacturing structures. Using a length constraint ensures that a design can be effectively manufactured. The benefits of this approach to attain stiffer design are indirectly observed in various numerical examples presented in subsection Appendix A.1. It has been noted that the approach can help avoid suboptimal designs, which may arise due to small features in the design. Removing such features can address potential manufacturability issues while aiding the geometry projection optimizer in finding a more robust and stiffer design.

### 5.2.1 Definition of Smooth functions and their utility in structure optimization

Topology optimization formulations that rely on feature mapping techniques often use the Heaviside function to represent struc-

tural boundaries in the design domain. However, the Heaviside function is inherently non-smooth, making it difficult to solve the topology optimization problem directly. During the optimization process, discrete intermediate design variables are obtained from the calculation using the Heaviside function, which cannot be used with existing gradient-based optimizer methods such as Sequential Linear Programming (SLP), Optimality Criteria (OC) method, or the method of moving asymptotes (MMA). It is necessary to smooth the Heaviside function to enable the use of gradient-based optimizers in the design problem.

Specifically, the geometry projection method uses a smooth piecewise function to define the component's boundary to approximate the Heaviside function as discussed in the Chapter 3. Thereby, the component boundaries in the computational domain can be identified as,

$$\rho_b(\mathbf{x}; \mathbf{z}_b) := \tilde{H} \left( \frac{\phi_b(\mathbf{x}; \mathbf{z}_b)}{r} \right). \quad (5.11)$$

The expression for  $\tilde{H}$  is given as,

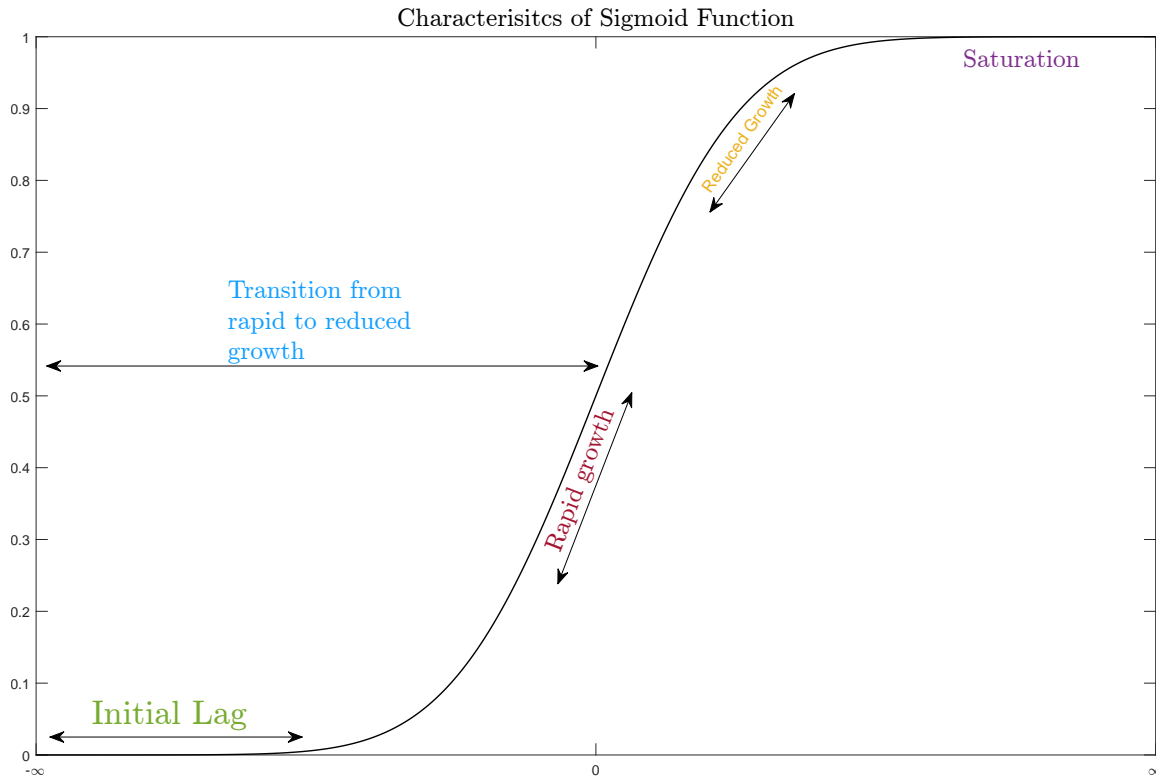
$$\tilde{H}(x) = \begin{cases} 0, & \text{if } x \leq -1 \\ 1 + \frac{1}{\pi} \left( x\sqrt{1-x^2} - \arccos x \right), & \text{if } |x| < 1 \\ 1, & \text{if } x \geq 1 \end{cases} \quad (5.12)$$

$$\frac{d\tilde{H}}{dx} = \begin{cases} 2\sqrt{1-x^2}/\pi, & \text{if } |x| < 1 \\ 0, & \text{otherwise} \end{cases}$$

The Heaviside function is a non-analytical smooth function whose value is 0 for negative and 1 for positive arguments.

The Sigmoid function is a continuous nonlinear activation function that can be used as an alternative to the Heaviside function. It is an analytical and smooth function with a one-to-one correspondence between two mathematical sets, making it a bijective function. The Sigmoid function can be loosely denoted as  $\mathcal{S} : \mathbb{R} \rightarrow [0, 1]$ . These functions are commonly used in topology optimization to identify the crisp boundary and penalized intermediate densities by transforming a continuous space value into a binary one.

**Figure 5.2:** Properties of a sigmoid function: Most functional forms share these characteristics—an initial lag with slow growth, rapid exponential growth, and reduced growth rate leading to saturation (adapted from [166]).



The optimization process mainly involves finding the best solution for feasible design spaces. However, the discrete nature of the problem can cause issues for gradient-based optimizers. Therefore, smooth functions can formulate a feasible design space by transforming the discrete feasible space with a smooth transition. This smooth transition zone can be helpful when satisfying multiple constraints and objective measures, as discrete constraints can cause gradient-based optimizers to oscillate. Instead of using hard bounds on the design space, smooth functions can introduce a smooth transition by computing smooth changes in the sensitivity analysis to drive the optimization problem. By doing this, smooth functions can capture the changes in the objective function and constraints more accurately and continuously. Optimization can then be more stable and effective, avoiding suboptimal solutions.

### 5.2.2 A weighting mechanism for components using the Sigmoid function.

The length constraint presented in this section can only be readily accommodated by techniques like the geometry projection method,

which has a high-level parametric representation of the structure available. This representation makes it possible to directly compute the length of the bars from the design variables. Although this is a simple concept, imposing a length constraint is notably impossible in density-based and level-set methods, where the geometric representation is such that the concept of a structural element's length is simply unavailable.

To define the length constraint in an optimization problem, one can set a minimum length for each bar as a constraint. However, this approach can lead to multiple constraints for all bars in the design, slowing the optimization process. A constraint can be applied to bars below the threshold instead of all bars to overcome this issue. A  $p$ -norm approximation can be used; however, for a value of  $p$  that is too large, the approximation becomes highly nonlinear, along with the hard bound on the feasible space. Therefore, using a smooth function, as discussed, is a reasonable and suitable choice for geometry projection.

The sigmoid function for the weighting mechanism is formulated using the error function as,

$$\mathcal{E} := \frac{1}{2} \left[ 1 + \operatorname{erf} \left( \frac{E\ell}{\sqrt{2}} \right) \right]; \quad (5.13)$$

The error function, often denoted by  $\operatorname{erf}$ , is a function defined as

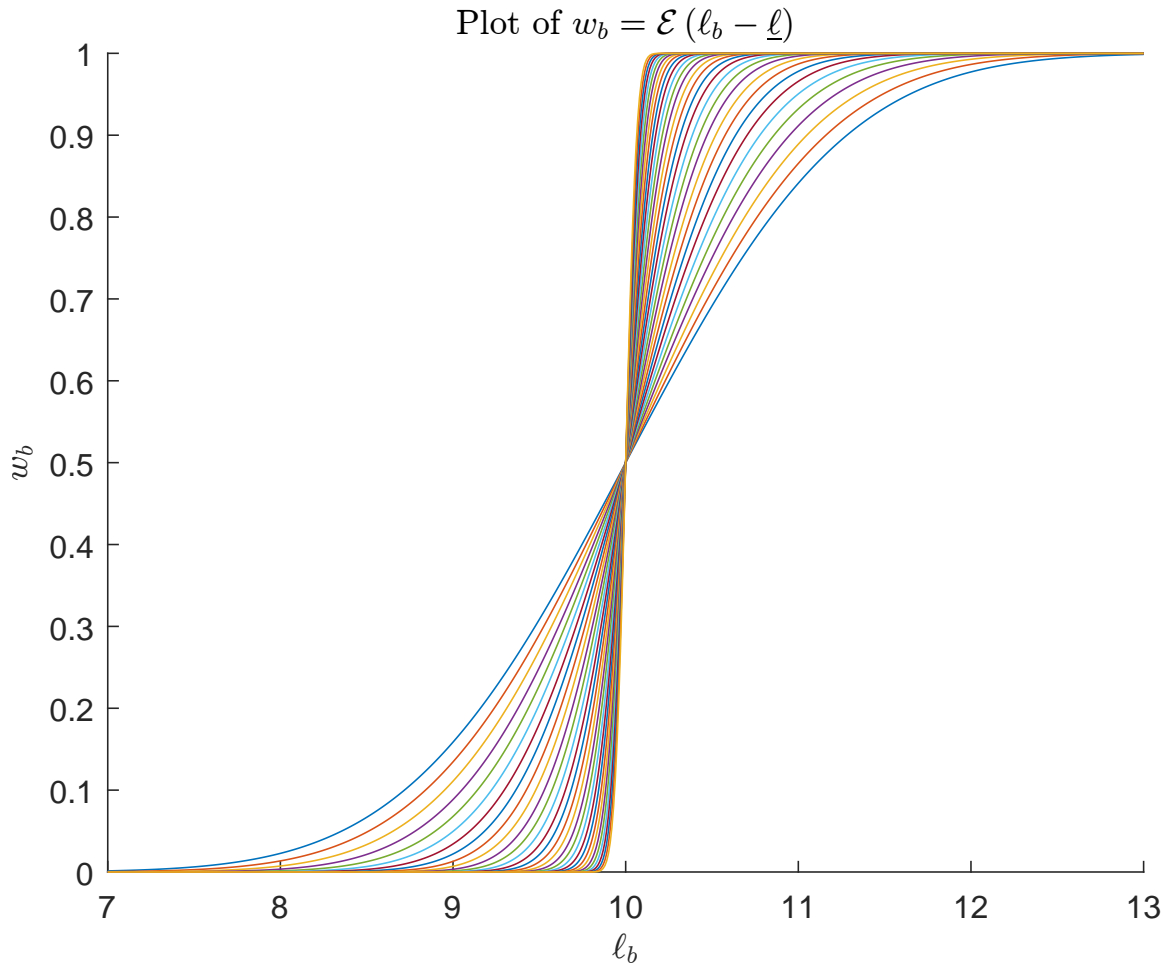
$$\begin{aligned} \operatorname{erf} z &= \frac{2}{\sqrt{\pi}} \int_0^z e^{-t^2} dt \\ \frac{d}{dz} \operatorname{erf} z &= \frac{2}{\sqrt{\pi}} e^{-z^2} \end{aligned} \quad (5.14)$$

Finally, the component's weight can be computed using the sigmoid-error function as,

$$w_b = \left[ \mathcal{E} (\ell_b - \underline{\ell}) \right] \quad (5.15)$$

Similarly, to the  $p$ -norm approximation that utilized  $p$  to find the extremum, in Eq. 5.13, the constant  $E = \exp(\eta)$  defines the steepness of the sigmoid curve, as indicated in Fig. 5.3, where  $\eta \in [0, 2]$ .

**Figure 5.3:** For  $\ell = 10$ —The plot shows how the steepness of the sigmoid function is increased using a continuation approach to achieve a discrete weight value.



Knowing that the compliance minimization problem is convex for  $q = 1$ <sup>167</sup> but better approximates solid–void solutions with values  $q \gg 1$  motivates the use of a continuation approach on the penalization parameter<sup>55</sup>. This consists of initially optimizing for  $q = 1$  (unique solution) and gradually increasing the penalization value during the optimization process to reduce the intermediate density values, thus driving the solution closer toward solid–void design. While this technique often converges to better designs, this cannot be guaranteed nor proven mathematically due to the multiple local minima for  $q > 1$ . Alternatively, a continuation scheme could be used on the filter radius instead, i.e., gradually decreasing the filter radius during optimization<sup>47</sup>. Therefore, instead of using a single constant, the range of  $E$  is chosen because of standard practices adopted in the topology optimization community of using a continuation approach. In this context, the idea

<sup>167</sup> Pettersson, “A finite element analysis of optimal variable thickness sheets,” 1999.

<sup>55</sup> Sigmund *et al.*, “Numerical instabilities in topology optimization: a survey on procedures dealing with checkerboards, mesh-dependencies and local minima,” 1998.

<sup>47</sup> Sigmund *et al.*, “Topology optimization approaches,” 2013.

of this continuation technique is to successfully scale the steepness of the sigmoid function through  $\eta$  during the optimization so that the weighting mechanisms gradually assign a discrete value to the bars.

### 5.3 Examples

For all four numerical examples—We consider bars made of carbon-fiber-reinforced polymer, and fiber orientation is aligned to the bar's axis and is continuous. Table (4.1) lists unidirectional carbon-epoxy AS4/3501-6 material properties used for the bars. More examples of in-plane loading conditions based on simple overlap formulation optimized for multi-layered VS-CFRP-Ls are discussed in Appendix A.

For all the examples in Fig. 5.4, the following settings are considered until mentioned otherwise. The method-of-moving-asymptotes (MMA)<sup>74</sup> is employed for the optimization routine, using the default parameters described in<sup>158</sup>, i.e.,  $a_0 = 1$  for the objective function, and  $a_i = 0, c_i = 1000$  and  $d_i = 1$  for every constraint  $i$  in the optimization. The void material is isotropic with Young's modulus  $E^{\text{void}} = 10^{-3}E_1$  and Poisson's ratio  $\nu^{\text{void}} = 0.3$ . During initialization, the radius of the bars is set to the average of their upper and lower bounds. The sizing variable is set to  $\alpha = 0.5$ , and the move limit is fixed to  $m = 0.02$  throughout the optimization process.

The optimization procedure involves three stopping criteria. The first criterion is met when the 2-norm of the change in the design variable vector is less than 0.002. The second criterion is reached when the norm of the Karush-Kuhn-Tucker optimality conditions falls below 0.001. The third criterion is satisfied when the change in the objective function is less than  $10^{-9}$ . The optimization process is stopped if any of these criteria are met.

#### 5.3.1 A rectangular plate under 3-point bending—MMB

The first example considered the MMB problem with an aspect ratio of 1 : 6; the volume fraction limit is set to 0.4. Since the problem is symmetrical, only the right side of the geometry has been modeled as depicted in Fig. 5.4. The whole plate has been initialized with 27 bars, and the design variables have been restricted within the following bounds.

$$\begin{Bmatrix} (0, 0) \\ 3 \\ 0 \end{Bmatrix} \leq \begin{Bmatrix} (\mathbf{x}_{b1}, \mathbf{x}_{b2}) \\ r_b \\ \alpha_b \end{Bmatrix} \leq \begin{Bmatrix} (300, 100) \\ 6 \\ 1 \end{Bmatrix} \quad (5.16)$$

<sup>74</sup> Svanberg, "The method of moving asymptotes—a new method for structural optimization," 1987.

<sup>158</sup> Svanberg, "MMA and GCMMA, versions September 2007," 2007.

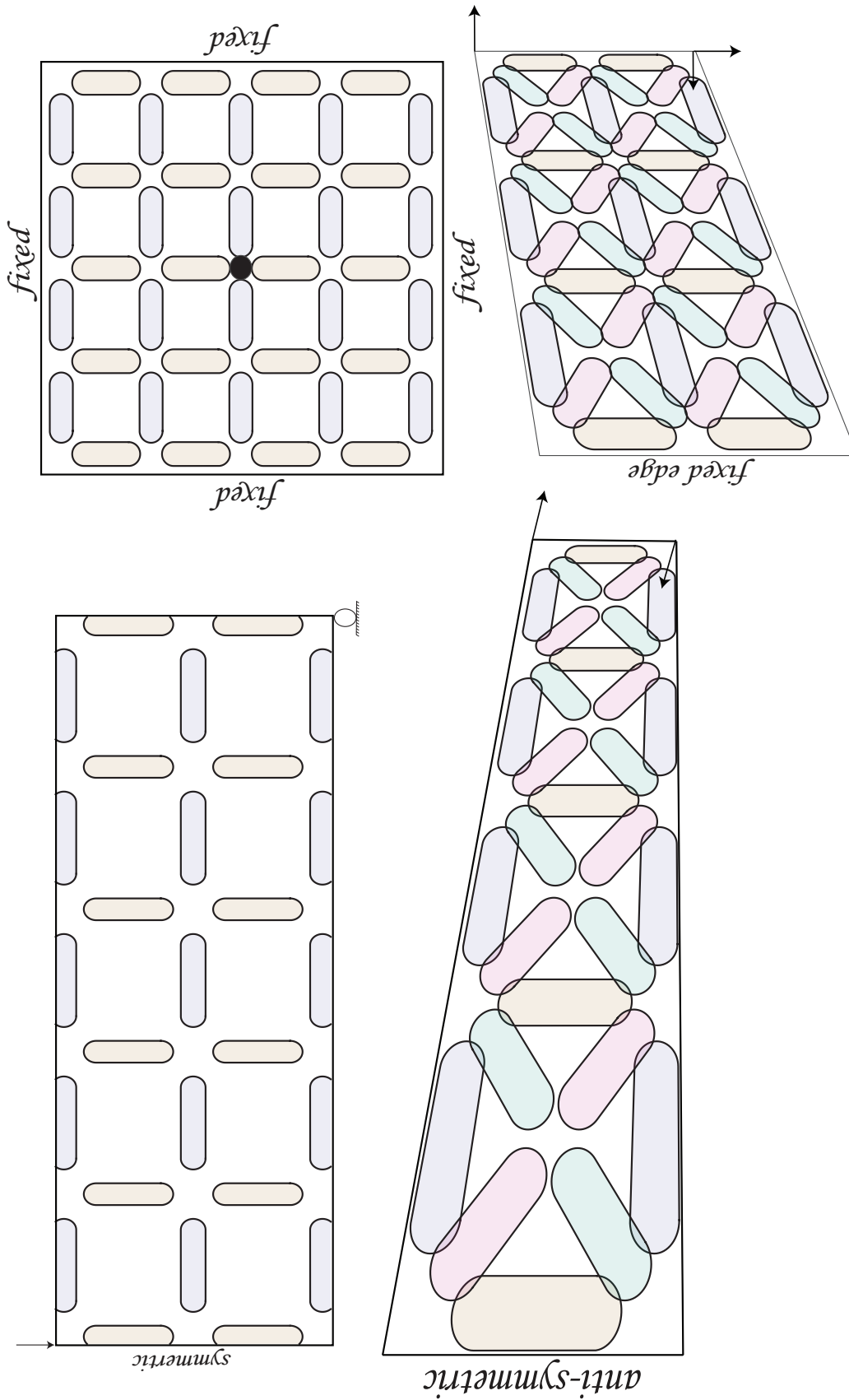


**Figure 5.4:** The features initial arrangement in rectangular plates of varying aspect ratios, which are subjected to different loading conditions, including 3-point bending  $1 \times 6$ , pure torsional  $1 \times 1$ ; and multi  $1 \times 2$ .

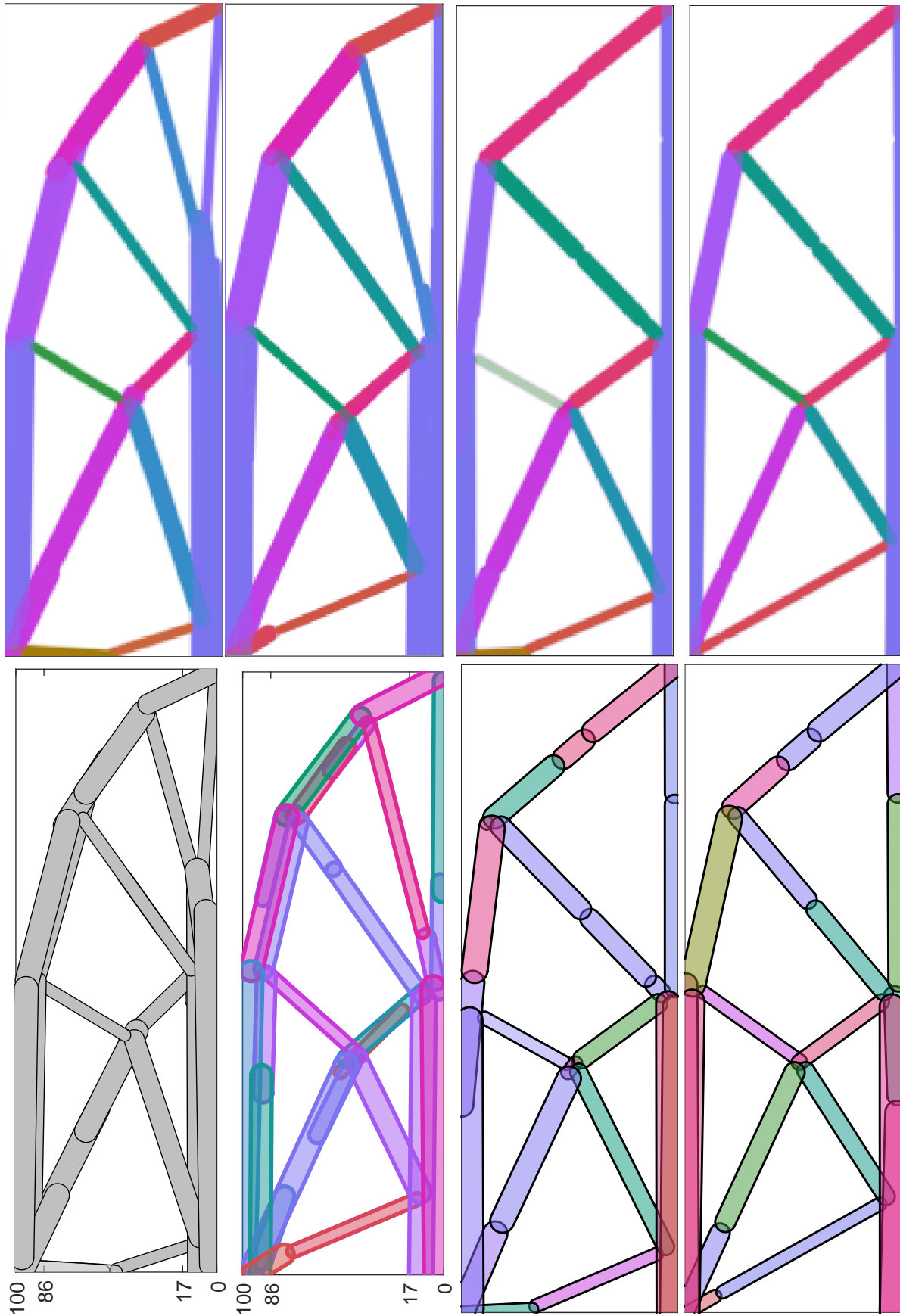
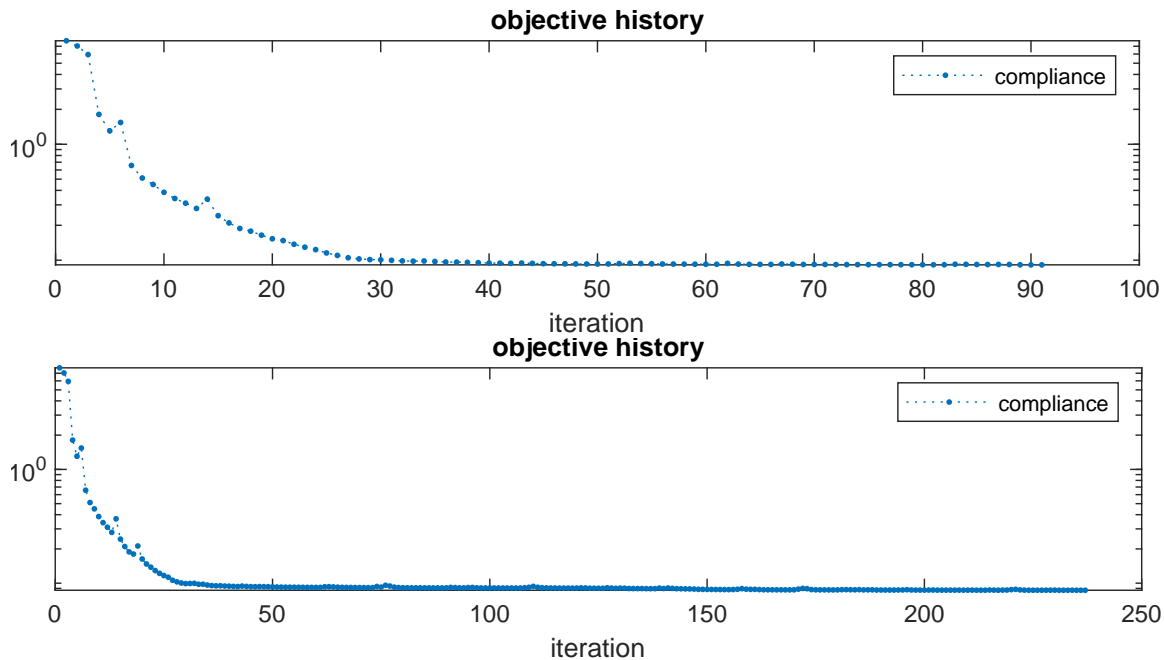


**Figure 5.5: MBB**—The design and density of all formulations used to optimize single-layer VS-CFRP-L are listed row-wise. Starting with GP, GP-AM with overlapping criterion, and LGP-AM without and with length constraint.

**Figure 5.6: MBB**—The objective history plot demonstrates that the optimization traces a typical smooth convergence behavior for compliance with a sharp drop in the first few iterations, followed by small design variable adjustments in the later optimization stage for with and without length constraint formulation.



The lower bound on the FRBs' length is set to  $\ell = 10$  for the LGP-AM method.

**Table 5.1: MBB**—The compliance value for all the geometry projection formulations developed to optimize VS-CFRP-L.

Methods	GP	GP-AM	LGP-AM	LGP-AM
Compliance	1.199431	1.138311	1.084029	1.028333

The design of MBB achieved through all the formulations discussed in Chapter 5 and Chapter 4 is illustrated in Fig. 5.5. When we compare the stiffness of different designs as presented in Tab. 5.1, the LGP-AM design is comparatively stiffer than the others. This suggests that simpler overlap formulations with or without length constraints lead to stiffer designs. This is because allowing components to overlap results in higher bending stiffness (overlapping FRBs on the top and bottom regions on the left side of the structure) than designs that restrict the overlapping area or avoid it altogether, such as the GP-AM and GP methods. It is worth noting that the LGP-AM approach exhibits more favorable characteristics when compared to its counterpart, the LGP-AM. One of the reasons for this is that the LGP-AM method employs a

length constraint, which enables a stiffer structure by eliminating small features that may cause the design to become locked into a sub-optimal solution, simultaneously ensuring that the VS-CFRP-Ls can be manufactured easily.

From a manufacturing perspective, the design of the GP can be used as a baseline to evaluate the ease of printability of the optimized design achieved through alternative methods. The GP technique pushes the optimizer to seek distinct components, resulting in a clearly defined fiber path in a layer without compromising the design's performance. This comparison is only valid for MBB examples or designs optimized for in-plane loading conditions, as further demonstrated in the Appendix A. For other examples, the GP method results in poor design in terms of manufacturability and performance, as already discussed in the Chapter 4. When evaluating the LGP-AM design, the only region of the overlapping FRBs is in the upper left region (where the load is applied), which experiences the highest bending stress, and in the bottom left region, where the normal stresses are tensile and of the FRBs assembly results in the discrete components that ensure printability of the VS-CFRP-L seamlessly.

The optimized design with LGP-AM ( $\ell = 0$ ) results in printable assembly of the components; however, the method results in the intermediate membership value for a single element that questions the reliability of gP-IAM methodology to optimize the design for complex loading conditions, as demonstrated in the subsequent examples. The component that attained intermediate membership value can be visualized in the density plot (Fig. 5.5) and tabulated in the Tab. 5.2

Finally, the plot of the objective history for the LGP-AM methods, shown in Fig. 5.6, follows a similar trend. This is because both methods allow for freely overlapping FRBs without restrictions, which differs from the GP-AM approach. The weighting mechanism is only active when the FRBs' length is below the minimum bar length ( $\ell_b \leq \ell$ ); otherwise,  $w_b = 1$ . However, a key difference is that LGP-AM ( $\ell > 0$ ) takes a considerably large number of iterations before convergence. The reason behind it can be deduced from the parameter that defines the steepness of the error function, i.e.,  $E = \exp(\eta)$ . The larger the value of  $E$ , the closer the approximation is to the binary weights. The approximation becomes highly nonlinear as  $E$  becomes prominent in the latter optimization stages due to a continuation process, which gradually increases the value of  $\eta$  from 0 to 3. This means that the approximations of this constraint made by gradient-based optimizers become highly sensitive to any slight change in the FRBs' length (close to the threshold value). Therefore, the optimization would take many

iterations to converge. Nevertheless, allowing length constraint results in better design in terms of stiffness and manufacturability.

**Table 5.2:** MBB—FRBs' length and membership values are tabulated—for LGP-AM methods—only for the bars that define the final topology as shown in Fig. 5.5. The minimum lengths of FRBs achieved by LGP-AM are bolded when the length's threshold value is set to  $\ell = 10$ .

$\ell_0$	$\alpha_0$	$\ell_{10}$	$\alpha_{10}$
60.8998	0.9995	83.4464	1.0
141.172	1.0000	91.7409	1.0
31.4035	0.9999	<b>14.0891</b>	1.0
90.2941	1.0000	37.0567	1.0
142.545	1.0000	69.0612	1.0
72.7031	1.0000	141.225	1.0
133.604	1.0000	76.3229	1.0
1.199431	1.0000	143.049	1.0
43.3232	0.9999	47.2478	1.0
05.1974	0.9999	45.6555	1.0
43.1690	0.7642	55.1339	0.9998
56.8873	1.0000	150.664	1.0
37.1845	1.0000	49.2090	1.0
84.7051	1.0000	82.0541	1.0
52.9917	1.0000	50.2496	1.0
65.9778	1.0000	78.1616	1.0
58.9169	1.0000	58.6222	1.0
36.1575	1.0000	27.7991	1.0
12.6213	1.0000	<b>13.5528</b>	1.0
47.4761	1.0000	46.3714	1.0

### 5.3.2 A square plate under point bending load

We present results for analyzing a clamped square plate under point loading, i.e.,  $q \equiv 1$ , which is uniformly distributed over a circular region of radius,  $r = 4$ , and the center is at the point of application as depicted in Fig 5.4. The design region has dimensions  $150 \times 150 \times 2$ . Although the problem definition has two planes of symmetry, the symmetry conditions are not considered because these boundary conditions limit the overlapping regions of the design space. Thus, for comparison, the entire plate is analyzed. The whole plate is initialized with 48 bars, and the bounds imposed on the design variables are as follows:

$$\begin{Bmatrix} (0, 0) \\ 3 \\ 0 \end{Bmatrix} \leq \begin{Bmatrix} (\mathbf{x}_{b1}, \mathbf{x}_{b2}) \\ r_b \\ \alpha_b \end{Bmatrix} \leq \begin{Bmatrix} (150, 150) \\ 6 \\ 1 \end{Bmatrix} \quad (5.17)$$

As discussed in the Chapter 4, a density-based topology optimization framework demonstrates that the optimized topology comprises four arms interconnected to a central region where the fibers are arranged in a circular pattern and have an edge over feature-based methods in achieving fiber arrangements with a strong curvature, thus enriches the topology space. The figures shown below, Fig. 5.7 and Fig. 5.8, depict the GP and GP-IAM designs, respectively. By comparing these designs with the one shown in Fig. reffig:bending-designs-0.5, it can be seen that the geometry projection method, by default, restricts topology space. Moreover, allocating the topology space with overlapping bars results in a suboptimal solution—one major limitation of the simple overlap formulation that cannot be avoided. In the following chapter, a layer-wise formulation is introduced in the geometry projection, which allows for the simultaneous optimization of each layer’s topology, material, and stacking sequence in the composite laminate. This leads to discrete fiber paths within each layer and overlapping bars through the adjacent layer to optimize intersection load paths, overcoming the limitations of LGP-AM and GP. This approach, named GP-MUL2, introduces a unified framework for achieving a more comprehensive and effective optimization of multi-layered VS-CFRP-Ls (MUL-VS-CRPF-Ls).

**Table 5.3: Bending**—The compliance value for different length constraint

	$\underline{\ell}_b = 0$	$\underline{\ell}_b = 5$	$\underline{\ell}_b = 10$	$\underline{\ell}_b = 15$
Compliance	0.212375	0.219199	0.234320	0.242954

Knowing the limitation of the geometry projection method, we investigated the LGP-AM method for various minimum length constraints that were imposed on the FRBs for values of  $\underline{\ell}_b$  ranging from 0 to 15 in increments of 5. The compliance value obtained for the VS-CFRP-L, as depicted in Fig. 5.11, has been tabulated in Tab. 5.3. All the designs have a similar range of stiffness, and the arrangement of FRBs forms a "plus" symbol for any value of  $\underline{\ell}_b$ . It can be concluded that all cases always result in a similar topology regardless of the initial condition. This means that even if the number of bars increases or decreases, the simple overlap formulation will always produce a suboptimal design. This is because, during the early stages of optimization, the penalized effective densities of FRBs (Eq. (5.10)) are significantly low; thus, the resulting stiffness causes the optimizer to drive more FRBs towards the concentrated load and gradually lock design as the membership value grew over iteration. The excessive overlapping can be avoided in the GP formulation (as in Fig 5.7), but it cannot

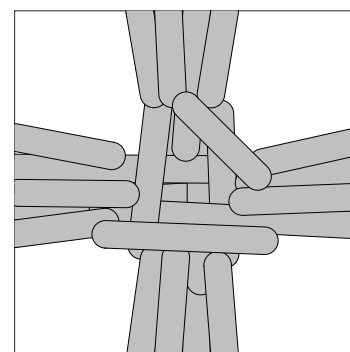


**Figure 5.7: Bending**—The optimized design using GP formulation for bending example

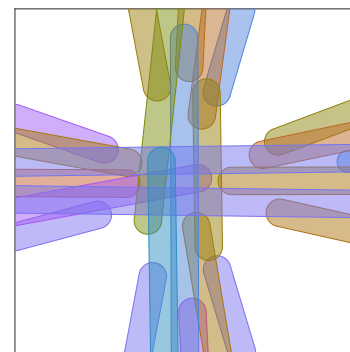
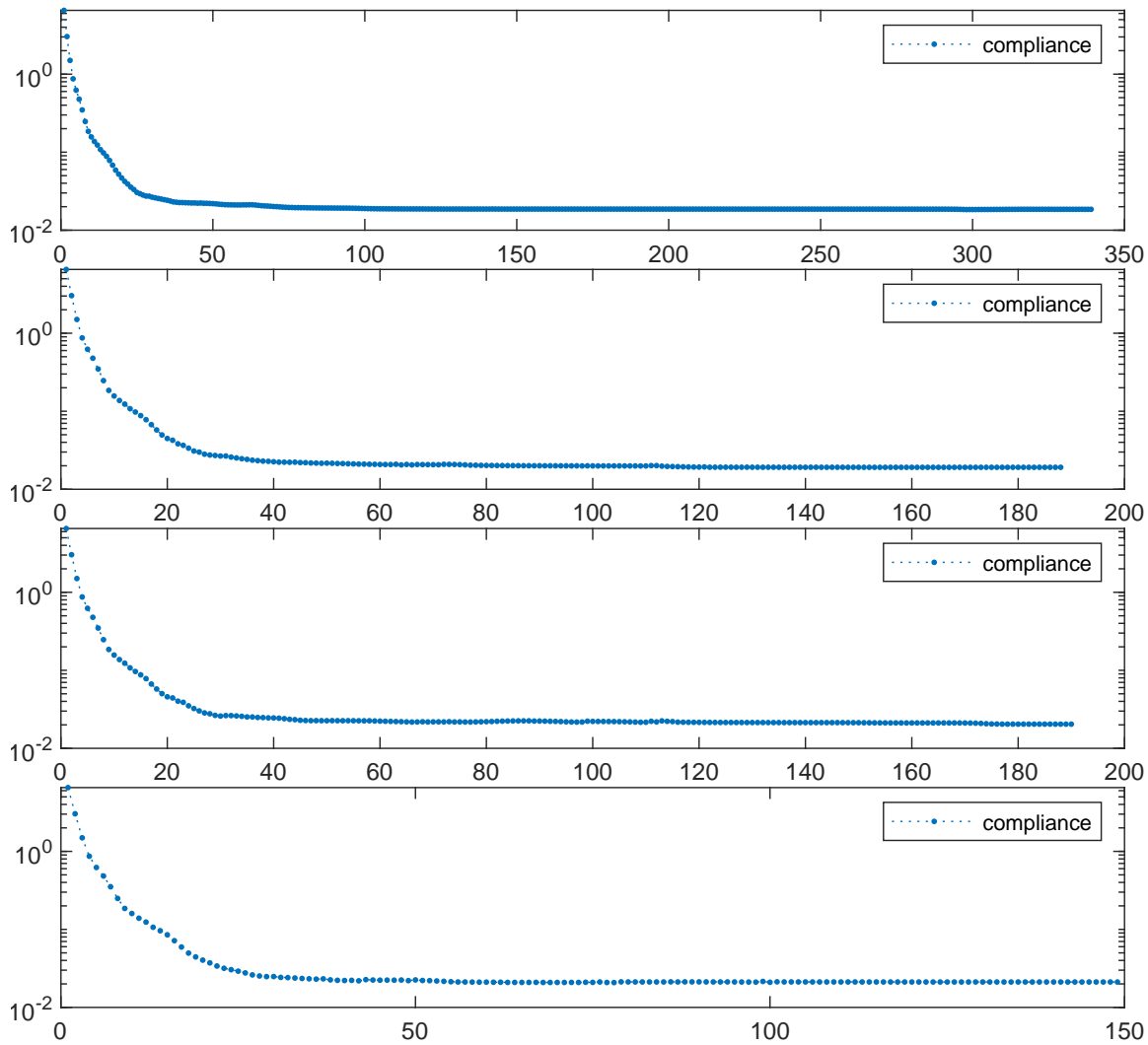


**Figure 5.8: Bending**—The optimized design using GP-IAM formulation for bending example

be designed for intersecting load paths, for example, plate under pure torsion.

**Figure 5.9: Bending**—The objective history plot depicts that LGP-AM ( $\ell = 0$ ) takes more iterations compared to LGP-AM( $\ell > 0$ ) formulation. This is because small features get stuck in the overlapping bars listed in Table 5.4. Moreover, LGP-AM( $\ell > 0$ ) takes a similar number of iterations to converge, irrespective of the imposed threshold length,  $\ell$ , on FRBs. This indicates that small features cause manufacturing issues and lead to optimizer oscillation. The plot is arranged in increasing order of  $\ell$ .



When comparing the compliance achieved by the simple overlap method with or without length constraint to the GP and GP-AM methods, it was observed that the simple overlap method increases stiffness by approximately 85.7%. This is because the constant thickness of the FRBs, when stacked, increases the bending stiffness of the VS-CFRP-L, leading to lower compliance. Consequently, the

LGP-AM ( $\ell > 0$ ) method results in the lowest compliance because the small features are locked near the application of point load.

Several non-manufacturable components are tightly locked beneath the long vertical FRBs in the given scenario. The optimizer can't remove these components because the long vertical feature is dominant and effectively subdues the displacement field generated by the FE analysis. The optimization is limited to single-layer analysis, which means that the component densities in the overlapping regions are driven by the displacement field obtained for the homogenized structure's stiffness in the reference plane. However, updating all the components in the overlapping region using the reference displacement doesn't accurately update each feature in the design. Obtaining a displacement field for each component is crucial because updating schemes, particularly in geometry projection, are carried out for each geometric variable, i.e., for high-level parametric design space. Therefore, the overlapping region of the components is tightly locked, and the resulting displacement field subdues any attempt by the optimizer to adjust or remove it.

The figures of a plate's design and density plot under predetermined conditions are displayed in Fig. 5.10 and 5.11 respectively. The design produced by the LGP-AM ( $\ell = 0$ ) method contained non-manufacturable features, which were eliminated by the LGP-AM method by setting a lower bound on the minimum length of the FRBs ( $\ell_b = 5$ ). Gradually increasing this threshold limit resulted in a more distinct design by removing features and reducing overlaps of FRBs, which slightly increased compliance. However, all of the designs were suboptimal due to the limited topology space of the feature-mapping-based topology optimization framework. The purpose of this example was to demonstrate the effectiveness of the LGP-AM formulation, which can impose distinct bounds on the minimum length of the FRBs. The method efficiently removes any features that fall below the threshold value as detailed in Tab. 5.4, resulting in discernable overlapping components and a manufacturing design with minimal post-processing steps.

### 5.3.3 A rectangular plate under pure torsion

In the third example, we consider a rectangular plate with dimensions of  $400 \times 100 \times 2$ , subjected to pure torsion. The plate is shown in Fig. 5.4. Thanks to anti-symmetry conditions, we performed an FE analysis on half of the plate, which was discretized using  $200 \times 50$  plate elements. The initial design comprised of 29 bars,

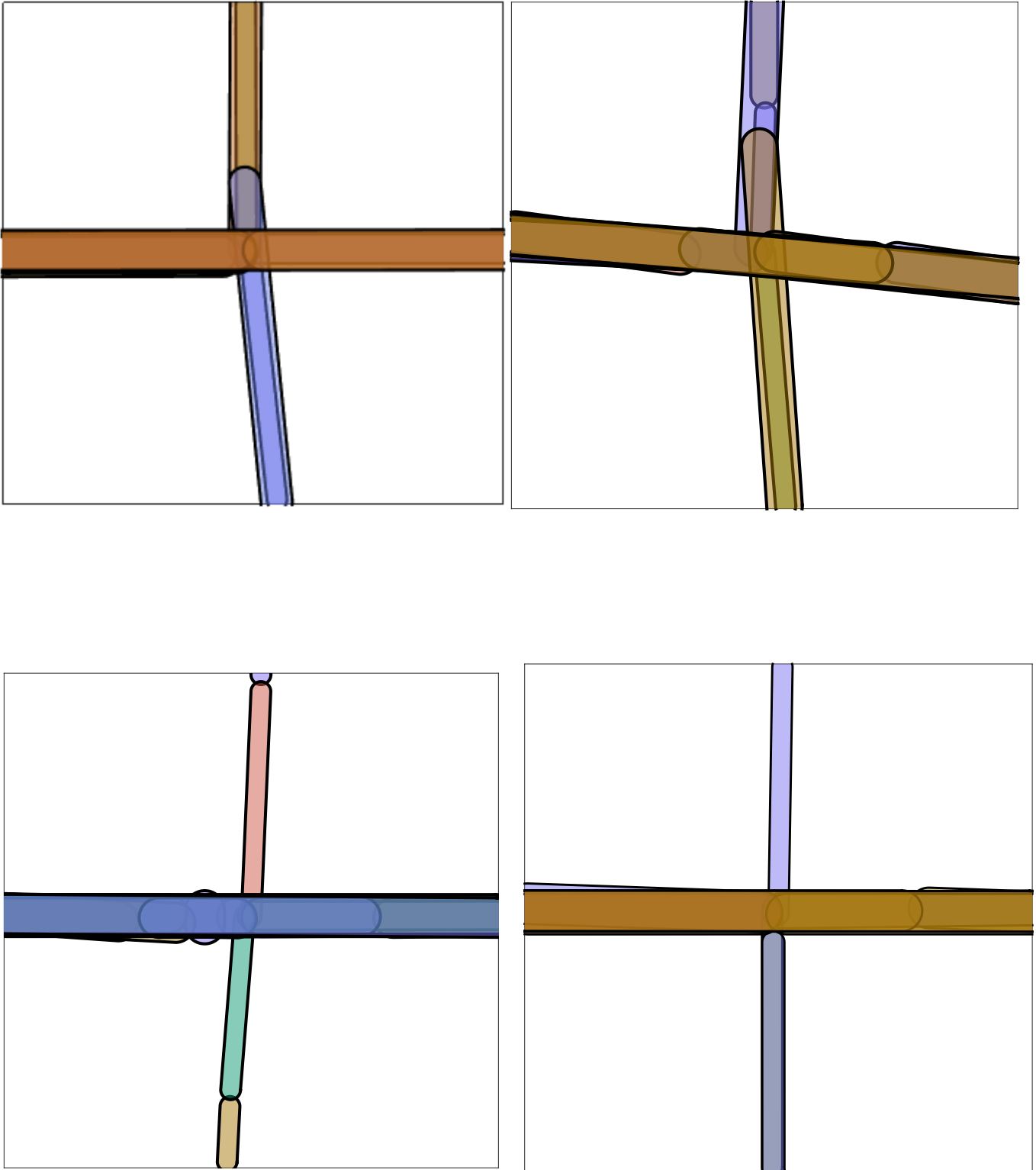


**Figure 5.10: Bending**—The components are imposed with various minimum length constraints, ranging from 0 to 15 with 5 unit increments—design plotted column-wise.

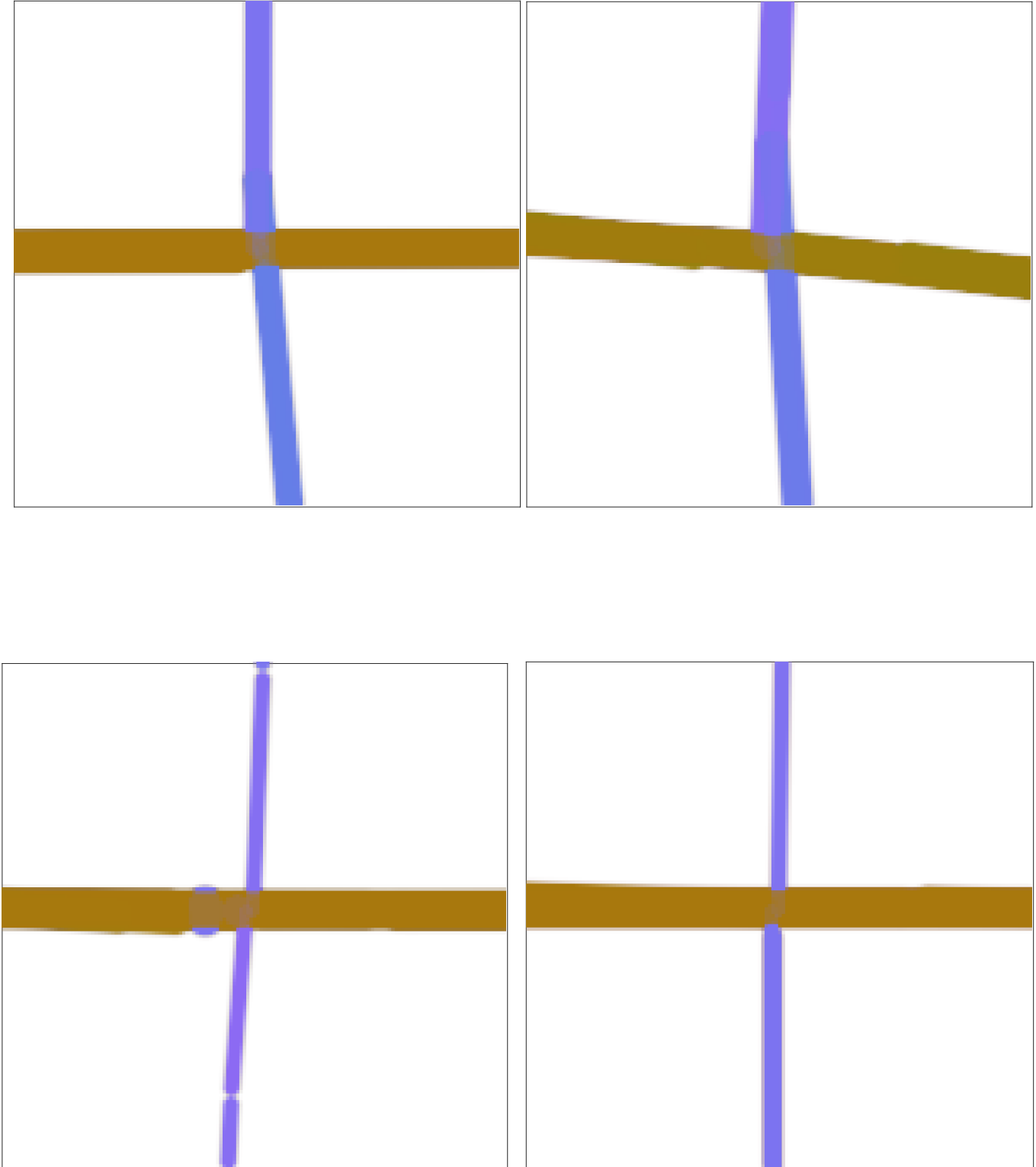


**Figure 5.11: Bending**—The components are imposed with various minimum length constraints, ranging from 0 to 15 with 5 unit increments—density plotted column-wise.

**Table 5.4: Bending**—The lengths, membership variable, and their corresponding weight for FRBs achieved by LgP-IAM when the length's threshold value is set to  $\ell = \{0, 5, 10, 15\}$  are shown. For gP-IAM, a special case of LgP-IAM ( $\ell = 0$ ) results in non-manufacturable design features. Implementing threshold value,  $\ell > 0$  still results in the membership variable acquiring intermediate values; however, the corresponding weights attain a discrete value based on the bar's length in the design. Tabulated data indicates that the design does not retain intermediate membership value by augmenting the geometry projection method with a weighting mechanism because their corresponding weights always attained discrete values.

$\underline{\ell}_b = 0$	$\alpha_{gP-IAM}$	$\underline{\ell}_b = 5$	$\alpha_{LgP-IAM}$	$w_{LgP-IAM}$	$\underline{\ell}_b = 10$	$\alpha_{gP-IAM}$	$w_{LgP-IAM}$	$\underline{\ell}_b = 15$	$\alpha_{gP-IAM}$	$w_{LgP-IAM}$
16.7386	0.9997	2.3525	0.8649	0	6.7827	0.8434	0	10.9598	0.7586	0
52.5412	0.9999	67.2753	0.9999	1.0000	96.0195	1.0000	1	106.7646	1.0000	1
0.0002	0.0021	0.8269	0.9800	0	4.1830	0.7376	0	12.8847	0.6686	0
61.2074	1.0000	74.9060	0.9999	1.0000	75.1040	0.9998	1	75.3914	0.9999	1
0.0029	0.0002	1.9231	0.4829	0	7.7977	0.5020	0	10.9367	0.5155	0
149.0244	1.0000	148.9791	1.0000	1.0000	148.9711	1.0000	1	149.9838	1.0000	1
31.3894	0.9999	29.9178	1.0000	1.0000	5.8260	0.6604	0	9.7136	0.6758	0
148.6742	1.0000	148.7396	1.0000	1.0000	148.8155	1.0000	1	106.8551	1.0000	1
70.0457	1.0000	110.9313	1.0000	1.0000	69.3150	1.0000	1	69.4629	1.0000	1
<b>0.3886</b>	<b>0.9999</b>	4.7470	0.9801	0.0000	72.6851	1.0000	1	41.4837	0.9999	1
51.4982	1.0000	69.4304	1.0000	1.0000	65.2506	1.0000	1	12.1357	0.9824	0
4.1335	0.9999	2.7469	0.9804	0	6.8767	0.9577	0	14.3450	0.9800	0
33.9501	0.9999	2.1200	0.9800	0	5.0160	0.6453	0	10.6720	0.6784	0
71.4982	1.0000	72.0348	1.0000	1.0000	71.3824	1.0000	1	72.2378	1.0000	1
74.1859	1.0000	73.9419	1.0000	1.0000	73.6861	1.0000	1	94.0610	1.0000	1
69.3244	1.0000	69.3117	1.0000	1.0000	69.1869	1.0000	1	69.2419	1.0000	1
68.4778	0.9998	73.0940	0.9998	1.0000	73.0593	0.9999	1	72.4956	1.0000	1
48.8264	0.9999	68.9874	1.0000	1.0000	63.1639	1.0000	1	49.1779	1.0000	1
<b>0.3704</b>	<b>0.9926</b>	1.3685	0.9800	0	9.0259	0.9801	0	12.0349	0.9800	0
0.0014	0.0021	0.6888	0.9800	0	8.3754	0.9800	0	26.6259	0.9999	1
0.2328	0.0002	1.7355	0.4378	0	8.8238	0.4484	0	11.8575	0.4780	0

and we imposed the following bounds on the design variables:

$$\begin{Bmatrix} (0, 0) \\ 3 \\ 0 \end{Bmatrix} \leq \begin{Bmatrix} (\mathbf{x}_{b1}, \mathbf{x}_{b2}) \\ r_b \\ \alpha_b \end{Bmatrix} \leq \begin{Bmatrix} (200, 50) \\ 6 \\ 1 \end{Bmatrix} \quad (5.18)$$

The problem has been solved for two volume fraction limits,  $\bar{v} = \{0.5, 0.6\}$ , each with corresponding lower bounds on the FRBs' length set to  $\ell = \{0, 5, 10\}$ .

**Table 5.5: Torsion**—The compliance values for two different volume fraction limits are indicated for comparison among formulations.

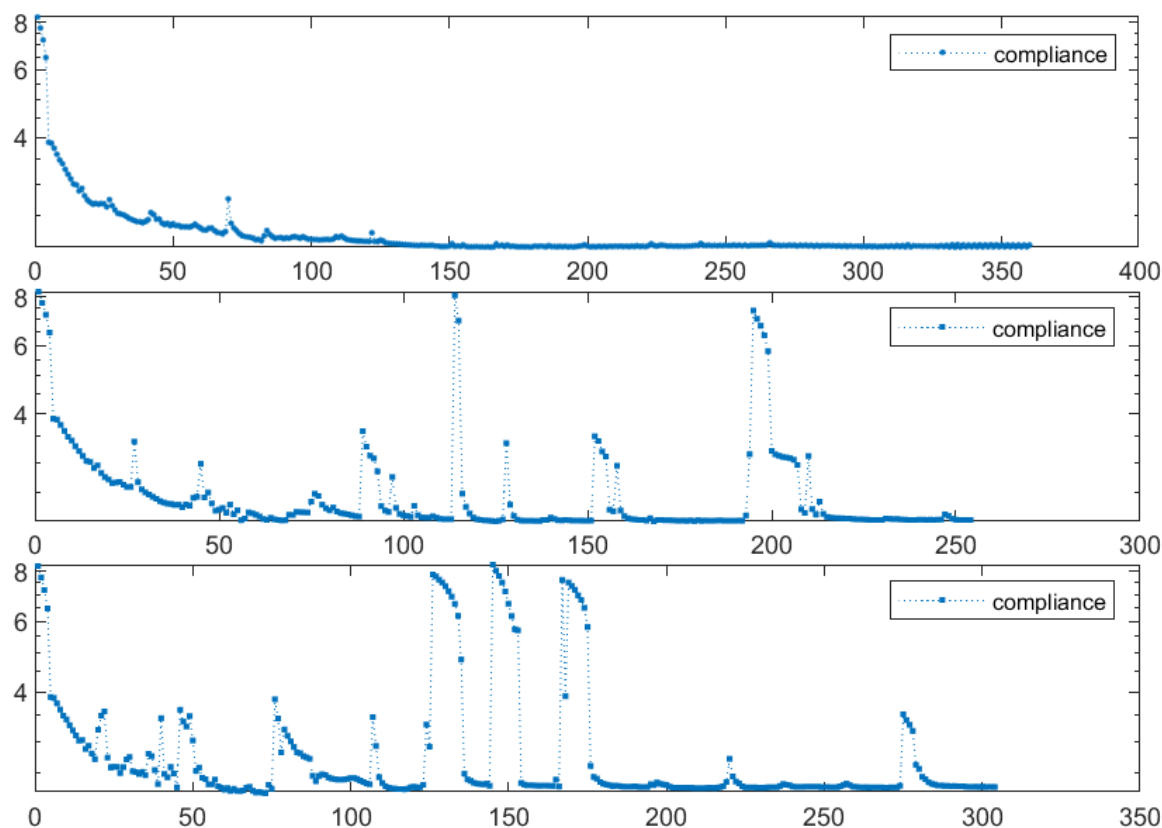
	GP	GP-1AM	$\underline{\ell}_b = 0$	$\underline{\ell}_b = 5$	$\underline{\ell}_b = 10$
$\bar{v} = 0.5$	184.893393	141.048719	80.634837	84.258939	103.316065
$\bar{v} = 0.6$	135.665506	112.607709	91.586009	93.730293	83.373807

In Chapter 4, it was shown that the arrangement of components in a crossover pattern at angles of  $45^\circ$  and  $135^\circ$  should be the dominant feature in the computational design domain. However, the GP-AM method produced a design requiring multiple post-processing steps to replicate the design ready for manufacturing, including overlapping FRBs and a moderate free-form component arrangement. This is necessary to accurately capture the essence of the design and ensure that it can be replicated even in the manufactured VS-CFRP-Ls. Therefore, the simple overlap with length formulation was derived from overcoming these challenges and pursuing our goal to design and optimize additively manufacturable VS-CFRP-Ls, which is demonstrated through designs plotted in Fig. 5.14, 5.15.

Fig. 5.14 presents the design and density plots for a volume fraction constraint of 0.5 considering several length thresholds of  $\underline{\ell} = \{0, 5, 10\}$ . When  $\underline{\ell} = 0$ , the design has small features and overlapping FRBs that make manufacturing challenging. These non-manufacturable features also contribute to the stiffness of the VS-CFRP-L, which can be overestimated and unachievable in some cases. For example, overlapping FRBs near the boundary conditions require an approximate representation of the fiber deposition in a layer to achieve the same stiffness as the overlapping FRBs. When  $\underline{\ell} = 5$ , the design improves significantly by removing all small features. This frees up the design space for a better solution, such as introducing easy-to-print features. However, the overlapping features present in the design near the boundary condition may cause difficulty in printing and replicating the optimized VS-CFRP-Ls. It is worth noting that the design plot

shows several small features not present in the corresponding density plot. These are included deliberately to demonstrate that components with lengths below the threshold value are not considered in the design, regardless of their membership variable value. This can be understood from the previous example wherein a table (Tab. 5.4) is populated comprising the length, corresponding membership variable, and weight of components.

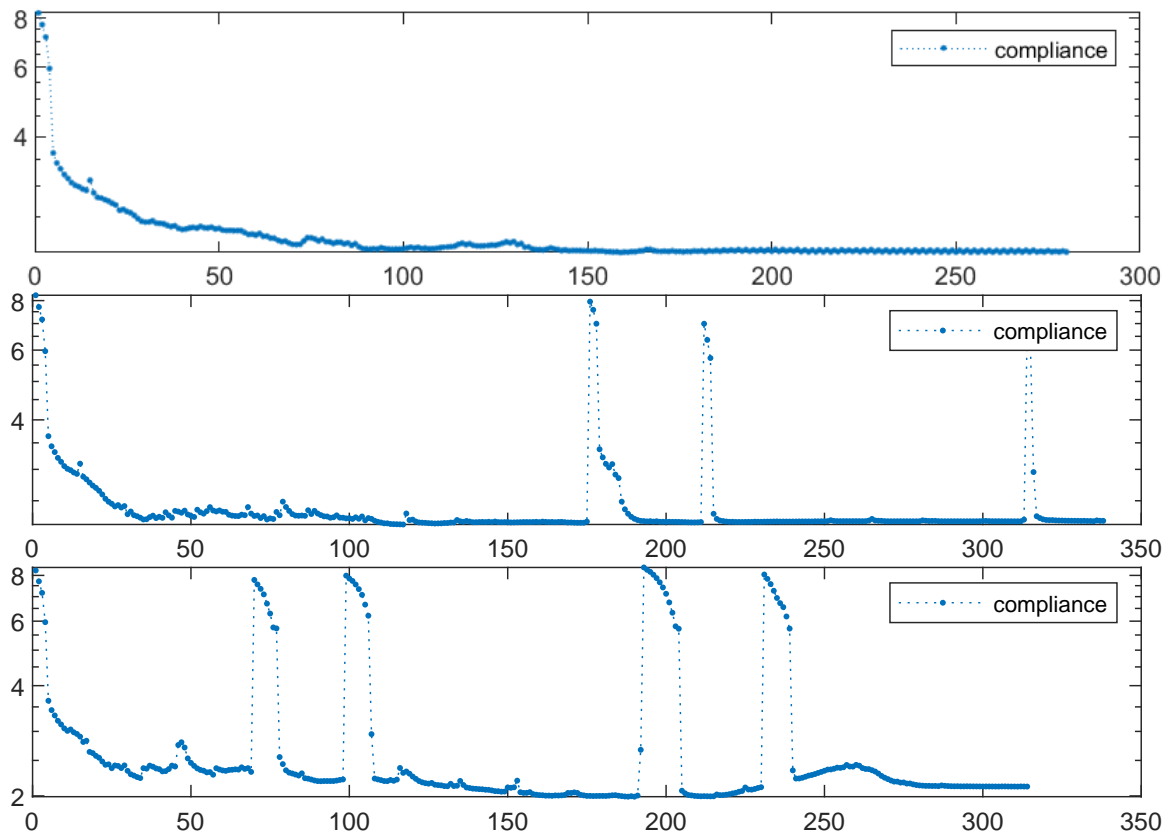
**Figure 5.12: Torison**—The objective history plots for volume fraction constraint of 0.5 with corresponding length thresholds of  $\underline{\ell} = \{0, 5, 10\}$  are shown.



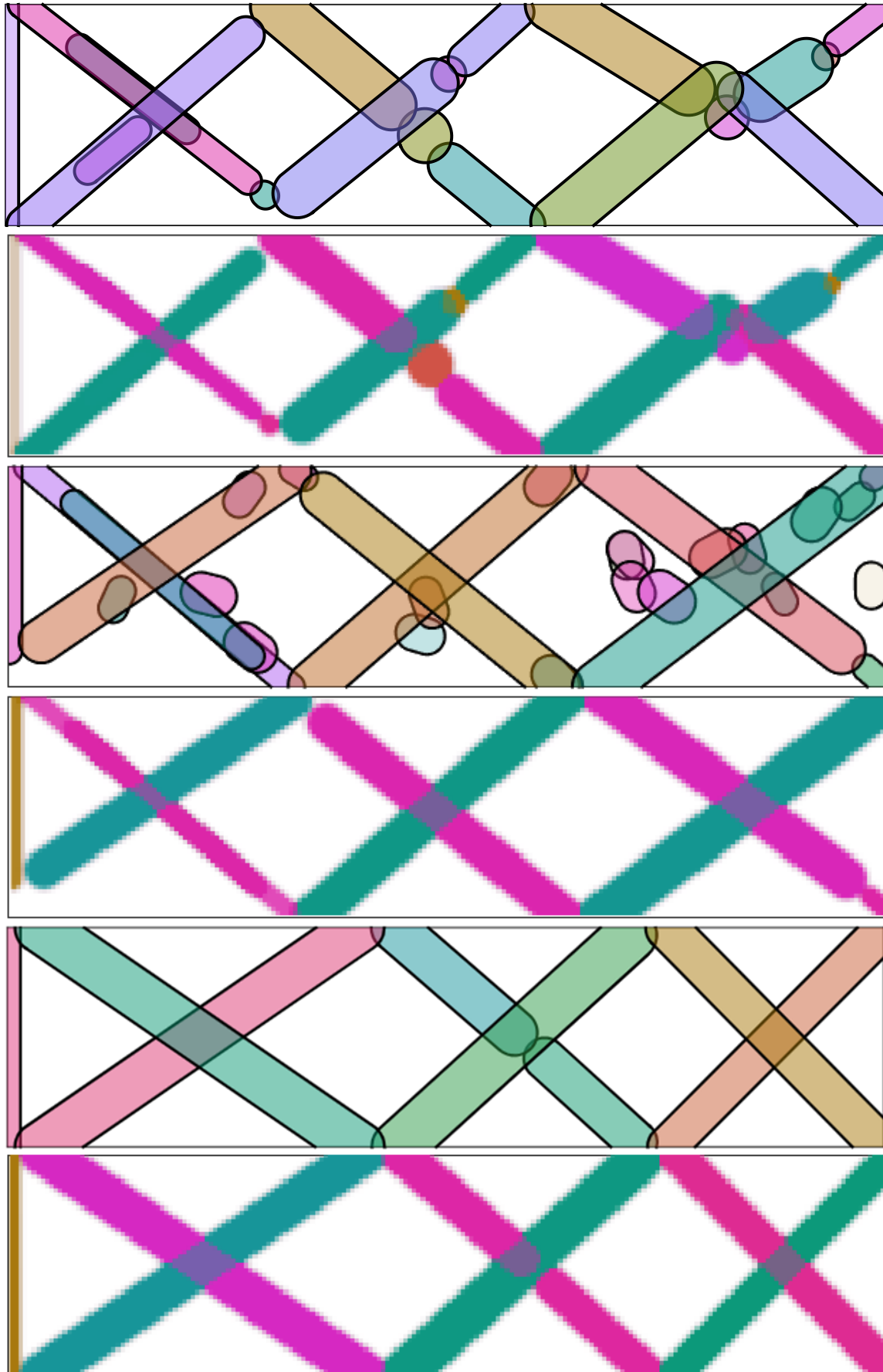
Finally, the design for  $\underline{\ell} = 10$  is free from features that require post-processing steps or cannot be printed. The compliance values for the final designs are tabulated in Tab. 5.5, and a significant difference can be observed. The design with the lowest stiffness—with a minimum length constraint of  $\underline{\ell} = 10$ —shows a considerable difference in the stiffness than the other two designs. Although the topology of the designs is roughly similar, the difference in stiffness is primarily due to the presence of overlapping bars in the  $\underline{\ell} = 10$  design. This confirms that overlapping features can overestimate stiffness, and such overlaps can lead to poor performance due to manufacturing inconsistencies, even if they are conceivable.

Fig 5.12 shows a smoother compliance history for  $\underline{\ell} = 0$  compared to when  $\underline{\ell} > 0$ . The jumps seen in the plots result from removing features shorter than the minimum threshold length set for the optimization problem. This leads to a disconnected structure, which increases compliance. When components are removed near the load application, there is a strong peak, while less intense peaks occur when the bars are removed in the central regions of the computational design space. However, these peaks gradually subside because other components occupy the design space left by the removed features.

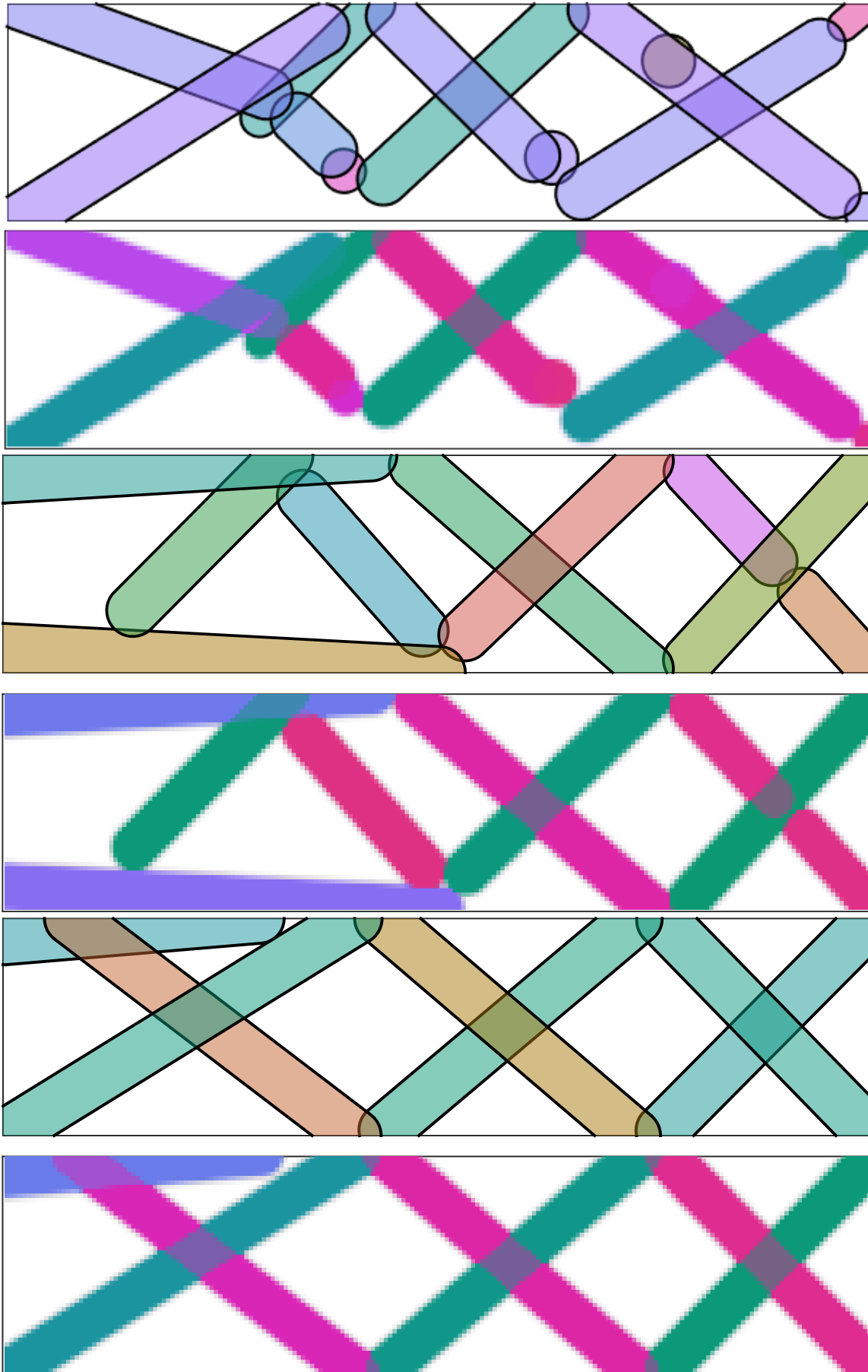
**Figure 5.13: Torison**—The objective history plots for volume fraction constraint of 0.5 with corresponding length thresholds of  $\ell = \{0, 5, 10\}$  are shown.



**Figure 5.14: Torison**—Adjacent design and density plots for volume fraction constraint of 0.5 with corresponding length thresholds of  $\ell = \{0, 5, 10\}$  are shown.



**Figure 5.15: Torison**—Adjacent design and density plots for volume fraction constraint of 0.5 with corresponding length thresholds of  $\ell = \{0, 5, 10\}$  are shown.

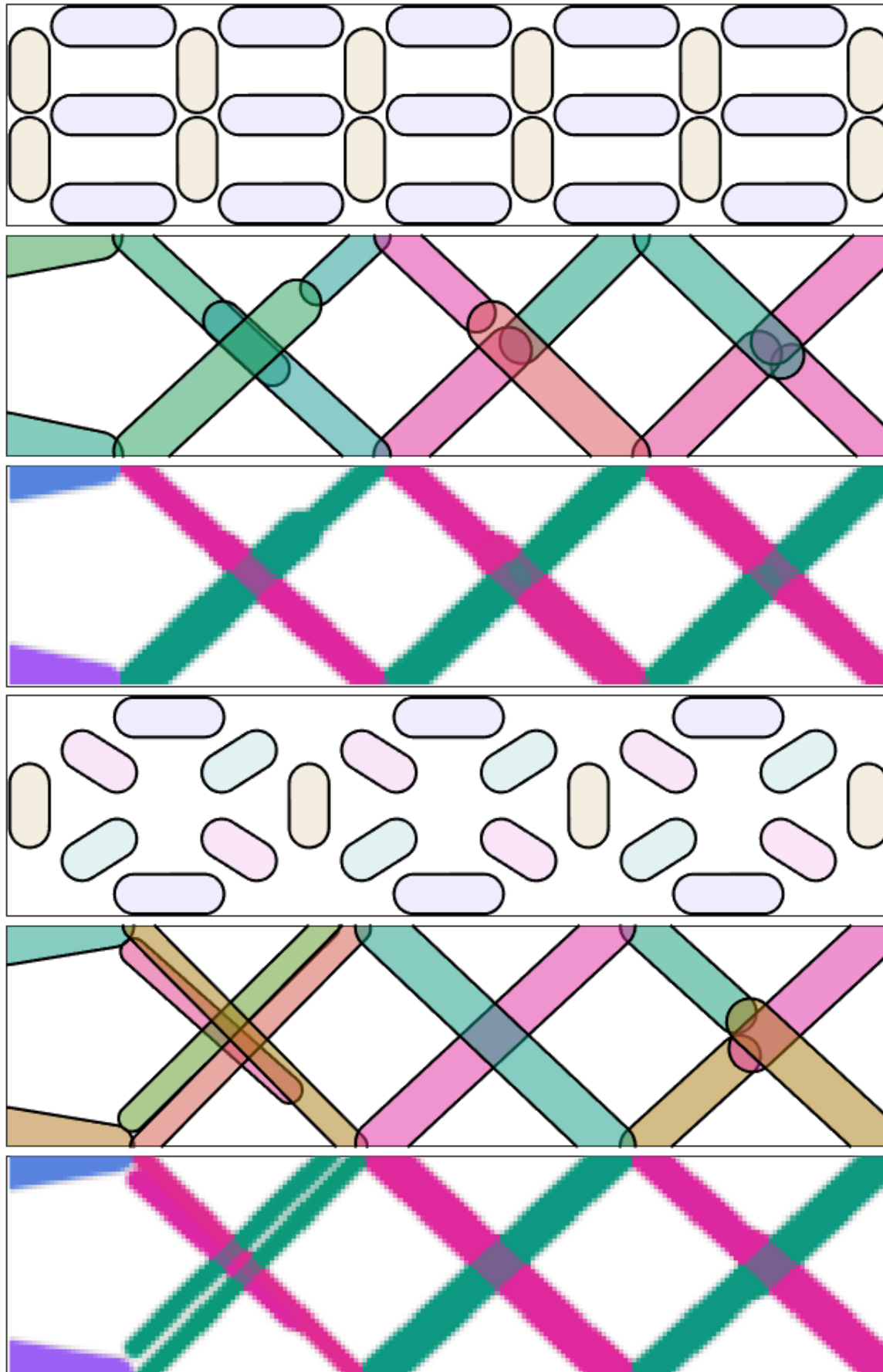


To explore the potential of the LGP-AM method, we optimized the same problem for a volume fraction constraint of 0.6. As discussed earlier in the Chapter 4, the method is prone to getting stuck in sub-optimal solutions if necessary restrictions are not implemented. For example, the overlapping criterion introduced in the GP-AM method. This issue is even more apparent in the simple formulation ( $\underline{\ell} = 0$ ), where the optimizer can lock the design in earlier stages if necessary restrictions are not in place, as shown in Fig. 5.15. It is evident that the optimizer generates non-manufacturable designs and results in the least stiff structure compared to the other two cases with an increase in the volume fraction. This reinforces our argument that when using the geometry projection method to design and optimize CFRP structures, the formulations must include necessary restrictions in the design space to reduce the likelihood of the optimizer falling into sub-optimal solutions. These sub-optimal solutions are characterized by the dissolution of components, excessive FRBs overlapping, and small design features. Finally, the designs obtained using LGP-AM are stiff and manufacturable for  $\underline{\ell} = \{5, 10\}$ .

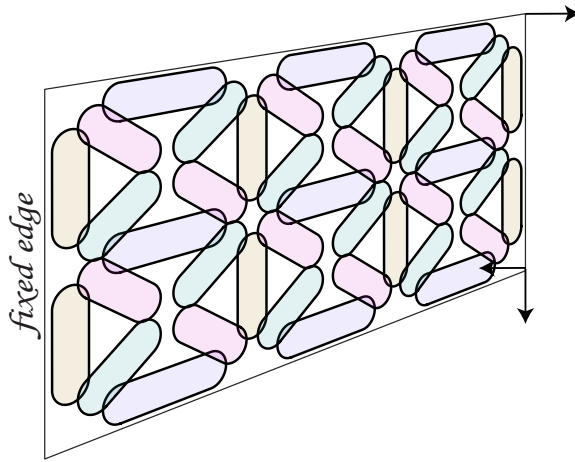
Finally, FRBs' initial arrangement, i.e., the number of FRBs, their orientation, and their length due to the nonconvexity of the optimization, highly impact the final topology. A numerical experiment that examines the impact of the initial arrangement of features on an optimization workflow. The experiment has two cases. The first case looks at the effect of changes in the orientation of features, while the second case examines how changes in the initial length of features and their number affect the optimization workflow, as shown in Fig. 5.16.

Comparing the topology obtained in Fig. 5.14 to the topology attained when the initial arrangement of the feature changed, the FRBs still form the intersecting FRBs to compensate for the torsion load applied at the right end and horizontal features at the left edge where the boundary condition is applied. Still, slight variations in the topology can be observed in all three cases, which start with the different initial configurations, which is generally the case when solving non-convex optimization problems, which are highly dependent on the initial settings. Despite that, LGP-AM formulation handles non-convexity robustly, which is demonstrated by keeping the dominating features in the design for all three cases.

**Figure 5.16: Torison**—The LGP-AM design ( $\ell = 10$ ) is plotted for two different initial conditions. The bound on the design variables is given in (5.18), and the volume fraction is set to  $\bar{v} = 0.5$ .



### 5.3.4 Multiple load cases



The following example considers a rectangular plate with dimensions of  $160 \times 80 \times 2$  subjected to two load cases. The plate is fixed at the left edge, and a unit out-of-plane load is applied at the bottom-right corner while a couple is applied at the right edge corner, as shown in Fig. ?? . The initial design comprises 41 bars, and the design variables are bounded as follows:

$$\begin{Bmatrix} (0, 0) \\ 3 \\ 0 \end{Bmatrix} \leq \begin{Bmatrix} (\mathbf{x}_{b1}, \mathbf{x}_{b2}) \\ r_b \\ \alpha_b \end{Bmatrix} \leq \begin{Bmatrix} (160, 80) \\ 6 \\ 1 \end{Bmatrix} \quad (5.19)$$

Furthermore, we define the objective compliance function for the two load cases in this example according to equation(5.20) the net compliance, i.e., the sum of the compliance of each load case

$$c := \sum c_i. \quad (5.20)$$

The design with a length constraint shares several similarities with the design that has no length constraint. For instance, by overlapping FRBs, two crossover components can offset a torsion load that is exerted on the right edge. This load is applied to mimic the short cantilever benchmark problem. This method is similar to the MBB problem case study and is commonly employed to validate the new TO framework. In both designs, the transversal load applied at the right corner of the bottom edge is optimized by arranging components at the top edge of the structure and projecting extended features at the bottom of the design.

Fig. 5.17 shows plots for minimum length constraints of  $\underline{\ell} = 0$  and  $\underline{\ell} = 10$ . The design without length constraint reached a compliance of 50.497352 after 271 iterations, while the other design

reached a compliance of 53.159720 after 280 iterations. Despite the former having higher stiffness, there are concerns about the actual stiffness of the printed VS-CRPL-L. The design's fiber path arrangement allows for lower compliance, but significant effort is required to ensure printability by connecting components of multiple length scales, such as short bars with circular bars.

The LGP-AM ( $\ell > 0$ ) technique is a method that optimizes the arrangements of FRBs, making them suitable for production using either additive or conventional methods. It should be noted that the optimized design requires no extra post-processing, except for the fiber path planning strategy, which mainly depends on the CF4 unit being considered. This example demonstrates the technique's ability and flexibility to solve complex problems while ensuring that the final design is easy to manufacture.

## 5.4 Conclusion

One further development of the LGP-AM method is to optimize the maximum length scale to improve structural redundancy, even if it comes at the expense of the nominal objective value. Regarding the minimum length scale, the continuum approach offers well-established solutions, such as projection techniques<sup>168</sup> and the robust topology optimization method<sup>68</sup>. However, imposing a maximum length scale in continuum topology optimization is more challenging. This issue has been addressed by **Guest2009** **ength** as well as more recently in Wu *et al.* and Lazarov *et al.*, and it is still the focus of ongoing research. Despite this, all of the solutions offered by the continuum approach deal with this issue by implicitly determining the characteristic sizing, which can sometimes require additional computational effort. In contrast, the LGP-AM method explicitly imposes a length scale and is almost straightforward, as it is carried out for minimum length constraints.

<sup>168</sup> Guest *et al.*, "Achieving minimum length scale in topology optimization using nodal design variables and projection functions," 2004.

<sup>68</sup> Sigmund, "On the usefulness of non-gradient approaches in topology optimization," 2011.

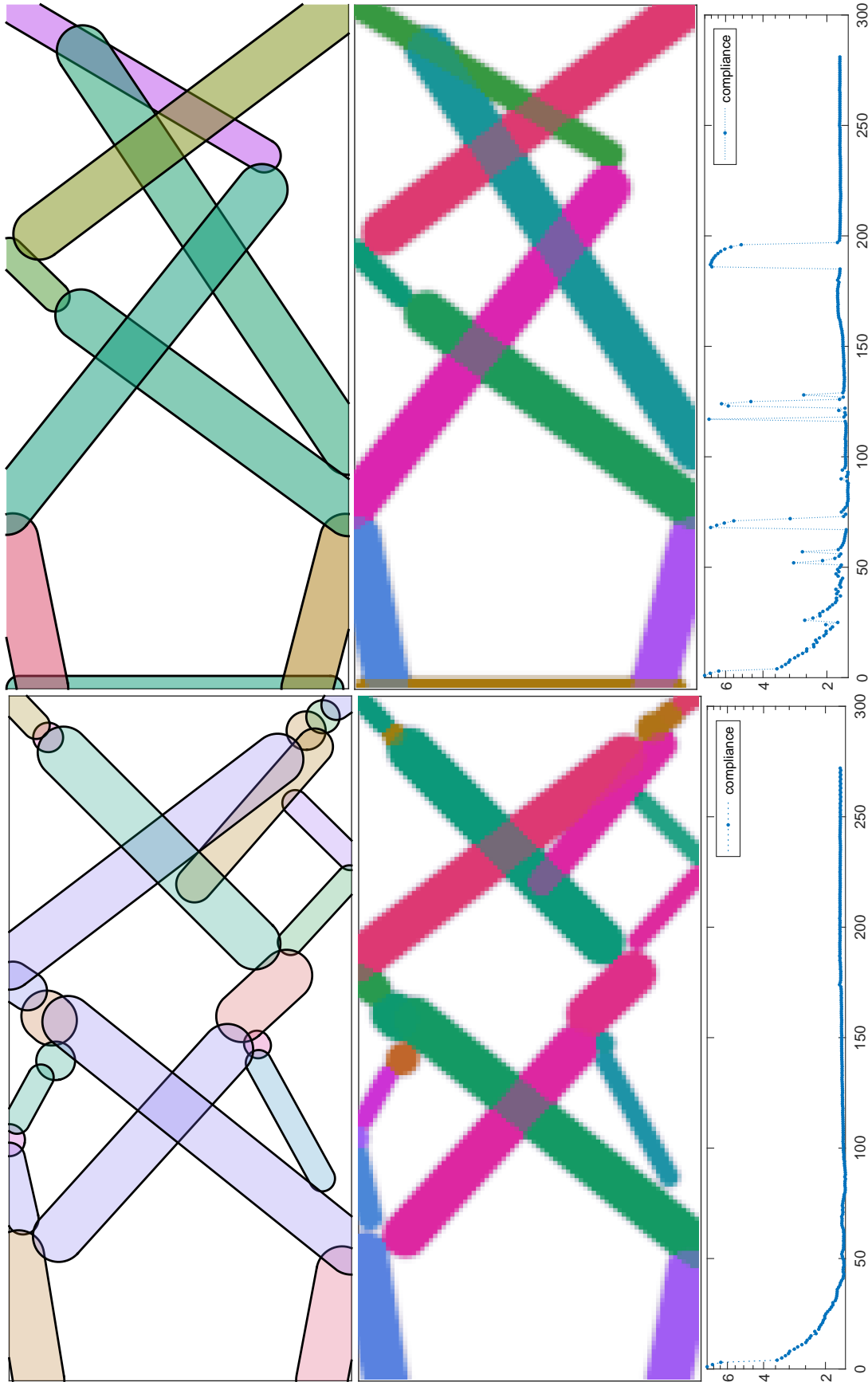


**Figure 5.17: Multiloading**—The design, density, and objective history plot of gP-IAM and LgP-IAM ( $\ell = 10$ ) are illustrated in column-wise fashion, respectively.

## *A Unified Topology Optimization Framework for Multilayered Variable Stiffness Composite Laminates.*

### 6.1 Continuous Fiber FUsed Fabrication—Markforged Printers

In 2014, Markforged released the world’s first commercial printer that enabled the 3D printing of composites with 1K continuous fiber reinforcement. Other researchers have also developed in-house printers for CCFRP composites by impregnating fibers with a thermoplastic matrix before extruding or within the printer nozzle. However, Markforged is one of the few companies commercially offering CFRP additive manufacturing technology. It uses a dual nozzle extrusion method—one nozzle is used for the matrix, and the other is used for the reinforcing fiber. Embedding continuous fiber into the molten polymer involves extruding the polymer matrix onto the print bed using the matrix nozzle. The fiber nozzle embeds the continuous fiber into the molten polymer. The print head irons the fiber bundle into a flat layer as the fiber bundle is extruded. The fibers provide most of the stiffness in this composite type, whereas the matrix bonds them together and determines the component’s geometry.

Markforged printers utilize the Eiger slicing software to define the components’ fiber routing and infill strategy. These printers have limited flexibility for changes in print parameters like nozzle temperature, speed, and layer thickness. However, the mechanical properties of the printed object can be adjusted by modifying process parameters like infill density, infill pattern, fiber pattern, and fiber orientation. The printers offer two fiber patterns—unidirectional and concentric, which can be combined in a single layer. Fibers can be printed at any angle with a resolution of 0.01 degrees. The fibers are continuous in each layer but do not bridge layers. The user has two choices of matrix, nylon, or onyx and three options for fiber reinforcement- carbon, glass, or Kevlar. The

fiber volume fraction can be adjusted by changing the number of fiber layers.

Onyx	
Property	Value
Young's modulus, $E$	2.4GPa
Poisson's ratio, $\nu$	0.38

**Table 6.1:** Elastic material properties of Onyx[171]

Carbon fiber	
Property	Value
Young's modulus 1, $E_1$	231GPa
Young's modulus 2, $E_2$	12.9GPa
Young's modulus 3, $E_3$	12.9GPa
Poisson's ratio 12, $\nu_{12}$	0.3
Poisson's ratio 13, $\nu_{13}$	0.3
Poisson's ratio 23, $\nu_{23}$	0.46
Shear modulus 12, $G_{12}$	11.3GPa
Shear modulus 13, $G_{13}$	11.3GPa
Shear modulus 23, $G_{23}$	4.45GPa

**Table 6.2:** Anisotropic material properties of carbon fiber [171]

The Markforged printer uses filaments that contain thousands of continuous carbon fibers. Each filament has a diameter of 0.4mm and a density of 1.2g/cm<sup>3</sup> with a fiber volume fraction of 34%. A cutting mechanism has been added to the printer, which allows for the scission of carbon fibers to print discrete paths <sup>172</sup>.

### 6.1.1 Recent studies on CF4 technology with the Markeforged system.

In a study <sup>173</sup> on achieving better lightweight performance—topology and fiber orientation optimization were combined sequentially. Customized fiber placement was performed using an extrusion-based 3D printing technique to manufacture composite preforms. The optimized design was then compared to a benchmark printed sample using the commercial Markforged printing system. A finite element model was built based on the actual printing paths to understand the effect of customized fiber paths on lightweight performance. This model was used to analyze the strain distribution in the topology-optimized geometry and how stress-lines continuous fibers transferred and carried the loading.

Almeida et al. [174] have developed and implemented a framework for optimizing parts with both isotropic and orthotropic

<sup>172</sup> Fernandes *et al.*, "Experimental investigation of additively manufactured continuous fiber reinforced composite parts with optimized topology and fiber paths," 2021.

<sup>173</sup> Zhang *et al.*, "3D printing of continuous carbon fibre reinforced polymer composites with optimised structural topology and fibre orientation," 2023.

material properties by optimizing the topology and fiber orientation. Their study found that for parts subjected to 3-point bending, onyx parts exhibited a significant increase in structural stiffness compared to nylon parts. The stiffness increase was observed to be 282%, 282%, and 165% for onyx parts at admissible volumes of 30%, 40%, and 50%, respectively. Similarly, for parts subjected to 4-point bending, onyx parts also showed greater stiffness and strength compared to nylon parts. The stiffness increase was measured to be 169%, 62%, and 137% for onyx parts at admissible volumes of 30%, 40%, and 50%, respectively.

The study <sup>175</sup> aimed to increase the strength of 3D-printed carbon fiber-reinforced composite structures using a design framework incorporating local latticing. The framework utilized the intermediate material fraction obtained in topology optimization. An anisotropic topology optimization, which considered both material fraction and orientation, was used, and the phase field-based technique was used to determine the 3D printing path. The toughness of the 3D-printed carbon fiber-reinforced composite structure was improved by the framework when tested on a three-point bending beam problem using Anisoprint.

Markforged allows users to choose the orientation of fibers on each layer. The standard options for fiber orientation are 0°, 45°, 90°, and 135°. However, it is possible to have variable fiber orientation on any layer to achieve specific goals. The printer can handle more complexity, but the direction parallel option limits the fiber to only one direction per layer. This is done to maintain structural integrity, improve manufacturability, and reduce complexity. The fixed fiber orientation within a layer provides sufficient design freedom for optimization while preserving manufacturability, especially for smaller builds, as proposed by Forward et al. [171].

When creating 3D-printed parts for functional applications, using unidirectional composites is not common because of the complex stress state they undergo. Instead, a laminate with an optimized stacking sequence is preferred. Sugiyama *et al.* demonstrated that the stiffness and strength per unit weight of the optimized variable fiber volume and stiffness composites were 9.4 and 1.6 times greater than those of conventional linear laminates, respectively. This means the composite layers are stacked to align with the desired properties. Although any stacking sequence can be achieved in the 3D printing of composite laminates, there are a few differences to consider when interpreting the lay-ups of 3D-printed specimens. The composite is enclosed within a shell of the matrix, which is made up of layers of floor (bottom), roof (top), and wall/shell (surrounding) layers. Further, In Markforged 3D

<sup>175</sup> Ichihara *et al.*, "3D-printed high-toughness composite structures by anisotropic topology optimization," 2023.

printers, each layer can only be a fiber or a matrix.

### 6.1.2 A unified topology optimization framework for multi-layered composite laminates.

In the previous chapters, we discussed the printability of single-layer VS-CFRP-Ls and formulated various approaches for designing and optimizing these laminates using the geometry projection method. However, the manufacturing process of these laminates involves additional constraints that must be imposed on each layer. This means that designing VS-CFRP-Ls requires an approach that considers the physical optimization of each layer, in contrast to previous formulations that analyze multi-layered laminates using equivalent single-layered theory. Therefore, developing a new formulation that considers these additional constraints is necessary to ensure the manufacturability of multilayered variable stiffness composite laminates (MUL-VSCLs), for example, designing and optimizing for thick composite laminates.

Thick laminated composite structures exhibit complex behavior that cannot be accurately predicted by classical plate and shell theories due to oversimplified transverse shear deformation. Although shear deformation can be ignored in thinner composite structures, it causes significant errors in predicting mechanical behavior in thicker ones. The first-order shear deformation theory uses a shear correction factor to address this issue, and the high-order theory uses a tangential transverse shear effect. However, these methods are inadequate for composite laminates with multiple layers because of the zigzag shape of in-plane displacement and the interlaminar continuity of transverse stresses. In response to these challenges, researchers have proposed several solutions, including the layerwise theory, which addresses the zigzag displacement and interlaminar continuity of transverse stress issues<sup>162</sup>.

This chapter presents a unified topology optimization framework for optimizing multi-layered variable stiffness composite laminates (MUL-VSCLs). The proposed method combines the geometry projection technique and the MUL<sup>2</sup> software—based on Carrera Unified Formulation—developed by the MUL<sup>2</sup> research group at Politecnico di Torino in Italy. The objective is to integrate CUF-based analysis with the geometry projection method to optimize MUL-VSCLs more efficiently and effectively. The proposed framework—GP-MUL<sup>2</sup>—can enable general additive manufacturing constraints, irrespective of CF4 technology in consideration, making it modular and enabling multi-objective and multi-physics analysis.

The Carrera Unified Formulation (CUF) is a widely used

<sup>162</sup> Carrera, “Theories and finite elements for multilayered, anisotropic, composite plates and shells,” 2002.

method for formulating finite elements (FEs) for various structures. The CUF approach includes one-dimensional (beam) and two-dimensional (plate and shell) theories beyond classical theories such as Euler, Kirchhoff, Reissner, Mindlin, etc. The critical feature of CUF is using a condensed notation, which allows for expressing displacement fields in terms of expansion or thickness functions. The benefits of using CUF are that it enables the performance of related assembly techniques more efficiently, and one-dimensional and two-dimensional FEs provide results comparable to 3D elements but with lower computational costs. The CUF approach has been widely used to develop efficient and accurate 2D FEs, which can analyze various structures with complex geometries.

Since the CUF-based topology optimization approach has yet to be demonstrated, the chapter details the integration of a CUF-based geometry projection framework utilizing the same problem statement discussed in the previous chapters. The GP-MUL<sup>2</sup> framework can optimize topology with multi-objective functions and consider multi-physics, including several CF4 constraints. However, these adaptations are not considered in the chapter and are postponed for future work.

## 6.2 Multilayered Composite Laminates—A brief background

Layered structures are referred to as "transversely anisotropic" materials because they exhibit distinct physical and mechanical properties in the direction of thickness. Due to the discontinuous mechanical properties in the transverse direction, a displacement field occurs in the thickness direction. The slope of this displacement field changes abruptly at each layer interface, resulting in a zigzag or ZZ form of the displacement field. Although the in-plane stresses may discontinue at each layer interface, the transverse stresses must be continuous at each layer interface for reasons of equilibrium, as stated in Cauchy's theorem. This continuity of transverse stresses is known as interlaminar continuity (IC).

Developing a theory suitable for multilayered composite laminates requires meeting the  $C_z^0$  and IC requirements<sup>176</sup>. A composite, multilayered structure can be developed by following the three points discussed in detail here<sup>177,178</sup>.

1. Elimination of the thickness coordinate  $z$ 
  - Asymptotic type approaches
  - Axiomatic type approaches
2. Choice of the unknown variable

<sup>176</sup> Carrera, "C0 Reissner-Mindlin multilayered plate elements including zig-zag and interlaminar stress continuity," 1996.

<sup>177</sup> Carrera *et al.*, "Classical and advanced multilayered plate elements based upon PVD and RMVT. Part 1: Derivation of finite element matrices," 2002.

<sup>178</sup> Carrera *et al.*, "Classical and advanced multilayered plate elements based upon PVD and RMVT. Part 2: Numerical implementations," 2002.

- Displacement formulation
- Mixed formulation

3. Choice of the description of the variables

- Equivalent Single-Layer Models
- Layer-Wise Models

### 6.2.1 Axiomatic Theories for Multilayered Structures

The asymptotic method approximates theories that are known to be accurate compared to the 3D exact solution. Developing asymptotic theories is generally more complex than developing axiomatic ones. In axiomatic theory, several hypotheses about the behavior of the unknown functions are introduced to simplify the mathematical complexity of the 3D differential equations, as described below.

**Equivalent single layered theories (ESL)** The CLTs (Classical Lamination Theories) are based on the assumption that the normals to the reference surface remain normal in the deformed states and do not change in length. This means that transverse shear and normal strains are considered negligible concerning the other strains. The first-order shear deformation theory extends the CLTs, including transverse shear strains, to layered structures as discussed in Chapter 4. Higher-order theories are based on displacement models that are more complex than the ones used in FSDT.

$$\mathbf{u}_i(x, y, z) = \mathbf{u}_0 + z\mathbf{u}_1 + z^2\mathbf{u}_2 + \dots + z^N\mathbf{u}_N \quad (6.1)$$

where  $N$  is the order of expansion used for the displacement variables.

**Zigzag Theories** ESL models to multilayered VSCLs do not permit the fulfillment of  $C_z^0$  requirements. Refined theories, called zigzag (ZZ), have been developed to meet these requirements due to the form of the displacement field in the thickness direction. In ZZ theories, a particular displacement model is assumed in each layer, and compatibility and equilibrium conditions are used at the interface to reduce the number of unknown variables.

**Layer-Wise Theories** The ESL models are "kinematically homogeneous," meaning they are not sensitive to individual layers as assumed variables are independent regardless of the number of layers. These models are typically referred to as a given reference plate or shell surface, for example, Eq. (4.8).

Incorporating the ZZ effect into an ESL model that only uses displacement variables can attain a detailed response from individual layers. This means that each layer is treated as an independent plate, and the compatibility of displacement components is imposed as a constraint for each interface. Each layer  $k$  is considered an independent plate or shell.

### 6.3 Introduction to the Carrera Unified Formulation

Considering a plate, the variable in-plane displacement, considering all the components, over the cross-section is written as,

$$\mathbf{u}_\tau(x, y) \rightarrow \mathbf{u}_\tau(x, y, z) \quad (6.2)$$

where,

$$\mathbf{u}_\tau = (u_\tau, v_\tau, w_\tau)$$

Then, the CUF technique expresses components of the displacement field using expansion terms to approximate the displacements along the thickness as,

$$\begin{cases} u(x, y, z) = \sum_{\tau=0}^n F_\tau(z)u_\tau(x, y) \\ v(x, y, z) = \sum_{\tau=0}^n F_\tau(z)v_\tau(x, y) \\ w(x, y, z) = \sum_{\tau=0}^n F_\tau(z)w_\tau(x, y) \end{cases} \quad (6.3)$$

The thickness function  $F_\tau$  is the powers of  $z$ , and the distribution of displacements can be a Taylor or Lagrange expansion at order  $n$  of coefficient  $u_\tau, v_\tau, w_\tau$ . In vector form, the displacement can be rewritten then as,

$$\mathbf{u} = F_\tau(z)\mathbf{u}_\tau(x, y) \quad (6.4)$$

CUF builds upon the FE method by employing structural theories along the thickness, which allows FE matrices and vectors to be derived from fundamental nuclei. The CUF expands index notation beyond the traditional  $i$  and  $j$  indices used in FE procedures and incorporates the use of  $\tau$  and  $s$  indices commonly used in the theory of structures. A fundamental nucleus (FN) is obtained, expressed in four indices:  $\tau, s, i,$  and  $j$ . The resulting FN is a  $3 \times 3$  array or a  $3 \times 1$  vector, and its shape remains constant across 1D, 2D, and 3D problems<sup>179</sup>.

<sup>179</sup> Carrera et al., *Finite element analysis of structures through unified formulation*, 2014.

### 6.4 Unified Formulation for Multilayered Structure

The assumptions about displacements can be made at either the layer or the multilayer level. For layer-wise description,  $\mathbf{u}_\tau$  are layer variables that differ for each layer. On the other hand, in the ESL description,  $\mathbf{u}_\tau$  are the same for the entire multilayer. The potential

outcomes of employing ESL models for the geometry projection method have already been discussed. Specifically, the focus is on GP-MUL<sup>2</sup> and its advantages and limitations when using the LW model. However, it is worth noting that any model can be utilized due to the modular nature of MUL<sup>2</sup> software, which allows for the swapping of theories.

For example, higher-order ESLMs appear in the following form:

$$\begin{aligned} u(x, y, z) &= u_0(x, y) + zu_1(x, y) + z^2u_1(x, y) + \dots + z^N u_N(x, y) \\ v(x, y, z) &= v_0(x, y) + zv_1(x, y) + z^2v_1(x, y) + \dots + z^N v_N(x, y) \\ w(x, y, z) &= w_0(x, y) + zw_1(x, y) + z^2w_1(x, y) + \dots + z^N w_N(x, y) \end{aligned} \quad (6.5)$$

According to the unified formulation, these can be written in the following compact form:

$$\mathbf{u} = F_0\mathbf{u}_0 + F_1\mathbf{u}_1 + \dots + F_N\mathbf{u}_N = F_\tau\mathbf{u}_\tau, \quad \tau = 0, 1, 2, \dots, N \quad (6.6)$$

where  $N$  is the *order of the expansion*, and the thickness function  $F_\tau$  is defined as

$$F_0 = 1, \quad F_1 = z, \quad F_0 = z^2, \dots, F_N = z^N \quad (6.7)$$

#### 6.4.1 Layerwise Theory with Legendre Expansion

All the examples carried out for GP-MUL<sup>2</sup> considered each layer independent, and the compatibility of displacement components at each interface is imposed. The following expansion is employed in terms of Legendre polynomials:

$$\begin{aligned} u^k &= F_t u_t^k + F_b u_b^k \\ v^k &= F_t v_t^k + F_b v_b^k \\ w^k &= F_t w_t^k + F_b w_b^k \end{aligned} \quad (6.8)$$

The subscripts  $t$  and  $b$  denote values related to the top and bottom layer surface, respectively. For first-order expansion, the thickness functions  $F_\tau(\zeta_k)$  are now defined at the  $k$ -layer level,

$$F_t = \frac{P_0 + P_1}{2}, \quad F_b = \frac{P_0 - P_1}{2} \quad (6.9)$$

in which  $P_j = P_j(\zeta_k)$  is the Legendre polynomial of the  $j$ th order defined in the  $\zeta_k$  domain:  $\zeta_k = 2z_k/h_k$  and  $-1 \leq \zeta_k \leq 1$ .

The Legendre polynomials allow one to have interface values as unknown variables, avoiding the inclusion of constraint equations to impose  $C_z^0$  requirements. In a unified form

$$u^k = F_t u_f^k + F_b u_b^k = F_\tau u_z^k, \quad \tau = t, b \quad (6.10)$$

**Table 6.3:** The first five Legendre polynomials

$P_0$	$P_1$	$P_2$	$P_3$	$P_4$
1	$\zeta_k$	$(3\zeta_k^2 - 1)/2$	$\frac{5}{2}\zeta_k^3 - \frac{3}{2}\zeta_k$	$\frac{35}{8}\zeta_k^4 - \frac{15}{4}\zeta_k^2 + \frac{3}{8}$

Higher-order LW theories used in the examples are formulated as,

$$\begin{aligned}
 u_x^k &= F_t u_t^k + F_b u_b^k + F_2 u_2^k \\
 u_y^k &= F_1 v_t^k + F_b v_b^k + F_2 v_2^k \\
 u_z^k &= F_1 w_t^k + F_b w_b^k + F_2 w_2^k
 \end{aligned} \tag{6.11}$$

where

$$F_r = P_r - P_{r-2}, \quad r = 2, 3, \dots, N \tag{6.12}$$

In a unified form

$$u^k = F_r u_i^k + F_b u_b^k + F_r u_r^k = F_\tau u_r^k, \quad \tau = t, b, \quad r = 2, 3, \dots, N \tag{6.13}$$

## 6.5 A Four-Index Fundamental Nucleus

The virtual displacement (PVD) principle derives the weak form of governing equations. This variational statement allows writing the governing equations in integral form using a displacement formulation [180].

According to PVD, the total virtual variation of the total work in the body under deformation is zero:

$$\delta \mathcal{L} = \mathcal{U}_{int} - \mathcal{W}_{ext} = 0$$

The total virtual internal work is the strain energy developed during the deformation, which is given as,

$$\mathcal{U}_{int} = \frac{1}{2} \int_V \delta \boldsymbol{\varepsilon}^T \boldsymbol{\sigma} dV$$

The total virtual external work will be expressed by the work done by the external load:

$$\mathcal{W}_{ext} = \frac{1}{2} \int_V \delta \mathbf{u}^T \mathbf{F} dV$$

By using the above definitions, the PVD can be written as:

$$\int_V \delta \boldsymbol{\varepsilon}^T \boldsymbol{\sigma} dV = \int_V \delta \mathbf{u}^T \mathbf{F} dV \tag{6.14}$$

Using the constitutive equation and the geometrical relation to rearrange the expression of the PVD and obtain an equation only in terms of displacements:

$$\begin{aligned}\delta \boldsymbol{\varepsilon} &= [\mathbf{B}] \delta \mathbf{u} \\ \boldsymbol{\sigma} &= [\mathbf{C}] \boldsymbol{\varepsilon} = [\mathbf{C}][\mathbf{B}]\{\mathbf{u}\}\end{aligned}\quad (6.15)$$

Substituting the above two relations into an expression of PVD Eq. (6.14), obtaining:

$$\int_V \delta \mathbf{u}^T [\mathbf{b}]^T [\mathbf{C}][\mathbf{b}] \mathbf{u} dV = \int_V \delta \mathbf{u}^T \mathbf{F} dV$$

The unified formulation (see Eq. (6.4)) can be applied to displacement fields. Note two separate indexes,  $\tau$  and  $s$ , are used because the displacement fields are independent,

$$\begin{aligned}\mathbf{u} &= F_\tau(z) \mathbf{u}_\tau(x, y) \\ \delta \mathbf{u} &= F_s(z) \delta \mathbf{u}_s(x, y)\end{aligned}\quad (6.16)$$

### 6.5.1 Implementing finite element method

Considering the discretization of the domain by a Q4 element, the displacement field can be rewritten as:

$$\mathbf{u}_\tau(x, y) = \sum_{i=0}^N N_i \mathbf{u}_{\tau_i}(x, y) \quad (6.17)$$

Substituting the discretization in-plane displacement field in the Eq. (6.16) allows to rewrite the displacements of the two systems as,

$$\begin{aligned}\mathbf{u} &= F_\tau(z) N_i \mathbf{u}_\tau(x, y) \\ \delta \mathbf{u} &= F_s(z) N_j \delta \mathbf{u}_s(x, y)\end{aligned}\quad (6.18)$$

Finally, the finite element formulation of the PVD is written as,

$$\left[ \int_V F_s N_j [\mathbf{B}]^T [\mathbf{C}][\mathbf{B}] N_i F_\tau dV \right] \mathbf{u}_{\tau_i} = \int_V F_s N_j \mathbf{F} dV \quad (6.19)$$

And the fundamental nucleus can be obtained

$$\begin{aligned}\delta \mathcal{L}_{int} &= \int_V \delta \boldsymbol{\varepsilon}^T \boldsymbol{\sigma} dV = \delta \mathbf{u}_{sj} \mathbf{k}^{\tau s i j} \mathbf{u}_{\tau i} \\ &= \delta \mathbf{u}_{sj}^T \int_V \underbrace{[F_s(z) N_j \underbrace{[\mathbf{b}^T]_{3 \times 6} \underbrace{[\mathbf{C}]_{6 \times 6} \underbrace{[\mathbf{b}]_{6 \times 3}}_{3 \times 3}}_{3 \times 3}] N_i F_\tau(z)}_{\mathbf{k}^{\tau s i j}} dV \mathbf{u}_{\tau i}\end{aligned}\quad (6.20)$$

For all the components of the displacement are considered, the fundamental nucleus becomes a  $3 \times 3$  matrix:

$$\mathbf{k}^{\tau s i j} = \int_V F_s(x, z) N_j(\mathbf{y}) \mathbf{b}^T \mathbf{C} \mathbf{b} N_i(\mathbf{y}) F_\tau(x, z) dV \quad (6.21)$$

### 6.5.2 CUF Assembly Technique

After defining the PVD for a single element of the discretized domain, the total stiffness matrix is calculated by considering the common nodes between elements in the mesh. To do this, we need to define the fundamental nucleus of the stiffness matrix for each element in the domain and then combine these nuclei.

Note that the indexes  $\tau$  and  $s$  define the accuracy of the model in the thickness by order of expansion,  $\tau, s = 1, 2, \dots, M$  to describe the displacements field, and the indexes  $i$  and  $j$ , are fixed the number of nodes that have been chosen for the single element of the mesh, i.e.,  $i, j = 1, 2, \dots, N_n$ , as follows,

$$\begin{matrix}
 & & \overbrace{\tau = 1 \quad \dots \quad \tau = M}^{i=1} & & \overbrace{\tau = 1 \quad \dots \quad \tau = M}^{i=N_{N_n}} & & \\
 j = 1 & \left\{ \begin{array}{l} s = 1 \\ \vdots \\ s = M \end{array} \right. & \begin{matrix} \mathbf{k}^{1111} & \dots & \mathbf{k}^{1M11} & \dots & \mathbf{k}^{111N_n} & \dots & \mathbf{k}^{1M1N_n} \\ \vdots & & \vdots & & \vdots & & \vdots \\ \mathbf{k}^{M111} & \dots & \mathbf{k}^{MM11} & \dots & \mathbf{k}^{M11N_n} & \dots & \mathbf{k}^{MM1N_n} \end{matrix} \\
 \\
 j = N_n & \left\{ \begin{array}{l} s = 1 \\ \vdots \\ s = M \end{array} \right. & \begin{matrix} \mathbf{k}^{11N_n1} & \dots & \mathbf{k}^{1MN_n1} & \dots & \mathbf{k}^{11N_nN_n} & \dots & \mathbf{k}^{1MN_nN_n} \\ \vdots & & \vdots & & \vdots & & \vdots \\ \mathbf{k}^{M1N_n1} & \dots & \mathbf{k}^{MMN_n1} & \dots & \mathbf{k}^{M1N_nN_n} & \dots & \mathbf{k}^{MMN_nN_n} \end{matrix}
 \end{matrix}$$

So, since the dimension of the fundamental nucleus, for each element, has dimension  $3M \times 3M$ , the global stiffness matrix will have dimension  $3M \cdot N_n \times 3M \cdot N_n$ .

The matrix assembly consists of four loops on indexes  $i, j, \tau$  and  $s$ , and an FN is calculated for each combination of these indexes. Each FN is reported as  $\mathbf{k}^{\tau s i j}$  and works as the matrix construction's core. The indexes indicate the nucleus's position in the global matrix.

The total number of DOFs in the structural model discretized by Q4 element and uses the model given by Eq. (6.8)

$$\begin{aligned}
 \text{DOFs} = & \underbrace{3 \times 2}_{\text{DOFs per node}} \times [(\underbrace{2}_{\text{nodes per edge}} - 1) \times \underbrace{N_{Ex}}_{\text{elements along } x} + 1] \\
 & \times [(\underbrace{2}_{\text{nodes per edge}} - 1) \times \underbrace{N_{Ey}}_{\text{elements along } y} + 1]
 \end{aligned} \quad (6.22)$$

FN for fixed  $i, j$  using linear Legendre expansion function is reported,  $k^{\tau sij}$ , as

$$\left[ \begin{array}{ccc|ccc} k_{xx}^{1,1} & k_{xy}^{1,1} & k_{xz}^{1,1} & k_{xx}^{1,z} & k_{xy}^{1,z} & k_{xz}^{1,z} \\ k_{yx}^{1,1} & k_{yy}^{1,1} & k_{yz}^{1,1} & k_{yx}^{1,z} & k_{yy}^{1,z} & k_{yz}^{1,z} \\ k_{zx}^{1,1} & k_{zy}^{1,1} & k_{zz}^{1,1} & k_{zx}^{1,z} & k_{zy}^{1,z} & k_{zz}^{1,z} \\ \hline k_{xx}^{z,1} & k_{xy}^{z,1} & k_{xz}^{z,1} & k_{xx}^{z,z} & k_{xy}^{z,z} & k_{xz}^{z,z} \\ k_{yx}^{z,1} & k_{yy}^{z,1} & k_{yz}^{z,1} & k_{yx}^{z,z} & k_{yy}^{z,z} & k_{yz}^{z,z} \\ k_{zx}^{z,1} & k_{zy}^{z,1} & k_{zz}^{z,1} & k_{zx}^{z,z} & k_{zy}^{z,z} & k_{zz}^{z,z} \end{array} \right]_{ij} \quad (6.23)$$

The superscripts indicate the expansion functions involved in each component of the stiffness matrix, i.e., one and z. The explicit expression of two components is reported here:

$$\begin{aligned} k_{xx}^{1,1} &= \tilde{C}_{11} \int_A 1 \cdot 1 dz \int_{\Omega} N_{i,x} N_{j,x} d\Omega + C_{66} \int_A 1 \cdot 1 dz \int_{\Omega} N_{i,y} N_{j,y} d\Omega \\ k_{yz}^{1,z} &= C_{23} \int_A 1 \cdot \frac{\partial z}{\partial z} dz \int_{\Omega} N_{i,y} N_{j,z} d\Omega = C_{23} \int_A 1 \cdot 1 dz \int_{\Omega} N_{i,y} N_{j,z} d\Omega \end{aligned} \quad (6.24)$$

where  $\Omega$  indicates the in-plane domain and  $A$  the through-the-thickness domain. Interested readers can refer to the book [179] for a complete derivation of components of the fundamental nucleus and a thorough understanding of the CUF modeling.

## 6.6 Intergating CUF-based analysis in the geometry projection method

The geometry projection comprises three modules—geometric design space, finite element analysis, and optimization module—which are independent in their functionalities and thus provide flexibility for using the geometry projection method with CUF-based modules by replacing the FE module. It is possible to use any geometry projection formulations with the CUF framework. This is because the MUL<sup>2</sup> software can efficiently model and analyze multilayered VSCLs using different theories, allowing the user to apply any theories available in the literature.

The GP formulation is a suitable method for designing and optimizing MUL-VSCLs. It involves using the softmax function to identify discrete components within a layer, allowing maximum stiffness and enabling stacking sequence optimization. Optimizing for the fiber orientation in the stack of physical layers indirectly optimizes for the intersecting load path. However, this method is unsuitable for optimizing single-layer monolithic structures, as it can result in suboptimal solutions by dissolving components in

overlapping regions to pursue a discrete component in the design domain.

Implementing the GP-MUL<sup>2</sup> framework has two significant computation changes, which are allocated to the MUL<sup>2</sup> software, wherein the mathematical formulation is the same as the GP except instead of discretizing the computational domain using a single layer, a multilayered formulation is introduced. Further, the laminate is modeled using layer-wise theory as stated in Eq. (??).

The first computation in the MUL<sup>2</sup> software is the evaluation of stiffness matrices and the assembly of the stiffness matrices. Referring to Chapter 4, for the anisotropic material, elasticity tensors are calculated for the GP-MUL<sup>2</sup> method as carried out in the GP method:

$$\mathbf{C}_e = \mathbf{C}^v + \sum_b w_{be} \check{\rho}_{be}^{\text{eff}} (\mathbf{C}_b - \mathbf{C}^v) \quad (6.25)$$

Second, to evaluate  $\nabla_z c$ , the following equations are modeled in the MUL<sup>2</sup> software. In the GP method, the derivative of the elemental stiffness matrix  $\mathbf{K}^{(e)}$  concerning a specific design variable  $z_i$  is computed as the elasticity tensor design sensitivity  $\nabla_z \mathbf{C}^{(e)}$ , which is computed as follows:

$$\nabla_z \mathbf{C}^{(e)} = \sum_b \left[ \nabla_z \left( w_{be} \check{\rho}_{be}^{\text{eff}} \right) \right] (\mathbf{C}_b - \mathbf{C}^v) + w_{be} \check{\rho}_{be}^{\text{eff}} (\nabla_z \mathbf{C}_b) \quad (6.26)$$

where, we denote the design sensitivity operator as  $\nabla_z := \frac{\partial}{\partial z_i}$ . The sensitivity of the compliance is given as follows:

$$\nabla_z c = - \sum_e \mathbf{u}^\top \left( \nabla_z \mathbf{K}^{(e)} \right) \mathbf{u} \quad (6.27)$$

However, a different approach is adopted in the GP-MUL<sup>2</sup> formulation. For a given design variable, first, the relevant element set ( $E \forall \nabla_z \mathbf{C}^{(e)} \neq 0$ ) is attained, and then  $\left( \nabla_z \mathbf{K}^{(E)} \right)$  is assembled into a sparse matrix  $(\mathbf{K}^{\mathcal{E}})$ , where  $E \subset \mathcal{E}$ , where indices of the nonzero elements of the sparse matrix  $(\mathbf{K}^{\mathcal{E}})$  given by the degree of freedoms assigned to the relevant elements. The sensitivity of the compliance for GP-MUL<sup>2</sup> is given as follows:

$$\nabla_z c = - \sum \mathbf{U}^\top \left( \nabla_z \mathbf{K}^{(\mathcal{E})} \right) \mathbf{U} \quad (6.28)$$

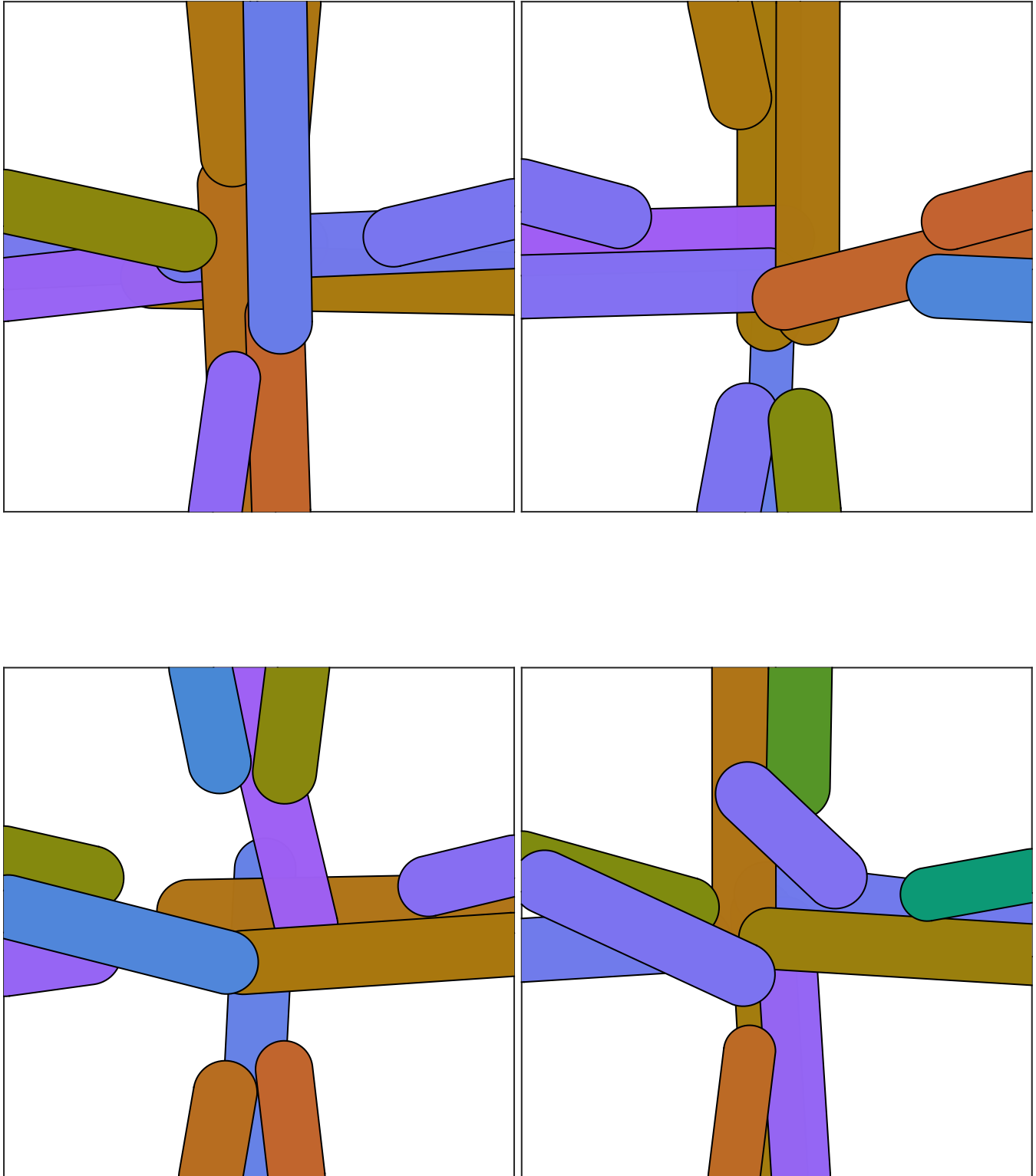


**Figure 6.1: Bending**—The design plots for volume fraction constraint of 0.4 for each layer are arranged in two columns—the 1<sup>st</sup> column contain the 1<sup>st</sup> and 2<sup>nd</sup> layers and 2<sup>nd</sup> column contain the 3<sup>rd</sup> and 4<sup>th</sup> layers.

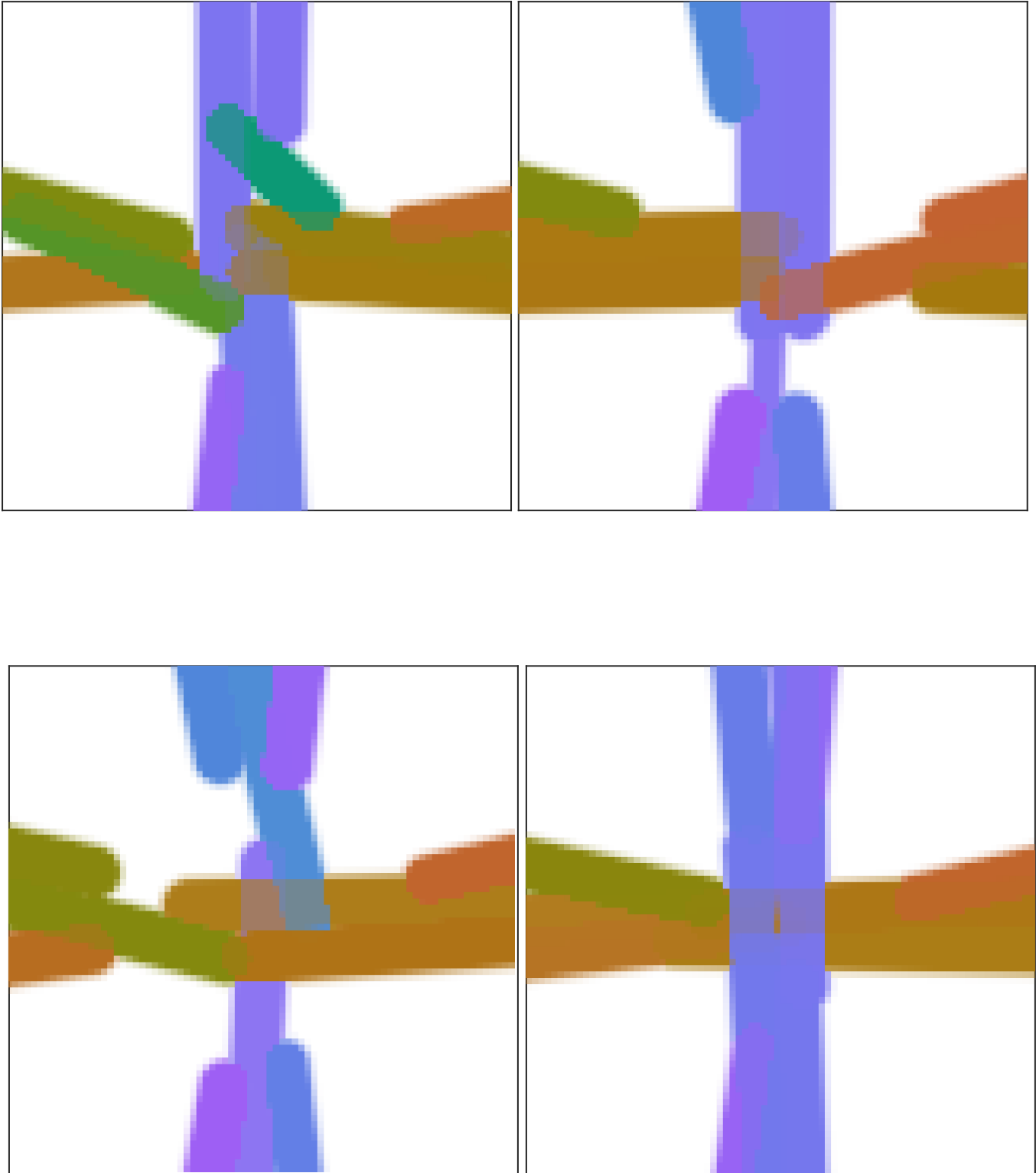


**Figure 6.2: Bending**—The design plots for volume fraction constraint of 0.4 for each layer are arranged in two columns—the 1<sup>st</sup> column contain the 1<sup>st</sup> and 2<sup>nd</sup> layers and 2<sup>nd</sup> column contain the 3<sup>rd</sup> and 4<sup>th</sup> layers.

## 6.7 Examples

In the two numerical examples—We consider bars made of carbon-fiber-reinforced polymer; fiber orientation is aligned to the bar’s axis and is continuous. Table (4.1) lists unidirectional carbon-epoxy AS4/3501-6 material properties used for the bars.

For all the examples in Fig. 5.4, the following settings are considered until mentioned otherwise. Four layers are initialized in both examples; however, any number can be used; each layer is initialized with several FRBs projected on their corresponding layer and independent from other layers. Discretization is based on the Q4 element, and the cross-section of the layer is discretized using the B3 element. The total thickness of MUL-VSCL is equal to 2 unit, and each layer is of equal thickness, similar to what is considered in the single-layer formulations. Unlike other formulations, the symmetric condition is not applied along the stack direction; thus, a different topology is most likely to be obtained in each layer. It must be noted that length constraints can be easily implemented in the GP-MUL<sup>2</sup> framework,

Parameters for method-of-moving-asymptotes (MMA), employed for the optimization routine, using the default parameters described in Section 6.7.

### 6.7.1 A square plate under point bending load

A clamped square plate under point loading, i.e.,  $q \equiv 3$ , is considered, and the center of the plate is under point load. The design region has dimensions  $80 \times 80 \times 2$ . Although the problem definition has two planes of symmetry, the symmetry conditions are not applied at the top and right edge of the square design domain. Each layer is initialized with 12 bars, and the bounds imposed on the design variables are as follows:

$$\begin{Bmatrix} (0, 0) \\ 2 \\ 0 \end{Bmatrix} \leq \begin{Bmatrix} (\mathbf{x}_{b1}, \mathbf{x}_{b2}) \\ r_b \\ \alpha_b \end{Bmatrix} \leq \begin{Bmatrix} (80, 80) \\ 5 \\ 1 \end{Bmatrix} \quad (6.29)$$

Figures 6.1 and 6.2 show the design and density for each layer in the MUL-VSCL, wherein the volume fraction constraint of 0.4 is assigned to each layer. Utilizing the layerwise model to update each lamina’s topology and fiber orientation enables the capture of the actual displacement field for a MUL-VSCL across the thickness direction by satisfying the  $C_z^0$  requirement. As a result, each lamina achieved a unique topology and fiber orientation. In contrast to the design shown in the Appendix A wherein the ESL model is used to update each lamina’s topology and fiber orientation,

which is unsuitable for capturing the displacement field across the thickness direction.

Even though the symmetric laminate is not considered, a common feature can be identified (Fig. 6.2), resulting in the feature of symmetric and asymmetric laminates. Comparing the FRBs arrangement near the left and top edge of 1<sup>st</sup> layer and the left and bottom edge of 4<sup>th</sup> layers resulting in similar topology. Further, the assembly of components attached to the bottom edge of the 1<sup>st</sup> layer is replicated in the 4<sup>th</sup> layer at the right edge. Similarly, the deduction can be carried out for 2<sup>nd</sup> and 3<sup>rd</sup>, i.e., identical features are obtained in symmetric or asymmetric order across the laminate. Note that each layer obtained discrete components by penalizing other overlapping components using the softmax function in the GP method. Therefore, fiber orientation at each point in the laminate can be procured from the density plot(Fig. 6.2).

Comparing the design of the GP-MUL<sup>2</sup> framework with others (see 6.3 and 6.4), it is clear that the method further enriched the topology space, which is limited for the ESL model. Still, the default limitation of the geometry projection compared to the density-based method exists and cannot be circumvented—limited topology design space.

Finally, Fig. 6.5 depicts the total number of iterations required before all the layers satisfy the convergence criteria. By assuming a piecewise linear variation of the in-plane displacements and parabolic transverse displacement in the thickness direction, the formulation updates each layer corresponding to their displacement field; thus, each lamina can converge separately once it reaches the convergence criteria as defined. Global convergence criteria, however, could cause several iterations before the design converges; thus, well-defined criteria can be investigated in future works. For simplicity, the local convergence criteria work well for current examples; thus, no modifications are made. As shown in Fig. 6.5, all the layers converge separately; however, the difference is nominal in that local convergence is well-defined, and none of the layers falls into suboptimal solution with respect to other layers in the laminate.

### 6.7.2 A square plate under torsion load

The second example considers a square plate of dimension 75×50×2 under torsion load, and The plate is clamped on the left edge. The initial design consists of 12 bars, and the bounds imposed on the

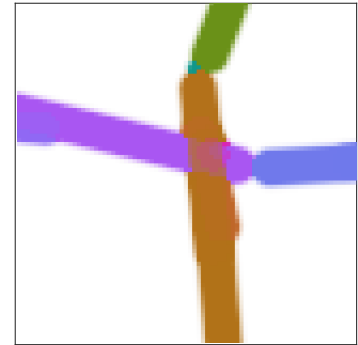


**Figure 6.3: Bending**—The optimized design using GP method.

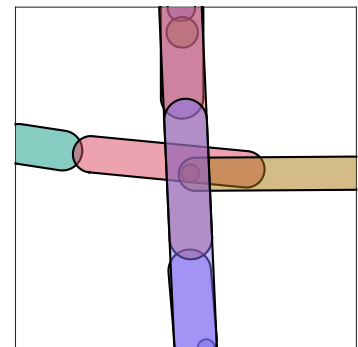
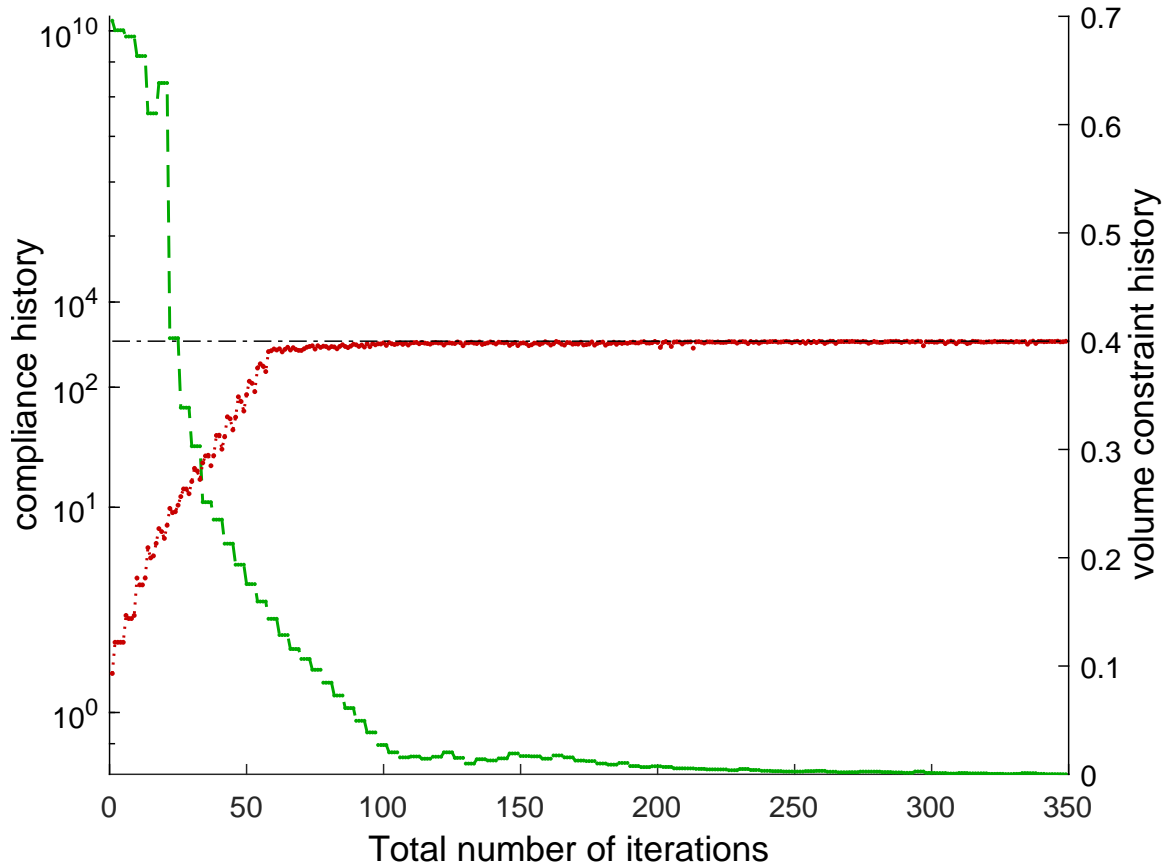


**Figure 6.4: Bending**—The optimized design using GP-AM method.

**Figure 6.5: Bending**—The graph shows the history of objectives and constraints for all the layers on a logarithmic and linear scale, plotted on the left and right axes, respectively. Each iteration generates four data points for every layer. Therefore, the x-axis represents the total number of iterations to converge all the layers. The first layer converged on the 89<sup>th</sup> iteration, the 353<sup>rd</sup> iteration overall. The second layer converged on the 79<sup>th</sup> iteration and the 314<sup>th</sup> iteration overall. The third and fourth layers converged on the 90<sup>th</sup> iteration, which is the 359<sup>th</sup> and 360<sup>th</sup> overall.

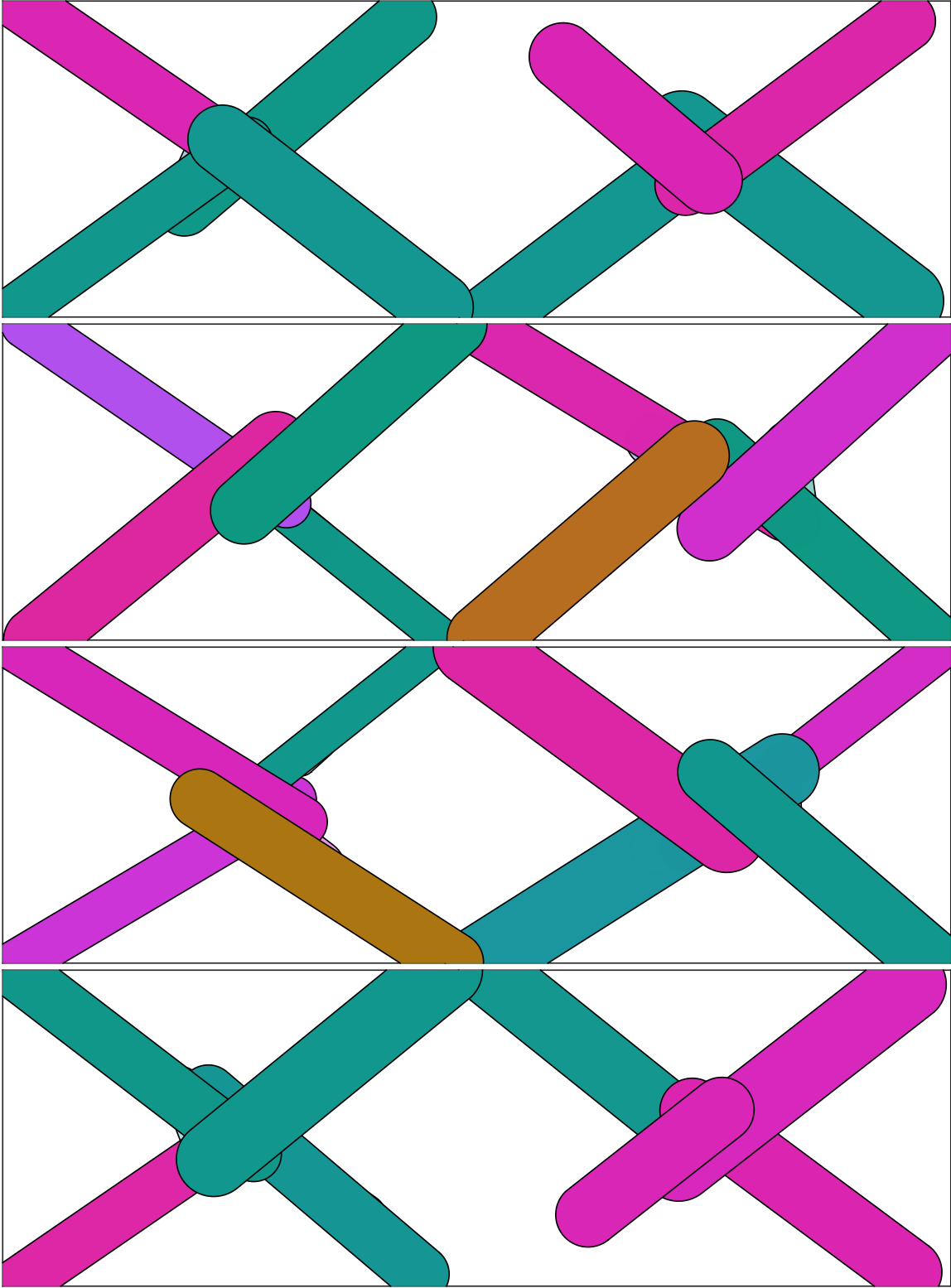


design variables are as follows:

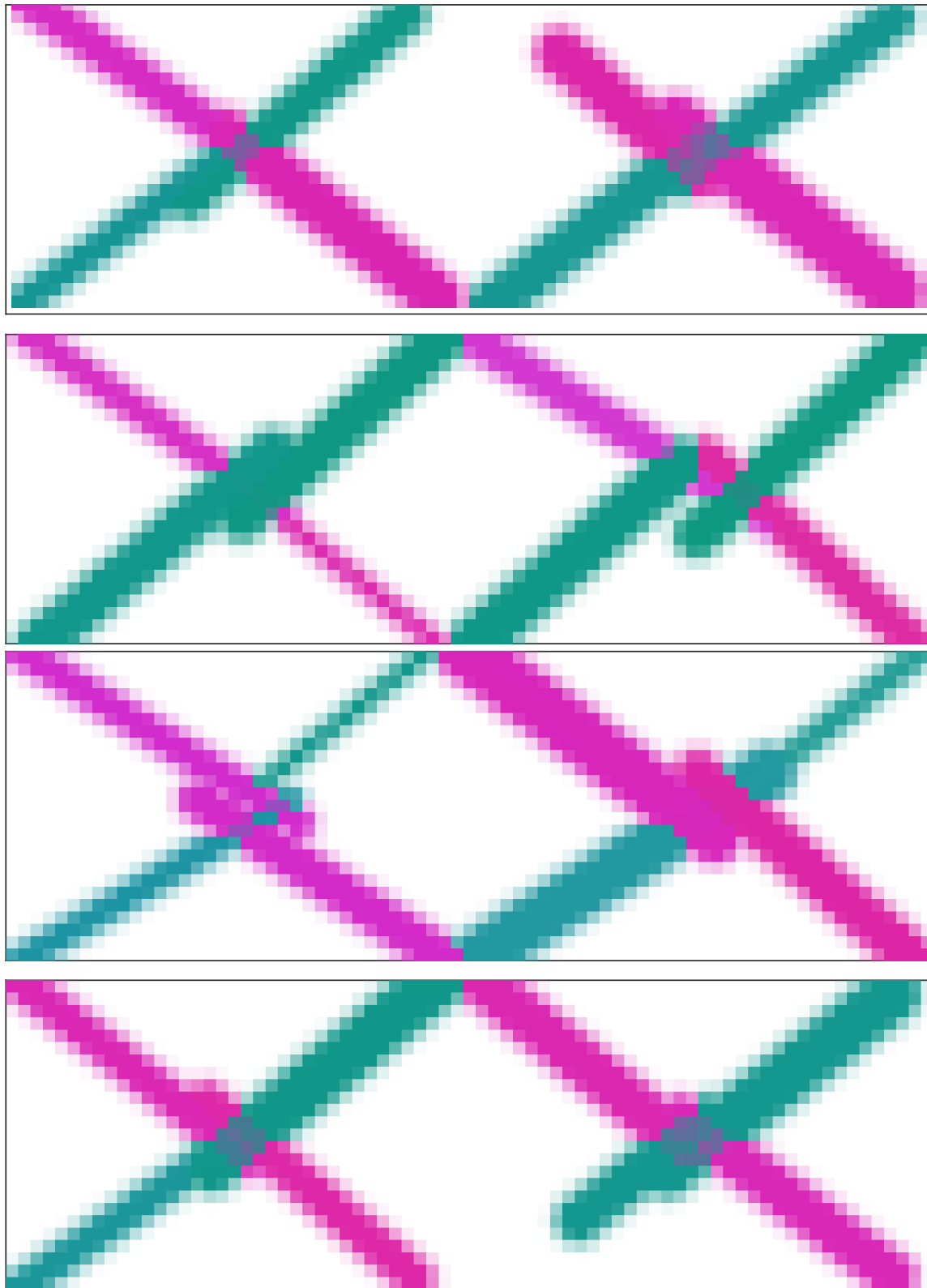
$$\begin{Bmatrix} (0, 0) \\ 1 \\ 0 \end{Bmatrix} \leq \begin{Bmatrix} (\mathbf{x}_{b1}, \mathbf{x}_{b2}) \\ r_b \\ \alpha_b \end{Bmatrix} \leq \begin{Bmatrix} (75, 50) \\ 4 \\ 1 \end{Bmatrix} \quad (6.30)$$

Fig. 6.6 and 6.7 show the design and density for each layer in the MUL-VSCL, wherein the volume fraction constraint of 0.4 is assigned to each layer. Mainly for this example, the left edge is clamped instead of being provided with an anti-symmetric condition, as carried out in the previous chapters—still, a comparison can be drawn between several formulations as dictated until now. When comparing GP-MUL<sup>2</sup> with GP, the multilayered formulation used in GP-MUL<sup>2</sup> helps to retain overlapping FRBs. This

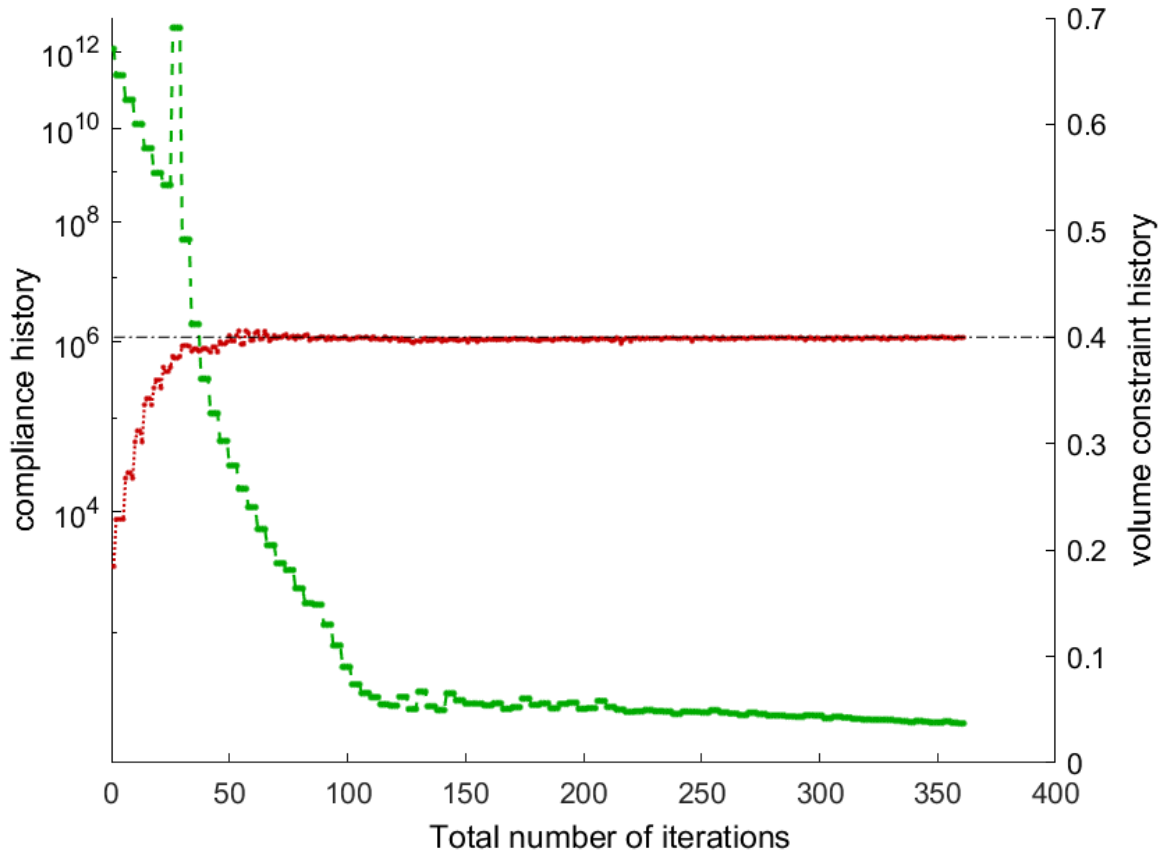
**Figure 6.6: Torison**—The design plots for volume fraction constraint of 0.4 for each layer.



**Figure 6.7: Torison**—The density plots for volume fraction constraint of 0.4 for each layer.



**Figure 6.8: Torsion**—The graph shows the history of objectives and constraints for all the layers on a logarithmic and linear scale, plotted on the left and right axes, respectively. Each iteration generates four data points for every layer. Therefore, the x-axis represents the total number of iterations to converge all the layers. The second layer converged on the 81<sup>th</sup> iteration, the 322<sup>nd</sup> iteration overall. The first, third, and fourth layers converged on the 93<sup>rd</sup> iteration, which is the 370, 371<sup>st</sup> and 372<sup>nd</sup> overall.



is because the overlap can be accommodated in adjacent layers, allowing for optimization of intersecting load paths. By doing so, the features do not dissolve as overlapping features are done separately in different layers. It is important to note that the softargmax penalization factor,  $\beta$ , is set at 100, just like in GP. Therefore, the GP-MUL<sup>2</sup> formulation takes full advantage of attaining discrete components in each layer, making the manufacturing process more accessible. Secondly, the primitive form overlap can expand the material design space, limited to transversely isotropic material in the GP method.

Several similarities can be drawn between GP-MUL<sup>2</sup> and the GP-AM method. The final design incorporates features that ensure it aligns with the laminate’s intersecting load path while limiting long features in the design space. Figure 6.7 demonstrates that a

discrete orientation is always preferred when components overlap in a layer. However, the limitations of the GP method are overcome by reinforcing the penalized features in subsequent layers, enabling overlapping. For comparison, utilizing the similar initial condition GP and GP-AM design is shown in Fig ???. The main difference between the GP-MUL<sup>2</sup> and GP-AM methods, aside from the optimization of stacking sequences, is that the formulation of the latter provides a better way to integrate fiber path-planning strategies. This is because discrete orientation can uniquely define the fiber trajectory, and optimizing simultaneously to satisfy objective functions such as cost can be more straightforward than with single-layer formulations. These goals are postponed for future work and have not been carried out in the thesis.

The different methods proposed for designing and optimizing multilayered structures, including LGP-AM, all lead to similar final designs. This shows that the suitability of geometry projection for monolithic multilayered structures is robust. In LGP-IAM, the feature's length determines the FRBs' dominance. This means that small features may be swallowed if the computational design can realize long FRBs—a limitation of LGP-AM—thus offering limited variability of fiber path in the laminate. Wherein GP-MUL<sup>2</sup> offer FRBs to concatenate and produce ample freedom in the spatial variability of fiber path. However, the designs realized through the several formulations, it can be speculated that the LGP-AM method results in a stiffer and more manufacturable design than other single-layer formulations. Therefore, the density-based approaches, where material distribution offers enriched topology space, can offer better solutions than feature-mapping or ground structure-based topology optimization, which can be contradicted by more research in feature-mapping approaches as carried out for density-based techniques.

Notably, the 1<sup>st</sup> and 4<sup>th</sup> layer results in a disconnected structure. For compliance-based problems, these disconnected components are not an issue as the laminated is fully connected. However, for stress-based topology optimization, each must result in a connected structure; therefore, it is necessary to formulate and postpone it for future work. At the same time, MUL<sup>2</sup> provides excellent flexibility to introduce multi-physics quickly.

## 6.8 Conclusion

The GP-MUL<sup>2</sup> method aims to integrate and validate the GP approach with single-layer formulations, resulting in a unified topology optimization framework for multilayered composite laminates. However, several challenges must be addressed before



**Figure 6.9: Torsion**—The optimized design using GP method.

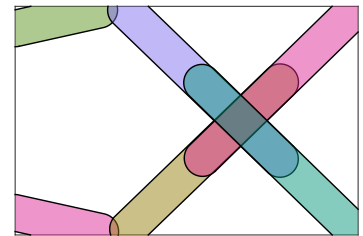


**Figure 6.10: Torsion**—The optimized design using GP-AM method.

tackling a more general problem. For example, the first task can be to optimize the MUL<sup>2</sup> software to handle the high-resolution computational domain. While the MUL<sup>2</sup> method can capture the exact field response even for highly coarse mesh, high resolution is required to capture the structure boundaries, but not necessarily; for example, higher-order elements can be used. Figure 6.7 shows the components' staggered boundaries; thus, a refined mesh is needed to capture the boundaries. However, even a moderate increase in resolution to  $200 \times 50$  can take days to converge due to the need to read and write a file at each iteration and the use of nested for-loops. Using higher-order elements may be helpful, but in general, when using advanced compilers such as the Intel® oneAPI DPC++/C++ Compiler can provide more straightforward and faster strategies for vectorizing (co-arrays), and using high-performance computing tools in the FORTRAN to exploit the full potential of the software.

## *Conclusion and Recommendations*

The design flexibility offered by the CF4 process enables multilayered variable-stiffness composite laminates to be manufactured, which allows the directional properties of CFRP materials to be fully exploited. Steering fiber paths such that the fiber angle orientation varies spatially enables significant improvements in structural performance. Despite the apparent potential, the design tools currently available to engineers only partially exploit the steering capabilities of the CF4 process, for example, using sequential-based topology optimization or performing topology optimization for isotropic material and then laying the fiber along the structural boundaries. The goal of the research conducted and presented in this thesis was outlined in the Section 1.1.2 and ultimately summarized as follows—to demonstrate that developing an efficient design tool for additively manufacturable variable stiffness composite structures is both productive and worthwhile.

A conclusion and future aspect of the research remain to be drawn. To this end, an overview of the study and results presented within this thesis and the conclusions to which they lead are presented in this chapter, including recommendations. The discussion is divided into two parts. The Section 7.1, in which the generic implementation and conclusion of the novel unified design optimization framework for multilayered variable stiffness composite structures scheme are discussed, and Section 7.2, in which several extensions to the developed design framework can be envisaged to improve the structural performance of MUL-VSCLs further.

For conclusions explicitly related to each of the issues presented within this thesis, the reader should refer to the relevant section at the end of each chapter.

### 7.1 Conclusion

We are proposing a tool that can replace heavy structures with lighter ones made of CFRP materials. To achieve this, we are addressing the topology optimization problem for structures made

of anisotropic materials. Our work's significant contribution is developing a method that can optimize the material density and anisotropy distributions concurrently for structures made of any material and further manufactured additively. We are considering transversely isotropic material in 2D and orthotropic materials in 3D, and the proposed method is for additively manufacturable MUL-VSCLs. Our approach has no such assumptions, unlike existing methods that assume a fixed and predefined shape, topology, and anisotropy distribution to ease out the manufacturing process. We start with a maximum 2D and 3D design volume and prescribe boundary conditions, loadings, and manufacturing constraints, which can be extrapolated to several other problem statements because of the full integration of MUL<sup>2</sup> software, for example, frequency or stress-based problem.

The proposed framework combines several ingredients: high-level parameterization of the topology and the material anisotropy, manufacturing constraints, a suitable algorithm for structural optimization for 2D and 3D computational design space, and a simple problem formulation. The maximization of global structural stiffness is solved by reformulating it into a minimization of complementary energy for high-level parameterized primitive design variables, and these primitives come from the definition of the geometry projection method. The combination of the SIMP method with geometry projection to parameterize the topology with the definition of primitives (transversely isotropic material in 2D and orthotropic materials in 3D) to parameterize the elasticity tensor is a very efficient method to deal with the concurrent optimization of the topology and the material anisotropy. Indeed, by doing so, the minimizations of the complementary energy to the design variables are performed analytically, including sensitivity analysis (as well-established sensitivity analysis is available for density-based formulation), and render the computationally efficient design space by dramatically reducing the inordinate amount of design variables that cannot be overlooked in the density-based formulation. Since integrating anisotropy behavior into structural optimization is complex, the advantage of this algorithm is its simplicity. Furthermore, its numerical cost is lower than the main structural optimization algorithms; however, criteria other than global structural stiffness are included.

The numerical application of the method on test cases shows its effectiveness. The numerical test cases are processed by gradually adding complexity to the optimization problem with several boundary conditions, loading conditions, various geometrical aspect ratios, and manufacturing and volume constraints. The framework is based on the MMA algorithm (Method of Mov-

ing Asymptote), a general nonlinear optimizer that can perform practical applications considering several nonlinear performance measures and constraints. Real structures are subjected to one and multiple load cases; thus, solving a multi-load case example demonstrates the framework's versatility. For such a configuration, a transversely isotropic material that exhibits a privileged direction may not be sufficient; thus, several geometry projection formulations are discussed to attain a stiffer and more manufacturable design. Moreover, we introduce a novel framework (LgP-IAM) that allows the definition of multiple orientations in a single layer to optimize material properties to accommodate intersecting load paths locally. Even addressing the various orientations, the final design can be manufactured using conventional or additive manufacturing processes with low computational cost compared to a 3D framework.

Generally speaking, the post-processing of the topology is necessary for density-based formulation. Because the assembly of voxels defines the optimal topology, the shape boundaries could be more precise, transparent, and smoother. Extensive studies are directed to define the geometric surfaces of the optimal shape and to identify the zones of the optimal shape that are thin (structure-like a shell) and slender (structure-like truss). However, such postprocessing steps are entirely taken care of during the optimization by imposing several constraints on the primitives, such as their thickness (radius) and length, which enable ready-to-manufacturable structure without losing any topology characteristics that can be lost during the postprocessing step.

## 7.2 Recommendation

Design studies have been conducted thus far, and both theoretical and numerical results are presented in this thesis for designing and optimizing multilayered variable stiffness composite laminates. The developed optimization framework has proven to be an efficient design tool for variable stiffness composite structures. However, several challenges remain in designing and optimizing multi-layered variable stiffness composite laminates.

It is recommended to conduct numerical and experimental investigations to study the proposed methodology further to enhance confidence in it and create benchmarks to improve its capabilities. For instance, optimizing a plate with a hole can be helpful. It is also recommended that the framework be validated experimentally. The function-to-print workflow, such as the MBB beam problem, is already available, which can almost directly translate into a three-point bend test. An alternative goal could

be to automate the translation of the CAD representation of the components' assembly into an STL file and subsequently be printed by a 3D printer.

The proposed technique has the potential to be extended for laminated-shell structures, which can be quickly accomplished using the GP-MUL<sup>2</sup> formulation. The primary aim of this thesis is to provide a comprehensive tool and methodology for concurrent optimization of material density and anisotropy for MUL-VSCLs, which can be applied to real structures. To achieve this goal, it is necessary to consider additional criteria beyond the global structural stiffness. While a global criterion provides an understanding of the overall behavior of a structure, it only offers a partial picture. For instance, local criteria like maximum displacement at some points are essential for a more comprehensive method. Additionally, structures can be subject to multiple physical phenomena, including buckling and material failure, which must be considered in the optimization process. Integrating the failure of the material in the optimization process by considering a stress constraint<sup>181</sup> using the alternate algorithm must be attempted. However, since considering multiple constraints with this algorithm is challenging, stress constraint aggregation is commonly used for stress-based topology optimization frameworks. Though the local minimizations and the global constraint on stress are difficult to relate to, integrating the stress constraint is complex; therefore, a new algorithm must be devised with the proposed framework. Although these problems couldn't be captured in this academic term, the GP-MUL<sup>2</sup> formulation provides a general framework to develop this practical problem without devising a new formulation altogether.

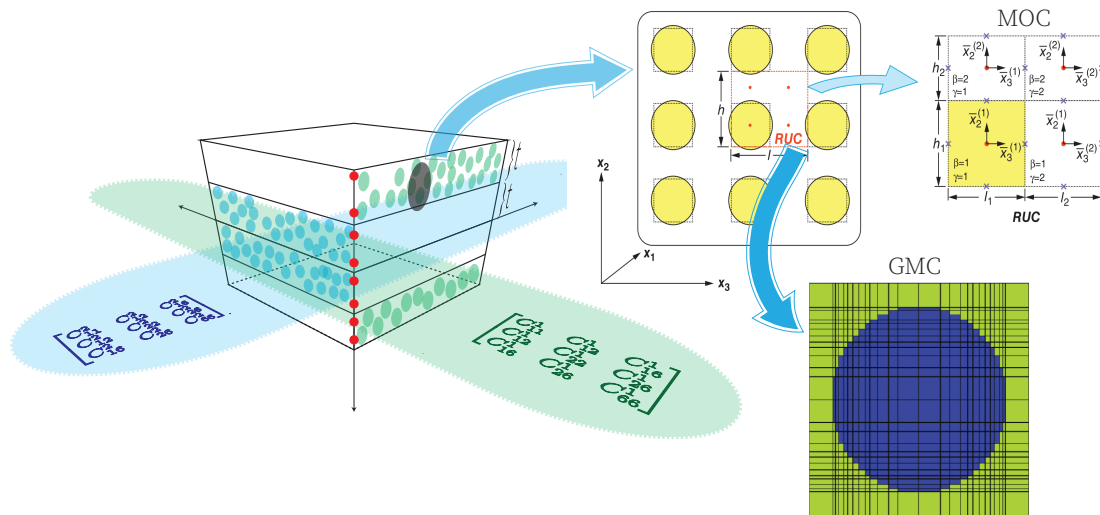
The proposed method is conceptual and involves using a general transversely isotropic and orthotropic material in two and three dimensions (GP-MUL<sup>2</sup>) within the conditions of the linear elasticity regime. The method can be further developed using an anisotropic material in three dimensions, which can accurately predict the response of composite structures. A first step in that direction could be to use a technique like generalized method cells, as depicted in the illustration.

3D printing is a rapidly growing manufacturing method that offers new possibilities for creating materials with complex compositions. With the potential of 3D printing, it may be possible to find a manufacturable material close to the ideal solution; thus, investigating multiscale framework within the geometry projection method can cover a broader range of general materials suitable for multiple load cases and the perfect material obtained through this method is described by the elasticity tensor coefficients that repre-

181 Biyikli *et al.*, "Proportional topology optimization: a new non-sensitivity method for solving stress constrained and minimum compliance problems and its implementation in MATLAB," 2015.

sent a homogenized material. This ideal material can be achieved through a post-processing step that searches for the material’s microstructure, which would be exciting.

**Figure 7.1: Method of Cells**—Illustration of a laminate whose plies are now represented with micromechanics, thereby incorporating the detail of the fiber and matrix constituent materials at a lower length scale. Adapted from [182]



The work completed during this project has opened up numerous exciting possibilities. The developed technique has shown promising results in numerical experiments. The fiber placement process can be incorporated into the method that simultaneously seeks fiber paths based on the CF4 constraints, including the cost function. Several techniques, such as principal stress and loading path analysis in a structure, are implemented for path planning. The path-planning stage largely determines the efficiency of reinforcing fiber placement. Papapetros et al.<sup>104</sup> proposed several optimization schemes to maximize the stiffness of continuous fiber-reinforced parts while subjected to minimum weight constraints. Eckrich et al.<sup>183</sup> utilize a dilate filter from SIMP to constrain feature width and avoid transverse undercuts to the plane’s placement. Sugiyama et al.<sup>27</sup> focused on optimizing the curved fiber trajectories for bolt-jointed panels under tension. This was achieved by minimizing the effective stress concentration, while the fiber orientation was determined based on preliminary stress field calculations. These works can be integrated into the proposed methodology to achieve an effective tool for design for additive manufacturing.

104 Papapetrou et al., “Stiffness-based optimization framework for the topology and fiber paths of continuous fiber composites,” 2020.

183 Eckrich et al., “Structural topology optimization and path planning for composites manufactured by fiber placement technologies,” 2022.

27 Sugiyama et al., “3D printing of optimized composites with variable fiber volume fraction and stiffness using continuous fiber,” 2020.

## References

- 1 Leissa, A. and Martin, A., "Vibration and buckling of rectangular composite plates with variable fiber spacing," *Composite structures*, vol. 14, no. 4, 1990, pp. 339–357. cited on pp. 5, 6
- 2 Gurdal, Z. and Olmedo, R., "In-plane response of laminates with spatially varying fiber orientations-variable stiffness concept," *AIAA journal*, vol. 31, no. 4, 1993, pp. 751–758. cited on pp. 5, 6
- 3 Racionero Sánchez-Majano, A. and Pagani, A., "Buckling and fundamental frequency optimization of tow-steered composites using layerwise structural models," *AIAA Journal*, vol. 61, no. 9, 2023, pp. 4149–4163. cited on p. 5
- 4 Pagani, A., Petrolo, M., and Sánchez-Majano, A., "Stochastic characterization of multiscale material uncertainties on the fibre-matrix interface stress state of composite variable stiffness plates," *International Journal of Engineering Science*, vol. 183, 2023, p. 103787. cited on p. 5
- 5 Peeters, D. and Abdalla, M., "Optimization of ply drop locations in variable-stiffness composites," *AIAA Journal*, vol. 54, no. 5, 2016, pp. 1760–1768. cited on p. 6
- 6 Sjølund, J., Peeters, D., and Lund, E., "A new thickness parameterization for discrete material and thickness optimization," *Structural and Multidisciplinary Optimization*, vol. 58, no. 5, 2018, pp. 1885–1897. cited on pp. 6, 27
- 7 Peeters, D. and Abdalla, M., "Stacking sequence constraints in non-conventional composite laminate optimisation," *57th AIAA/ASCE/AHS/ASC Structures, Structural Dynamics, and Materials Conference*, 2016, p. 1969. cited on p. 6
- 8 Tian, X., Liu, T., Yang, C., Wang, Q., and Li, D., "Interface and performance of 3d printed continuous carbon fiber reinforced pla composites," *Composites Part A: Applied Science and Manufacturing*, vol. 88, 2016, pp. 198–205. cited on pp. 6, 10
- 9 He, Q., Wang, H., Fu, K., and Ye, L., "3d printed continuous cf/pa6 composites: Effect of microscopic voids on mechanical performance," *Composites science and technology*, vol. 191, 2020, p. 108077. cited on pp. 6, 10, 39, 40

- 10 Ghiasi, H., Pasini, D., and Lessard, L., "Optimum stacking sequence design of composite materials Part I: Constant stiffness design," *Compos. Struct.*, vol. 90, 2009, pp. 1–11. DOI: 10.1016/j.compstruct.2009.01.006 cited on pp. 6, 10, 21
- 11 Ye, M., Gao, L., and Li, H., "A design framework for gradually stiffer mechanical metamaterial induced by negative poisson's ratio property," *Materials & Design*, vol. 192, 2020, p. 108751. DOI: 10.1016/j.matdes.2020.108751 cited on p. 9
- 12 Luo, Y., Li, Q., and Liu, S., "Topology optimization of shell-infill structures using an erosion-based interface identification method," *Computer Methods in Applied Mechanics and Engineering*, vol. 355, 2019, pp. 94–112. DOI: 10.1016/j.cma.2019.05.017 cited on p. 9
- 13 Kokkinis, D., Schaffner, M., and Studart, A. R., "Multimaterial magnetically assisted 3D printing of composite materials," *Nat. Commun.*, vol. 6, 2015, pp. 1–10. DOI: 10.1038/ncomms9643 cited on p. 9
- 14 Berrocal, L., Fernández, R., González, S., Perriñán, A., Tudela, S., Vilanova, J., Rubio, L., Martín Márquez, J. M., Guerrero, J., and Lasagni, F., "Topology optimization and additive manufacturing for aerospace components," *Prog. Addit. Manuf.*, vol. 4, 2019, pp. 83–95. DOI: 10.1007/s40964-018-0061-3 cited on p. 9
- 15 Wu, C., Gao, Y., Fang, J., Lund, E., and Li, Q., "Discrete topology optimization of ply orientation for a carbon fiber reinforced plastic (cfrp) laminate vehicle door," *Mater. Des.*, vol. 128, 2017, pp. 9–19. DOI: 10.1016/j.matdes.2017.04.089 cited on p. 9
- 16 Cramer, A. D., Challis, V. J., and Roberts, A. P., "Physically realizable three-dimensional bone prosthesis design with interpolated microstructures," *J. Biomech. Eng.*, vol. 139, 2017. DOI: 10.1115/1.4035481 cited on p. 9
- 17 Fleck, N. A., Deshpande, V. S., and Ashby, M. F., "Micro-architected materials: past, present and future," *Proc. R. Soc. A Math. Phys. Eng. Sci.*, vol. 466, 2010, pp. 2495–2516. DOI: 10.1098/rspa.2010.0215 cited on p. 9
- 18 Maskery, I., Hussey, A., Panesar, A., Aremu, A., Tuck, C., Ashcroft, I., and Hague, R., "An investigation into reinforced and functionally graded lattice structures," *J. Cell. Plast.*, vol. 53, 2017, pp. 151–165. DOI: 10.1177/0021955x16639035 cited on p. 9
- 19 Aremu, A. O., Brennan-Craddock, J. P. J., Panesar, A., Ashcroft, I. A., Hague, R. J. M., Wildman, R. D., and Tuck, C., "A voxel-based method of constructing and skinning conformal and functionally graded lattice structures suitable for additive manufacturing," *Addit. Manuf.*, vol. 13, 2017, pp. 1–13. DOI: 10.1016/j.addma.2016.10.006 cited on p. 9

cited on p. 9

- 20 Cheng, L., Liang, X., Belski, E., Wang, X., Sietins, J. M., Ludwick, S., and To, A., "Natural Frequency Optimization of Variable-Density Additive Manufactured Lattice Structure: Theory and Experimental Validation," *J. Manuf. Sci. Eng.*, vol. 140, 2018. DOI: 10.1115/1.4040622
- 21 Parandoush, P. and Lin, D., "A review on additive manufacturing of polymer-fiber composites," *Compos. Struct.*, vol. 182, 2017, pp. 36–53. DOI: 10.1016/j.compstruct.2017.08.088 cited on p. 9
- 22 Sano, Y., Matsuzaki, R., Ueda, M., Todoroki, A., and Hirano, Y., "3D printing of discontinuous and continuous fibre composites using stereolithography," *Addit. Manuf.*, vol. 24, 2018, pp. 521–527. DOI: 10.1016/j.addma.2018.10.033 cited on p. 9
- 23 Wang, T., Li, N., Link, G., Jelonnek, J., Fleischer, J., Dittus, J., and Kupzik, D., "Load-dependent path planning method for 3d printing of continuous fiber reinforced plastics," *Composites Part A: Applied Science and Manufacturing*, vol. 140, 2021, p. 106 181. DOI: 10.1016/j.compositesa.2020.106181 cited on pp. 10, 38
- 24 Yan, J., Guo, X., and Cheng, G., "Multi-scale concurrent material and structural design under mechanical and thermal loads," *Comput. Mech.*, vol. 57, no. 3, 2016, pp. 437–446. DOI: 10.1007/s00466-015-1255-x cited on p. 10
- 25 Kabir, S. F., Mathur, K., and Seyam, A.-F. M., "A critical review on 3d printed continuous fiber-reinforced composites: History, mechanism, materials and properties," *Composite Structures*, vol. 232, 2020, p. 111 476. cited on p. 10
- 26 Ghiasi, H., Fayazbakhsh, K., Pasini, D., and Lessard, L., "Optimum stacking sequence design of composite materials Part II: Variable stiffness design," *Compos. Struct.*, vol. 93, 2010, pp. 1–13. DOI: 10.1016/j.compstruct.2010.06.001 cited on pp. 10, 21, 26
- 27 Sugiyama, K., Matsuzaki, R., Malakhov, A. V., Polilov, A. N., Ueda, M., Todoroki, A., and Hirano, Y., "3D printing of optimized composites with variable fiber volume fraction and stiffness using continuous fiber," *Compos. Sci. Technol.*, vol. 186, 2020, p. 107 905. DOI: 10.1016/j.compscitech.2019.107905 cited on pp. 10, 145, 170
- 28 Malakhov, A. V. and Polilov, A. N., "Design of composite structures reinforced curvilinear fibres using FEM," *Compos. Part A Appl. Sci. Manuf.*, vol. 87, 2016, pp. 23–28. DOI: 10.1016/j.compositesa.2016.04.005 cited on p. 10
- 29 Arian Nik, M., Fayazbakhsh, K., Pasini, D., and Lessard, L., "Surrogate-based multi-objective optimization of a composite laminate with curvilinear fibers," *Compos. Struct.*, vol. 94, 2012, pp. 2306–2313. DOI: 10.1016/j.compstruct.2012.03.021 cited on p. 10

- 30 Zhang, J., Zhang, W.-H., and Zhu, J.-H., "An extended stress-based method for orientation angle optimization of laminated composite structures," *Acta Mech. Sin.*, vol. 27, 2011, pp. 977–985. DOI: 10.1007/s10409-011-0506-0 cited on p. 10
- 31 Xu, Y., Zhu, J., Wu, Z., Cao, Y., Zhao, Y., and Zhang, W., "A review on the design of laminated composite structures: constant and variable stiffness design and topology optimization," *Adv. Compos. Hybrid Mater.*, vol. 1, 2018, pp. 460–477. DOI: 10.1007/s42114-018-0032-7 cited on p. 10
- 32 Plocher, J. and Panesar, A., "Review on design and structural optimisation in additive manufacturing: Towards next-generation lightweight structures," *Mater. & Des.*, vol. 183, 2019, p. 108 164. DOI: 10.1016/j.matdes.2019.108164 cited on pp. 10, 11
- 33 Bendsøe, M. P. and Kikuchi, N., "Generating optimal topologies in structural design using a homogenization method," *Comput. Methods Appl. Mech. Eng.*, vol. 71, 1988, pp. 197–224. DOI: 10.1016/0045-7825(88)90086-2 cited on pp. 11, 20
- 34 Bendsøe, M. P., "Optimal shape design as a material distribution problem," *Struct. Optim.*, vol. 1, 1989, pp. 193–202. DOI: 10.1007/bf01650949 cited on pp. 11, 20
- 35 Rozvany, G. I. N., Zhou, M., and Birker, T., "Generalized shape optimization without homogenization," *Struct. Optim.*, vol. 4, 1992, pp. 250–252. DOI: 10.1007/bf01742754 cited on pp. 11, 20
- 36 Wang, M. Y., Wang, X., and Guo, D., "A level set method for structural topology optimization," *Comput. Methods Appl. Mech. Eng.*, vol. 192, 2003, pp. 227–246. DOI: 10.1016/s0045-7825(02)00559-5 cited on p. 11
- 37 Allaire, G., Jouve, F., and Toader, A.-M., "Structural optimization using sensitivity analysis and a level-set method," *J. Comput. Phys.*, vol. 194, 2004, pp. 363–393. DOI: 10.1016/j.jcp.2003.09.032 cited on p. 11
- 38 Xie, Y. M. and Steven, G. P., "A simple evolutionary procedure for structural optimization," *Comput. Struct.*, vol. 49, 1993, pp. 885–896. DOI: 10.1016/0045-7949(93)90035-c cited on p. 11
- 39 Bourdin, B. and Chambolle, A., "Design-dependent loads in topology optimization," *ESAIM: Control, Optimisation and Calculus of Variations*, vol. 9, 2003, pp. 19–48. cited on p. 11
- 40 Rozvany, G. I. N., "A critical review of established methods of structural topology optimization," *Struct. Multidiscip. Optim.*, vol. 37, 2009, pp. 217–237. DOI: 10.1007/s00158-007-0217-0 cited on p. 11

- 41 Van Dijk, N. P., Maute, K., Langelaar, M., and Van Keulen, F., "Level-set methods for structural topology optimization: A review," *Struct. Multidiscip. Optim.*, vol. 48, 2013, pp. 437–472. DOI: 10.1007/s00158-013-0912-y
- 42 Deaton, J. D. and Grandhi, R. V., "A survey of structural and multidisciplinary continuum topology optimization: Post 2000," *Struct. Multidiscip. Optim.*, vol. 49, 2014, pp. 1–38. DOI: 10.1007/s00158-013-0956-z cited on p. 11
- 43 Liu, J. S., Parks, G. T., and Clarkson, P. J., "Metamorphic Development: A new topology optimization method for continuum structures," *Struct. Multidiscip. Optim.*, vol. 20, 2000, pp. 288–300. DOI: 10.1007/s001580050159 cited on p. 11
- 44 Liu, C., Du, Z., Zhang, W., Zhu, Y., and Guo, X., "Additive Manufacturing-Oriented Design of Graded Lattice Structures Through Explicit Topology Optimization," *J. Appl. Mech.*, vol. 84, 2017. DOI: 10.1115/1.4036941 cited on p. 11
- 45 Li, H., Luo, Z., Xiao, M., Gao, L., and Gao, J., "A new multiscale topology optimization method for multiphase composite structures of frequency response with level sets," *Comput. Methods Appl. Mech. Eng.*, vol. 356, 2019, pp. 116–144. DOI: 10.1016/j.cma.2019.07.020 cited on p. 11
- 46 Bendsoe, M. P. and Sigmund, O., *Topology optimization: theory, methods, and applications*. Springer Science & Business Media, 2013. cited on p. 11
- 47 Sigmund, O. and Maute, K., "Topology optimization approaches," *Structural and Multidisciplinary Optimization*, vol. 48, no. 6, 2013, pp. 1031–1055. cited on pp. 11, 120
- 48 Xia, L., Xia, Q., Huang, X., and Xie, Y. M., "Bi-directional evolutionary structural optimization on advanced structures and materials: A comprehensive review," *Archives of Computational Methods in Engineering*, vol. 25, 2018, pp. 437–478. DOI: 10.1007/s11831-016-9203-2 cited on pp. 11, 19
- 49 Wein, F., Dunning, P. D., and Norato, J. A., "A review on feature-mapping methods for structural optimization," *Struct. Multidiscip. Optim.*, vol. 62, 2020, pp. 1597–1638. DOI: 10.1007/s00158-020-02649-6 cited on pp. 11, 29
- 50 Ferreira, I., Machado, M., Alves, F., and Torres Marques, A., "A review on fibre reinforced composite printing via FFF," *Rapid Prototyping Journal*, vol. 25, 2019, pp. 972–988. DOI: 10.1108/rpj-01-2019-0004 cited on p. 11
- 51 Sigmund, O., "Morphology-based black and white filters for topology optimization," *Structural and Multidisciplinary Optimization*, vol. 33, 2007, pp. 401–424. cited on p. 12  
cited on p. 11

- 52 Nikbakt, S., Kamarian, S., and Shakeri, M., "A review on optimization of composite structures part i: Laminated composites," *Composite Structures*, vol. 195, 2018, pp. 158–185.
- 53 Nikbakht, S., Kamarian, S., and Shakeri, M., "A review on optimization of composite structures part ii: Functionally graded materials," *Composite Structures*, vol. 214, 2019, pp. 83–102. cited on p. 11
- 54 Talischi, C., Paulino, G. H., Pereira, A., and Menezes, I. F., "Polytop: A matlab implementation of a general topology optimization framework using unstructured polygonal finite element meshes," *Structural and Multidisciplinary Optimization*, vol. 45, no. 3, 2012, pp. 329–357. cited on p. 14
- 55 Sigmund, O. and Petersson, J., "Numerical instabilities in topology optimization: A survey on procedures dealing with checkerboards, mesh-dependencies and local minima," *Structural optimization*, vol. 16, no. 1, 1998, pp. 68–75. cited on pp. 15, 20, 120
- 56 Eschenauer, H. A., Kobelev, V. V., and Schumacher, A., "Bubble method for topology and shape optimization of structures," *Structural Optimization*, vol. 8, 1994, pp. 42–51. cited on p. 15
- 57 Sokolowski, J. and Zochowski, A., "On the topological derivative in shape optimization," *SIAM journal on control and optimization*, vol. 37, no. 4, 1999, pp. 1251–1272. cited on p. 15
- 58 Novotny, A. A., Feijóo, R. A., Taroco, E., and Padra, C., "Topological sensitivity analysis," *Computer methods in applied mechanics and engineering*, vol. 192, no. 7-8, 2003, pp. 803–829. cited on p. 15
- 59 Upadhyay, B. D., Sonigra, S. S., and Daxini, S. D., "Numerical analysis perspective in structural shape optimization: a review post 2000," *Adv. Eng. Softw.*, vol. 155, 2021. DOI: 10.1016/j.advengsoft.2021.102992 cited on p. 15
- 60 Wang, Y., Wang, Z., Xia, Z., and Poh, L. H., "Structural design optimization using isogeometric analysis: a comprehensive review," *Comput. Model. Eng. Sci.*, vol. 117, 2020, pp. 455–507. DOI: 10.31614/cmcs.2018.04603 cited on p. 15
- 61 Gao, J., Xiao, M., Zhang, Y., and Gao, L., "A comprehensive review of isogeometric topology optimization: methods, applications and prospects," *Chinese J. Mech. Eng. (English Ed.)*, vol. 33, 2020, pp. 1–14. DOI: 10.1186/s10033-020-00503-w/figures/12 cited on p. 15
- 62 Sethian, J. A., *Level set methods and fast marching methods: Evolving interfaces in computational geometry, fluid mechanics, computer vision, and materials science*. Cambridge university press, 1999, vol. 3. cited on p. 16
- 63 Sethian, J. A., "Evolution, implementation, and application of level set and fast marching methods for advancing fronts," *Journal of computational physics*, vol. 169, no. 2, 2001, pp. 503–555. cited on p. 16

- 64 Burger, M. and Osher, S. J., "A survey on level set methods for inverse problems and optimal design," *European journal of applied mathematics*, vol. 16, 2005, pp. 263–301. cited on p. 16
- 65 Sivapuram, R., Picelli, R., and Xie, Y. M., "Topology optimization of binary microstructures involving various non-volume constraints," *Computational Materials Science*, vol. 154, 2018, pp. 405–425. DOI: 10.1016/j.commatsci.2018.08.008 cited on p. 19
- 66 Munk, D. J., "A bidirectional evolutionary structural optimization algorithm for mass minimization with multiple structural constraints," *International Journal for Numerical Methods in Engineering*, vol. 118, 2019, pp. 93–120. DOI: 10.1002/nme.6005 cited on p. 19
- 67 Wang, Z. and Sobey, A., "A comparative review between Genetic Algorithm use in composite optimisation and the state-of-the-art in evolutionary computation," *Compos. Struct.*, vol. 233, 2020. DOI: 10.1016/j.compstruct.2019.111739 cited on p. 19
- 68 Sigmund, O., "On the usefulness of non-gradient approaches in topology optimization," *Struct. Multidiscip. Optim.*, vol. 43, 2011, pp. 589–596. DOI: 10.1007/s00158-011-0638-7 cited on pp. 19, 21, 141
- 69 Borrvall, T., "Topology optimization of elastic continua using restriction," *Archives of Computational Methods in Engineering*, vol. 8, no. 4, 2001, pp. 351–385. cited on p. 20
- 70 Hasançebi, O., Çarbas, S., and Saka, M. P., "Improving the performance of simulated annealing in structural optimization," *Struct. Multidiscip. Optim.*, vol. 41, 2010, pp. 189–203. DOI: 10.1007/s00158-009-0418-9 cited on p. 21
- 71 Reuschel, D. and Mattheck, C., "Three-dimensional fibre optimisation with computer aided internal optimisation," *Aeronaut. J.*, vol. 103, no. 1027, 1999, pp. 415–420. DOI: 10.1017/s0001924000027962 cited on p. 21
- 72 Voelkl, H. and Wartzack, S., "Design for composites: tailor-made, bio-inspired topology optimization for fiber-reinforced plastics," *Proc. Int. Des. Conf. Des.*, vol. 1, 2018, pp. 499–510. DOI: 10.21278/idc.2018.0126 cited on p. 21
- 73 Andreassen, E., Clausen, A., Schevenels, M., Lazarov, B. S., and Sigmund, O., "Efficient topology optimization in matlab using 88 lines of code," *Structural and Multidisciplinary Optimization*, vol. 43, 2011, pp. 1–16. cited on pp. 21, 44, 57
- 74 Svanberg, K., "The method of moving asymptotes—a new method for structural optimization," *Int. J. Numer. Methods Eng.*, vol. 24, 1987, pp. 359–373. DOI: 10.1002/nme.1620240207 cited on pp. 21, 22, 54, 121

cited on p. 21

- 75 Dunning, P. D. and Kim, H. A., "Introducing the sequential linear programming level-set method for topology optimization," *Structural and Multidisciplinary Optimization*, vol. 51, 2015, pp. 631–643. DOI: 10.1007/s00158-014-1174-z
- 76 Shen, Y. and Branscomb, D., "Orientation optimization in anisotropic materials using gradient descent method," *Compos. Struct.*, vol. 234, 2020, p. 111 680. DOI: 10.1016/j.compstruct.2019.111680 cited on p. 21
- 77 Kim, N. H., Dong, T., Weinberg, D., and Dalidd, J., "Generalized optimality criteria method for topology optimization," *Appl. Sci.*, vol. 11, 2021. DOI: 10.3390/app11073175 cited on p. 21
- 78 Patnaik, S. N., Guptill, J. D., and Berke, L., "Merits and limitations of optimality criteria method for structural optimization," *Int. J. Numer. Methods Eng.*, vol. 38, 1995, pp. 3087–3120. DOI: 10.1002/nme.1620381806 cited on p. 22
- 79 Fuchs, M. and Ali, R. H., "A family of homogeneous analysis models for the design of scalable structures," *Structural optimization*, vol. 2, no. 3, 1990, pp. 143–152. cited on p. 22
- 80 Fleury, C., "Conlin: An efficient dual optimizer based on convex approximation concepts," *Structural optimization*, vol. 1, 1989, pp. 81–89. DOI: 10.1007/bf01637664 cited on p. 22
- 81 Barthelemy, J. -. M. and Haftka, R. T., "Approximation concepts for optimum structural design — a review," *Structural optimization*, vol. 5, 1993, pp. 129–144. DOI: 10.1007/bf01743349 cited on p. 22
- 82 Zowe, J., Kocvara, M., and Bendsøe, M. P., "Free material optimization via mathematical programming," *Math. Program.*, vol. 79, 1997, pp. 445–466. DOI: 10.1007/bf02614328 cited on p. 24
- 83 Ben-Tal, A., Kocvara, M., Nemirovski, A., and Zowe, J., "Free material design via semidefinite programming: the multiload case with contact conditions," *SIAM J. Optim.*, vol. 9, 1999, pp. 813–832. DOI: 10.1137/s1052623497327994 cited on p. 24
- 84 Nomura, T., Kawamoto, A., Kondoh, T., Dede, E. M., Lee, J., Song, Y., and Kikuchi, N., "Inverse design of structure and fiber orientation by means of topology optimization with tensor field variables," *Composites Part B: Engineering*, vol. 176, 2019, p. 107 187. DOI: 10.1016/j.compositesb.2019.107187 cited on p. 24
- 85 Michell, A. G. M., "Lviii. the limits of economy of material in frame-structures," *The London, Edinburgh, and Dublin Philosophical Magazine and Journal of Science*, vol. 8, no. 47, 1904, pp. 589–597. cited on p. 24
- 86 Pedersen, P., "On optimal orientation of orthotropic materials," *Struct. Optim.*, vol. 1, 1989, pp. 101–106. DOI: 10.1007/bf01637666 cited on pp. 24, 89  
cited on p. 24

- 87 Pedersen, P., "Bounds on elastic energy in solids of orthotropic materials," *Struct. Optim.*, vol. 2, 1990, pp. 55–63. DOI: 10.1007/bf01743521
- 88 Pedersen, P., "On thickness and orientational design with orthotropic materials," *Struct. Optim.*, vol. 3, 1991, pp. 69–78. DOI: 10.1007/bf01743275 cited on pp. 24, 89
- 89 Cheng, H. C., Kikuchi, N., and Ma, Z. D., "An improved approach for determining the optimal orientation of orthotropic material," *Struct. Optim.*, vol. 8, 1994, pp. 101–112. DOI: 10.1007/bf01743305 cited on pp. 24, 25
- 90 Zhou, M. and Rozvany, G. I. N., "Dcoc: An optimality criteria method for large systems part i: Theory," *Structural optimization*, vol. 5, 1992, pp. 12–25. DOI: 10.1007/bf01744690 cited on p. 24
- 91 Zhou, M. and Rozvany, G. I., "Dcoc: an optimality criteria method for large systems part ii: algorithm," *Struct. Optim.*, vol. 6, 1993, pp. 250–262. DOI: 10.1007/bf01743384 cited on p. 24
- 92 Suzuki, K. and Kikuchi, N., "A homogenization method for shape and topology optimization," *Comput. Methods Appl. Mech. Eng.*, vol. 93, no. 3, 1991, pp. 291–318. DOI: 10.1016/0045-7825(91)90245-2 cited on p. 24
- 93 Díaz, A. R. and Bendsøe, M. P., "Shape optimization of structures for multiple loading conditions using a homogenization method," *Struct Optim.*, vol. 4, 1992, pp. 17–22. DOI: 10.1007/bf01894077 cited on p. 24
- 94 Gea, H. C. and Luo, J. H., "On the stress-based and strain-based methods for predicting optimal orientation of orthotropic materials," *Struct. Multidiscip. Optim.*, vol. 26, 2004, pp. 229–234. DOI: 10.1007/s00158-003-0348-x cited on p. 25
- 95 Lu, Y. and Tong, L., "Concurrent optimization of topologies and fiber orientations for laminated composite structures," *Composite Structures*, 2022, p. 115749. cited on p. 25
- 96 Qiu, Z., Li, Q., Luo, Y., and Liu, S., "Concurrent topology and fiber orientation optimization method for fiber-reinforced composites based on composite additive manufacturing," *Computer Methods in Applied Mechanics and Engineering*, vol. 395, 2022, p. 114962. cited on pp. 25, 28, 29, 38
- 97 Luo, J. H. and Gea, H. C., "Optimal orientation of orthotropic materials using an energy based method," *Struct. Optim.*, vol. 15, no. 3-4, 1998, pp. 230–236. DOI: 10.1007/bf01203536 cited on p. 25
- 98 Luo, J. H. and Gea, H. C., "Optimal bead orientation of 3D shell/plate structures," *Finite Elem. Anal. Des.*, vol. 31, 1998, pp. 55–71. DOI: 10.1016/s0168-874x(98)00048-1 cited on p. 25
- cited on p. 25

- 99 Yan, X., Xu, Q., Hua, H., Huang, D., and Huang, X., "Concurrent topology optimization of structures and orientation of anisotropic materials," *Eng. Optim.*, vol. 52, 2020, pp. 1598–1611. DOI: 10.1080/0305215x.2019.1663186
- 100 Bruyneel, M. and Zein, S., "A modified fast marching method for defining fiber placement trajectories over meshes," *Comput. & Struct.*, vol. 125, 2013, pp. 45–52. DOI: 10.1016/j.compstruc.2013.04.015 cited on p. 26
- 101 Lemaire, E., Zein, S., and Bruyneel, M., "Optimization of composite structures with curved fiber trajectories," *Compos. Struct.*, vol. 131, 2015, pp. 895–904. DOI: 10.1016/j.compstruct.2015.06.040 cited on p. 26
- 102 Hao, P., Liu, C., Liu, X., Yuan, X., Wang, B., Li, G., Dong, M., and Chen, L., "Isogeometric analysis and design of variable-stiffness aircraft panels with multiple cutouts by level set method," *Compos. Struct.*, vol. 206, 2018, pp. 888–902. DOI: 10.1016/j.compstruct.2018.08.086 cited on p. 26
- 103 Brampton, C. J., Wu, K. C., and Kim, H. A., "New optimization method for steered fiber composites using the level set method," *Struct. Multidiscip. Optim.*, vol. 52, 2015, pp. 493–505. DOI: 10.1007/s00158-015-1256-6 cited on p. 26
- 104 Papapetrou, V. S., Patel, C., and Tamijani, A. Y., "Stiffness-based optimization framework for the topology and fiber paths of continuous fiber composites," *Compos. Part B Eng.*, vol. 183, 2020, p. 107681. DOI: 10.1016/j.compositesb.2019.107681 cited on pp. 26, 37, 170
- 105 Tian, Y., Pu, S., Shi, T., and Xia, Q., "A parametric divergence-free vector field method for the optimization of composite structures with curvilinear fibers," *Comput. Methods Appl. Mech. Eng.*, vol. 373, 2021, p. 113574. DOI: 10.1016/j.cma.2020.113574 cited on p. 26
- 106 Riche, R. L. and Haftka, R. T., "Optimization of laminate stacking sequence for buckling load maximization by genetic algorithm," *AIAA journal*, vol. 31, no. 5, 1993, pp. 951–956. cited on p. 26
- 107 Nagendra, S., Jestin, D., Gürdal, Z., Haftka, R. T., and Watson, L. T., "Improved genetic algorithm for the design of stiffened composite panels," *Computers & Structures*, vol. 58, 1996, pp. 543–555. DOI: 10.1016/0045-7949(95)00160-i cited on p. 26
- 108 Liu, B., Haftka, R. T., Akgün, M. A., and Todoroki, A., "Permutation genetic algorithm for stacking sequence design of composite laminates," *Computer methods in applied mechanics and engineering*, vol. 186, no. 2-4, 2000, pp. 357–372. cited on p. 26

- 109 Stegmann, J. and Lund, E., "Discrete material optimization of general composite shell structures," *Int. J. Numer. Methods Eng.*, vol. 62, no. 14, 2005, pp. 2009–2027. DOI: <https://doi.org/10.1002/nme.1259>
- 110 Bendsøe, M. P. and Sigmund, O., "Material interpolation schemes in topology optimization," *Arch. Appl. Mech.*, vol. 69, 1999, pp. 635–654. DOI: 10.1007/s004190050248 cited on pp. 26, 50
- 111 Yin, L. and Ananthasuresh, G. K., "Topology optimization of compliant mechanisms with multiple materials using a peak function material interpolation scheme," *Struct. Multidiscip. Optim.*, vol. 23, 2001, pp. 49–62. DOI: 10.1007/s00158-001-0165-z cited on pp. 26, 28
- 112 Bruyneel, M., "SFP—a new parameterization based on shape functions for optimal material selection: application to conventional composite plies," *Struct. Multidiscip. Optim.*, vol. 43, 2011, pp. 17–27. DOI: 10.1007/s00158-010-0548-0 cited on p. 26
- 113 Gao, T., Zhang, W., and Duysinx, P., "A bi-value coding parameterization scheme for the discrete optimal orientation design of the composite laminate," *Int. J. Numer. Methods Eng.*, vol. 91, 2012, pp. 98–114. DOI: <https://doi.org/10.1002/nme.4270> cited on p. 26
- 114 Sørensen, S. N., Sørensen, R., and Lund, E., "Dmto—a method for discrete material and thickness optimization of laminated composite structures," *Structural and Multidisciplinary Optimization*, vol. 50, no. 1, 2014, pp. 25–47. cited on p. 26
- 115 Sørensen, R. and Lund, E., "Thickness filters for gradient based multi-material and thickness optimization of laminated composite structures," *Structural and Multidisciplinary Optimization*, vol. 52, no. 2, 2015, pp. 227–250. cited on p. 27
- 116 Hozicić, D., Thore, C.-J., Cameron, C., and Loukil, M., "A new method for simultaneous material and topology optimization of composite laminate structures using hyperbolic function parametrization," *Composite structures*, vol. 276, 2021, p. 114374. cited on p. 27
- 117 Kiyono, C. Y., Silva, E. C. N., and Reddy, J. N., "A novel fiber optimization method based on normal distribution function with continuously varying fiber path," *Compos. Struct.*, vol. 160, 2017, pp. 503–515. DOI: 10.1016/j.compstruct.2016.10.064 cited on pp. 27, 28
- 118 Silva, A. L. F. da, Salas, R. A., and Silva, E. C. N., "Topology optimization of composite hyperelastic material using spimfo-method," *Meccanica*, vol. 56, no. 2, 2021, pp. 417–437. DOI: 10.1007/s11012-020-01277-0 cited on p. 27

- 119 Salas, R. A., Ramírez-Gil, F. J., Montealegre-Rubio, W., Silva, E. C. N., and Reddy, J. N., "Optimized dynamic design of laminated piezo-composite multi-entry actuators considering fiber orientation," *Comput. Methods Appl. Mech. Eng.*, vol. 335, 2018, pp. 223–254. DOI: 10.1016/j.cma.2018.02.011
- 120 Luo, Y., Chen, W., Liu, S., Li, Q., and Ma, Y., "A discrete-continuous parameterization (dcp) for concurrent optimization of structural topologies and continuous material orientations," *Composite Structures*, vol. 236, 2020, p. 111 900. cited on pp. 27, 28
- 121 Nomura, T., Dede, E. M., Lee, J., Yamasaki, S., Matsumori, T., Kawamoto, A., and Kikuchi, N., "General topology optimization method with continuous and discrete orientation design using isoparametric projection," *Int. J. Numer. Methods Eng.*, vol. 101, 2015, pp. 571–605. DOI: <https://doi.org/10.1002/nme.4799> cited on p. 27
- 122 Xia, Q. and Shi, T., "Optimization of composite structures with continuous spatial variation of fiber angle through shepard interpolation," *Compos. Struct.*, vol. 182, 2017, pp. 273–282. DOI: 10.1016/j.compstruct.2017.09.052 cited on p. 28
- 123 Xia, Q. and Shi, T., "A cascadic multilevel optimization algorithm for the design of composite structures with curvilinear fiber based on shepard interpolation," *Compos. Struct.*, vol. 188, 2018, pp. 209–219. DOI: 10.1016/j.compstruct.2018.01.013 cited on p. 28
- 124 Ding, H. and Xu, B., "A novel discrete–continuous material orientation optimization model for stiffness-based concurrent design of fiber composite," *Composite Structures*, vol. 273, 2021, p. 114 288. cited on p. 28
- 125 Norato, J. A., Bell, B. K., and Tortorelli, D. A., "A geometry projection method for continuum-based topology optimization with discrete elements," *Comput. Methods Appl. Mech. Eng.*, vol. 293, 2015, pp. 306–327. DOI: 10.1016/j.cma.2015.05.005 cited on pp. 32, 44, 51, 53, 71, 73, 75, 82, 95, 111–113
- 126 Smith, H. and Norato, J. A., "Topology optimization with discrete geometric components made of composite materials," *Computer Methods in Applied Mechanics and Engineering*, vol. 376, 2021, p. 113 582. DOI: 10.1016/j.cma.2020.113582 cited on pp. 32, 34, 53, 68, 70, 71, 73, 82, 110, 189
- 127 Sun, Z., Song, Z., Song, J., and Li, H., "Structural optimization of fiber-reinforced material based on moving morphable components (mmcs)," *Acta Mechanica Solida Sinica*, 2022, pp. 1–15. cited on p. 32
- 128 Udupa, G., Rao, S. S., and Gangadharan, K. V., "Functionally graded composite materials: An overview," *Procedia Materials Science*, vol. 5, 2014, pp. 1291–1299. DOI: 10.1016/j.mspro.2014.07.442 cited on p. 32
- cited on p. 34

- 129 Fernandez, F., Compel, W. S., Lewicki, J. P., and Tortorelli, D. A., "Optimal design of fiber reinforced composite structures and their direct ink write fabrication," *Computer Methods in Applied Mechanics and Engineering*, vol. 353, 2019, pp. 277–307. DOI: 10.1016/j.cma.2019.05.010
- 130 Jiang, D., Høglund, R., and Smith, D. E., "Continuous fiber angle topology optimization for polymer composite deposition additive manufacturing applications," *Fibers*, vol. 7, no. 2, 2019, p. 14. cited on p. 34
- 131 Chandrasekhar, A., Kumar, T., and Suresh, K., "Build optimization of fiber-reinforced additively manufactured components," *Structural and Multidisciplinary Optimization*, vol. 61, no. 1, 2020, pp. 77–90. cited on p. 34
- 132 Lee, J., Kim, D., Nomura, T., Dede, E. M., and Yoo, J., "Topology optimization for continuous and discrete orientation design of functionally graded fiber-reinforced composite structures," *Compos. Struct.*, vol. 201, 2018, pp. 217–233. DOI: 10.1016/j.compstruct.2018.06.020 cited on p. 34
- 133 Desai, A., Mogra, M., Sridhara, S., Kumar, K., Sessa, G., and Ananthasuresh, G., "Topological-derivative-based design of stiff fiber-reinforced structures with optimally oriented continuous fibers," *Structural and Multidisciplinary Optimization*, vol. 63, no. 2, 2021, pp. 703–720. cited on p. 34
- 134 Wu, J., Sigmund, O., and Groen, J. P., "Topology optimization of multi-scale structures: a review," *Struct. Multidiscip. Optim.*, vol. 63, 2021, pp. 1455–1480. DOI: 10.1007/s00158-021-02881-8 cited on p. 35
- 135 Kim, D., Lee, J., Nomura, T., Dede, E. M., Yoo, J., and Min, S., "Topology optimization of functionally graded anisotropic composite structures using homogenization design method," *Comput. Methods Appl. Mech. Eng.*, vol. 369, 2020, p. 113 220. DOI: 10.1016/j.cma.2020.113220 cited on pp. 35, 36
- 136 Jung, T., Lee, J., Nomura, T., and Dede, E. M., "Inverse design of three-dimensional fiber reinforced composites with spatially-varying fiber size and orientation using multiscale topology optimization," *Composite Structures*, vol. 279, 2022, p. 114 768. DOI: 10.1016/j.compstruct.2021.114768 cited on p. 35
- 137 Boddeti, N., Tang, Y., Maute, K., Rosen, D. W., and Dunn, M. L., "Optimal design and manufacture of variable stiffness laminated continuous fiber reinforced composites," *Scientific reports*, vol. 10, no. 1, 2020, pp. 1–15. cited on pp. 35, 94
- 138 Hvejsel, C. F. and Lund, E., "Material interpolation schemes for unified topology and multi-material optimization," *Struct. Multidiscip. Optim.*, vol. 43, 2011, pp. 811–825. DOI: 10.1007/s00158-011-0625-z cited on p. 36

- 139 Kennedy, G. J. and Martins, J. R., "A laminate parametrization technique for discrete ply-angle problems with manufacturing constraints," *Structural and Multidisciplinary Optimization*, vol. 48, 2013, pp. 379–393. cited on p. 36
- 140 Lund, E., "Discrete material and thickness optimization of laminated composite structures including failure criteria," *Structural and Multidisciplinary Optimization*, vol. 57, 2018, pp. 2357–2375. DOI: 10.1007/s00158-017-1866-2 cited on p. 36
- 141 Gandhi, Y., Pirondi, A., and Collini, L., "Optimal design of shape memory alloy composite under deflection constraint," *Materials*, vol. 12, no. 11, 2019, p. 1733. cited on p. 37
- 142 Tsai, S. W. and Pagano, N. J., "Invariant properties of composite materials." 1968, pp. 233–253. cited on p. 37
- 143 Albazzan, M. A., Harik, R., Tatting, B. F., and Gürdal, Z., "Efficient design optimization of nonconventional laminated composites using lamination parameters: A state of the art," *Composite Structures*, vol. 209, 2019, pp. 362–374. cited on p. 37
- 144 Bohrer, R. Z. G. and Kim, I. Y., "Concurrent topology and stacking sequence optimization of composite laminate plates using lamination parameters," *Composite Structures*, vol. 276, 2021, p. 114556. cited on p. 37
- 145 Demir, E., Yousefi-Louyeh, P., and Yildiz, M., "Design of variable stiffness composite structures using lamination parameters with fiber steering constraint," *Composites Part B: Engineering*, vol. 165, 2019, pp. 733–746. cited on p. 37
- 146 Peeters, D., Hong, Z., and Abdalla, M., "A compliance approximation method applied to variable stiffness composite optimisation," *Structural and Multidisciplinary Optimization*, vol. 58, no. 5, 2018, pp. 1981–2001. cited on p. 37
- 147 Peeters, D., Baalen, D. van, and Abdallah, M., "Combining topology and lamination parameter optimisation," *Structural and Multidisciplinary Optimization*, vol. 52, no. 1, 2015, pp. 105–120. cited on p. 37
- 148 Chen, Y. and Ye, L., "Topological design for 3D-printing of carbon fibre reinforced composite structural parts," *Compos. Sci. Technol.*, vol. 204, 2021, p. 108644. DOI: 10.1016/j.compscitech.2020.108644 cited on p. 38
- 149 Liu, J. and Yu, H., "Concurrent deposition path planning and structural topology optimization for additive manufacturing," *Rapid Prototyping Journal*, vol. 23, 2017, pp. 930–942. DOI: 10.1108/rpj-05-2016-0087 cited on p. 38
- 150 Schmidt, M. P., Couret, L., Gout, C., and Pedersen, C. B., "Structural topology optimization with smoothly varying fiber orientations," *Struct. Multidiscip. Optim.*, vol. 62, 2020, pp. 3105–3126. DOI: 10.1007/s00158-020-02657-6 cited on p. 38

- 151 Kubalak, J. R., Wicks, A. L., and Williams, C. B., "Investigation of parameter spaces for topology optimization with three-dimensional orientation fields for multi-axis additive manufacturing," *Journal of Mechanical Design*, vol. 143, 2020. DOI: 10.1115/1.4048117 cited on p. 38
- 152 Fedulov, B., Fedorenko, A., Khaziev, A., and Antonov, F., "Optimization of parts manufactured using continuous fiber three-dimensional printing technology," *Composites Part B: Engineering*, vol. 227, 2021, p. 109406. DOI: 10.1016/j.compositesb.2021.109406 cited on p. 38
- 153 Lyu, N. and Saitou, K., "Topology optimization of multicomponent beam structure via decomposition-based assembly synthesis," *Journal of Mechanical Design*, vol. 127, 2005, pp. 170–183. DOI: 10.1115/1.1814671 cited on p. 38
- 154 Zhou, Y. and Saitou, K., "Gradient-based multi-component topology optimization for stamped sheet metal assemblies (MTO-s)," *Structural and Multidisciplinary Optimization*, vol. 58, 2018, pp. 83–94. DOI: 10.1007/s00158-017-1878-y cited on p. 38
- 155 Smith, H. and Norato, J., "Topology optimization of structures made of fiber-reinforced plates," *Structural and Multidisciplinary Optimization*, vol. 65, no. 2, 2022, p. 58. cited on pp. 44, 68, 73
- 156 Smith, H. and Norato, J., "Simultaneous material and topology optimization of composite laminates," *Computer Methods in Applied Mechanics and Engineering*, vol. 404, 2023, p. 115781. cited on pp. 44, 68, 73
- 157 Bergen, S. van, Norte, R. A., and Aragón, A. M., "An interface-enriched generalized finite element method for the analysis and topology optimization of 2-d electromagnetic problems," *Computer Methods in Applied Mechanics and Engineering*, vol. 421, 2024, p. 116748. cited on p. 46
- 158 Svanberg, K., "Mma and gmma, versions september 2007," *Optimization and systems theory*, vol. 104, 2007. cited on pp. 54, 121
- 159 Zegard, T. and Paulino, G. H., "Grand—ground structure based topology optimization for arbitrary 2d domains using matlab," *Structural and Multidisciplinary Optimization*, vol. 50, 2014, pp. 861–882. cited on p. 56
- 160 Smith, H. and Norato, J. A., "A matlab code for topology optimization using the geometry projection method," *Structural and Multidisciplinary Optimization*, vol. 62, no. 3, 2020, pp. 1579–1594. cited on pp. 71, 75
- 161 Reddy, J. N., *Mechanics of laminated composite plates- Theory and analysis(Book)*. 1997. cited on p. 77
- 162 Carrera, E., "Theories and finite elements for multilayered, anisotropic, composite plates and shells," *Archives of computational methods in engineering*, vol. 9, 2002, pp. 87–140. cited on pp. 77, 146

- 163 Ramos, A. S. and Paulino, G. H., "Filtering structures out of ground structures—a discrete filtering tool for structural design optimization," *Structural and Multidisciplinary Optimization*, vol. 54, 2016, pp. 95–116. cited on p. 111
- 164 Groen, J. P. and Sigmund, O., "Homogenization-based topology optimization for high-resolution manufacturable microstructures," *Internat. J. Numer. Methods Engrg.*, vol. 113, 2017, pp. 1148–1163. DOI: 10.1002/nme.5575 cited on p. 111
- 165 Smith, H. A. and Norato, J. A., "Geometric constraints for the topology optimization of structures made of primitives," *SAMPE 2019-Charlotte, NC, May 2019*, 2019. cited on p. 115
- 166 Dean III, D. C., O'Muircheartaigh, J., Dirks, H., Waskiewicz, N., Lehman, K., Walker, L., Han, M., and Deoni, S. C., "Modeling healthy male white matter and myelin development: 3 through 60 months of age," *Neuroimage*, vol. 84, 2014, pp. 742–752. cited on p. 118
- 167 Petersson, J., "A finite element analysis of optimal variable thickness sheets," *SIAM journal on numerical analysis*, vol. 36, no. 6, 1999, pp. 1759–1778. cited on p. 120
- 168 Guest, J. K., Prévost, J. H., and Belytschko, T., "Achieving minimum length scale in topology optimization using nodal design variables and projection functions," *International journal for numerical methods in engineering*, vol. 61, no. 2, 2004, pp. 238–254. cited on p. 141
- 169 Wu, J., Aage, N., Westermann, R., and Sigmund, O., "Infill Optimization for Additive Manufacturing—Approaching Bone-Like Porous Structures," *IEEE Trans. Vis. Comput. Graph.*, vol. 24, 2018, pp. 1127–1140. DOI: 10.1109/tvcg.2017.2655523 cited on p. 141
- 170 Lazarov, B. S. and Wang, F., "Maximum length scale in density based topology optimization," *Computer Methods in Applied Mechanics and Engineering*, vol. 318, 2017, pp. 826–844. cited on p. 141
- 171 Forward, C. and Kim, I. Y., "Layered fiber orientation optimization for continuous fiber reinforced polymer additive manufacturing using multi-material topology optimization," *Progress in Additive Manufacturing*, 2023, pp. 1–12. cited on pp. 144, 145
- 172 Fernandes, R. R., Werken, N. van de, Koirala, P., Yap, T., Tamijani, A. Y., and Tehrani, M., "Experimental investigation of additively manufactured continuous fiber reinforced composite parts with optimized topology and fiber paths," *Addit. Manuf.*, vol. 44, 2021, p. 102056. DOI: 10.1016/j.addma.2021.102056 cited on p. 144
- 173 Zhang, H., Wang, S., Zhang, K., Wu, J., Li, A., Liu, J., and Yang, D., "3d printing of continuous carbon fibre reinforced polymer composites with optimised structural topology and fibre orientation," *Composite Structures*, vol. 313, 2023, p. 116914. cited on p. 144

- 174 Almeida Jr, J. H. S., Christoff, B. G., Tita, V., and St-Pierre, L., "A concurrent fibre orientation and topology optimisation framework for 3d-printed fibre-reinforced composites," *Composites Science and Technology*, vol. 232, 2023, p. 109 872. cited on p. 144
- 175 Ichihara, N. and Ueda, M., "3d-printed high-toughness composite structures by anisotropic topology optimization," *Composites Part B: Engineering*, vol. 253, 2023, p. 110 572. cited on p. 145
- 176 Carrera, E., "C0 reissner–mindlin multilayered plate elements including zig-zag and interlaminar stress continuity," *International Journal for Numerical Methods in Engineering*, vol. 39, no. 11, 1996, pp. 1797–1820. cited on p. 147
- 177 Carrera, E. and Demasi, L., "Classical and advanced multilayered plate elements based upon pvd and rmvt. part 1: Derivation of finite element matrices," *International Journal for Numerical Methods in Engineering*, vol. 55, no. 2, 2002, pp. 191–231. cited on p. 147
- 178 Carrera, E. and Demasi, L., "Classical and advanced multilayered plate elements based upon pvd and rmvt. part 2: Numerical implementations," *International Journal for Numerical Methods in Engineering*, vol. 55, no. 3, 2002, pp. 253–291. cited on p. 147
- 179 Carrera, E., Cinefra, M., Petrolo, M., and Zappino, E., *Finite element analysis of structures through unified formulation*. John Wiley & Sons, 2014. cited on pp. 149, 154
- 180 Carrera, E., "Theories and finite elements for multilayered plates and shells: A unified compact formulation with numerical assessment and benchmarking," *Archives of Computational Methods in Engineering*, vol. 10, 2003, pp. 215–296. cited on p. 151
- 181 Biyikli, E. and To, A. C., "Proportional topology optimization: A new non-sensitivity method for solving stress constrained and minimum compliance problems and its implementation in matlab," *PloS one*, vol. 10, no. 12, 2015, e0145041. cited on p. 169
- 182 Aboudi, J., Arnold, S. M., and Bednarczyk, B. A., *Practical micromechanics of composite materials*. Butterworth-Heinemann, 2021. cited on p. 170
- 183 Eckrich, M., Arrabiyeh, P. A., Dlugaj, A. M., and May, D., "Structural topology optimization and path planning for composites manufactured by fiber placement technologies," *Compos. Struct.*, vol. 289, 2022, p. 115 488. DOI: 10.1016/j.compstruct.2022.115488 cited on p. 170

## *Appendices*

# A

## Examples for Multi-layered Variable-Stiffness Composite Laminate—Simple Overlap formulation

### A.1 Examples

For all three numerical examples—Bars made of continuous, unidirectional carbon-fiber-reinforced polymer (CFRP) aligned with the bar's axis are considered as carried out for previous examples. The simple overlap formulation is used, denoted by the gP-IAM notation.

Examples in Appendix A.1.1 Appendix A.1.2, and Appendix A.1.3 consider only in-plane loading conditions, which are further optimized for multi-layered VSCLs using simple overlap formulation.

Parameters for method-of-moving-asymptotes (MMA), employed for the optimization routine, using the default parameters described in Section 3.4. The void material is isotropic with Young's modulus  $E^{\text{void}} = 10^{-3}E_1$  and Poisson's ratio  $\nu^{\text{void}} = 0.3$ . During initialization, the radius of the bars is set to the average of their upper and lower bounds. The sizing variable is set to  $\alpha = 0.5$ , and the move limit is fixed to  $m = 0.02$  throughout the optimization process.

#### A.1.1 A square plate under bi-axial loading

The second example considered the bi-axial loading problem with an aspect ratio of 1 : 1; the volume fraction limit is set to 0.4. Since the problem is symmetrical, only a quarter of the geometry has been modeled as depicted in Fig. A.1. The whole plate has been initialized with 24 bars, and the design variables have been restricted within the following bounds.

$$\begin{Bmatrix} (0, 0) \\ 3 \\ 0 \end{Bmatrix} \leq \begin{Bmatrix} (\mathbf{x}_{b1}, \mathbf{x}_{b2}) \\ r_b \\ \alpha_b \end{Bmatrix} \leq \begin{Bmatrix} (100, 100) \\ 6 \\ 1 \end{Bmatrix} \quad (\text{A.1})$$

In Figure A.1, two methodologies, namely GP (as described in [126]) and LGP-AM with a simple overlap formulation, are compared

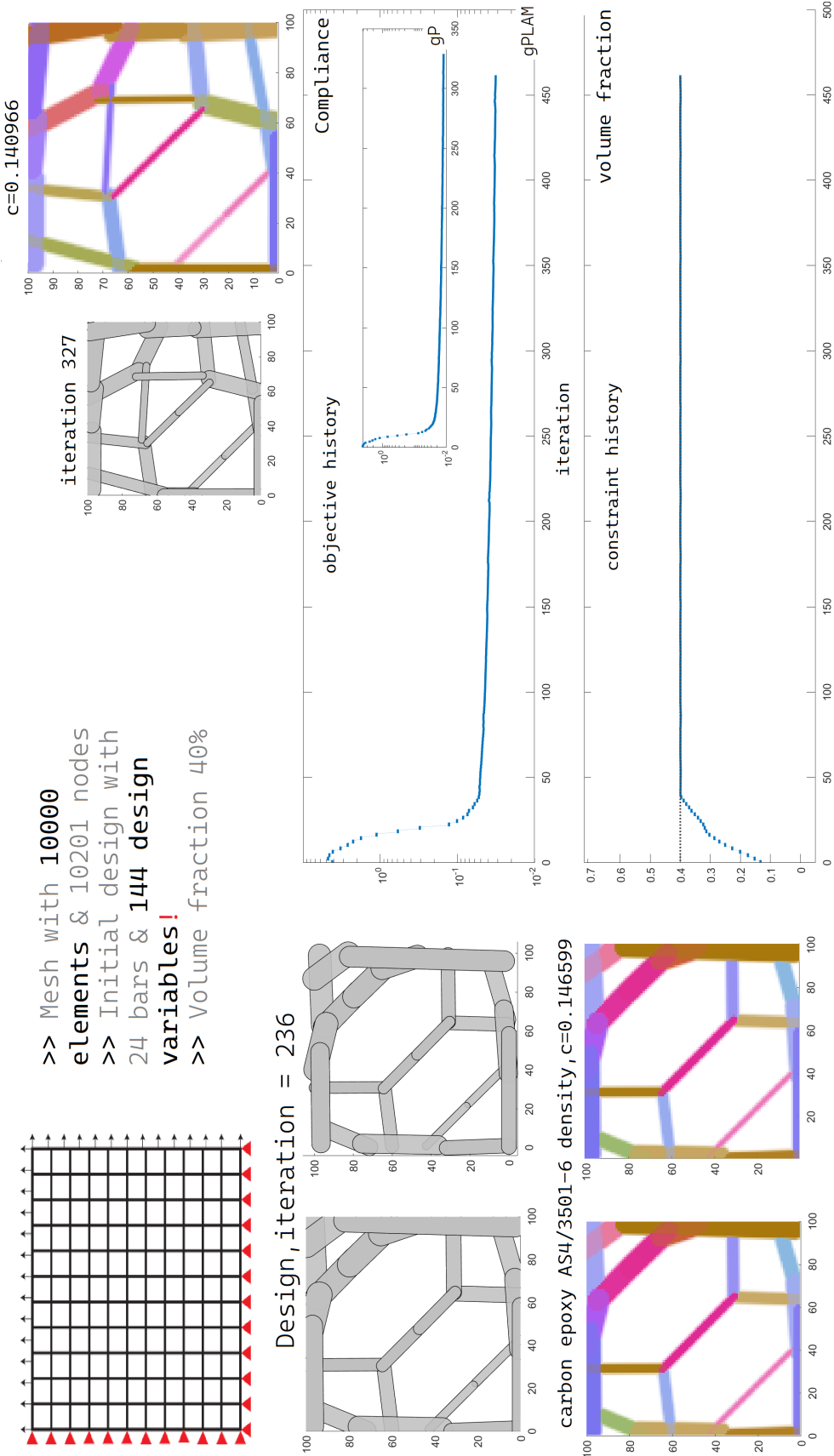


Figure A.1: Comparing GP and gP-IAM design for a plate under unit bi-axial load.

to showcase the modeling capabilities of overlapping FRBs in the GP method. The GP design and density plot are displayed in the top-right corner, while the LGP-AM plots can be seen in the bottom-right corner, and the positions of plots are referenced to the landscape view. The GP method is optimized for single-layer, whereas the LGP-AM optimizes for multilayered VSCLs; in this case, two-layer are optimized simultaneously.

It is worth noting that the multilayered LGP-AM formulation results in the same topology in both layers—layers' design sensitivities updates (Eq. (5.6)) are driven by reference displacement fields obtained from FSDT theory. When we compare the LGP-AM design with GP, we can notice only a slight difference in the stiffness of VSCL. However, the resulting topology is entirely different as expected. Unlike the discrete FRBs in GP, the LGP-AM design involves the formation of concatenate FRBs (like a sausage string) through simple overlap. This introduces fiber path variability in the structure.

Moreover, introducing overlapping FRBs results in a manufacturable design using conventional and additive techniques but also attains faster convergence by simultaneously seeking local orthotropic behavior in the design domain.

### A.1.2 A square plate under shear loading

The third example considered the shear loading problem with an aspect ratio of 1 : 1; the volume fraction limit is set to 0.4. The applied loading and boundary conditions are depicted in Fig. A.2. The whole plate has been initialized with 24 bars, and the design variables have been restricted within the following bounds.

$$\begin{Bmatrix} (0, 0) \\ 3 \\ 0 \end{Bmatrix} \leq \begin{Bmatrix} (\mathbf{x}_{b1}, \mathbf{x}_{b2}) \\ r_b \\ \alpha_b \end{Bmatrix} \leq \begin{Bmatrix} (100, 100) \\ 6 \\ 1 \end{Bmatrix} \quad (\text{A.2})$$

As seen in the previous example in section A.1.1, the multilayered LGP-AM formulation yields the same topology in both layers, which is depicted by the design and density plot at the bottom-right corner of Fig. A.2. In this example, the design attained by GP is comparatively stiffer than the one attained by LGP-AM, and the resulting topology is again entirely different for both methods. Further, topology with concatenate bars with branching (tree-like structure) attained by the LGP-AM is far richer than that of the GP method, without a trade-off in terms of manufacturability of the VSCL.

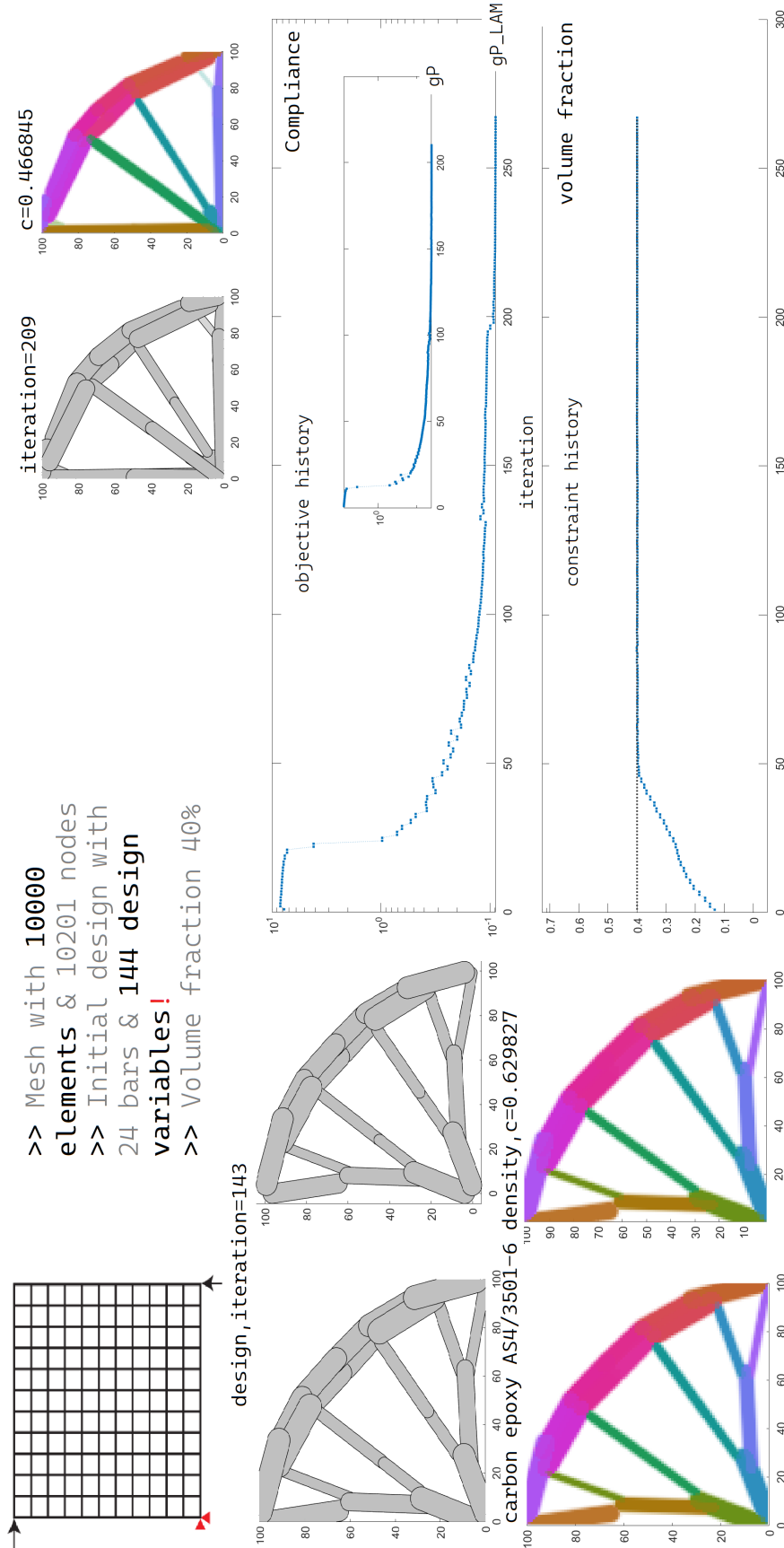


Figure A.2: Comparing GP and gP-LAM design for a plate under shear load.

### A.1.3 Variable volume fraction multi-layered VS-CFRP-Ls

For design variable volume fraction multi-layered VS-CFRP-L, this example considered the biaxial and shear loading problems with an aspect ratio of 1 : 1, with the volume fraction limit set to 0.4 and 0.3 for each layer. The whole plate has been initialized with 24 bars; the applied loading and boundary conditions and the bounds on the design variables are the same, as described in the previous examples, for each case, respectively.

The optimized multi-layered VS-CFRP-L for bi-axial and shear load is illustrated in Figure shown in Fig. A.3. Unlike previous examples,—each layer has the same topology—indicating the ability to optimize for multi-layered VS-CFRP-L with varying CFRP material volume fractions and introduce different topologies across each layer. Furthermore, the examples for in-plane loading conditions show that the layers adhere to the same CFRP material distribution for a fixed layer's volume fraction, which is possible due to the evaluation of membrane stiffness  $\mathbf{D}_{me}$  as a convex combination of layers in the composite laminate. This suggests that stacking FRBs with the same material orientation is preferable to stacking those with varying material orientations.

The same reasoning cannot be applied to the bending stiffness  $\mathbf{D}_{be}$  of the laminate due to the nonlinear material distribution along the stacking direction. In addition, using a simple overlap formulation results in poor local minima for out-of-plane loading conditions, as discussed in Chapter 5.

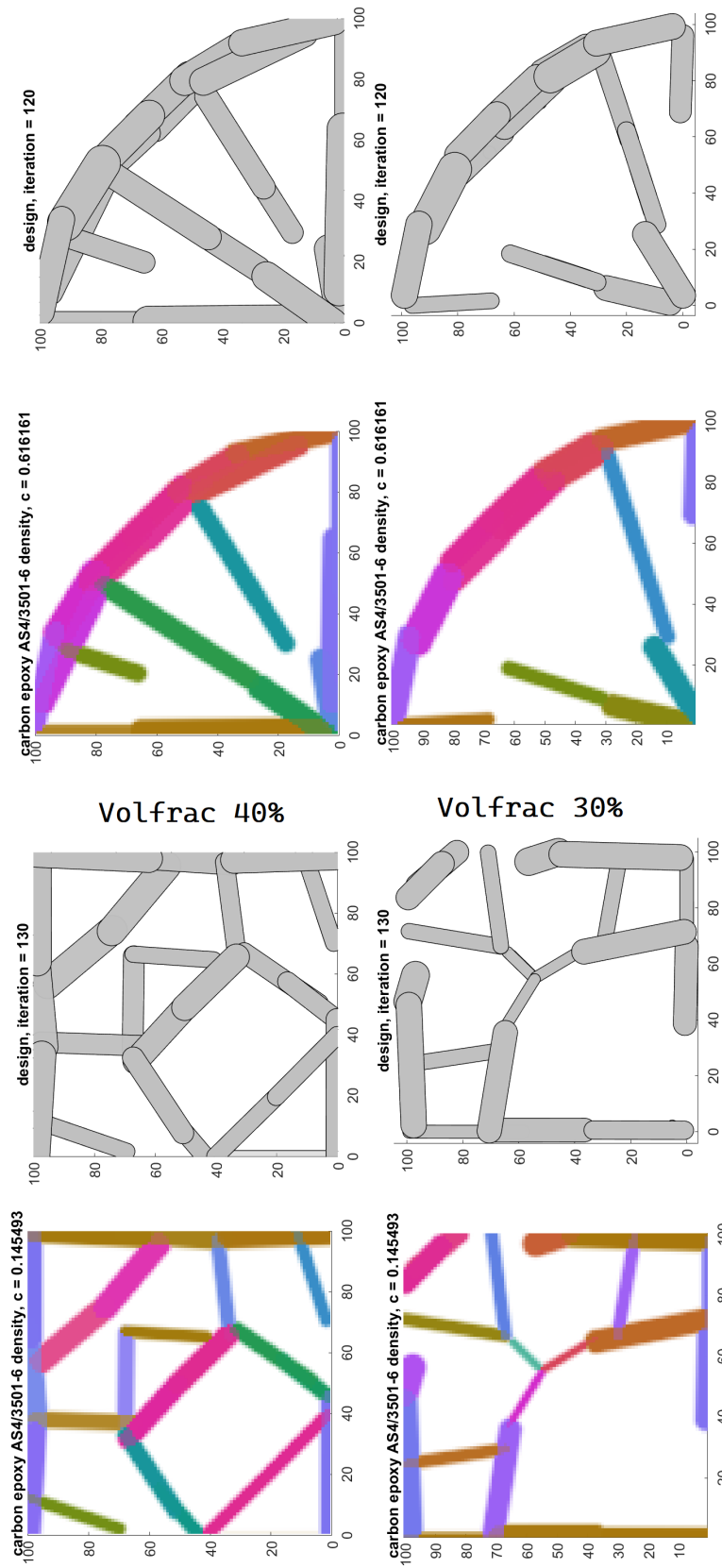


**Figure A.3:** Design and density plots for multi-layered VS-CFRP-L structures with variable volume fractions—analysis considers bi-axial and shear loading conditions and their respective boundary conditions.

# B

## Examples for Single layer Variable-Stiffness Composite Laminate—Overlap Criterion

In the Chapter 4, we discussed that allowing a less strict definition of overlaps (such as having a  $\rho_{b\omega_e}$  value of 0.5 or higher) would result in the formation of multiple overlapping FRBs that can achieve different fiber orientations in the design space, thus can also lead to complications in the manufacturing process. For completeness, the following results demonstrate the sensitivity of overlapping criteria toward the optimization process.

All the designs are attained using the same conditions defined in the ?? . Fig B.1 represents the design obtained for the initial condition defined in the example ?? . The final compliance achieved is 1.473194, and the design converged in 104 iteration, similar to optimized GP-AM method results (see Fig. 4.16), except that the topology enables long FRBs and comparatively several overlapping FRBs because of less restrictive definition of overlapping criterion.

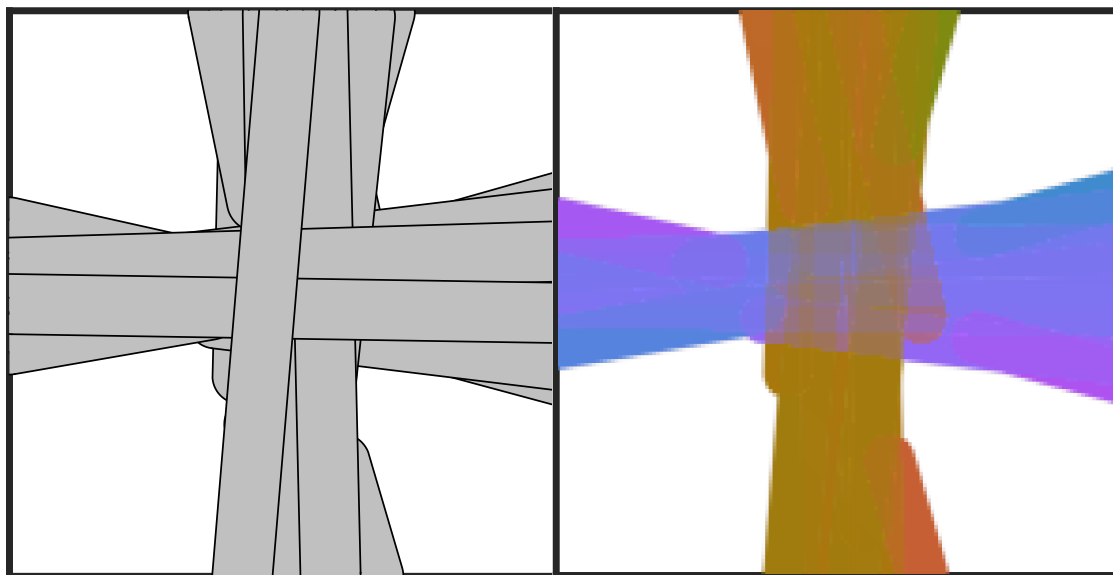


**Figure B.1: Bending**—The plot for volume fraction limit of  $\bar{v} = 0.50$

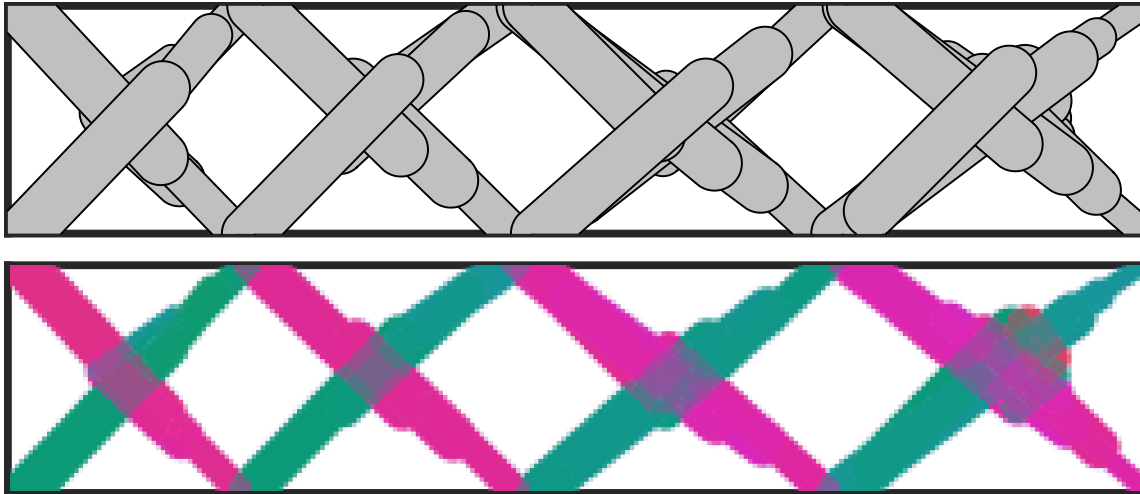


**Figure B.2: Torsion**—The plot for volume fraction limit of  $\bar{v} = 0.50$ . The final compliance achieved is 173.642046, and the design converged in 253 iterations.

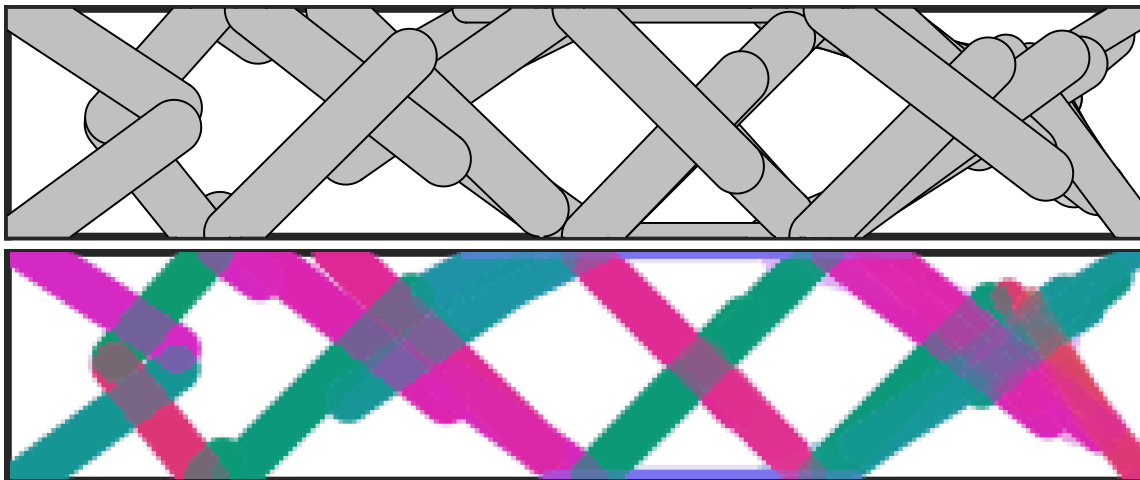


**Figure B.3: Torsion**—The plot for volume fraction limit of  $\bar{v} = 0.60$ . The final compliance achieved is 157.389650, and the design converged in 323 iterations.

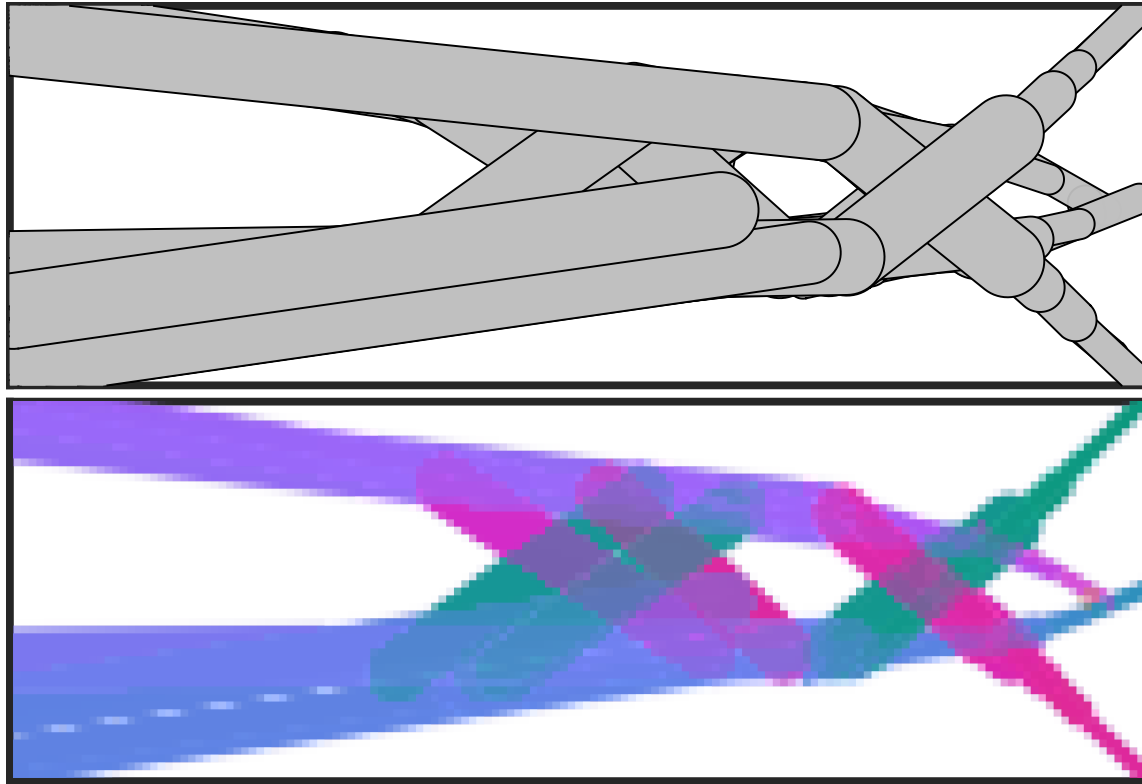


**Figure B.4: Multiload**—The plot for volume fraction limit of  $\bar{v} = 0.50$ . The final compliance achieved is 192.429452, and the design converged in 220 iterations.

Similarly, Fig B.2, B.3 represents the design for the same aspect ratio and boundary and loading conditions in the ?? and ??. Compared to the results obtained, using a less restrictive approach produces a more compliant design and slower convergence. Finally, Fig. B.4 represents the design for the aspect ratio of  $1 \times 3$  but considering boundary and loading conditions defined in the ??—the design resulted in excessive overlap, which makes it unsuitable for printing purposes.